博士論文

水同位体大気陸面結合モデルの開発及び同位体気候プロキシデータによる検証

（Development of stable water isotope incorporated atmosphere-land coupled model and comparison with climate proxies）

Atsushi Okazaki

岡崎 淳史

March 2016

Acknowledgments

The author is deeply grateful for Prof. Kei Yoshimura for his enthusiastic teaching, invaluable suggestions, and continuous encouragement throughout his master and PhD course. The author is also grateful to Prof. Taikan Oki for his helpful suggestions. The author is indebted to Prof. Masahide Kimoto, Prof. Toshio Koike, and Prof. Takeshi Nakatsuka, for their critical comments and constructive discussions. The author would not have completed the dissertation without their help. Thanks are extended to Prof. Ayako Abe-Ouchi, Prof. Hiroyasu Hasumi, Dr. Hyungjun Kim, Prof. Ryoichi Imasu, Prof. Kazuo Oki, and Prof. Masahiro Watanabe. The author also appreciates Dr. Naoyuki Kurita for his technical support. The author would like to acknowledge assistance offered by the members and ex-members of Oki laboratory, the Institute of Industrial Science, and of Division of Climate System Research, Atmosphere and Ocean Research Institute, the University of Tokyo.

Figures in this paper are produced by Grid Analysis and Display System, and NCAR Command Language. This study is partially supported by Research Fellowships of the Japan Society for the Promotion of Science for Young Scientists.

Finally the author would like to express his gratitude for his parents and sisters for their supports throughout his life.

Thesis Abstract

Knowledge about past climate change is invaluable to understand the climate system and to predict the future. Climate proxies have offered wide range of information on the climate of past which we cannot directly know because there are no instrumental records. Now, the paleoclimate have been becoming clear thanks to the reconstruction based on proxies. Basically what we can reconstruct from a proxy is one variable at the location where the proxy is sampled. To reconstruct the climate at not only the points where proxy observations are available but also the points where no empirical relation exists, recently data assimilation technique is beginning to be applied to the field of paleoclimate. Although all the previous studies assimilated reconstructed temperature, the temperature contains large uncertainty stems from the reconstruction method. Furthermore the assimilation of the reconstructed value does not use full information we could have otherwise. The assimilation of not reconstructed value but measured proxy data itself is one way to eliminate the uncertainty and to make the most of information in paleoclimatology. To directly assimilate proxy data, however, a forward model which predicts the proxy (proxy model) is necessary. Up to now, several proxy models for stable water isotope, which is one of the most major proxies, have been developed, but they have not been globally evaluated. In this study, to build a basis for proxy data assimilation, following studies are conducted. In Chapter 2, stable water isotopes are incorporated into a state-of-the-art general circulation model (GCM). After the rigorous evaluation of the GCM, proxy models are driven by the GCM output and evaluated in Chapter 3. In Chapter 4, the feasibility of proxy data assimilation is examined using isotopic data in precipitation. In Chapter 5, the feasibility of proxy data assimilation is examined by using the models developed in the previous chapters. The abstracts for each chapter are expanded below.

Chapter 2 is devoted to the development of an isotope enabled GCM. The author implemented stable water isotope into MIROC5. The model is evaluated for the present condition from the view point of isotopic spatiotemporal distribution. The spatial correlation and relative root mean square error for the mean field of isotope ratio in precipitation and atmospheric vapor are found to be the same level as those of temperature and precipitation. However the reproducibility of interannual variability in isotope ratio in precipitation is relatively worse than those of temperature and precipitation. On the other hand, the reproducibility is found to be the best among the existing isotope enabled GCMs, which is especially clear over the low latitudes. The reason for the high performance may be because of newly implemented precipitation scheme in MIROC5; indeed the

model showed the highest reproducibility for precipitation among the models. As for the isotopic composition in soil water, the seasonality is roughly comparable with the observation for the near surface layer, but that in deeper layer is found to be largely different from the observation. This suggests that the vertical water movement within the soil layer should be problematic. Since the water movement there plays an important role in simulating river discharge, this process should be evaluated more rigorously in the future.

In Chapter 3, proxy models are evaluated using the output of the isotope enabled GCM developed in Chapter 2 as their inputs. The isotope enabled GCM is nudged toward 20th Century Reanalysis to make possible the direct comparison between the simulation and the observation. Only the output of last 50 years is used for the evaluation to retain the reliability. The proxy models are used to simulate isotope ratio in tree ring cellulose and coral. As for ice core, the GCM simulated isotope ratio in precipitation is directly compared against observation data. The simulation and data are compared on the interannual timescale for all the proxies. The result shows that the reproducibility for tree-ring cellulose and coral is comparable with that of isotope ratio in precipitation with the metrics of temporal correlation; around 70% of the proxies are well reproduced by the models. Meanwhile, with less than 20% of the proxies reproduced, ice cores exhibited the lowest reproducibility. The reasons for this is partly due to relatively poor skill of the reanalysis used to force the GCM over the ice core drilling sites and deposition noise included in ice core data. Even though the reproducibility is somewhat limited by the quality of the input and/or the poor representation of the proxy models, the models seem to represent the key mechanisms in the proxies, especially for tree-ring cellulose and coral.

The feasibility of proxy data assimilation is examined in Chapter 4. Since this is the first challenge to assimilate temporally averaged isotopic information, the isotope ratio in precipitation is assimilated in an idealized way for the sake of simplicity. The data assimilation algorithm used in this study is the ensemble filtering modified to assimilate time averaged data. The results shown are promising. By assimilating the isotopic information, the analysis fields of temperature, precipitation, and pressure as well as isotope ratio in precipitation become closer to the truth than the first guess over almost all the globe. The skills for temperature, precipitation, and pressure are especially high over low latitude. The reason is because the isotope ratio in precipitation is largely affected by El Niño-Southern Oscillation (ENSO); indeed the first mode of the isotope ratio in precipitation is confirmed to be ENSO by empirical orthogonal function (EOF) analysis. Although the leading modes confirmed by the EOF analysis are only ENSO and North Atlantic Oscillation (NAO), the analysis reproduced the interannual variability in major climate indices e.g. Southern Annular Mode (SAM), Pacific North American (PNA) pattern, All Indian Summer Monsoon Rainfall and Sahel Rainfall. Moreover, the results of isotopic data assimilation show comparable or higher performance than the case in which reconstructed temperature is assimilated. Thus, proxy data assimilation is confirmed to work well, and the performance is better than the previous studies of paleoclimate data

assimilation.

Finally proxy data assimilation is conducted using the models developed and evaluated in Chapter 2 and 3 and the assimilation method used in Chapter 4. Here the assimilated variable is not isotope ratio in precipitation but that of proxy. First, the idealized simulation was conducted. The skill is found to be comparable with the isotope ratio in precipitation assimilated case. Successively the robustness of the result is examined by changing the experimental setting. In the first sensitivity experiment, simulation run is created by the simulation forced by modeled SST. The modeled SST is obtained from the historical simulation by atmosphere-ocean coupled version of MIROC5. Here the truth run is created by the simulation forced by the observed SST as in the previous experiments. Thus the discrepancy between the simulation and the observation is intentionally enlarged in this experiment. Even with larger difference between them, the skill does not differ significantly from the previous experiment. This is because the spatial pattern of modeled ENSO is similar to the observed pattern. Next, the observed proxy data is assimilated to the simulation which is forced by the modeled SST. Thus this experiment is genuine proxy data assimilation. Although the reproducibility becomes entirely worse, the decrease in skill can be explained by the use of the modeled SST and the temporally short coverage of the proxy data. Notable result is that the reproducibility for ENSO; the correlation coefficient between the analysis and the observation is as high as 0.6 ($p < 0.01$). Therefore, we can expect to reconstruct ENSO activity fairly well by proxy data assimilation. Furthermore because the reproducibility is highly sensitive to the spatial distribution of proxy observation, the reproducibility of proxy data assimilation is expected to be better by increasing the number of proxies to be assimilated.

The final chapter summarizes the thesis.

和文要旨

過去の気候変動に関する知見は，気候システムを理解し，将来を予測するうえで重要である．測器観測が無い時代の気候を直接知ることはできないが，気候の代替指標（プロキシ）を用いた復元により過去の気候変動がおおまかに明らかになりつつある．プロキシから復元される情報は基本的にはプロキシが得られる場所におけるあるひとつの変数についてであるが，プロキシが得られない場所・あるいはプロキシと関係性が得られない変数についての尤もらしい情報を得るために，最近では古気候研究においても観測とシミュレーションを融合するデータ同化が利用され始めている．これまでの古気候データ同化はプロキシから復元された気温を同化してきたが，復元気温には大きな不確実性が含まれるため，プロキシを直接同化することが望まれている．一方，プロキシを同化するためには，プロキシのフォワードモデル（以下プロキシモデル）が必要である．代表的なプロキシである水の同位体比（δD，δ18O；以下同位体）について，既にいくつかのプロキシモデルが提案されているが，これらの検証は十分に行われていない．これはプロキシモデルを走らせるのに必要な同位体の長期観測データが存在しないためであった．以上のような背景を鑑み，本研究ではプロキシデータ同化の基礎を築くことを目的とし，以下の研究を行った．まず第二章では同位体の振る舞いを最新の大循環モデル（GCM）に導入し，信頼性の高い同位体データを作成した．第三章では，このデータを用いてプロキシモデルの検証を行った．第四章では降水同位体情報を用いたデータ同化の実現可能性について検討を行った．第五章では，開発・検証を行ったモデル群およびデータ同化技術を用いてプロキシデータ同化の実現可能性について検討を行った．以下に各章の詳細を記す．

第二章では，同位体大気陸面結合 GCM の開発を行った．同位体を導入したモデルは MIROC5 である．本モデルは IPCC にも用いられている GCM であり，その信頼性は高い．同位体はパッシブなトレーサーであり他変数には影響を与えないため，ここでは同位体の再現性についてのみ記述する．再解析データを用いてナッジングをした実験から得られた降水同位体比，水蒸気同位体比，土壌水同位体比について観測と比較し，検証を行った．年平均値の空間分布については，降水同位体比，水蒸気同位体比の再現性は，気温や降水量と同程度であった．しかし年々変動の再現性を気温や降水量の再現性と比較すると，降水同位体比の再現性は劣ることが分かった．一方で，降水同位体比年々変動の再現性を既

往の同位体 GCM と比較すると，本モデルは最高の成績を示し，この傾向は低緯度において顕著であった．これは同地域における降水量の再現性が優れているためであると考えられる．土壌水同位体比についても，地表付近では観測と合致する季節変化を再現することができた．一方で，深い点の土壌水同位体比の季節変化は再現されず，土壌中の水の移動が適切に再現されていない可能性が示唆された．土壌水同位体比の観測例は少ないため，本研究では二点のみでしか比較を行うことができなかったが，土壌中の水の移動は，河川流量等を再現するうえで非常に重要であるため，今後はより精力的な検証を行い，モデルを鍛える必要があるだろう．

第三章では，上記の同位体 GCM の出力を入力値として用いてプロキシモデルの検証を行った．同位体 GCM シミュレーションは二十世紀再解析を用いてナッジングを行うことで，シミュレーション結果の時系列を観測値と直接比較できるようにした．検証には再解析の信頼性が比較的高い過去五十年の出力を用いたシミュレーション結果について検証を行った．対象としたプロキシはアイスコア，サンゴ，樹木セルロースの同位体比であり，サンゴおよび樹木セルロース同位体比については，同位体 GCM の出力を入力値としたプロキシモデルのシミュレーション結果と比較し，アイスコア同位体比については同位体 GCM の出力である降水同位体比と直接比較した．この結果，およそ七割程度のサンゴおよび樹木セルロースについて同位体比の年々変動を再現することができた．これは降水同位体比と同程度の再現性であり，プロキシモデルが十分にロバストであることを確認できた．一方アイスコアについては再現性が確認できたのは二割程度であった．これはアイスコアが採掘された地点における同位体 GCM の再現性が低いためであった．このことは極域における循環場の再現性が二十世紀再解析より優れる NCEP 再解析を用いたナッジングに用いることで同地域における循環場およびアイスコア同位体比の再現性が向上したことからも確認できた．加えて積雪量が少ない地点で採取されたアイスコアの再現性が低い傾向も確認され，既往研究で指摘されているように，積雪量が少ない地点で採取されたアイスコア同位体比は堆積過程における影響を受けていることも示唆された．今後はプロキシ採取地点における同位体の長期観測を行う事でこれらの影響を切り分けて評価することと，堆積過程を包括的に表現する堆積モデルを開発することが求められる．

第四章では，プロキシデータ同化の実現可能性を検討した．同位体情報を古気候データ同化に用いた研究は過去に例を見ないため，まずは実装および結果の解釈が容易な降水同位体比を同化する場合について，理想化実験の枠組みで評価した．プロキシの時間解像度を考慮して，降水同位体比の年平均値を同化した．ここで，降水同位体比は全 GNIP 観測点で欠損なく観測情報が入手可能であることを仮定した（全 349 点）．用いたデータ同化アルゴリズムはアンサンブルカルマンフィルタを基礎としたものであるが，同化する変数の時

間解像度がモデルの予測可能時間よりもはるかに長いことから，データ同化の結果をシミュレーションにフィードバックしない「オフラインデータ同化」と呼ばれる考え方を採用しており，これに合わせて変更が加えられている．降水同位体比を同化することにより，対象としたすべての変数（降水同位体比，気温，降水量，海面気圧）について，ほぼ全球で第一推定値より解析値が真値に近づくことが確認された．降水同位体比以外の変数については低緯度において特に高い再現性が確認された．これは降水同位体比が ENSO のシグナルを強く反映しているためであることが主成分分析から明らかになった．全球を対象とした主成分分析から確認できた降水同位体比の主たるモードは ENSO および北大西洋振動だけであったが，降水同位体データ同化の結果では，これらに以外にも，南半球環状モードや太平洋・北米パターン，アジアモンスーン降水量，西アフリカモンスーン降水量等の主たる気候指標の年々変動を精度よく再現した．これは降水同位体比が，広域の気温や降水量に影響を受けていて，豊富な情報を保持していることを示している．実際，復元気温を同化した場合に比べて，より多くの現象・変数を精度よく再現できることが確認できた．

第五章では，第二章および第三章で開発および検証を行ったモデル群と第四章で用いたデータ同化手法を用いて，プロキシデータ同化を行った．ここでは同化する変数は降水同位体比ではなく，プロキシ同位体比である．まず前章と同様に，理想化実験を行った．この結果，降水同位体比を同化した場合とほぼ変わらないスキルを得ることができた．さらに，これらの結果がどの程度ロバストなものであるか，実際のプロキシデータ同化の条件に近づけていったときに再現性がどの程度変化するかを調査した．実際の条件とは，観測 SST が存在せず，プロキシデータのみが入手可能であるような状況である．まず観測 SST が存在しないという条件を考慮し，シミュレーションはモデル SST を用いた実験から作成した．観測値はこれまでと同様に観測 SST を用いた実験から作成している．モデル SST には大気海洋結合版 MIROC5 のヒストリカル実験を用いた．この実験による再現精度については，これまでの実験と比べて大きな変化は見られなかった．これはモデル SST の ENSO の空間パターンが現実とよく似ていることによる．続く実験では，モデル SST を用いた実験から作成したシミュレーションと実際のプロキシデータの融合を行った．この実験設定は，実際のプロキシデータ同化そのものである．この結果，同化スキルは，全体的に低下したものの，その低下幅は，モデル SST を使用したことと，プロキシデータには欠損があることで説明できる程度であり，129 地点のデータを同化するだけで 30%以上の面積における気温を有意に再現することができた. とくに ENSO の再現性は, 相関係数 0.6（$p < 0.01$）以上を保っており, プロキシデータ同化を用いた ENSO の再現性には大きな期待が持てる．さらに，プロキシデータ同化により再現される空間パターンは，プロキシの空間分布によって大きく変化することが分かっているが，これらの結果から，今後プロキシ情報が拡充

されていくことにより，プロキシデータ同化の精度はさらに向上していくことが期待される．

第六章には全体のまとめを示した．

Publication list

Chapter 2

- 岡崎淳史，芳村圭，同位体大循環モデルの同位体境界条件への応答の定量的評価，水文・水資源学会 2014 年度総会・研究発表会，2014 年 9 月，宮崎.

Chapter 3

- Okazaki, A and K. Yoshimura, Time slice simulation for LIA and MCA with stable water isotopes and comparison with modern situation, PP31D-1179, AGU Fall Meeting 2014, San Francisco, US.

Appendix A

- Okazaki, A., Y. Satoh, G. Tremoy, F. Vimeux, R. Scheepmaker, and K. Yoshimura, Interannual variation of vapor isotope in western Africa and its relation to ENSO, Atmos. Chem. Phys., 15, 3193-3204, doi:10.5194/acp-15-3193-2015, 2015.

Appendix B

- Okazaki, A., P. J.-F. Yeh, K. Yoshimura, M. Watanabe, M. Kimoto, and T. Oki, Changes in Flood Risk under Global Warming Estimated Using MIROC5 and the Discharge Probability Index, J. Meteor Soc. Japan, 90, 4, doi:10.2151/jmsj.2012-405, 2012.

Contents

List of Figures

List of Tables

Chapter 1.

General Introduction

Global warming is one of the most pressing issues we must cope with. For the proper countermeasure, reliable future projection of climate is required. Studying paleoclimate is one of the strategies to enhance our understanding of climate system, which in turn contribute to more reliable climate simulation. It is expected that we can gain the insight about the sensitivity of the climate system to the external forcing and the behavior of the climate system internal variability through studying paleoclimate.

Two distinctive approaches have been taken in the field of paleoclimate; one is climate proxy based reconstruction, and the other is process based simulation. Here, the climate proxy is the indirect observation of past climate states (e.g. tree ring width). The former relies on the empirical relationship between proxy and climate observed in the present condition. Using the relationship, various climatic variables have been reconstructed (Mann et al. 1998; Shanahan et al. 2009; Cobb et al. 2013; Sinha et al. 2015). The latter is based on the physical lows given by climate models, and through which mechanism behind past climate changes have been analyzed (Ammann et al. 2007; Schurer et al. 2013). Although both approaches are powerful, the outcomes from each approach often contradict each other. For instance, the reconstructed pattern in temperature difference between Medieval Climate Anomaly (MCA) and Little Ice Age (LIA) shows La Niña like pattern but the simulated patterns do not (Fernández-Donado et al. 2013; Masson-Delmotte et al. 2013). Because both approaches have uncertainty stems from reconstruction methods, forcings, and models, it is difficult to attribute the reason for the discrepancy. How to fill the gap has been a big issue to reconstruct the reliable climate.

Stable water isotopes (HDO and $H_2{}^{18}O$) have long been used to reconstruct paleoclimate. Due to the differences in the thermodynamic properties, “heavy” and “normal ($H_2{}^{16}O$)” water is partitioned unevenly during phase changes depending on their environmental conditions. Therefore the ratio of isotopes (heavy to normal) in moisture, or in precipitation, records the integrated history of phase changes during its transport. As a consequence, isotopic ratio in precipitation and atmospheric vapor exhibit clear link with temperature and precipitation amount (Dansgaard 1964; Rozanski et al. 1993). As such, paleoclimate have been reconstructed by using the isotope ratios recorded in climate archives which contain paleo-precipitation (e.g. ice core). The beauty of the stable water isotope as climate proxy is that the behavior of stable water isotopes can be intimately implemented into general circulation model (GCM) since the ratio is determined purely by hydrological circulation. This enables us to explain quantitatively the variability recorded in climate archives. The first isotope enabled GCM is developed by

Joussaume et al. (1984). In his pioneering work, he described the possibility of isotope enabled GCM as following way: "*Once it has been validated against modern data, AGCM isotope modeling can be used in palaeoclimatic simulations; this may be a first step towards a better interpretation of isotope changes from ancient to present times in terms of changes in atmospheric parameters*". Since that time plentiful number of studies investigated how climatic information is imprinted into isotope ratio in precipitation (Schmidt et al. 2007; Lee & Fung 2008; Risi et al. 2008; Yoshimura et al. 2008). Thus, isotope enabled GCM is expected to reduce the uncertainty of climate reconstruction by providing proper interpretation of isotopic signals. Furthermore the simulation may be directly validated by comparing the simulated and observed isotopic ratio.

As Joussaume et al. (1984) noted, however, the climate archives do not directly record isotopic information of precipitation; the signals may be further modified due to the physical, chemical, and/or biological property of the archives. Therefore, what we have to investigate or to compare with is the isotopic composition in the climate archives. For that purpose, "forward proxy models" are necessary.

Data assimilation is another way to fill the gap between model simulation and reconstructions (Goosse et al. 2010). Though the technique for weather forecast cannot directly be used for paleoclimate simulation with a much smaller number of observations or climate proxies (Bhend et al. 2012), recently several studies have started applying the technique to the paleoclimate field (e.g. H. von Storch et al. 2000; Goosse et al. 2006; Crespin et al. 2009). All the previous studies assimilate temperature reconstructed from climate proxies. To avoid the reconstruction uncertainty, however, the direct assimilation of proxy data is desirable (Hughes & Ammann 2009; Yoshimura et al. 2014). For this purpose, again, forward proxy models are necessary.

Hughes and Ammann (2009) claimed that it is essential for the forward models to be as simple as possible while still capturing the essential features of the relationship with climate, and that they should be validated rigorously against a wide range of observations of climate proxies. At this stage, such models are relatively few, and many of them have not been thoroughly evaluated (Evans et al., 2013) due to the lack of isotopic data to run the models. Therefore the evaluation of the forward proxy models and the development of reliable isotopic data are the urgent tasks.

The objective of this study is to develop a basis for proxy data assimilation. To achieve the goal, the author first implements stable water isotopes into a state-of-the-art GCM to create the reliable isotopic dataset. Next, forward proxy models proposed before now are rigorously evaluated using the output of isotope enabled GCM as their input. Furthermore, a possibility of the combined use of the isotope enabled GCM and the proxy models are examined. Brief descriptions of each chapter are shown below.

The second chapter introduces stable water isotopes into a state-of-the-art GCM, MIROC5 (Watanabe et al., 2010), and evaluates its performance. The purpose of the development is to produce realistic isotopic information than ever. Despite CMIP5 generation of GCMs outperform previous generations, the development of isotope enabled GCM has been recently stopped. Considering that CMIP5 experimental design includes paleoclimate simulations and isotope enabled GCM is a powerful tool for such

simulations, it is worthwhile to update isotope enabled models.

The third chapter evaluates forward proxy models by using the output of GCM developed at Chapter 2 as their input. Following the suggestion by Hughes and Ammann (2009) as many as possible proxies are used to test the proxy models. The comparison is made for isotope ratio in ice core, coral, and tree ring cellulose on the interannual timescale by considering the temporal resolution of the proxies and the duration of the simulation. Especially the focus will be on tree ring cellulose, because of its novelty. After the evaluation, the proxy models are analyzed to understand the factors controlling the proxies.

The feasibility of isotopic data assimilation is examined in Chapter 4. In this chapter, precipitation isotope is first assimilated to the simulation on the interannual timescale. The assimilation algorithm is largely different from that used in weather forecast. Thus the assimilation system is evaluated in an idealized way.

Finally, Chapter 5 examined the proxy data assimilation using forward proxy models developed and evaluated in Chapter 2 and 3 and data assimilation technique evaluated in Chapter 4 as a conclusive part of this study.

In this study the stable isotopes are expressed in δ notation which is defined as

$$\delta = \left(\frac{\mathrm{R_{sample}}}{R_{standard}} - 1\right) \times 1000\ [‰] \tag{1.1}$$

where R denotes the isotope abundance ratio (R=[number of heavy isotopic molecules]/[number of normal molecules]). Note that R is always written as the ratio of the heavy isotope to the right isotope. Usually R_{VSMOW} (VSMOW: Vienna Standard Mean Ocean Water) is used as the standard. In this study the isotope ratio will be presented in the δ notation as following $\delta^{18}O$ and δD for $H_2{}^{18}O$ and HDO respectively. In case abundance ratio is used, it will be positively expressed in R notation.

Oxygen isotope ratio in mineral and rocks have been reported in δ notation but different standard from VSMOW has been used. For isotope ratio in calcium carbonate, the standard is from Pee Dee Belemnite (PDB). To make the story simple, the entire isotope ratio will be expressed with respect to VSMOW scale. To convert the ratio, following equation is used (Friedman and O'Neil, 1997).

$$\delta^{18}O_{VSMOW} = 1.03086 \times \delta^{18}O_{PDB} + 30.86 \tag{1.2}$$

Also the term "isotope ratio" stands for stable water isotope ratio, unless otherwise noted.

Chapter 2.
Implementation of stable water isotopes into GCM

2.1. Introduction

Since the work of Joussaume et al. (1984), atmospheric general circulation models (GCM) equipped with stable water isotopes have been used to investigate the relationships between the isotopic composition in precipitation and climate. Up to now, more than dozen of GCMs have been equipped with water isotopes (Table 2-1). Two points are clear from the table. First, the development of new isotope enabled GCM have been stopped since Werner et al. (2011) (note that isotope enable Earth System Models have been developed (Roche 2013; S Dee et al. 2015)). On the other hand the improvements in GCMs are clearly shown in the Intergovernmental Panel on Climate Change (IPCC) Fifth Assessment Report (AR5; IPCC 2013). Considering that the one of the objectives using isotope enabled GCMs is to validate the model in paleoclimate simulation (Pausata et al. 2011; Liu et al. 2012; Caley et al. 2014) or their physical parameterization (Schmidt et al. 2005; Risi et al. 2012; Risi et al. 2013), water isotope should be implemented into the latest version of the GCMs.

The second point is that few models take into account the isotopic fractionation processes over land. Historically evaporation is assumed to occur without fractionation over land since the time of the first isotope enabled GCM. This assumption was based on the work of Zimmerman et al. (1967) who found plant transpiration results in practically no enrichment. The models thus assume that transpiration is a dominant component of evapotranspiration. On the other hand, fractionation does occur during evaporation from bare soil. Allison & Hughes (1983) observed that the soil water is strongly enriched in heavy isotopes compared with precipitation in semi-arid area of southern Australia, with maximum enrichment as high as 9 ‰ for oxygen isotope. Up to now, a few papers investigate the impact of land surface processes using GCMs. The first example to test the model sensitivity to the assumption is conducted by Jouzel et al (1991). They compared the result assuming that all the continental evaporation is from transpiration (fractionation does not take place) over land and the other assuming all the continental evapotranspiration is from evaporation (fractionation takes place). The results were largely different and up to 6 ‰ decrease in precipitation $\delta^{18}O$ was found in over North America and Siberia. Although the experimental design is unrealistic, the sensitivity may not be small. On the other hand, Aleinov et al. (2006) and Haese et al. (2013) conducted the similar sensitivity experiments and

concluded that the impact of isotopic fractionation over land on the precipitation isotope is very limited, whereas the impact on soil moisture isotope is huge (Haese et al. 2013; Kanner et al. 2013).

More important reason that we have to take into account the effect is that many terrestrial proxies (e.g. isotope ratio in tree-ring cellulose and speleothem) are not formed in direct isotopic equilibrium with precipitation, but rather with soil water which may be affected by preferential loss of light isotope via evaporation. To better understand the variability in isotope ratios in climate proxies in consistent with atmospheric processes, the fractionation over land surface should be included.

In this paper, the stable water isotope behavior is implemented into a state-of-the-art GCM, the fifth version of Model for Interdisciplinary Research on Climate (MIROC5; Watanabe et al. 2010). The model has been developed jointly at the Atmosphere and Ocean Research Institute (AORI), University of Tokyo; National Institute for Environmental Studies (NIES); and Japan Agency for Marine-Earth Science and Technology (JAMSTEC).

The main goal of this chapter is to evaluate the general reproducibility of the model. Since one of the future applications of the model is to create dataset to run forward proxy models, the reproducibility on the interannual timescale, which is the major temporal resolution of proxies, will be especially focused. For that purpose, nudging technique is applied in this study to fully exploit the limited data. The secondary goal is to evaluate the impact of isotopic fractionation over land surface on atmosphere (e.g. precipitation and vapor) and on land (e.g. soil moisture).

This chapter is constructed as follows: The second part of the chapter will describe the model. In Section 2-3, I evaluate the simulation of the isotopic composition for the present day climatology, and interannual variability. Subsequently, I evaluate the impact of isotopic fractionation over land surface. Conclusion and perspective will follow in Section 2-5.

Table 2-1 List of GCMs equipped with stable water isotopes. ATM, OCN, and LND stand for atmosphere, ocean, and land. The component to which isotopic fractionation is introduced is checked.

GCM	Reference	Model component		
		ATM	OCN	LND
LMD	Joussaume et al. (1984)	x		
GISS	Jouzel et al. (1987)	x		
ECHAM3	Hoffmann et al. (1998)	x		
Genesis	Mathieu (2002)	x		
MUGCM	Noone & Simmonds (2002)	x		
GISS-ModelE	Schmidt et al. (2005)	x	x	x
CAM2	Lee et al. (2007)	x		
IsoGSM	Yoshimura et al. (2008)	x		
HadCM3	Tindall et al. (2009)	x	x	
LMDZ4	Risi et al. (2010)	x		[a]
ECHAM5	Werner et al. (2011)	x		[b]

[a](Risi et al. 2013) coupled the atmospheric component with isotope enabled land surface model ORCHIDEE. [b](Haese et al. 2013) coupled the atmospheric component with isotope enabled land surface model JSBACH.

2.2. Model description

Isotopic processes are implemented into atmospheric and land surface components of a GCM, MIROC5 (Watanabe et al. 2010). Even though the previous version of the model MIROC3.2 (Hasumi & EMORI 2004) showed mean states that were relatively close to the average of coupled GCMs (CGCM) participated in Coupled Model Intercomparison Project Phase 3 (CMIP3), there were deficiencies in the natural variability and climate sensitivity. Thus most parts of the model have been updated with new parameterization schemes in MIROC5. The updates include parameterization for cumulus convection and cloud and cloud microphysics. With the new schemes, improvements are found in precipitation, zonal mean atmospheric fields, equatorial ocean subsurface fields, and the simulation of El Niño-Southern Oscillation (ENSO) (Watanabe et al., 2010). Though some of the previous versions of the MIROC have been equipped with stable water isotopes (Numaguti, 1996; Kurita et al., 2011; Ishizaki et al., 2012), much new physics has been incorporated into the model since that time as described above, and these should have considerable effects on the isotope signal.

Here the isotopic implementation is detailed. In the source codes, all species and transformation

process of $H_2{}^{16}O$ have been duplicated for HDO and $H_2{}^{18}O$. The implementation manner of isotopes into the atmosphere is based on Jouzel et al. (1987) as is the case in the other isotope-GCMs. The implementation into cloud micro physics is based on Federer et al. (1982) and Blossey et al. (2010). For the land surface, Yoshimura et al. (2006) is referred. For the processes which does not involve phase transition will not be included in the following part.

2.2.1. **Large scale condensation**

In this scheme, as in classical isotope incorporated large scale condensation scheme, the liquid condensate is formed in isotopic equilibrium. When vapor condenses to ice, a kinetic fractionation occurs because the air is supersaturated with respect to ice. Effective fractionation is expressed as a function of the equilibrium fractionation factor (α_{eq}), molecular diffusivities, and the supersaturation ratio over ice (S_{ice}) following Jouzel and Merlivat (1984). The effective fractionation (α_{eff}) is expressed as:

$$\alpha_{\mathrm{eff}} = \alpha_{\mathrm{eq}} \left[\frac{S_{ice}}{1 + \alpha_{eq}(S_{ice}) D/D_i} \right] \tag{2.1}$$

where D and D_i denote the molecular diffusivity of $H_2{}^{16}O$ and heavy isotopes (HDO or $H_2{}^{18}O$) in air. S_{ice} is here parameterized as following (Jouzel and Merlivat, 1984):

$$\mathrm{S_{ice}} = 1 - kT \tag{2.2}$$

where T is temperature in Celsius degree, and k is tunable parameter (note that it must be positive). The parameter k is originally proposed to be k=0.003, but the value used is different by model by model (ranging from 0.002 to 0.005). The parameter has large impact on deuterium excess (d-excess defined as $\delta D - 8\delta^{18}O$). The value of 0.003 is chosen in this study, and supersaturation is set to occur with temperature below -15°C.

The new large scale condensation scheme takes into account cloud microphysics. Thus isotopic interaction between vapor, liquid, and solid phases are incorporated into the scheme for the microphysical treatment following Federer et al. (1982) and Blossey et al. (2010). The newly added processes include homogenous and heterogeneous nucleation of ice, deposition and evaporation of ice, riming of liquid water by ice, melting of snow, and evaporation of rain (Wilson & Ballard 1999). The homogenous and heterogeneous nucleation of ice, riming of liquid water by ice is not accompanied by isotopic fractionation since the freezing time of droplets is so short that isotopic exchange does not take place (Federer et al. 1982). In those processes, the mass exchange is in proportion to their relative concentration in the source species. On the other hand, deposition and evaporation of ice are accompanied

by fractionation. According to Jouzel et al. (1975), the isotope ratios are distributed unevenly within individual particles of cloud ice, snow and graupel. Since the molecular diffusivity in the solid phase is so small that it would be expected that the isotopic content of the ice vary from layer to layer as the ice is deposited from vapor of varying isotopic content and during differing conditions. In the present simulations, however, this effect is not accounted for, and alternatively the uniform distribution of isotope ratio within ice particle is assumed. This may be oversimplified but I do this because tracking the size and composition of differing layers within the ice would be cumbersome. When vapor deposits onto ice, kinetic fractionation is considered and the same equation as Eq. (2.1) is used for this. On the contrary no fractionation occurs during melting and sublimation because of low diffusivity in the ice.

2.2.2. **Cumulus convection**

Even though substantial changes have been made in convective scheme itself, and accordingly substantial changes of coding the cycling of the water isotopes are necessary for the scheme, isotope modeling approach used are similar to the previous models. In the scheme, the partitioning of isotopes during condensation is treated similarly to that in large scale condensation; liquid is formed in isotopic equilibrium and solid condensates are accompanied by kinetic effect.

Above the cloud base, isotopic interaction between condensates and vapor is treated as it is in the large scale condensation. Below the cloud base, however, a kinetic fractionation occurs when the liquid condensate evaporates. This effect is included following Stewart (1975):

$$m\frac{\mathrm{dR_r}}{dm} = \beta(R_r - \gamma R_v)$$
$$\beta = \frac{1-\mu}{\mu}, \gamma = \frac{\alpha_{eq}h}{1-\mu}, \mu = \alpha_{eq}\left(\frac{D}{D_i}\right)^n (1-h) \tag{2.3}$$

where m is volume of rain droplet, R_r and R_v are the isotopic ratio of droplet and ambient vapor, n is the degree of freedom which is assumed 0.58 (Gat 2000), and h is relative humidity. Considering that the relative humidity evolves from its initial value to a final value generally close to 1, the influence of this kinetic effect must decrease during the course of the precipitation event. The net effect can be parameterized by approximating h to be always at a constant value between its initial value, h_i, and 1 as in Jouzel et al. (1987):

$$\mathrm{h_{eff}} = 0.75 + 0.25h_i \tag{2.4}$$

Integrating Eq. (2.3) yields

$$\mathrm{R_r} = \epsilon\left[(R_{r0} - \gamma R_{v0})\left(\frac{m}{m_0}\right)^{\beta} + \gamma R_{v0}\right] + (1-\epsilon)R_{r0} \tag{2.5}$$

$$R_v = [R_{v0} + (R_{r0} - R_r)m]/q$$

where subscript 0 indicates initial value before the isotopic exchange or evaporation occurs, and q is the volume of the vapor. ε is the fraction of the droplets reaching the isotopic equilibrium state. It is arbitrary assumed that ε=45% for convective rain and 95% for large scale condensation following Hoffmann et al. (1998). This parameter is determined with the consideration that convective precipitation produces primarily large drops, which takes longer time to equilibrate with ambient vapor and that large scale clouds produce small drops equilibrating nearly completely because of slow falling speed and fast equilibration time.

2.2.3. **Dry convection**

In case dry convection or turbulent involves condensation, the partitioning of isotopes during condensation is treated similarly to that in large scale condensation; liquid is formed in isotopic equilibrium and solid condensates are accompanied by kinetic effect.

2.2.4. **Evaporation from surface water**

The isotopic fractionation during evaporation from surface water (sea surface and lake surface) is expressed following Merlivat and Jouzel (1979):

$$R_E = \alpha_{k\_MJ} \frac{R_{sw}/\alpha_{eq} - hR_a}{1-h} \qquad (2.6)$$
$$\alpha_{k\_MJ} = \begin{cases} 1-a, & V < 7(m/s) \\ 1-(bV+c), & V \geq 7\ (m/s) \end{cases}$$

where R_E, R_{SW} and R_a are the isotope ratio of evaporative vapor, surface water and vapor above the water, respectively and V is surface wind speed. Constants of a, b, and c for $\delta^{18}O$ and δD is summarized in Table 2-2.

Table 2-2 Parameter set for calculation of isotopic content in evaporation from surface water (Merlivat and Jouzel, 1979).

isotope	a	b	c
$\delta^{18}O$	0.006	0.000285	0.00082
δD	0.00528	0.0002508	0.00072

2.2.5. **Land surface processes**

The isotopes are also implemented into land surface scheme. This study uses an updated-version of Minimal Advanced Treatments of Surface Interaction and RunOff (MATSIRO), which is the same as the one used in MIROC5. First of all I introduce the previously developed isotope equipped version of MATSIRO (Yoshimura et al. 2006), since isotopic treatment is largely unchanged from this version. Then the modification from the old version is followed. Note that coupling of land and atmospheric component of MIROC with stable water isotopes has never been conducted, and this is the first case.

The previous version of model consists of five soil layers down to a 4-m depth, single canopy layer with five inner leaf layers and one trunk layer, and up to three snow layers. The surface fluxes of water are written in the bulk formulae. When phase changes at any surface (i.e. soil, soma, canopy, and snow) occur in the model, equilibrium fractionation and kinetic fractionation are taken into account. General form of the surface flux is written as follows (Takata et al. 2003; Yoshimura et al. 2006):

$$\begin{aligned} \mathrm{F} &= \rho \mathrm{C}|V|(hq_{sat}(T) - q_a) \\ \mathrm{F_i} &= \rho C_i|V|(hq_{sat}(T)\alpha(T)R - q_a R_a) \end{aligned} \tag{2.7}$$

where F is a turbulent flux, ρ is density of atmosphere, V is the horizontal wind speed and h is a coefficient. F_i is the turbulent flux of isotope ($F_i=R_F F$). C and C_i are bulk change coefficients of water and isotopes fluxes, respectively. The isotope ratio in the flux is then calculated as;

$$\mathrm{R_F} = \frac{F_i}{F} = \frac{C_i}{C}\left[\frac{hq_{sat}(T)\alpha R - q_a R_a}{hq_{sat}(T) - q_a}\right] \tag{2.8}$$

Here the ratio of bulk coefficients (C_i/C) is the kinetic fractionation coefficient, and can be parameterized following Merlivat and Jouzel (1979) (α_{k_MJ} in Eq. 2.6). The corresponding parameters for each fluxes other than transpiration is summarized in Table 2-3. Please refer to Takata et al. (2003) for the list for bulk change coefficients. As summarized in the table, isotopic fractionation takes place for interception evaporation and sublimation from canopy layer, evaporation from the ground, and sublimation from the snow. When sublimation flux from frozen soil (not snow covered) occurs, its isotopic ratio is assumed to be the same as that of frozen soil water at the surface layer.

For transpiration flux, the model considers water conveyance driven by both transpiration and back diffusion in the leaf. Back diffusion is transpirational convection of unenriched water to the evaporating sites by the backward diffusion into the leaf (also known as Péclet effect). The isotope ratio in trunk water (R_{rootup}) is the mean of soil water taken up by root. Thus it is written as:

$$\mathrm{R_{rootup}} = \frac{\int R_g f_{root} dz}{\int f_{root} dz} \tag{2.9}$$

where f_{root} is root density in each layer and R_g is the isotope ratio in soil water in each layer. By taking into account water conveyance driven by transpiration and back diffusion, the isotope ratio in leaf water (R_l) can be described as;

$$\frac{\mathrm{dV_l}}{dz_l}\frac{\partial R_l}{\partial t} = \frac{1}{\rho}\left(\frac{E_t A_l}{LAI}\frac{\partial R_l}{\partial z_l} - D\tau\frac{\partial^2 R_l}{\partial z_l^2}\right) \tag{2.10}$$

Where z_l is the axis directed from leaf base to tip, V_l and A_l are water volume in leaf and area of leaf surface, which are specific to vegetation type and given. E_t is transpiration flux, D is liquid diffusivity, and τ is the crookedness of the leaf. Water conveyance flux E_t does not vary on the axis of z_l, and leaf water volume is assumed to be constant over time. The isotope ratio in transpired vapor is then calculated using Eq. 2.8 ($R=R_l$) but weighted by dry area fraction of canopy.

The model assumes an equilibrium fractionation for liquid to ice formation, but no fractionation is assumed for ice to liquid phase change because of the low diffusivity in ice. The model calculates soil water transfer and runoff, but the processes are not accompanied with isotopic fractionations, and the explanation is omitted here. Please refer to Yoshimura et al. (2006) for more information.

The modification of the land surface model is largely threefold. (1) The new version of MATSIRO has been added lake submodel. The submodel calculates the surface heat and water fluxes over lakes. Water temperature and mass are predicted for five vertical layers based on the thermal diffusion and mass conversion, considering vertical overturning, surface flux (precipitation, evaporation), and inflow and outflow to rivers. I calculate evaporation flux of isotope as in the same manner for evaporation from ocean (Eq. 2.6) but the isotope ratio in lake water is set to 0‰ and constant over time. Thus in this version of the model lake is treated similar to ocean. (2) A tile treatment of the land surface is introduced to the new version of MATSIRO to account for multiple land uses within one grid cell. The model includes 11 types of land cover, which represent the continental ice, broadleaf evergreen, broadleaf deciduous, mixed coniferous and broadleaf deciduous forest and woodland, coniferous forest, high latitude deciduous forest, C4 grassland, shrubs and bare ground, tundra, C3 grassland, and cultivation. One land surface grid is divided into three tiles: vegetation (one of the 11 types of land cover listed above), cropland and lake. All the diagnostic and prognostic variables, including isotope ratio, are calculated in each tile and averaged over the grid cell weighted by its areal fraction (Watanabe et al. 2010; Nitta et al. 2014). (3) The model has been expanded to six soil layers. The total thickness of the soil is changed to 14m everywhere. It is split into six layers with the thickness of layers being 0.05 m, 0.20 m, 0.75 m, 1 m, 2 m, and 10 m.

Table 2-3 List of parameters for surface fluxes

Type of surface	Fluxes	Ci/C	h	T	α	R
Snow-free canopy	Interception evaporation	α_{kin}	1	T_C	α_{eq}	R_C
	Interception sublimation	α_{kin}	1	T_C	α_{ice}	R_C
Snow-free ground	Evaporation	α_{kin}	h_g	T_g	α_{eq}	R_g
	Sublimation	Fractionation does not take place (R_F=R_g)				
Snow-covered ground	sublimation	α_{kin}	1	T_{Sn}	α_{ice}	R_{Sn}

The subscripts C, g, Sn denote canopy, ground, and snow respectively and h_g is the relative humidity at the surface.

2.3. Experimental design

The model resolution is set to horizontal spectral truncation of T42 (approximately 280km) and 40 vertical layers with σ-*p* hybrid coordinate. The atmospheric and land surface components are coupled, and sea surface temperature and sea ice concentration is prescribed (HadISST) (Rayner 2003). Greenhouse gasses (carbon dioxide, methane, and chlorofluorocarbon) and ozone are also prescribed. A nudging technique was applied to assimilate horizontal wind velocity in order to make direct comparison with observations possible. The time constant is set to 0.1 day. The reanalysis field is obtained from JRA25 (Onogi et al. 2007). After a spin-up of 100 year with the boundary conditions for 1979, the simulation started in January 1979 and end at December 2007.

For the lower boundary condition of the atmospheric isotopes, ocean water isotope ratio is uniformly set to 0‰. $\delta^{18}O$ in lake water is also set to uniformly 0‰. Both of them are assumed constant over time. Also The isotopic composition of the sea ice is prescribed (3‰ and 24‰ for $\delta^{18}O$ and δD, respectively) following Joussaume and Jouzel (1993).

To evaluate the sensitivity to the processes which involve isotopic fractionation over land, a sensitivity experiment is conducted. In the simulation, named NOF, isotopic fractionation is banned during

evaporation from bare soil, canopy layer, and lake water, sublimation from snow/ice, or dew and frost onto bare soil, canopy layer, and snow/ice. Except for these change, the compilation of the model and the setting of the simulation is the same as control simulation described first (named as CTL). Thus, NOF experiment mimics the setting of ordinal isotope enabled GCMs in which isotopic fractionation over land is not taken into account.

2.4. Observation data

2.4.1. In-situ measurement of isotope ratio in precipitation

Observations of the monthly isotope ratio in precipitation over the globe were obtained from the Global Network for Isotopes in Precipitation (GNIP) observational database (IAEA/WMO, 2015). While several stations have continuously collected samples for two or more decades, many GNIP stations have only been in operation for a much shorter period. For this study, 231 stations are selected. The selection criteria is following Werner et al. (2011): the observation period should cover at least 1 complete calendar year with full set of monthly mean 2 m air temperature, precipitation amount, as well as $\delta^{18}O$ in precipitation. From this set of 231 GNIP stations, I selected for some more quantitative analyses a subset of 70 stations that contained a minimum of 5 calendar years of those variables any time within the period 1953 to 2007. I notice that a 5 year record at a specific GNIP station might still be too short for representing an adequate climatological mean value at this station. However, there are too few GNIP locations with 10 year (35 stations) or even a 20 year isotope record (8 stations) for a reliable reconstruction of the global $\delta^{18}O$ pattern from these two subsets.

2.4.2. In-situ measurement of isotope ratio in vapor

GNIP collects and measures the isotopic composition of not only precipitation data but also surface vapor on monthly basis, though the observation points and the period are more limited. I selected 6 stations (Ankara, Azores, Lisbon, Madrid, Rehovot, and Vienna) and the site information is summarized in Table 2-4.

Table 2-4 Summary of GNIP observation site for vapor isotope

Site	Latitude	Longitude	Period
Ankara	39º57'N	32º52'E	Jan 2001 – Mar 2003
Azores	38 º40N	27 º15'W	Jul 1998 – Apr 1999
Lisbon	38 º48'N	9 º06'W	Oct 2002 – Apr 2003
Madrid	40 º24'N	3 º41'W	Nov 2000 – May 2003
Rehovot	31 º54'N	34 º39'E	Jan 2001 – May 2003
Vienna	48 º11'N	16 º23'E	Oct 2000 – May 2003

2.4.3. **Measurement of isotope ratio in soil water**

Continuous measurements of isotope ratio in soil water are rare. Kubota et al. (2012) is one of the exceptions. They measured soil water isotopic content from July 2006 through 2008 at Hitachi Ohta, Ibaraki, located on the east side of the main island of Japan (36º34'N, 140º35'E). The elevation is around 300 m above sea level. The area is covered by an artificial forest of *Ch. Obtusa* and *C. japonica*. Only sporadic winter snowfall and no persistent snowpacks were observed during the period of observation. They collected soil water approximately every two weeks with suction lysimeters from the depths of 0.1, 0.2, 0.4, 0.6, 0.8, 1.0, 1.5, and 2.0m. They also collected precipitation and throughfall for the period. The water isotopes were analyzed by spectrometry with the accuracy of ±0.02‰ for $\delta^{18}O$. Although they measured δD as well, I only use $\delta^{18}O$ data.

Additionally soil water data sets are obtained from Moisture Isotopes in the Biosphere and Atmosphere (MIBA). One station from Israel is selected for their observation length and frequency. The site is located in Yatir forest (31º21'N, 35º02'E) with a mean altitude of 650 m (Yaseef et al. 2009). The observation starts from January 2004 and end at November 2006. The soil water was collected approximately monthly basis using vacuum line from the depths of 0 (surface), 5, 10, 15, 20, 25, 30, 40, 50 cm.

2.4.4. **Satellite measurement**

Frankenberg et al. (2009) measured column-averaged isotopologue ratio (δD) values in water vapor using the SCanning Imaging Absorption spectroMeter for Atmospheric CHartographY (SCIAMACHY) onboard the European research satellite ENVISAT. In this stud the updated and extended version of this dataset from Scheepmaker et al. (2015) covering the years 2003 – 2007 is used. As measured δD is weighted by the H_2O concentration at all heights, it is largely determined by the isotopic abundance in the lowest tropospheric layers, where most water vapor resides. The footprint of each measurement is 120 km (across-track) × 30 km (along-track). This study applies the following selection criteria concerning the retrievals (Scheepmaker et al. 2015):

- Retrieved H_2O total column must be at least 70% of the a priori value.
- The CH_4 column in the same retrieval window must be at least within 10% of the a priori value.
- Root-mean-square variation of the spectral residuals must be below 5%.
- Convergence achieved in a maximum of four iteration steps.

Here, the first two criteria restrict large deviations from the a priori H_2O and CH_4 columns, which are normally the result of light scattering by clouds. Therefore, these two criteria function as a simple cloud filter. Due to high detector noise of SCIAMACHY in the short-wave infrared channels, the single measurement noise (1-sigma) is typically 40‰ – 100‰, depending on total water column, surface albedo, and viewing geometry. This random error can be further reduced by averaging multiple measurements. Therefore, the measurements are averaged following the procedure of Yoshimura et al. (2011); multiple measurements that were collected in a grid of T42 in 6 h are averaged. The threshold value for averaging is set to 10, meaning that the average of the SCIAMACHY measurements in every grid cell is based on at least 10 measurements taken within 6 h. From the MIROC5 simulation results, the times of the nearest satellite measurements were extracted (hereafter the process is called "collocation"). Thus, there was no difference in representativeness between the model and the satellite data.

2.4.5. **SWING2**

To compare the result with the other models, the data of Stable Water-Isotopes Intercomparison Group, Phase 2 (SWING2) is obtained from http://data.giss.nasa.gov/swing2/. Two nudged simulations from GISS (Schmidt et al. 2005) and IsoGSM (Yoshimura et al. 2008) are selected from eight participating models. The models are both nudged toward NCEP Reanalysis.

2.5. Results

2.5.1. **Climatology of global distribution of isotopes**

In this section, model-data comparison about spatial distribution and relationship with temperature and precipitation will be described.

Figure 2-1 shows annual average of precipitation $\delta^{18}O$ ($\delta^{18}O_P$) for observation (GNIP) and MIROC5. The well-known feature of isotopic effects (Dansgaard, 1964) is well simulated. That is, enhanced depletion along with increasing latitude (latitude effect), altitude (altitude effect), and continentality (continental effect). These effects are due to cooling and/or dehydration of air masses on their way to high latitude, high elevation, and inland. The cooling of air masses decreases their holding capacity of water vapor and condensates the vapor. Because heavy isotopes are preferentially removed from the air masses, successive cooling results in the isotopic gradient along with latitude and altitude. These isotopic effects are also known as temperature effect. The effect is apparent in the simulation. For instance, over the North

Atlantic where warm water of the Gulf Stream prevails avoids a strong rainout of the air masses and then high isotopic ratio is maintained compared to the same latitudes. The altitude effect can be found in Tibet, Andes, and the Rocky mountains. In those areas, the isotopic composition is lower than that of surrounding areas. Figure 2-2 evaluates the annual mean of $\delta^{18}O_P$ by comparing the model results with observations at the GNIP sites. Pearson product-moment correlation coefficient (hereafter correlation coefficient) and root-mean-square error (RMSE) are 0.93 and 1.76 ‰ respectively. These scores are similar to the other nudged isotope simulations from SWING2 members (Table 2-5). All the models simulate the spatial isotopic distribution fairly well. However, the models except for GISS underestimate the latitudinal gradient: relatively low isotope ratio over tropics and relatively high in high latitude. This is partly because of the overestimated temperature over polar region, which is common in many other GCMs (Jouzel et al. 1987; Risi et al. 2010; Werner et al. 2011). The most obvious deficit of the simulated annual mean is the left bottom plot in the Figure 2-2a. The point, which is corresponding to Halley Bay, located in Antarctica facing on Weddell Sea. Over the point, the simulated $\delta^{18}O$ is -31‰ against observed value of -21‰. To investigate the reproducibility of isotope ratio over Antarctica, where lots of valuable climate proxies are available, the simulated mean annual $\delta^{18}O$ in precipitation is compared with the selected subset of observations compiled by Masson-Delmotte et al. (2008) in Figure 2-3. Qualitatively the model captures the isotopic distribution: the most depleted values are found in the inner East Antarctica and less depleted values are in West Antarctica and the coastal area. The spatial correlation between them is 0.90, spatial slope is 0.82, and RMSE is 4.60‰, which are comparable with the global statistics. Hence the reproducibility over the Antarctica is not especially worse than that over the globe. Then, why is the discrepancy at Halley Bay large? Around the site, the spatial gradient is steep and which result in the altitude difference in the model (actual altitude of the site is 30m, on the contrary to 1366m in the model grids). Due to the difference, the temperature over the site is underestimated (-18.7°C and -26.9°C for the observation and the simulation, respectively). Thus the relatively large error in $\delta^{18}O$ in precipitation can be attributable to the misrepresentation of the altitude over the site.

In Figure 2-1 seasonal difference in $\delta^{18}O$ in precipitation (DJF-JJA) is also shown. The seasonality is large in high latitude, and precipitation is more depleted in heavy isotopes in winter because of temperature effect, which result in blue color in northern hemisphere and red color in southern hemisphere. The relation is, however, reversed in low latitude (30S-30N). The region is dominated by precipitation amount effect and gets most of precipitation in the local summer; therefore isotope ratio is low in summer. Figure 2-2b evaluates the seasonal difference in $\delta^{18}O_p$ by comparing the model results with observations at the selected GNIP sites. Correlation coefficient between the simulation and GNIP is 0.87. These scores are similar to the other nudged isotope enabled GCMs (0.85-0.89 for seasonality).

2.5.2. Spatial relationship between $\delta^{18}O_p$ and temperature and precipitation

Figure 2-4 compares the annual mean $\delta^{18}O_P$ and local temperature and precipitation amount. For the

comparison of isotope ratio and temperature, the stations whose annual mean 2m temperature is below 15 °C are selected (88 stations), and the stations whose annual mean 2m temperature is above 20°C for the comparison of isotope ratio and precipitation (16 stations). As expected from temperature effect $\delta^{18}O_p$ and temperature correlates positively. The relation between isotope ratio in precipitation and temperature is well captured: the calculated linear regression slope is 0.52 and 0.47 for the observation and the model. The relation with precipitation is also well simulated: the isotope ratio is more depleted over the sites which get more precipitation (amount effect). However the isotopic composition is uniformly underestimated by 1-3‰. The correlation coefficient is higher in the simulation than the observation. This means that the isotopic composition in precipitation is strongly coupled with precipitation in model than in the real world. Conroy et al. (2013) evaluated a set of multimodel simulations archived by SWING2, and they found that the all the models except for CAM2 overestimated the coupling. The overestimated coupling results from the oversimplified representation of raindrop interaction with subcloud vapor; in those models, the raindrop interaction with vapor is simply parameterized as 95% equilibration for stratiform rain and 45% equilibration for convective rain. Unlike the other models, CAM2 takes into account drop size, humidity, rain rate, and temperature when it calculates the degree of equilibrium. This results in less coupling between precipitation amount and $\delta^{18}O_p$ in the model as in the observation. Lee and Fung (2007) reported that precipitation reaches 70% equilibrium with surrounding vapor over low latitude on average. Since isotopic composition in lower tropospheric vapor is heavy, the enhanced equilibrium with ambient vapor should result in heavier $\delta^{18}O$ in precipitation. The underestimation of $\delta^{18}O_P$ may be explained by the relatively small parameter for equilibration factor with ambient vapor.

Table 2-5 Spatial correlation coefficients (R), linear reglession slope, and root mean square error (RMSE) between GNIP observation and the simulations (MIROC5, GISS, and IsoGSM) for annual mean $\delta^{18}O$ in precipitation

	MIROC5	GISS-ModelE	IsoGSM
R	0.92	0.92	0.90
Slope (Obs/Sim)	1.10	0.82	1.21
RMSE (‰)	1.76	2.54	2.02

Table 2-6 Spatial correlation coefficients, reglession slope, and RMSE between GNIP and the simulations (MIROC5, GISS, and IsoGSM) for seasonal difference (DJF-JJA) $\delta^{18}O$ in precipitation

	MIROC5	GISS-ModelE	IsoGSM
R	0.88	0.83	0.85
Slope (Obs/Sim)	0.77	0.87	0.85
RMSE (‰)	2.46	2.47	2.41

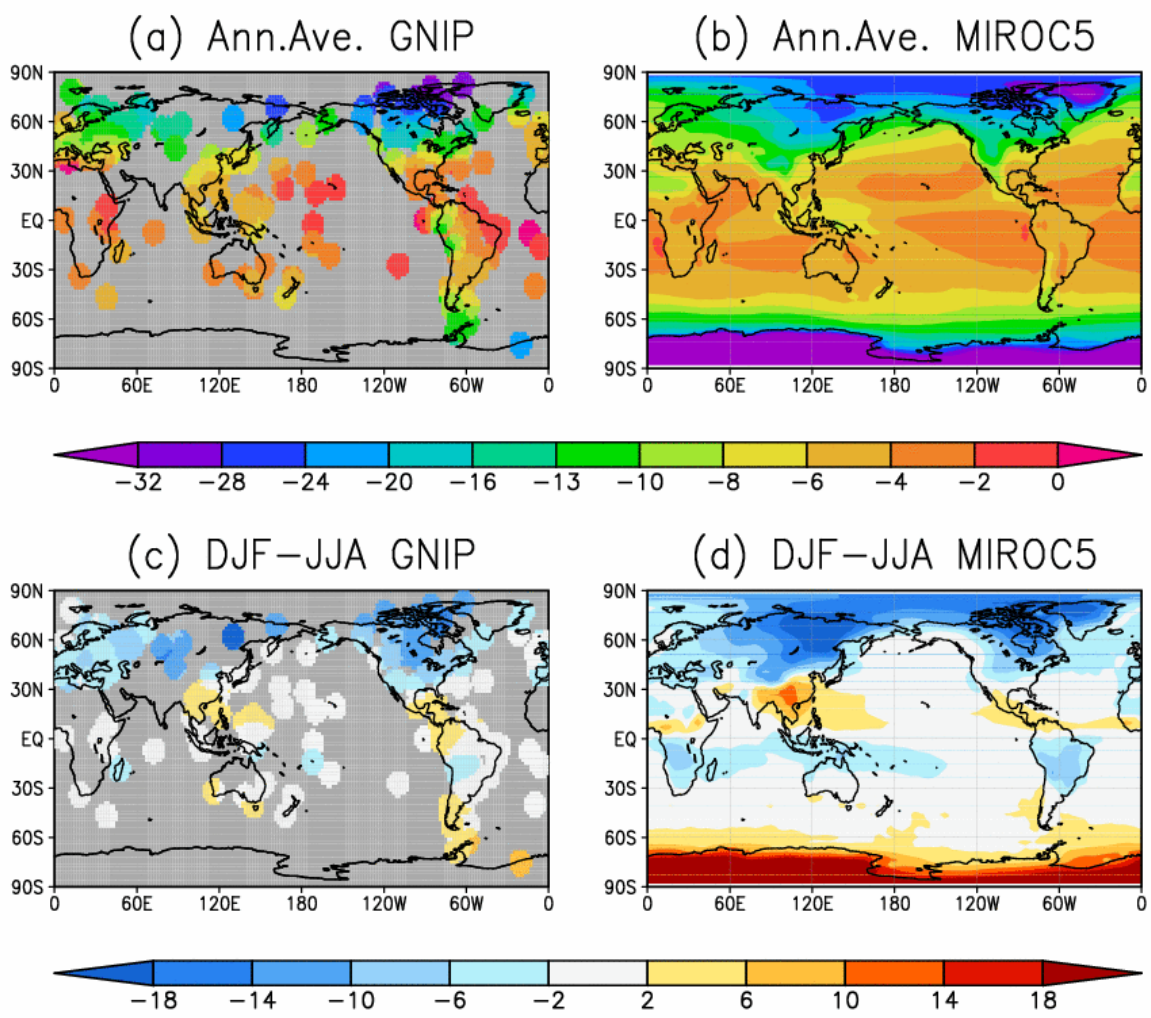

Figure 2-1 Annual average and seasonal difference (DJF-JJA) of precipitation isotope ratio ($\delta^{18}O$) by (a, c) GNIP observations and (b, d) MIROC5 simulation (‰)

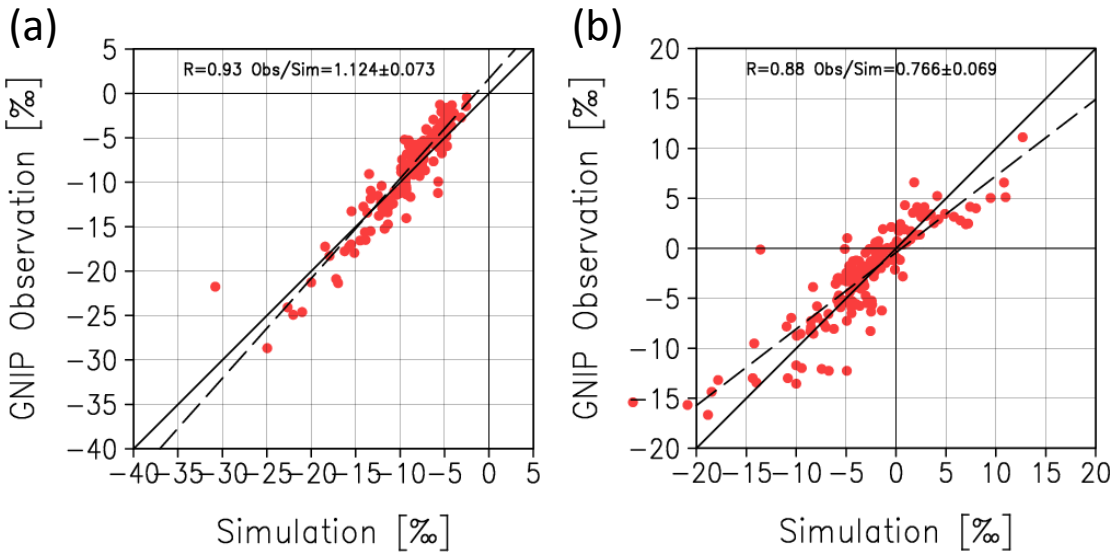

Figure 2-2 Scatter plot comparing GNIP observation and MIROC5 for annual mean and seasonal difference (DJF-JJA) of $\delta^{18}O$ in precipitation for MIROC5. The dash line represents the linear regression line.

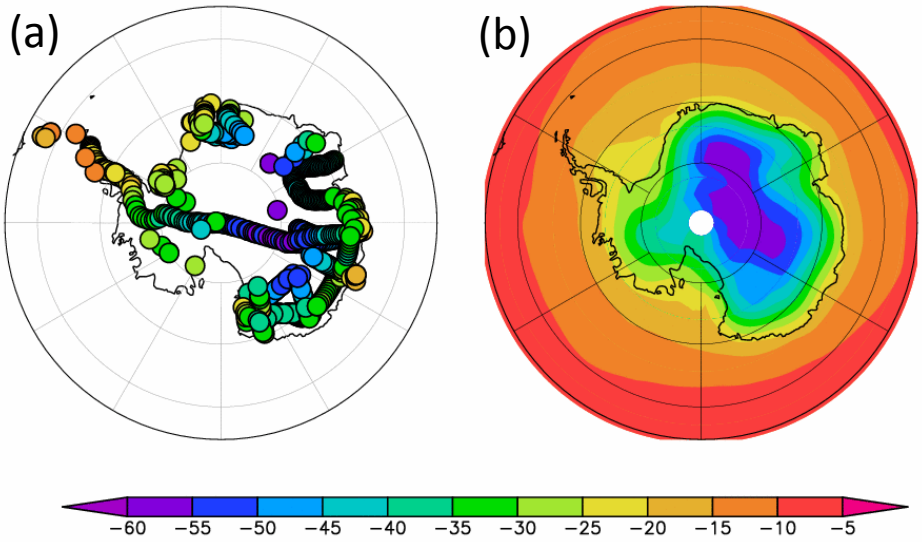

Figure 2-3 Annual mean $\delta^{18}O$ in precipitation for Antarctica (‰) from (a) observation (Masson-Delmotte et al. 2008) and (b) simulation

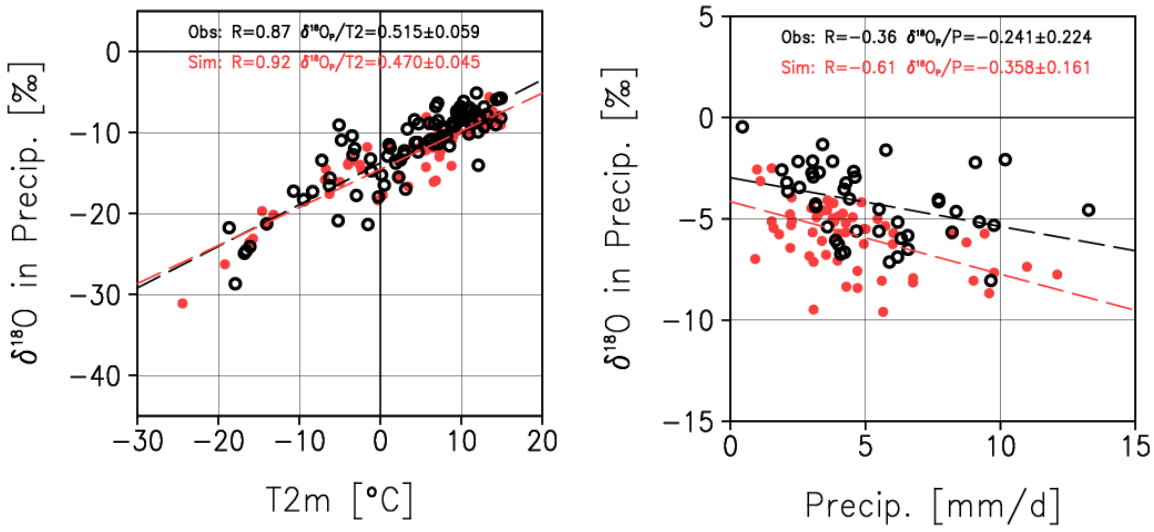

Figure 2-4 Spatial relation between the annual mean $\delta^{18}O$ in precipitation and (a) surface temperature, and (b) precipitation, derived from the GNIP observation (black) and MIROC5 (red). Dash lines represent the linear regression line between the two variables.

2.5.3. **Interannual variability**

Reproducibility of isotope ratio in precipitation

Figure 2-5 shows the monthly anomaly correlation between the modeled and the observed $\delta^{18}O$ in precipitation. Thanks to the nudging, at almost all the points they are statistically significantly correlated with each other. MIROC5 outperformed the other nudged GCMs as for the reproducibility of $\delta^{18}O$ in precipitation, especially in the tropics (Table 2-7). Since all the simulations are nudged toward reanalysis fields, the circulation does not explain the difference, even though the nudging technique and coefficients, or the nudged variables are different each other. Figure 2-6 compares the interannual correlation coefficients between the modeled and the observed precipitation (GPCP; Alder et al., 2003) for each grid point. The mean coefficient over the region is 0.58, 0.45, and 0.40 for MIROC5, IsoGSM, and GISS, respectively. As can be seen in the amount effect, $\delta^{18}O_p$ is influenced by precipitation amount over low latitude. Hence the relatively better reproducibility for $\delta^{18}O_p$ may be due to the better reproducibility for precipitation. This may be owing to the newly implemented convective parameterization scheme in MIROC5. If so, studying specifically what modification of the scheme produces the isotopic change would be interesting. By looking the topic in detail, in turn, we may be able to constrain the parameterization scheme by using isotopes like Risi et al. (2012) have tried, but this is beyond the scope of this study.

Temporal relationship with temperature and precipitation

Considering climate reconstruction, the temporal relationships between $\delta^{18}O_p$ and temperature and precipitation are important. Risi et al. (2010) use the simulated temporal slope to reconstruct paleotemperature. For such an application, the evaluation of temporal slope is necessary. Figure 2-7 and Figure 2-8 compare the temporal correlation and linear regression slope between $\delta^{18}O_P$ and local temperature and local precipitation amount for the simulation and observation on interannual scale (monthly anomaly). The area in which correlation does not reject the null hypothesis at the significance level of 0.001 is hatched.

For temperature the observation shows positive correlation at almost all the continental sites, whereas weak correlation and not significant correlation can be seen in oceanic area, including East Asia. The correlation ranges from -0.08 to 0.60 with the highest score in Central Europe. The slope is also the highest in Europe and North America. These features are well captured by all the models but the signals are stronger than the observation in general. The scarcity of the observation prohibits further comparison. Thus I focus on the similarity and the difference among the models. The most prominent difference between the models is the signal of correlation over tropical Pacific. MIROC5 shows strong positive correlation, while GSM does negative correlation and GISS does not show correlation. Accordingly, the slopes are positive in MIROC5 and negative in GSM. Over the region, the dominant factor controlling $\delta^{18}O_P$ is the amount of precipitation, and hence $\delta^{18}O_P$ co-vary with ENSO. In the positive phase of ENSO, central Pacific is warmer than usual and gets more precipitation which results in lower $\delta^{18}O_P$ than usual. Hence $\delta^{18}O_p$ and temperature are expected to co-vary negatively there. Given that the correlation between $\delta^{18}O_P$ and ENSO is simulated reasonably to be negative by MIROC5 over central Pacific (Figure 2-9) and the correlation is negative using annual mean but monthly anomaly, this unrealistic correlation should be spurious. The isotopic response to temperature is different in the signal also over Antarctica in which precipitation isotope ratio is controlled by temperature. In this case MIROC5 and GISS show positive correlation and slope, but GSM does negative. This may be because of the problem in transportation process over very dry region in GSM.

Isotopic composition in precipitation over low latitude is said to be mainly controlled of $\delta^{18}O_P$ by precipitation (Dansgaard, 1964). However, as Cole et al. [1999] shows, $\delta^{18}O_P$ correlates with precipitation even in high latitudes (Figure 2-8 a and b). The models are in agreement with observation in that sense. However the correlations and the slopes are simulated to be higher in all the models. The same reasoning as the strong coupling seen in the amount effect should holds true for this case.

Temporal relationship with climate indices

Figure 2-9 shows the global distribution of the correlation between monthly anomaly $\delta^{18}O_p$ and NINO3 index. The observation shows significant positive correlation over South East Asia, West Africa, Europe,

and western North America as previous study have showed (Ishizaki et al. 2012; Okazaki et al. 2015). All the models show the high positive correlation over Pacific warm pool including South East Asia, and Amazon. But the signals in West Africa, Europe, and western North America are missed in MIROC5 simulation.

Figure 2-10 shows the correlation between monthly anomaly $\delta^{18}O_p$ and Arctic Oscillation (AO) index. The monthly AO index is defined as the first empirical orthogonal function (EOF) of the sea level pressure. Since AO, or North Atlantic Oscillation (NAO), has been found to have large impact on isotope ratio in precipitation over Greenland (White et al. 1997; Sodemann, Masson-Delmotte, et al. 2008; Vinther et al. 2010), the reproducibility of the signal is of importance. The observation shows positive correlation over Europe and eastern North America. The models are in agreement with observation, although the correlation over eastern North America is suppressed. The spatial characteristics common in the models are negative correlation over Greenland. Although the signal is not clear in the observation due to the limited number of observations, the ice cores do exhibit negative correlation with NAO (e.g. White et al., 1997; Schneider and Noone, 2007). Hence the models, including MIROC5, reasonably capture the observed features.

Table 2-7 Number of GNIP sites where monthly anomaly of observed $\delta^{18}O$ are significantly correlated with simulations ($p < 0.05$) for 30°N-90°N (NH), 30°S-30°N (Tropics), and 90°S-30°S. Numbers in parenthesis show the number of GNIP sites available in each area.

	MIROC5	GISS-ModelE	IsoGSM
NH (205)	159	119	154
Tropics (95)	71	53	57
SH (31)	15	11	14

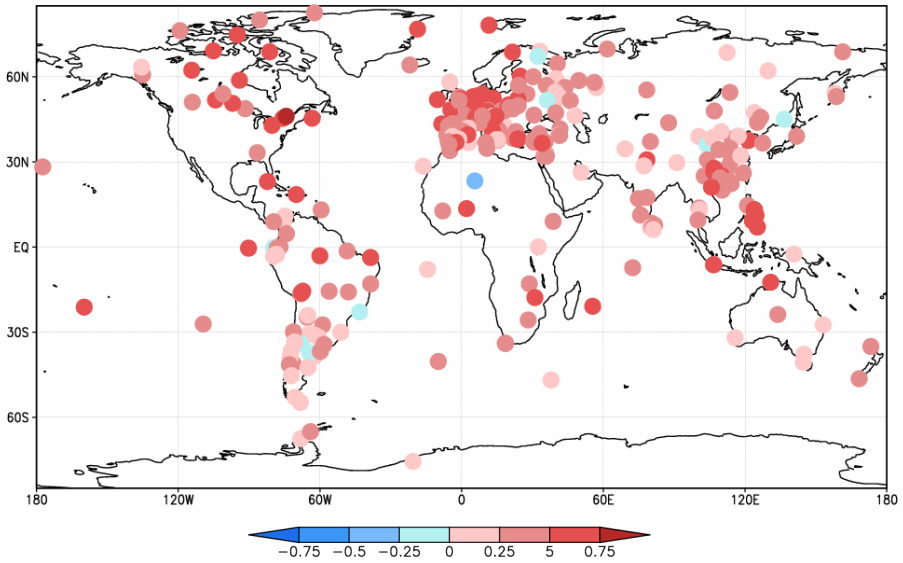

Figure 2-5 Correlation coefficients for monthly anomaly of $\delta^{18}O$ between the GNIP observation and MIROC5 from Jan 1980 to Dec 2007.

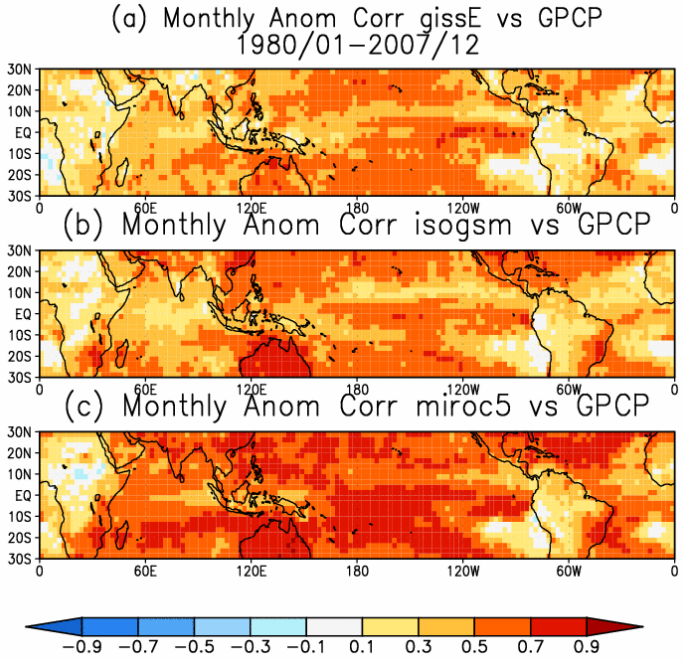

Figure 2-6 Correlation coefficients for precipitation amount on interannual timescale between GPCP (Adler et al. 2003) and (a) GISS, (b) IsoGSM, and (c) MIROC5

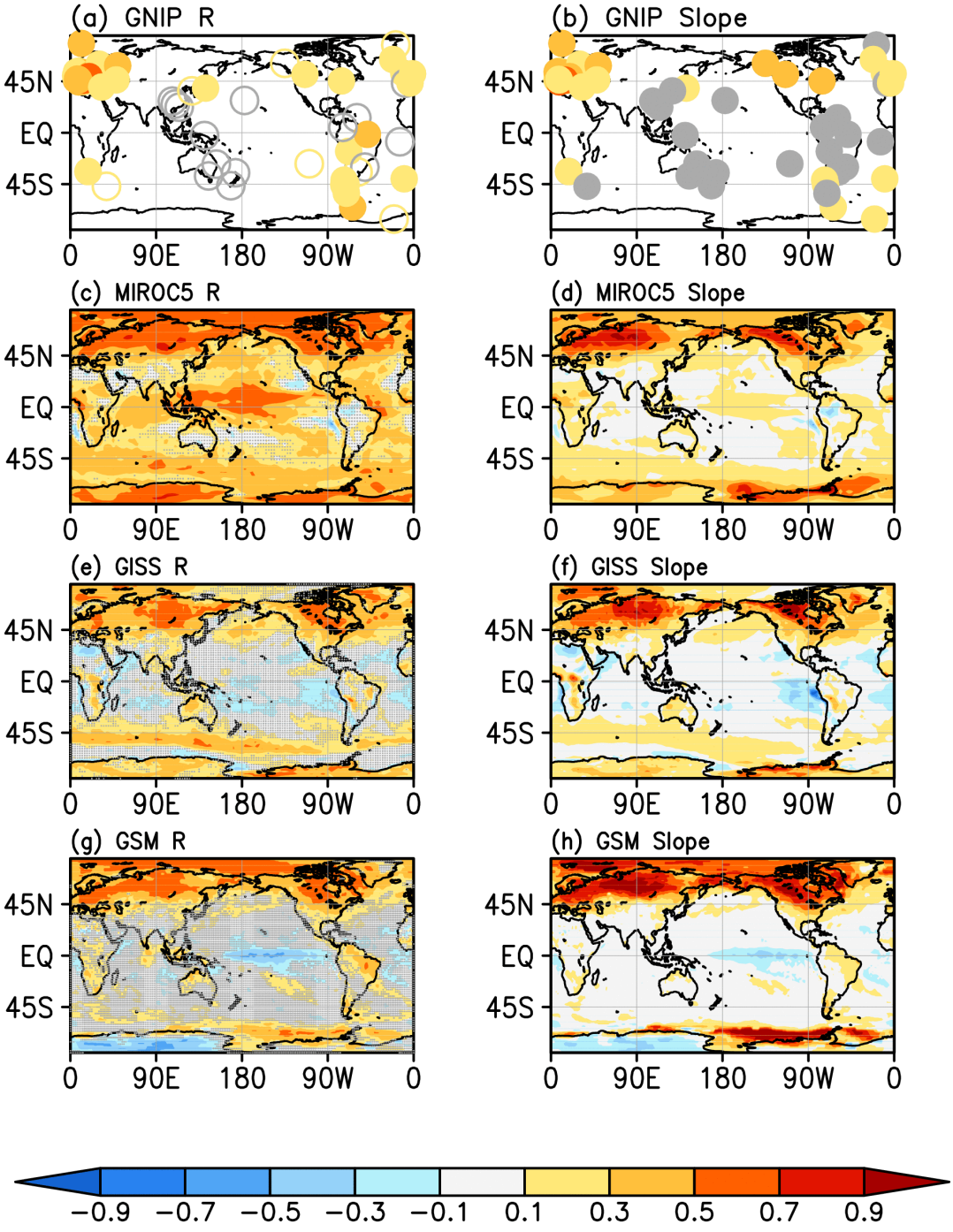

Figure 2-7 Monthly anomaly correlation and slope between $\delta^{18}O$ in precipitation and surface temperature on interannual timescale obtained from (a-b) GNIP observation, (c-d) MIROC5, (e-f) GISS, and (g-h) GSM. Grid in which the correlation is not significant is hatched.

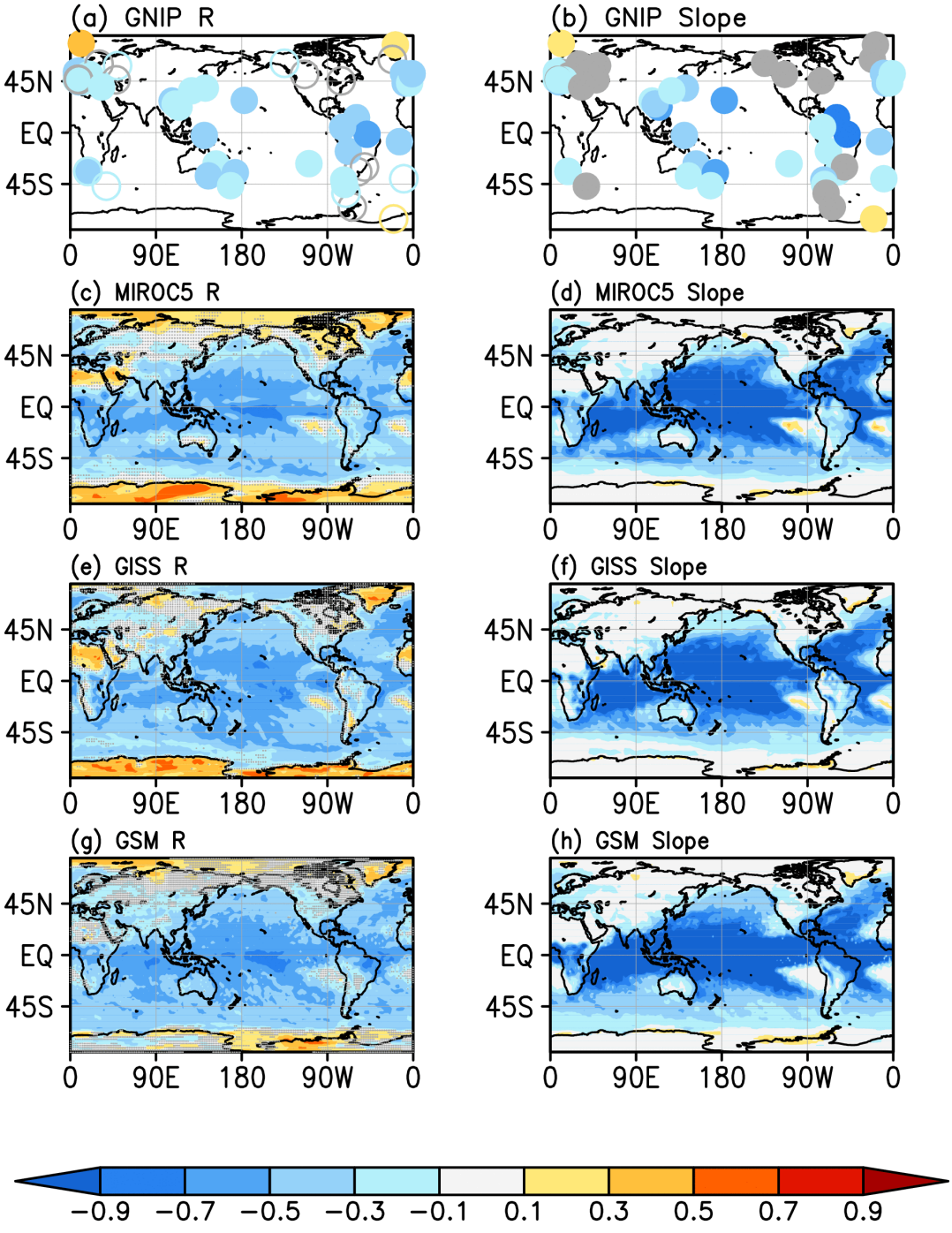

Figure 2-8 Same as in Figure 2-7 but for precipitation

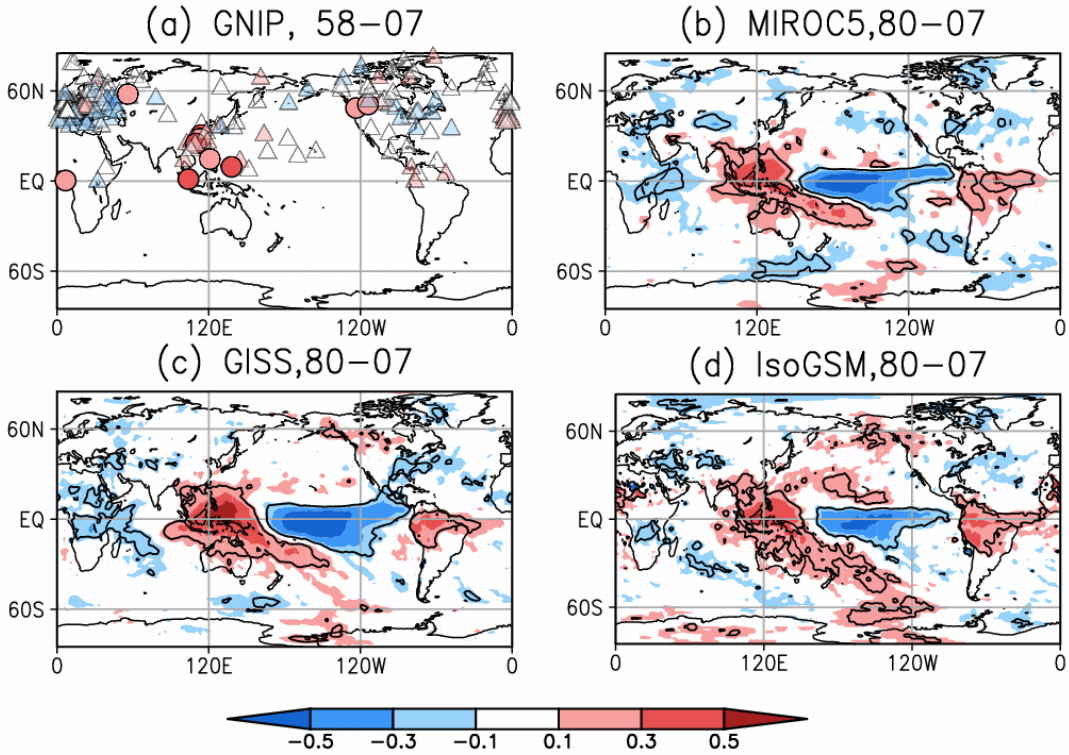

Figure 2-9 Correlation coefficients between monthly anomaly of $\delta^{18}O$ in precipitation and NINO3 for (a) GNIP, (b) MIROC5, (c) GISS, and (d) IsoGSM. In Figure 2-9a, correlations with significance levels greater than 95% are indicated by circles and others are shown by triangle. In Figure 2-9b-c, correlations higher than significance level of 95% are indicated by contour.

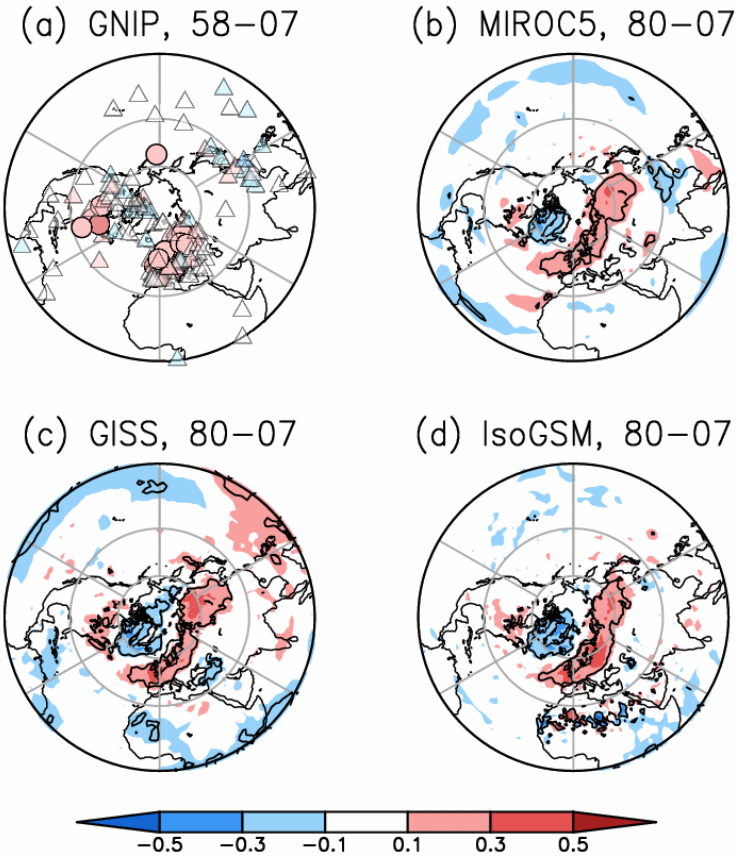

Figure 2-10 Correlation coefficients between monthly anomaly of $\delta^{18}O$ in precipitation and AO index for (a) GNIP, (b) MIROC5, (c) GISS, and (d) IsoGSM.

2.5.4. **Impact of land surface processes and evaluation of soil water**

To evaluate the impact of the fractionation processes over land, an additional experiment named "NOF" is conducted. In the experiment, all the isotopic fractionation which occurs over land has been turned off. That is, the simulation does not take into account fractionation in the process of evaporation from bare soil and canopy layer, transpiration from plants, sublimation from snow and ice, dew formation, or snow melt and refreeze. Thus this setting mimics the other isotope enabled GCM in which fractionation over land is not taken into account. From here, the NOF experiment will be compared with the previous simulation (CTL).

Precipitation isotope

Figure 2-11 compares difference in the annual mean $\delta^{18}O$ in precipitation between CTL and NOF (CTL

minus NOF). Precipitation is generally more depleted in heavy isotopes over the land. The difference is prominent in cold regions, e.g. Siberia, North America, and Tibetan Plateau. Evaporation from bare soil and canopy layer and sublimation from snow produce more depleted vapor in heavy isotopes by taking into account fractionation. The depleted flux results in depleted vapor, and subsequently produces depleted precipitation. Since the contribution of land evaporation become larger along with continentalty (Risi et al., 2013), vapor and precipitation become more depleted in inland area (e.g. Siberia). The difference is simulated to be larger in high latitude. This is because of temperature dependency of isotopic fractionation; the colder the temperature is, the more depleted flux is. The mean difference over land is 0.54‰ for $\delta^{18}O$. Thanks to the fractionation process the continental effect is closer to the observation over Europe (Figure 2-12). The spatial distribution is also slightly closer to the observation with isotopic fractionation over land (correlation coefficients are 0.93 and 0.92 for CTL and NOF, respectively).

The interannual variability of NOF is also compared with CTL but they are not different from each other. The minimum coefficient in the temporal correlation between the two simulations is found to be 0.91, so the simulations show only slight difference in the variability.

Vapor isotope

SCIAMACHY measures column averaged isotope ratio (δD) in water vapor. As measured δD is weighted by the H_2O concentration at all heights, it is largely determined by the isotopic abundance in the lowest tropospheric layers. Hence it is suited to evaluate the isotopic imprint of land surface processes. Figure 2-13 compares the annual mean climatology of the SCIAMACHY measurement and the collocated simulations. The "latitude effect" and maxima over Amazon and Central Africa are found in the satellite observation. In those regions, the "continental effect" is very small because of strong evapotranspilation, and recycling water (Frankenberg et al., 2009). Although the latitudinal gradient is underestimated as precipitation isotope, the simulations capture the spatial features well (temporal correlations are 0.81 for both simulations, RMSE is 39.1‰, and 40.3‰ for CTL and NOF respectively). The underestimation of the latitudinal gradient is common to GCMs. Moreover Scheepmaker et al. (2015) pointed out the possibility that the SCIAMACHY measurement is too depleted in high latitude. Thus, at this stage, I cannot conclude whether the underestimation of the gradient is significant or not. Nevertheless, CTL and NOF are indistinguishable in the annual mean field (Figure 2-13c) as well as seasonal climatology field (not shown).

To focus more on land surface process, next I compared the two simulations with near surface vapor observations. The observation data is obtained from GNIP site (

Table 2-4). At the sites close to the ocean (Azores, Lisbon, and Rehovot) the difference between the simulations are not apparent because of dominant water flux from ocean. On the other hand at the inland sites (Ankara, Madrid, and Vienna) the differences are clearer. In these sites NOF simulates enriched vapor in winter; the reasons are the same as discussed in this section. The scores of correlation coefficient, regression slope, and RMSE are summarized in Table 2-8 and CTL is better than NOF for those sites for all the metrics.

Soil water

In this subsection, the simulated and observed isotope ratio in soil moisture ($\delta^{18}O_{sw}$) will be compared. The observation data is obtained from MIBA and Kubota et al. (2012). At Yatir site, Israel, the seasonal cycle is well simulated by CTL run in the first soil layer. However, NOF run simulates antiphase seasonality and, besides, the amplitude is much muted (standard deviation; SD is 2.5‰, 1.5‰ for CTL and NOF at the depth of 2.5cm, and 4.5‰ and 3.8‰ for observation at the depth of 0cm and 5cm). The observation site belongs to Mediterranean climate, where dry summer and wet winter prevails. The dry air enhances preferential loss of lighter isotope via evaporation and results in enriched soil moisture in heavy isotopes in summer. As only precipitation can modify the isotopic content of soil moisture in NOF run, $\delta^{18}O_{sw}$ does not change in dry season, which result in the muted seasonality. In contrast, $\delta^{18}O_{sw}$ in the second layer (5cm-25cm) does not show clear seasonality for both simulations, and both are different from observation. The standard deviation of the observed $\delta^{18}O_{sw}$ is 3.8‰, 2.4‰, 1.8‰ at the depth of 10cm, 15cm, and 20cm. On the other hand that of simulation is 0.6‰ and 0.5‰ for CTL and NOF at the depth of 15cm.

At Hitachi Ohta site, though $\delta^{18}O_{sw}$ is around 2-3‰ higher in NOF than CTL throughout the year, both run shows the same seasonality at its second layer of the model (Figure 2-15c). The observed seasonality is similar to both simulations but with larger amplitude. At deeper soil layer, again both simulations show similar seasonality with muted variability compared to the observation. At this site NOF is closer to the observation than CTL for both depths.

Figure 2-16 show the vertical profiles of $\delta^{18}O$ in soil water for both sites. Each line show the monthly mean of the profile, thus the spread can be considered as seasonal change. For both sites, and both in simulation and observation, the seasonal change is larger in upper layer and the seasonal differences become smaller along with depth. The seasonal change is larger in CTL experiment than NOF experiment for both sites. At Yatir Forest, the observed vertical profiles tend to show strong enrichment at the surface and depleted logarithmically along with depth in summer. Again, this is because of preferential loss of lighter isotope by evaporation. In winter, the profile is close to vertical due to rainfall recharge. These features are well reproduced by CTL experiment. Meanwhile NOF experiment shows vertical distribution in all the seasons because of the lack of isotopic enrichment by evaporation.

At Hitachi Ohta site, the vertical distribution of $\delta^{18}O$ in soil water is different from Yatir Forest; the

observed $\delta^{18}O_{sw}$ distributes symmetry. $\delta^{18}O_{sw}$ is high in spring and low in summer in this site. This reflects the seasonality of $\delta^{18}O$ in precipitation. Those characteristics are roughly captured by both experiments, but the difference can be seen in the amplitude of variability; the amplitude is larger in CTL than NOF (SD=2.9‰ and 1.4‰ for CTL and NOF, respectively at the surface). Although the amplitude is closer to the observation in CTL than NOF, the soil water is simulated to be too enriched in CTL. Because $\delta^{18}O$ in precipitation calculated by both simulations at this site are similar to each other (-7.8 ‰ and -7.4‰ for CTL and NOF. c.f. -7.9‰ for the observation), the difference in $\delta^{18}O$ in precipitation does not explain the difference in $\delta^{18}O$ in soil water. Accordingly, the impact of evaporation is suggested to be too exaggerated in CTL simulation. For this site, the grid scale leaf area index (LAI) used in the simulation is the annual average of 1.3 with its maxima of 2.6 in June and July. Murakami (2002) measured LAI on the same site, and reported LAI ranges from 4 to 6 throughout the year. Thus LAI used should be too small for this specific site. Small LAI suppresses transpiration and enhance evaporation from the ground, which results in the enhanced $\delta^{18}O_{sw}$. Accordingly the too enriched soil water should be result from the small LAI.

On top of that, $\delta^{18}O$ in soil water does not vary in time at layers deeper than second or third layers. This must be because vertical water movement is strongly prohibited in both simulations compared with observation. The primal controller of water movement in soil is precipitation amount. When compared with annual mean precipitation amount measured at the closest meteorological station from Hitachi Ohta (Hitachi, 36°34'N, 140°39', data obtained from Japan Meteorological Agency), however, no difference is found (1456mm for both the observation and the simulation). Thus, the amount of precipitation does not explain the muted variability in the soil layers. Then the coefficient of permeability, or the amount of runoff must be responsible for the muted water movement. In this study, I do not go further beyond, but full investigation of the soil water movement with isotope data will lead to better understanding of runoff process and better simulation for river discharge, which is one of the most important variables for the impact assessment of the global warming.

Table 2-8 Comparison with vapor isotope at GNIP sites

	R	Slope (obs/sim)	RMSE (‰)
Rehovot	0.88 (0.67)	0.73 (0.69)	2.04 (2.00)
Vienna	0.86 (0.77)	1.00 (0.80)	2.14 (2.58)
Madrid	0.63 (0.60)	0.63 (0.58)	2.28 (2.27)
Lisbon	0.59 (0.52)	0.62 (0.53)	1.57 (1.61)
Ankara	0.77 (0.69)	0.62 (0.48)	3.18 (3.80)
Azores	0.26 (0.26)	0.17 (0.17)	2.60 (2.59)

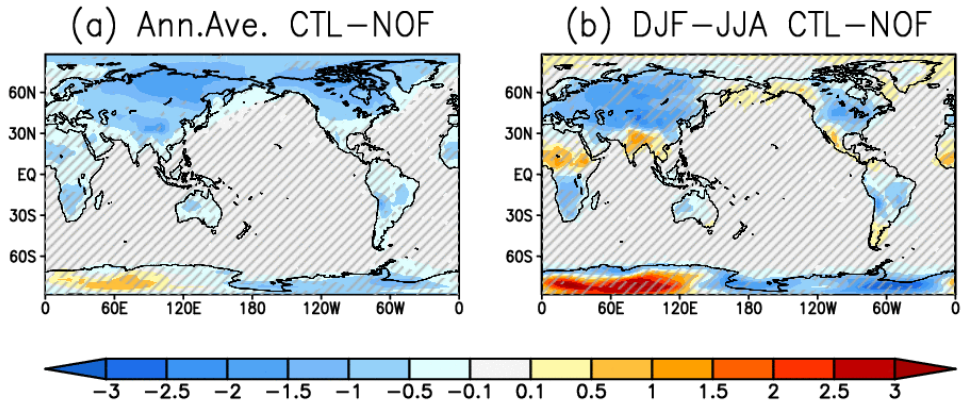

Figure 2-11 Difference between CTL and NOF for the field of annual mean and seasonal difference (DJF-JJA) in $\delta^{18}O$ in precipitation (CTL-NOF) Hatched area is the area in which the difference is not significant ($p < 0.05$).

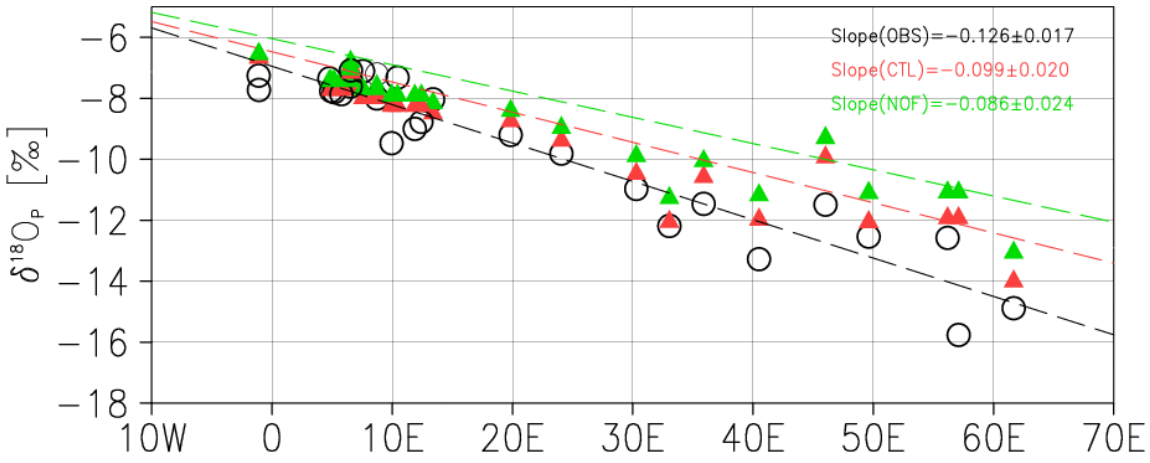

Figure 2-12 Continental effect for Europe (50°N-70°N). Black dot denotes the annual mean $\delta^{18}O$ of GNIP, red and blue denote the simulated annual mean $\delta^{18}O$ at the corresponding grid box. Red is for CTL and blue is for NOF.

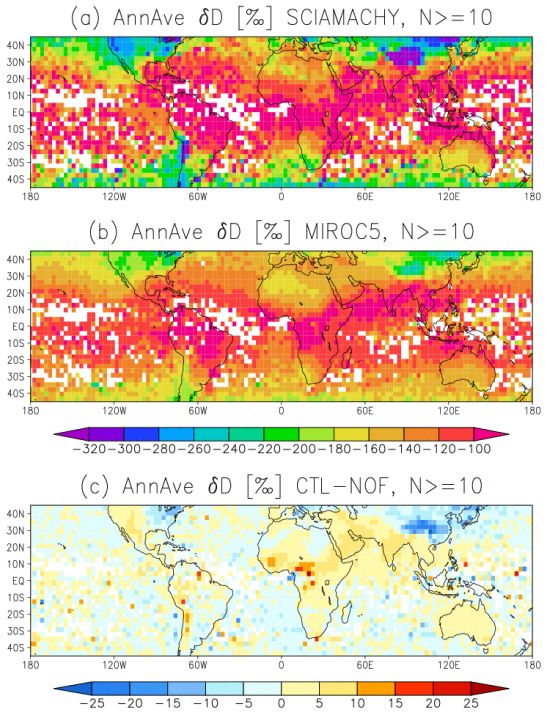

Figure 2-13 Annual mean of $\delta^{18}O$ in total column vapor obtained by (a) SCIAMACHY, (b) CTL, and (c) difference between CTL and NOF (CTL-NOF)

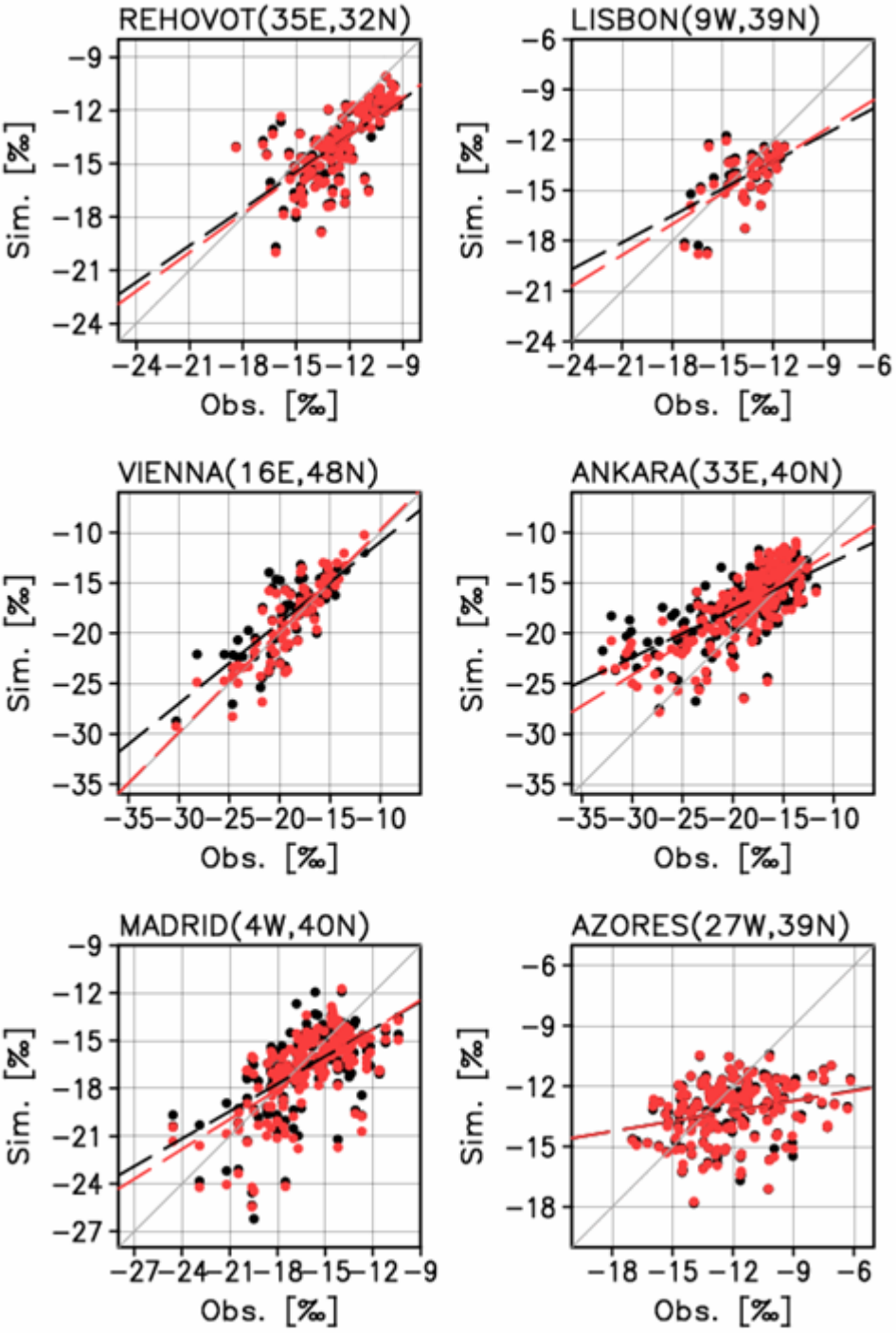

Figure 2-14 $\delta^{18}O$ in vapor measured on biweekly basis (black) and the daily mean simulation in CTL (green) and NOF (red) for GNIP observation sites

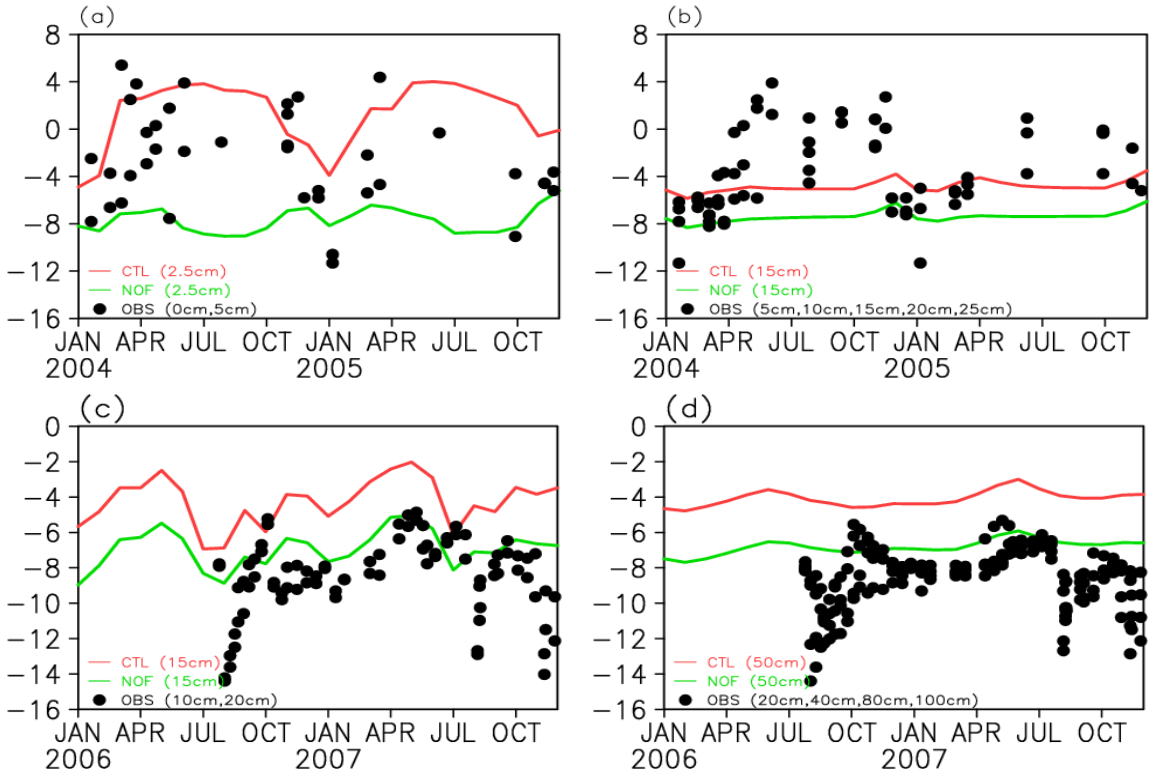

Figure 2-15 $\delta^{18}O$ in soil water for Yatir site, Israel at depth of (a) 0-5 cm and (b) 5-25 cm and for Hitachi Ohta site, Japan at depth of (c) 5-25 cm and (d) 25-100 cm. The Observation is shown in black dot and simulation is shown in red (CTL) and green (NOF).

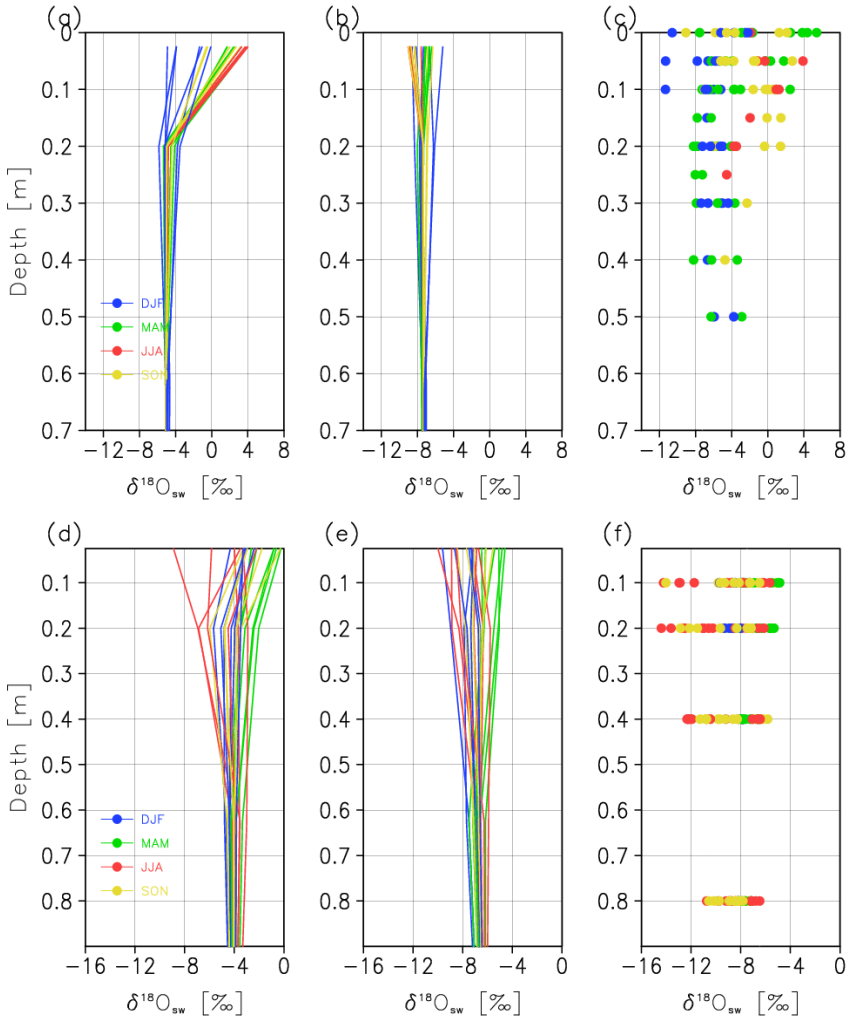

Figure 2-16 Vertical profile of $\delta^{18}O$ in soil water at Yatir site, Israel for (a) CTL, (b) NOF, and (c) Observation. (d-f) Same as in (a-c) but for Hitachi Ohta site, Japan. Each line represents the monthly mean of the vertical profile in (a, b, d, and e). Each dot represents single measurement in (c, and f). The colors represent seasons: blue is DJF, green is MAM, red is JJA, and SON is yellow.

2.6. Summary and Conclusion

In this chapter, stable water isotopes have been successfully implemented into state-of-the-art GCM; MIROC5. The simulated results are evaluated from many aspects. The reproducibility of $\delta^{18}O_P$ in mean field, seasonality, spatial relationships between $\delta^{18}O_p$ and temperature and precipitation are well reproduced and the skills evaluated by means of correlation coefficients, RMSE are found to be comparable with previous studies. On the other hand, the reproducibility of $\delta^{18}O_P$ on the interannual scale

is the best among the nudged simulations. Since this model is planned to be applied to paleoclimate study, this is pleasant result. The isotope enabled GCMs have been used to disentangle the isotopic variability from daily (Tremoy et al. 2012; Tremoy et al. 2014) to glacier-interglacier (Werner et al. 2000; Lee et al. 2008) timescale. Recently the other direction have emerged in which the simulated isotope-climate relationship is used to reconstruct paleoclimate (Risi et al. 2010) or use of the isotope ratio to constrain model physical parameters (Risi, Noone, Worden, Frankenberg, Stiller, Kiefer, Funke, Walker, Bernath, Schneider, Bony, et al. 2012; Risi et al. 2013). In such studies, the relationships between isotope and variables have to be well defined. On the interannual scale, however, large differences in the linear slope between isotope and temperature and precipitation among models are found. Although this is far beyond the scope of this study, the reason of the difference should be investigated as in Conroy et al. (2013).

This chapter also investigates the impact of isotopic fractionation over land. The mean field and the seasonal difference in $\delta^{18}O$ in precipitation over Siberia and North America are found to be significantly different from the control experiment as in Jouzel et al. (1991). Thanks to the process, the continental effect is more realistically reproduced. The difference is clearer if surface variables are compared. At the continental sites, the reproducibility of surface vapor isotope on synoptic timescale becomes better with the processes. The inclusion of isotopic fractionation over land surface most directly impacted on the isotopic composition in soil water. The $\delta^{18}O$ in soil water is better represented by the simulation with fractionation. In spite of the better agreement with the observations, inner soil processes exhibit a problem in the expression of soil water movement and need further improvements.

To wrap up, the conventional assumption in which all the land surface fluxes are not accompanied by isotopic fractionation may be legitimate, when one analyze atmospheric processes. If one use isotope enabled models to investigate processes close to land surface, or isotopic variability in terrestrial archives, the process has to be taken into account.

Chapter 3.
Evaluation of proxy models with proxy data

3.1. Introduction

The effect of isotopic composition on thermodynamic properties of simple chemical compounds shows that isotopic fractionation accompanies many of natural processes (Urey 1935). Consequently, the present isotopic composition of the lighter elements should reflect how their present state was reached (Epstein & Mayeda 1953). The finding prompted researchers to reconstruct paleotemperature using isotopic composition in carbonate of marine shells (Urey et al. 1951; Epstein et al. 1951). Subsequently Dansgaard (1954) found the relationship between the isotopic composition in precipitation and temperature. Based on those findings, many studies reconstructed paleoclimate using isotopic information archived in ice sheet and alpine glacier, coral, speleothem, tree ring cellulose, and lake and marine sediment. Because the instrumental measurements of weather or climate variables are especially limited before 1850, these climate proxies are invaluable to understand the Earth system which consists of various lengths of variabilities. However, the interpretations of such records are sometimes difficult. Isotopic composition may respond nonlinearly to multiple factors which are not necessarily related with climate. Furthermore there are no guaranties that the proxy-climate relationship is stationary over time. Therefore, factors which determine the variability of proxies must be well understood in the present climate. One way to disentangle the variability is the use of process based models. Isotope enabled GCMs have been used to understand the processes which have impact on isotope ratio in precipitation. It is an essential first step toward developing accurate climate-water isotope relationships for the past and the present to fully investigate the reproducibility and the relationship with climate on the timescale of proxy resolution. Most water isotope proxies, however, are not directly determined by isotopic composition of precipitation but influenced by additional factors, e.g. temperature, evaporation, vertical mixing, and advection of water masses in the case of coral records. When assessing the hydroclimate proxy potential of water isotope-based paleoclimate records, all these influences must be taken into account, which may serve to enhance or degrade the climate signal archived in the water isotope proxy (Conroy et al. 2013). Recently not reconstructed value but proxy data itself has been used for paleo-simulation validation (Pausata et al. 2011; Caley et al. 2014). Both studies validate the simulations by directly comparing simulated isotope ratio in speleothem with archived isotope ratio in the speleothem. Because the isotopic

signal recorded in speleothem is different from that in precipitation, what should be compared with data is simulated proxy isotope value, not precipitation isotope, as in their studies. For that purpose, models for each proxies should be developed and evaluated (Hughes & Ammann 2009). It becomes possible to evaluate paleo-simulations or disentangle climatic information recorded in paleo-proxies only by developing such models. Furthermore, with such models, data assimilation of proxy data would be possible (Hughes & Ammann 2009; Evans et al. 2013). Thus the developments of such forward models are of practical value.

Then, how is the current status of such forward models? Evans et al. (2013) concluded that forward proxy models are relatively few, and many of them have not been thoroughly evaluated. Dee et al. (2015a) integrated a set of existing proxy system models for ice core, coral, speleothem and tree-ring cellulose, and evaluated the models by using the output of SPEEDY-IER (Dee et al. 2015b). Though SPEEDY-IER shows satisfying result for the mean field, the physics of the model are simplified for the sake of fast computation. Moreover they run the model using the output of CGCM simulation. Therefore direct model-data comparison cannot be made in their paper. To fully evaluate the proxy system models, more realistic forcing should be used to run the forward models.

Responding to the background mentioned above, this chapter is aiming at the evaluation of the forward proxy models. The goal will be met by using the realistic atmospheric forcing. That will make direct comparison of the simulation with the observation possible. The "realistic" atmospheric observation will be constructed by isotope enabled GCMs simulations nudged toward reanalysis field. The use of such simulations may limit the length of comparison to recent several decades, but the period is suitable to model-data comparison because proxy data is the most abundant and the dating error is considered to be the smallest. In this work, the comparison is confined to ice core, coral and tree-ring cellulose by considering the temporal resolution of the proxies and the duration of the simulation.

This chapter is structured as follows: Section 2 describes forward model for ice core, coral, and tree ring cellulose and the experimental setting. The results are presented in Section 3 and discussion and conclusion will follow in Section 4.

3.2. Theory and model for climate proxy

3.2.1. **Ice core**

Glaciers and ice sheets preserve paleo-precipitation in its most direct form. Thus the isotopic compositions in ice cores can be considered primarily controlled by the isotope ratio in precipitation. However the isotopic signal in precipitation may be further modified by postdepositional processes. The processes include, sublimation, melting of ice, wind scoring and redistribution, and compaction, as well as diffusion in firn layer.

Generally drilling points of ice cores are selected to minimize the impact of postdepositional processes. However, the impacts are reported by numerous articles. Over high latitudes wind scoring has a

significant impact on isotopic profiles in ice cores. Fisher et al. (1983) showed that isotopic information recorded in two cores 1.3km apart are significantly distorted by the removal of winter snow by wind. Over low to mid latitudes, the impact of postdepositional processes on the isotopic composition recorded in ice cores may be further large (Schotterer et al. 2004). Melt can play an important role since many of glaciers there are temperate or close to temperate. To avoid this impact, the ice cores are often drilled in saddle or summit region. But unfortunately, such sites are frequently exposed to extreme meteorological conditions. In the dry regions of the tropical and subtropical Andes ice core drilling sites are additionally exposed to high solar radiation that favors sublimation. Consequently a glacier may undergo substantial loss in isotopic information under such conditions. Hardy (2003) reported that the Sajama ice core record relatively short proportion of time during January or February due to ablation by sublimation and wind scoring and argued that the $\delta^{18}O$ cannot be interpreted in terms of annual mean conditions. Similarly Bohleber et al. (2013) reported that isotopic ratio recorded in four ice cores drilled within the same saddle of Colle Gnifetti in the Monte Rosa do not correlate each other annually. They argued that this is because the difference in net snow accumulation, and in turn it depends on the mean local wind field and surface energy balance. According to them, after decadal scale smoothing, the isotopic ratio in cores show common variance.

From the review, it is clear that (1) ice cores may be seasonally biased, and (2) single ice core may not be spatially representative. To obtain meaningful information, ice core data has been temporally smoothed, stacked (Schneider and Steig, 2008), or applied to empirical orthogonal function analysis (Vuille et al., 2003). Such depositional noise is known to inversely relate with accumulation rate.

On the other hand, models for the postdepositional processes are very limited. Johnsen et al. (2000) formulated the effect of diffusion on $\delta^{18}O$ profile in firn layer, but the models for other processes, such as sublimation, wind scoring, or melting have not been developed to the best of my knowledge. Accordingly previous studies have directly compared ice core data with simulated isotopic composition in precipitation (Brown et al. 2006; Ortega et al. 2014).

To take account for the postdepositional noise, proxy model is not mature at this stage. In addition to that, to reduce the nose of data, duplicate ice cores are generally not available for one site and the targeting period of this study is not long enough to smooth the data. Therefore it is difficult to compare simulation and observation. In this study the simulated result will be briefly compared with the observation and more attention will be paid on the interannual variability in isotope ratio in precipitation.

3.2.2. **Coral**

The variability in $\delta^{18}O$ recorded in coral skeleton aragonite ($\delta^{18}O_{coral}$) depends on calcification temperature and local $\delta^{18}O$ in sea water ($\delta^{18}O_{sw}$) at the time of growth (Epstein & Mayeda 1953). Therefore previous studies modeled $\delta^{18}O_{coral}$ as the linear combination of sea surface temperature (SST) and the isotopic composition of sea water (Juillet-Leclerc & Schmidt 2001; Brown et al. 2006; Thompson

et al. 2011; Liu et al. 2013; 2014). Thus $\delta^{18}O_{coral}$ have been expressed as following way:

$$\delta^{18}O_{coral} = \delta^{18}O_{sw} + aSST + b \tag{3.1}$$

where a and b are the constants. A number of studies have investigated the slope a to reconstruct SST. Generally SST and $\delta^{18}O_{coral}$ are simply regressed for the present to obtain the slope by assuming that $\delta^{18}O_{sw}$ is constant. The reported slope ranges from -0.10 to -0.34 ‰/°C for the Porties genus of coral which is commonly used for paleoclimate reconstruction (Evans et al., 2000; Juillet-Leclerc and Schmidt, 2001). Brown et al. (2006) selected -0.20‰/°C to model $\delta^{18}O_{coral}$. More recently Liu et al. (2013; 2014) calculate the slope with consideration of covariance between SST and $\delta^{18}O_{sw}$. In this study, the slope of -0.22 ‰/°C is selected following Thompson et al. (2011), because the covariance between SST and $\delta^{18}O_{sw}$ is not always available for all the sites (Liu et al. 2014).

Isotopic composition in sea water is mainly determined by freshwater flux between ocean and atmosphere (i.e. evaporation and precipitation) (Cole and Fairbanks, 1990; Fairbanks et al., 1997). In addition to the net freshwater flux between ocean and atmosphere, the mixing with deep ocean body affects $\delta^{18}O$ in sea surface water (Brown et al. 2006; Liu et al. 2013; 2014). Accordingly the time variation of the surface water and its isotopic amount can be expressed as

$$\frac{\partial Q}{\partial t} = P - E + D \tag{3.2}$$

$$\frac{\partial R_{sw} Q}{\partial t} = R_P P - R_E E + R_D D \tag{3.3}$$

where Q is the depth of the upper layer, P is the precipitation, E is the evaporation, D is the mixing with the lower layer (damping factor), and R is the isotope ratio. Note that R_D corresponds to R in deep sea water. By multiplying R_{sw} by Eq. 3.2 and subtracting that from Eq. 3.3 yields

$$\frac{\partial R_{sw}}{\partial t} Q = (R_P - R_{sw})P - (R_E - R_{sw})E + (R_D - R_{sw})D \tag{3.4}$$

The equation can be transformed into delta notation.

$$\frac{\partial \delta_{sw}}{\partial t} = \frac{1}{Q}\{(\delta_P - \delta_{sw})P - (\delta_E - \delta_{sw})E + (\delta_D - \delta_{sw})D\} \tag{3.5}$$

The depth of upper layer and the damping factor by mixing are the tunable parameters. The parameters used are different from study to study: Brown et al. (2006) choose Q = 5 m and D/Q = 1.17 x 10^{-7} (s^{-1}).

Liu et al. (2013; 2014) choose Q = 20 (m) and D/Q = 0.4 (mon^{-1}), which is roughly equivalent to 1.5 x 10^{-7} (s^{-1}). Liu et al. (2013; 2014) calibrate the parameters with Philippines coral records and use that that value for the whole corals, and they succeeded in simulating the temporal variation better than Brown et al. (2006). Thus in this study, the parameter set of Liu et al. (2013; 2014) is used as a default. In both studies, the effect of horizontal advection, terrestrial runoff, and site-by-site difference in vertical mixing and upwelling are neglected, and they assume that the R_D is constant. Therefore the model cannot reproduce long time trend which stems from the long term change in the isotopic composition in deep sea water.

In the simulation, the forward proxy model is driven by using MIROC5 monthly outputs. Then the monthly values are simply averaged arithmetically to produce the annual mean. Therefore this procedure neglects the timing of coral growth. R_D is obtained from estimation of average $\delta^{18}O_{sw}$ based on point observations and regional relation between $\delta^{18}O_{sw}$ and salinity (LeGrande & Schmidt 2006).

3.2.3. **Tree ring cellulose**

Isotopic information has been extracted from tree-ring α-cellulose to reconstruct paleoclimate. Several models for tree-ring cellulose have been proposed (e.g. Roden et al. 2000; Barbour et al. 2004). In this study the model is constructed based on Roden et al. (2000). Although the oxygen atoms of cellulose are both from the water taken up by tree roots and carbon dioxide absorbed via leaves, the $\delta^{18}O$ values of cellulose can be thought of the water taken up by tree roots, to a first approximation (Roden et al. 2000). Isotopic fractionation does not occur when plants take up water by their roots, or transportation of water from root to leaf, thus the isotope ratio of water which enters leaves is the same as that of source water. The transported water subsequently evaporates from the leaves via stomata. This results in isotopically enriched leaf water in heavy isotopes. Flanagan et al. (1991) proposed a model for the evaporative enrichment, which was originally developed by Craig and Gordon (1965) (what we call "modified Craig-Gordon model). The model includes evaporative enrichment and leaf boundary layer considerations and diffusion through stomata. The equation for the isotope ratio in leaves is described as following:

$$R_l = \alpha^*[\alpha_k R_N \left(\frac{e_i - e_a}{e_i}\right) + \alpha_{kb} R_N \left(\frac{e_s - e_a}{e_i}\right) + R_a(\frac{e_a}{e_i})] \tag{3.6}$$

Where α^*, α_k, α_{kb} are liquid-vapor equilibrium fractionation factor, the kinetic fractionation factor associated with diffusion in air, and the kinetic fractionation associated with diffusion through the boundary layer, respectively. R is the molar ratio of heavy to light isotope forms and R_N and R_a are that of source water and bulk air. e_i, e_a and e_s are the partial pressures of water vapor in the leaf intercellular air spaces, the atmosphere respectively and the leaf surface. e_s is calculated as

$$e_s = \frac{g_{sw} w_i - E(1 - \frac{w_i}{2})}{g_{sw} - E/2} P_s \quad (3.7)$$

where, g_{sw} is stomatal conductance to water vapor, w_i is the mole fraction of intercellular vapor ($w_i = e_i/Ps$), E is transpiration rate (mol m^{-2} s^{-1}), and P_s is atmospheric pressure (Ball 1987). e_i is assumed to be saturation vapor pressure at the leaf temperature. The leaf temperature is arbitrary set to 1 K higher than atmospheric temperature. E is then calculated as

$$E = \left(\frac{1}{\frac{1}{g_{sw}} + \frac{1}{g_{bw}}} \right) (w_i - w_a) \quad (3.8)$$

where, g_{bw} is boundary layer conductance to water vapor, w_a is the mole fraction of air vapor.

The model assumes that the isotopic value in leaves is equivalent to the isotopic composition of water at the site of photosynthesis predicted in Eq. 3.6.

During the photosynthesis, $\delta^{18}O$ in leaf cellulose are 27‰ elevated (Sternberg, 1989). The synthesized sugar is then transported to xylem, and finally fixed in cellulose. In the process, the sugar is once decomposed. Consequently there occurs isotopic exchange between the carbohydrate and local xylem water. Taking into those effects account, tree-ring cellulose isotope ratio is expressed as;

$$\delta^{18}O_{cell} = f(\delta^{18}O_N + \epsilon) + (1 - f)(\delta^{18}O_l + \epsilon) \quad (3.9)$$

where f represents the fraction of carbon-bound oxygen that undergoes exchange with medium water, and ε is the isotopic elevation associated with carbohydrate synthesis (ε=27‰).

In the simulation, the forward proxy model is forced by using MIROC5 monthly outputs; relative humidity, surface temperature, surface pressure, $\delta^{18}O$ in precipitation and near surface vapor ($\delta^{18}O_p$, and $\delta^{18}O_v$). The isotopic composition of source water ($\delta^{18}O_{sw}$) is calculated by applying backward moving average (3 months) for $\delta^{18}O_p$ to account for hydrological memory in the soil. Using those data and Eq. 3.9, monthly $\delta^{18}O_{cell}$ is calculated. Then the monthly mean is weighted by net primary productivity (NPP) to produce the annual mean. The growth year is uniformly defined as January to December. In this study I use NPP data estimated by a sensor MODIS aboard Terra satellite. The data is obtained from NASA EARTH OBSERVATIONS (http://neo.sci.gsfc.nasa.gov/view.php?datasetId=MOD17A2_M_PSN).

3.3. Data and experimental design

3.3.1. **Proxy data**

National Oceanic and Atmospheric Administration (NOAA) archives paleoclimate data (https://www.ncdc.noaa.gov/data-access/paleoclimatology-data). The 2k Network of the Internatioanl

Geosphere-Biosphere Programme (IGBP) Past Global Changes (PAGES 2k) also provides data set as an appendix of their paper (Ahmed et al. 2013). In this study, those data is used for the model data comparison. Additionally 30 tree ring cellulose data and 6 ice core data are collected individually from published papers. All the proxies are mathematically averaged to calculate annual mean and proxies whose time resolution is greater than one year is excluded. The full list of proxies used in this study is in Appendix C.

3.3.2. **Experimental design**

The forcing to drive forward proxy models described in the previous section are created by newly developed isotope enabled GCM, MIROC5. Please see Chapter 2 and Appendix A for the performance of the GCM. The model resolution is set to horizontal T42 (approximately 280km) with 40 vertical layers. The atmospheric and land surface components coupled are coupled, and sea surface temperature and sea ice concentration is prescribed (HadISST; Rayner et al., 2003). Greenhouse gasses (carbon dioxide, methane, and chlorofluorocarbon) and ozone are also prescribed. Additionally, a nudging technique is used to assimilate horizontal wind in order to make direct comparison with observations possible. The time constant is set to 0.1 day. The reanalysis field is based on 20th Century Reanalysis (20CR; Compo et al. 2011) but the ensemble mean field with incremental correction is used following Yoshimura & Kanamitsu (2013). After a spin-up period of 100 years with the boundary conditions for 1871, the simulation started in January 1871 and end at December 2007. Last 58 years (1950-2007) of the simulation are used in this study to maintain the quality. Monthly average data is used to run the forward models. After running forward models on monthly timescale, they are weighted and averaged to calculate annual mean value. The way to weight the monthly data is described in previous section.

3.4. Result

3.4.1. **Ice core and precipitation isotope**

Figure 3-1 shows the observed time series of $\delta^{18}O$ recorded in ice cores for 35 sites along with thesimulated results for the sites. Multiple time series are available for Agassiz, Crete, Rongbuk, ITASE 00-1, and Law Dome C. For those sites, single simulated time series and multiple observed time series are compared in one panel to show the potential impact of the postdepositional processes.

The differences among adjacent ice cores are especially large at around Crete where 9 cores are available in one model grid. The correlation coefficients for $\delta^{18}O$ among the observed cores are reported to range from 0.19 to 0.69 among the cores (Clausen et al. 1988). Due to the large differences, the correlation coefficients between the simulation and the observation range from 0.10 to 0.60 ($p < 0.001$) at the site.

Similarly, $\delta^{18}O$ in 5 cores drilled at Agassiz show different variability (the correlation coefficients

among the cores range from -0.71 to 0.77). Even though the simulation does not correlate significantly with any of the observations, the simulation is enveloped by the observations in most years.

Although partial matches between the simulation and the observation are also found in many sites (for instance, B21, Muztagata, and Gomez), none of them correlate significantly. Figure 3-2 maps the temporal correlation coefficients for each site. 5 out of 35 sites are significantly correlated ($p < 0.05$). The reproducibility is relatively high in Northern Hemisphere than Southern Hemisphere. The 20CR used to nudge the atmospheric simulation is known for its relatively poor reproducibility over Southern Hemisphere (Compo et al. 2011). Thus the low reproducibility over Andes and Antarctica may partly be attributable to the quality of the atmospheric forcing used in the nudging. To confirm this hypothesis, Figure 3-3 compares the observation with an additional simulation which is nudged toward NCEP/NCAR Reanalysis (NNR; Kalnay et al. 1996). The additional simulation clearly results in better correlation over Antarctica while the reproducibility for Andes remains poor. As reviewed in Section 3.2.1, the depositional noise may be modified the isotopic signal recorded in the ice cores. However the impact of postdepositional processes is difficult to be estimated by the atmospheric simulation because of the scale difference. Furthermore the poor reproducibility over those areas hampers further model data comparison. Therefore focus will be paid on precipitation isotope variability rather than that in ice core hereafter in this section. Since most of the isotopic terrestrial paleoclimate archives are influenced by precipitation isotope, to understand the variability in $\delta^{18}O$ in precipitation is prerequisite to interpret the other isotopic proxies, as will be seen in the following sections. Given the reproducibility of isotope ratio in precipitation on the interannual timescale by isotope enabled MIROC5, the model field instead of the observation field will be analyzed.

Before analyzing the interannual variability in isotope ratio of precipitation, processes which have potential impact on it is briefly summarized here. Historically isotope ratios in precipitation have been interpreted as a proxy for temperature over high latitudes and precipitation over low latitudes (Dansgaard 1964). In his preceding paper, he argued that isotopic composition in vapor is determined by its hydrological history along its trajectory. That is, (1) evaporation temperature, (2) the origin of the vapor, and (3) earlier precipitation of water owing to cooling. The first and second are related to the initial condition of the moisture, and the third one describes the process in which the moisture become gradually depleted in heavy isotopes due to preferential loss of light isotope by condensation. The third process is called Rayleigh distillation process. Here the process will be described in detail.

The isotopic mixing ratio (q_i) change due to condensation can be described as follows:

$$\mathrm{d}q_\mathrm{i} = \alpha \left(\frac{q_i}{q}\right) dq \tag{3.10}$$

where α is isotopic fractionation factor and q is mixing ratio. By integrating both sides and by arranging the equation yield,

$$\frac{q_\mathrm{i}}{q} = \frac{q_{i0}}{q_0}\left(\frac{q}{q_0}\right)^{\alpha-1} \tag{3.11}$$

where subscript 0 means that the variable is in its initial value. The equation can be shown in VSMOW scale,

$$\mathrm{R_v} = \mathrm{R_{v0}} \left(\frac{q}{q_0}\right)^{\alpha-1} \tag{3.12}$$

Then, the isotopic composition of precipitation can be expressed as following:

$$\mathrm{R_p} = \alpha R_v = \alpha R_{v0} (\frac{q}{q_0})^{\alpha-1}. \tag{3.13}$$

This Rayleigh distillation model explains how the isotope ratio changes along the moisture precipitates rainfall due to the decrease in saturation vapor pressure by cooling. Thus, in this case, q is saturation vapor pressure, which is a function of temperature. Because isotopic fractionation factor is also a function of temperature, the isotopic composition in precipitation can be almost described by temperature. With this model, the observed spatial relation between precipitation isotope ratio and temperature has been successfully explained. Based on the observed relationship and the result of the model, many studies reconstructed paleotemperature using isotope record archived in ice cores. After that, however, they suggested that the isotope based reconstruction underestimated temperature difference between present and last glacial maximum. Boyle (1997) explained the reason by change in initial value of vapor isotope ratio. The dependency on initial value, which means that the isotopic composition in evaporative vapor is dependent on ambient temperature, relative humidity, and wind speed according to Merlivat and Jouzel (1979), implies the importance of moisture source area.

Precipitation amount, on the other hand, has also connected with $\delta^{18}O_P$ distribution, as amount effect. Although Dansgaard (1964) mentioned that "*when looking for reasons for the amount effect we are confronted with difficulties, mainly because of the extreme complexity of the isotopic turnover in the processes forming convective rain*", he suggested three possible mechanisms for the effect. The first one explains the effect by using Rayleigh distillation model as in temperature effect. The moisture can be more depleted along with mass loss due to precipitation. Hence more mass is condensed, the more depleted residual vapor and condensation from it are. The second one connects the amount effect and diffusive exchange between raindrop and the ambient vapor. Light rain tends to produce small raindrop whose falling speed is slow and whose isotopic equilibration time with the ambient vapor is small. Thus such small drops are easy to reach the isotopic equilibrium with the ambient vapor. Because vapor in lower troposphere is enriched in heavy isotopes compared with mid- to upper troposphere, isotope ratio in small raindrop collected in ground is expected to be more enriched. Contrary, heavy rainfall tends to produce large raindrop whose falling speed is faster and the equilibration time is longer, and hence they are less equilibrated with the ambient vapor. As a consequence, heavy rainfall results in low $\delta^{18}O_P$. The third one also connects the amount effect with post condensation process but in this case with re-evaporation from raindrop. When raindrops go through low altitude air whose humidity is low, the raindrops loose a great deal of liquid mass and thereby considerable enrichment in raindrops occurs. Currently those processes have been confirmed by using isotope enabled models (Lee & Fung 2008; Risi

et al. 2008).

Though the temperature effect and the amount effect have been used to explain the spatial distribution of $\delta^{18}O_P$ and/or monthly change in $\delta^{18}O_P$, these effects are observed also on the interannual timescale. For example, White et al. (1997) found temporal correlation between isotope record in stacked ice cores from Greenland and long term temperature record. Werner et al. (2002) similarly found the correlation for Greenland and Antarctica. For low latitude, Vuille and Werner (2005), Ishizaki et al. (2012), and Okazaki et al. (2015) found that what control isotope ratio in precipitation on the interannual timescale is precipitation amount fell in windward area for South America, South East Asia, and West Africa, respectively. Also the importance of moisture source is now recognized in the interannual variability (Vuille 2003) by model simulations.

Review work revealed that it is necessary for the understanding of the interannual variability in $\delta^{18}O_P$ to take into account not only local information at the site of interest but also windward information along with moisture trajectory. To investigate what factors control the interannual variability in $\delta^{18}O_p$, precipitation amount and relative humidity along the moisture trajectory, local temperature, and the initial value of vapor isotope ratio are picked out for all the model grids for all the precipitation events. The relative humidity is chosen to take into account the effect of evaporative recharge. Moisture trajectories are estimated by 10-day backward trajectory by using the 6 hourly outputs of the model simulation. Because most water vapor in the atmosphere exists at low levels, total column vapor flux is used to the trajectory following Yoshimura et al. (2003; 2004). The picked out four variables are weighted by precipitation amount at the end point of the trajectory to calculate the annual mean. Thus the method is largely similar to Sodemann et al. (2008). The calculation is conducted for the period from 1980 to 2007.

Figure 3-4 shows the variance of the interannual variability in $\delta^{18}O_p$ explained by all the variables and by each factor. Most areas in low latitude and high latitudes are well explained by the model, whereas arid and semi-arid areas in mid latitudes are not. The dominant factor is found to be temperature in high latitudes and is precipitation over low latitudes as previous researches have shown. Figure 3-5 show the percentage explained by upstream amount effect. The value is calculated as the difference between the determination coefficient with the effect (same as Figure 3-4a) and that without upstream effect. The upstream effect is large in Amazon, Indian monsoonal area, and West Africa as in previous research (Vuille et al. 2005; Ishizaki et al. 2012; Okazaki et al. 2015). Additionally, the large impact can be seen in Central Africa and north East Asia, Alaska, and east coast of Greenland.

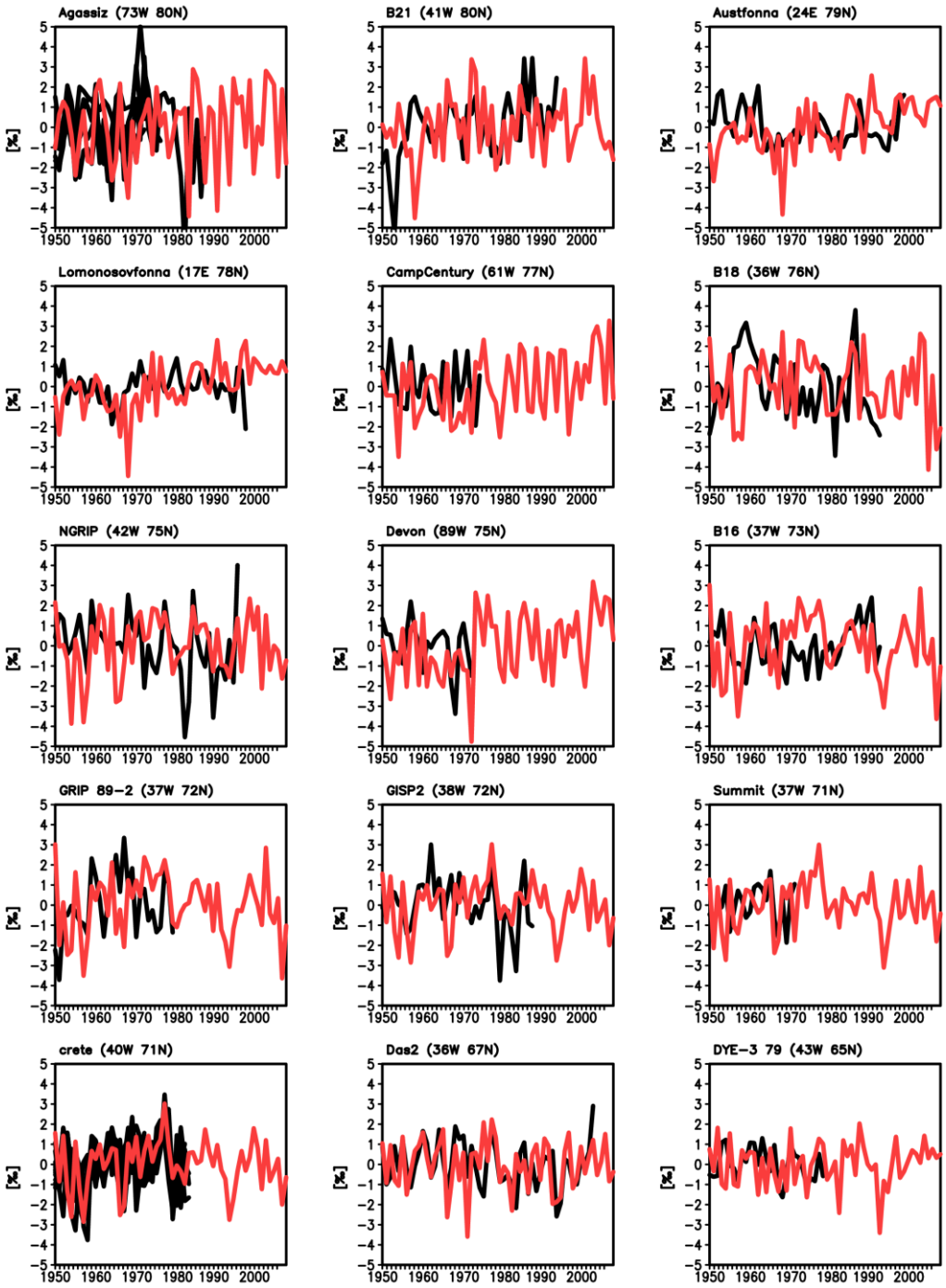

Figure 3-1 Timeseries of $\delta^{18}O$ anomaly in ice core obtained from measuremeents (black) and the simulation (red).

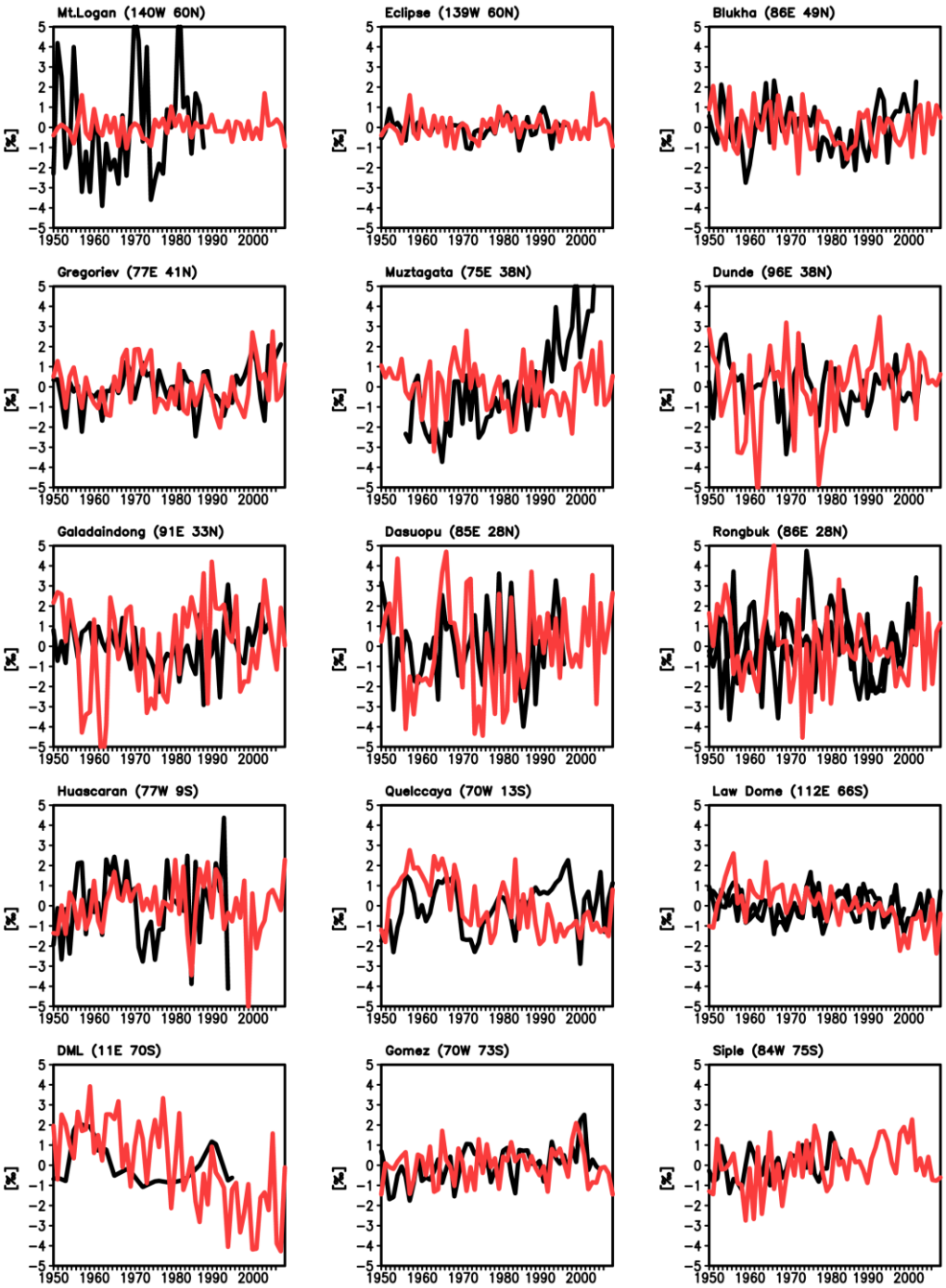

Figure 3-1 (continued)

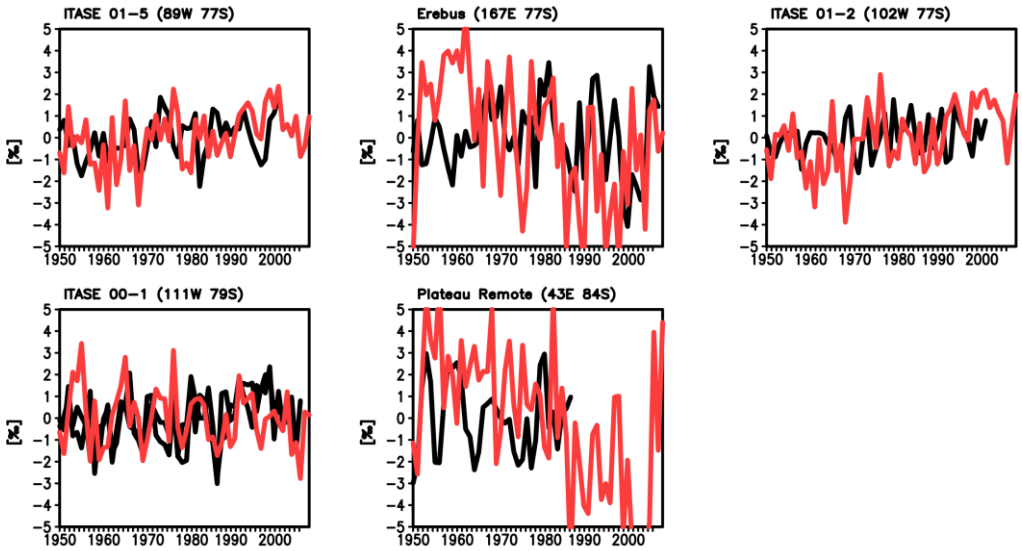

Figure 3-1 (continued)

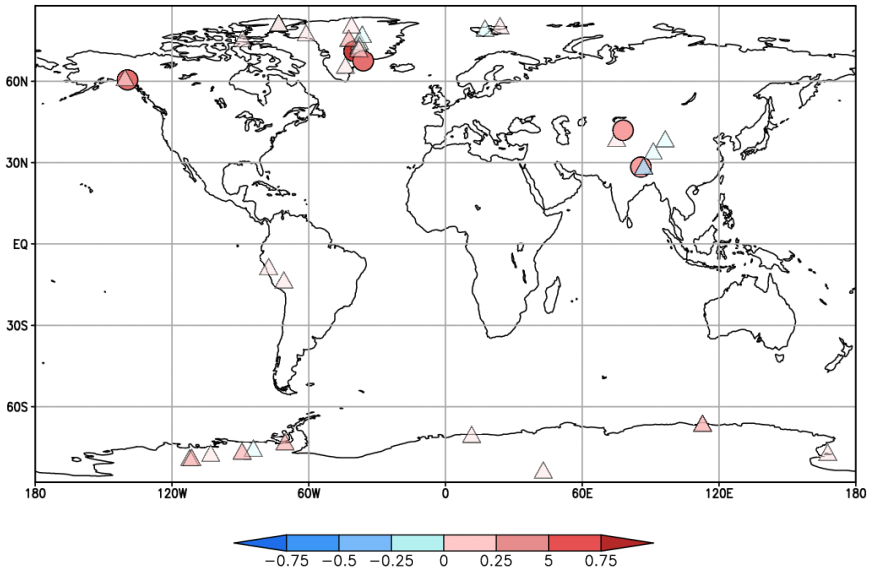

Figure 3-2 Correlation coefficients between the observation and the simulation for $\delta^{18}O$ in ice core on the interannual timescale. The site at which the simulation and the observation correlate each other at 5% significance level is drawn as circle. The other sites are drawn as triangle.

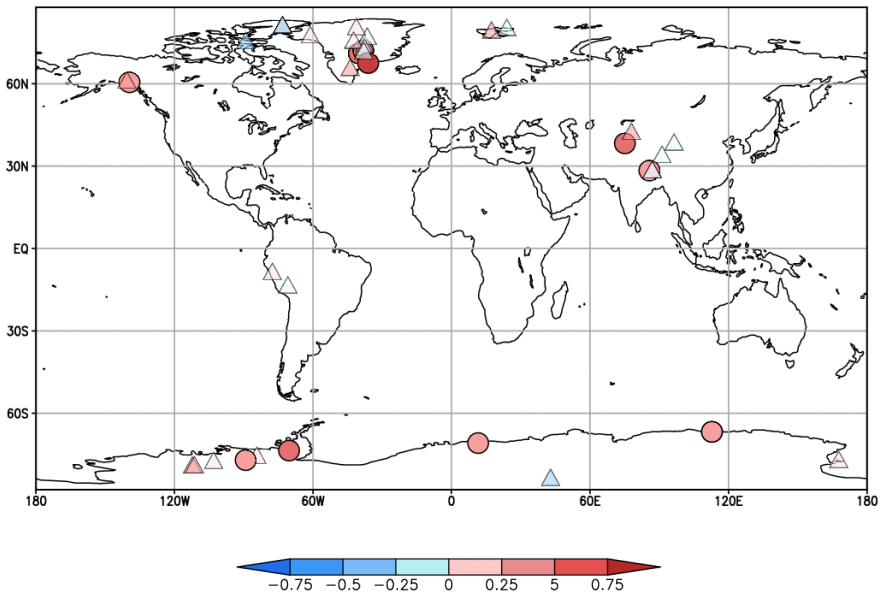

Figure 3-3 Same as in Figure 3-2 but the simulation is nudged toward NCEP/NCAR Reanalysis (Kalnay et al. 1996)

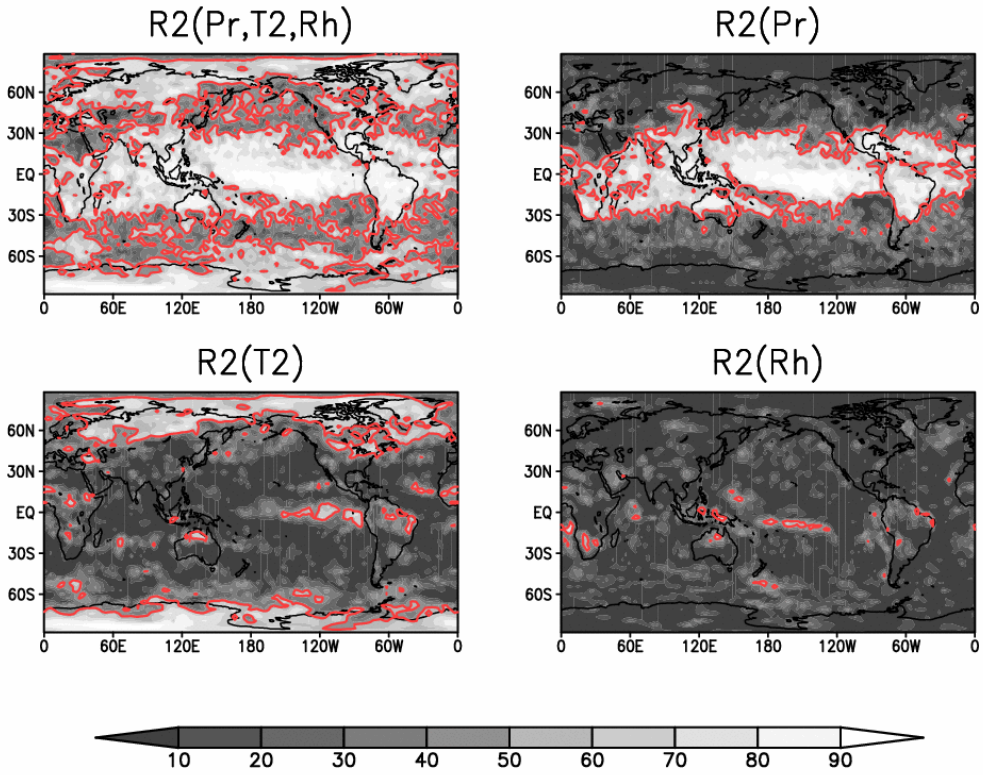

Figure 3-4 Determination coefficient (%). Explanatory variables are (a) precipitation amount, temperature, and relative humidity, (b) precipitation, (c) temperature, and (d) relative humidity.

Red contour separates the globe into the area where the determination coefficient is greater than or equal to50 % and less than 50%.

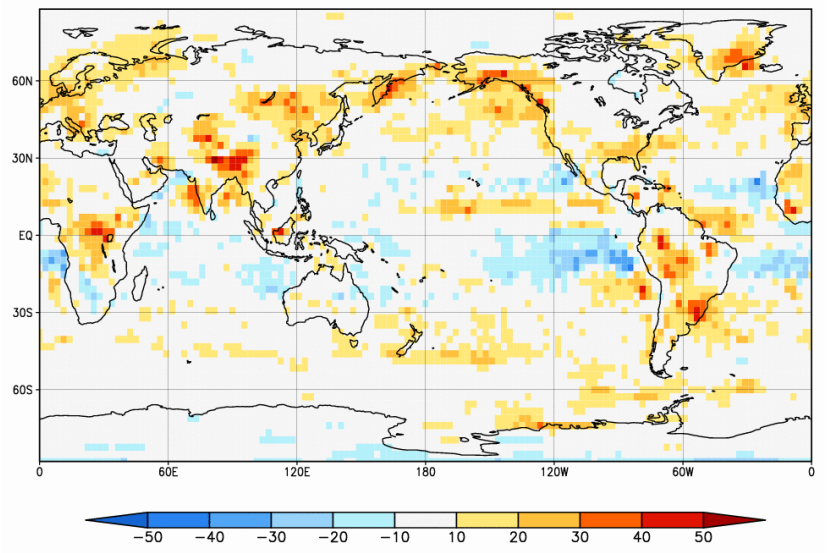

Figure 3-5 Upstream amount effect.

3.4.2. Coral

Temporal variability

Figure 3-6 compares the $\delta^{18}O_{coral}$ time series simulated by the model and recorded in the corals, and Figure 3-7 maps the correlation coefficients for each site. As in previous subsection, the time series are shown in anomaly form. The amplitude of variability and timing of ups and downs are well simulated; 33 out of 45 samples are significantly correlated with measured chronology ($p < 0.05$). Generally the reproducibility is better in Pacific basin than in Indian Ocean or Atlantic basin. Liu et al. (2014) showed that the reproducibility is largely dependent on precipitation amount at the site. This is because in such sites precipitation amount is dominant factor and the impact of other factors which are not included in the model is suppressed. The same tendency is confirmed in this study and this largely explains the spatial distribution of correlation coefficients. Since the model does not take into account the terrestrial runoff and the horizontal advection by sea current, the variability of corals located in the areas where those effects are large are not well reproduced by the model. At Buccoo (10°N, 61°W), $\delta^{18}O_{sw}$ and hence $\delta^{18}O_{coral}$ is reported to be influenced by the river discharge (Moses & Swart 2006). Also, the reason for the poor skill at Bermuda (32°N, 64°W) may be because of the strong sea current there; Gulf Stream. To confirm the effect of the sea current isotope incorporated OGCM is necessary, and this will be investigated in the future.

The coral model in this study has one empirical parameter and two tunable parameters;

temperature-isotope slope, depth of the upper layer, and damping factor by mixing. To confirm the robustness or the sensitivity of the model, the parameters are perturbed one by one. The parameter perturbation setting and the results are in Figure 3-8. The thick upper layer depth and the large damping factor act to mute the response to hydrological balance, and the thin depth and the small damping factor act to amplify the response (not shown) as expected from the Eq. 3.5. As a result, the result with thick upper layer depth and large damping factor is close to the experiment with constant $\delta^{18}O$ in sea water, and vice versa. The maximal difference in the correlation coefficient among the experiments is up to 1.14 (Punta Pitt; 1°S, 89°W). The result suggests that the $\delta^{18}O_{coral}$ is dominated by SST and is not sensitive to $\delta^{18}O_{sw}$. Actually the highest correlation coefficient for the coral is achieved when the forward model is driven by only SST for the site. 20 sites reveal the same feature as Punta Pitt. On the contrary, the highest correlation is achieved when the forward model is driven by only $\delta^{18}O_{sw}$ at 3 sites. The combination of both factors result in the highest correlation at 14 sites. This result suggests that the sensitivity to SST is different from site by site and the parameter (factor a in Eq. 3.1) must be estimated individually must be estimated individually as in Liu et al. (2014).

Controller of variability in $\delta^{18}O$ in coral

Even though there are several corals whose $\delta^{18}O$ variabilities are not well reproduced by the models, generally the model can capture the variability of $\delta^{18}O_{coral}$ fairly well. Hereafter controller of the isotopic composition in coral skeleton aragonite on the interannual timescale will be investigated by decomposing the model into five terms: temperature, precipitation, evaporation, $\delta^{18}O$ in precipitation, and $\delta^{18}O$ in evaporation. The contribution to the interannual variability of $\delta^{18}O$ in coral of each term is estimated following Liu et al. (2014). The variability of $\delta^{18}O$ in coral can be described by the variability of the factors:

$$\Delta\delta^{18}O_{coral} = \frac{\partial\delta^{18}O_{coral}}{\partial(SST)}\Delta(\mathrm{SST}) + \frac{\partial\delta^{18}O_{coral}}{\partial P}\Delta P + \frac{\partial\delta^{18}O_{coral}}{\partial\delta^{18}O_P}\Delta\delta^{18}O_P + \frac{\partial\delta^{18}O_{coral}}{\partial E}\Delta E + \frac{\partial\delta^{18}O_{coral}}{\partial\delta^{18}O_E}\Delta\delta^{18}O_E \quad (1)$$

The gradient terms in the equation are estimated individually by conducting sensitivity tests wherein $\delta^{18}O_P$ and $\delta^{18}O_E$ are increased by 0.2‰ and the precipitation and evaporation rate by 10%. The gradient term for SST is -0.22 as used in Eq. 3.1. Then the standard deviation of annual average of each terms are calculated as their variability. Here "contribution" is defined as the ratio of variability of each term to that of $\delta^{18}O$ in coral. Figure 3-9 shows the contribution of each term. In the arid basin, the contribution of $\delta^{18}O_{sw}$ is small (~20%). In such an area mainly SST determines the variability of $\delta^{18}O_{coral}$. The large impact of SST is not confined to the arid basin; SST exerts the influence on the whole tropical ocean basin. The contribution of SST amounts to 40 % even at the least affected area. The isotope enabled MIROC5 whose output is used for the forcing of the forward proxy model is originally forced by the observed SST.

Thus the SST used to drive the forward model can be considered as real. This fact and the large dependence of $\delta^{18}O_{coral}$ on the SST must result in the high reproducibility. The impact of $\delta^{18}O_{sw}$ on $\delta^{18}O_{coral}$ is secondary in many areas but the impact is larger than SST in the Pacific warm pool, where precipitation is the heaviest. The contribution of $\delta^{18}O_{sw}$ consists of that of precipitation, evaporation, $\delta^{18}O_P$, and $\delta^{18}O_E$ (Figure 3-9 c-f). $\delta^{18}O_{sw}$ in the areas in which precipitation amount is large (e.g. Pacific warm pool, ITCZ, and SPCZ) is mainly dominated by precipitation amount (up to 60%). The second largest factor is $\delta^{18}O_P$ and $\delta^{18}O_E$ (~30%). The impacts are large in the similar area in which the impact of precipitation is large. The contribution of evaporation is relatively large in subtropical gyres but still the contribution is less than 30%. Thus the signal in $\delta^{18}O_{coral}$ can be interpreted as SST except for the Pacific warm pool, ITCZ, and SPCZ. In such areas, the dominant factor is $\delta^{18}O_{sw}$ or both $\delta^{18}O_{sw}$ and SST. However caution is needed to interpret this figure; the relative contribution is dramatically changed with different factor a in Eq. 3.1. If the factor of -0.1 is used, which is the upper bound of reported value, the variability of $\delta^{18}O_{coral}$ is explained by $\delta^{18}O_{sw}$ more than 90% over pluvial areas. On the other hand, with that value, $\delta^{18}O_{coral}$ is still dominated by SST around Pacific gyres. Thus coral obtained from those areas would be faithful recorder of SST. Nevertheless the estimation of the factor is critical to obtain other information than SST from $\delta^{18}O_{coral}$.

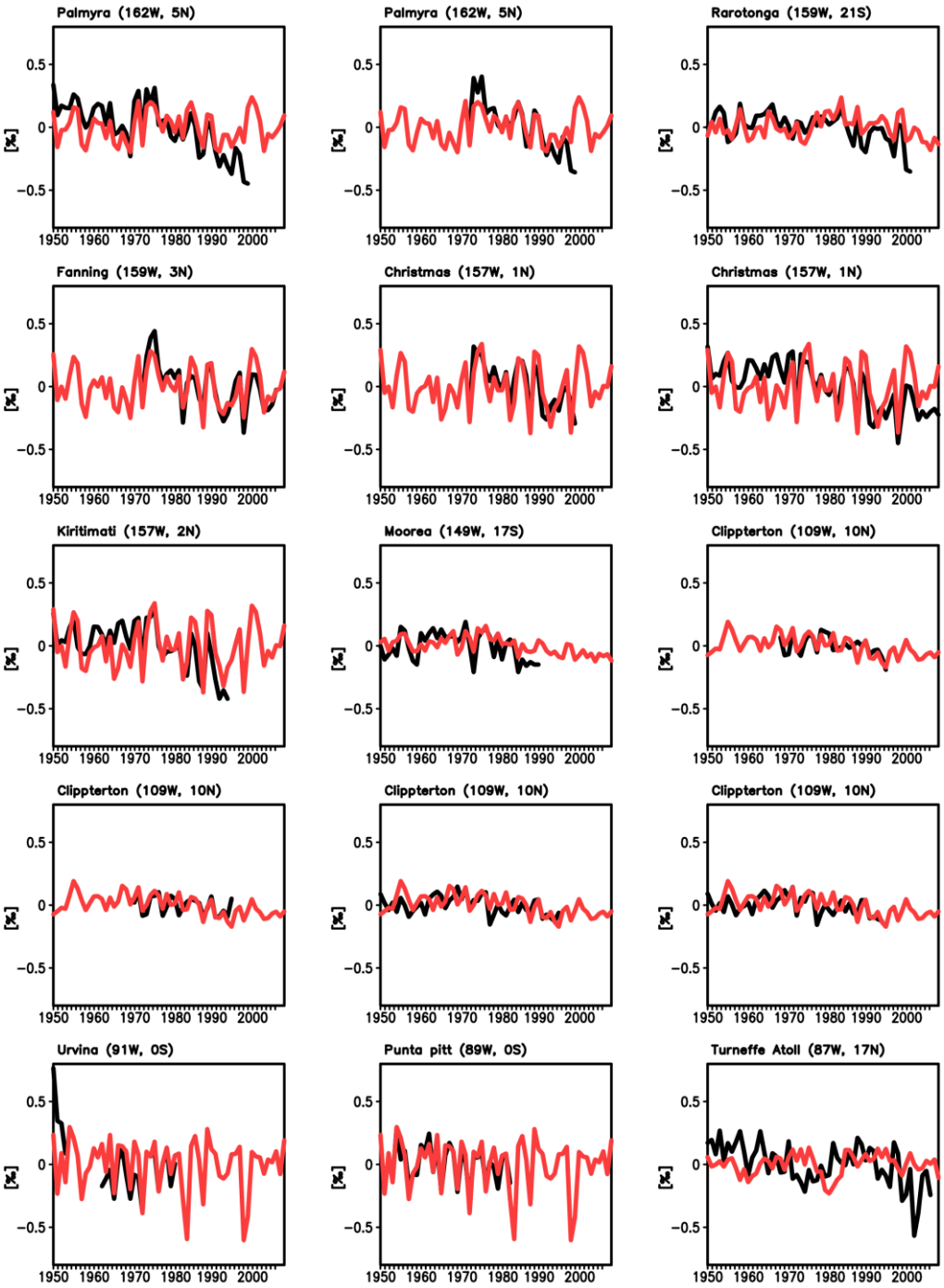

Figure 3-6 Same as in Figure 3-1 but for $\delta^{18}O$ in coral

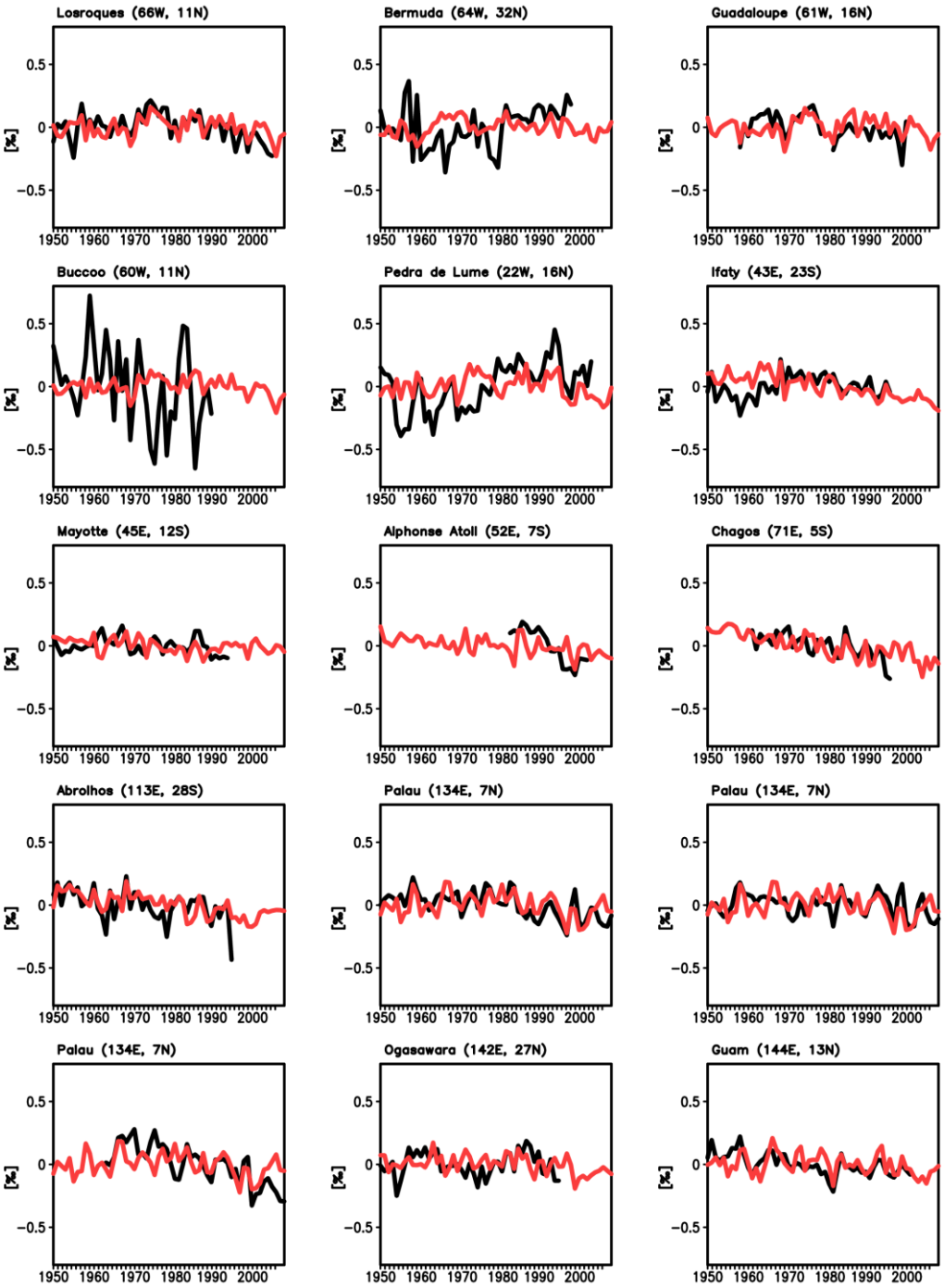

Figure 3-6 (Continued)

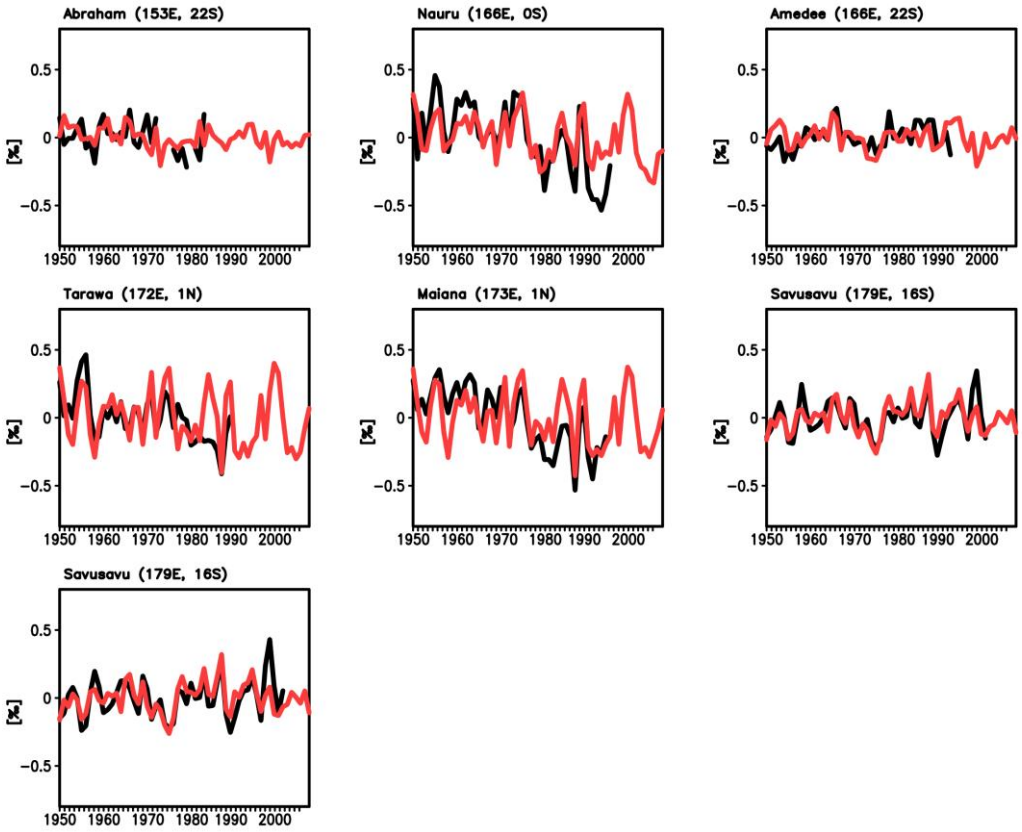

Figure 3-6 (Continued)

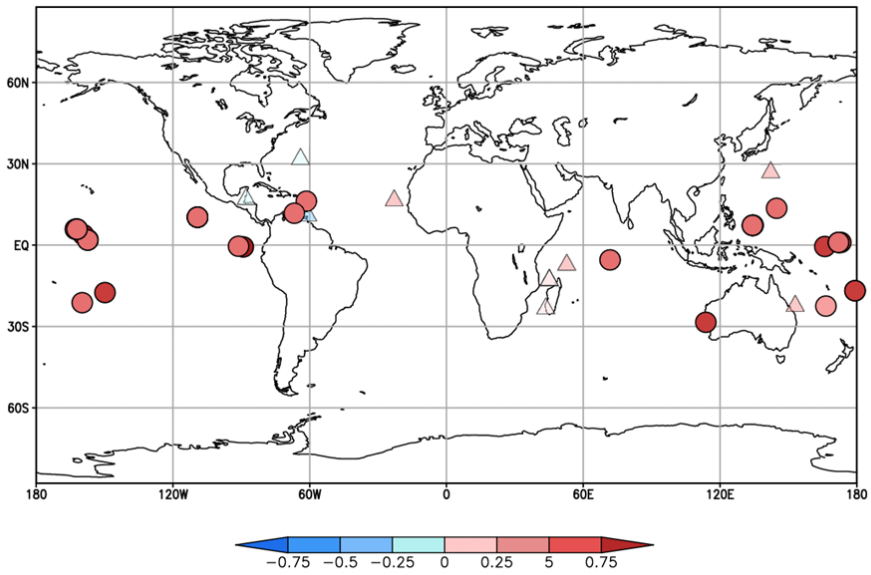

Figure 3-7 Correlation coefficients for $\delta^{18}O$ in coral skeleton aragonite on the interannual timescale

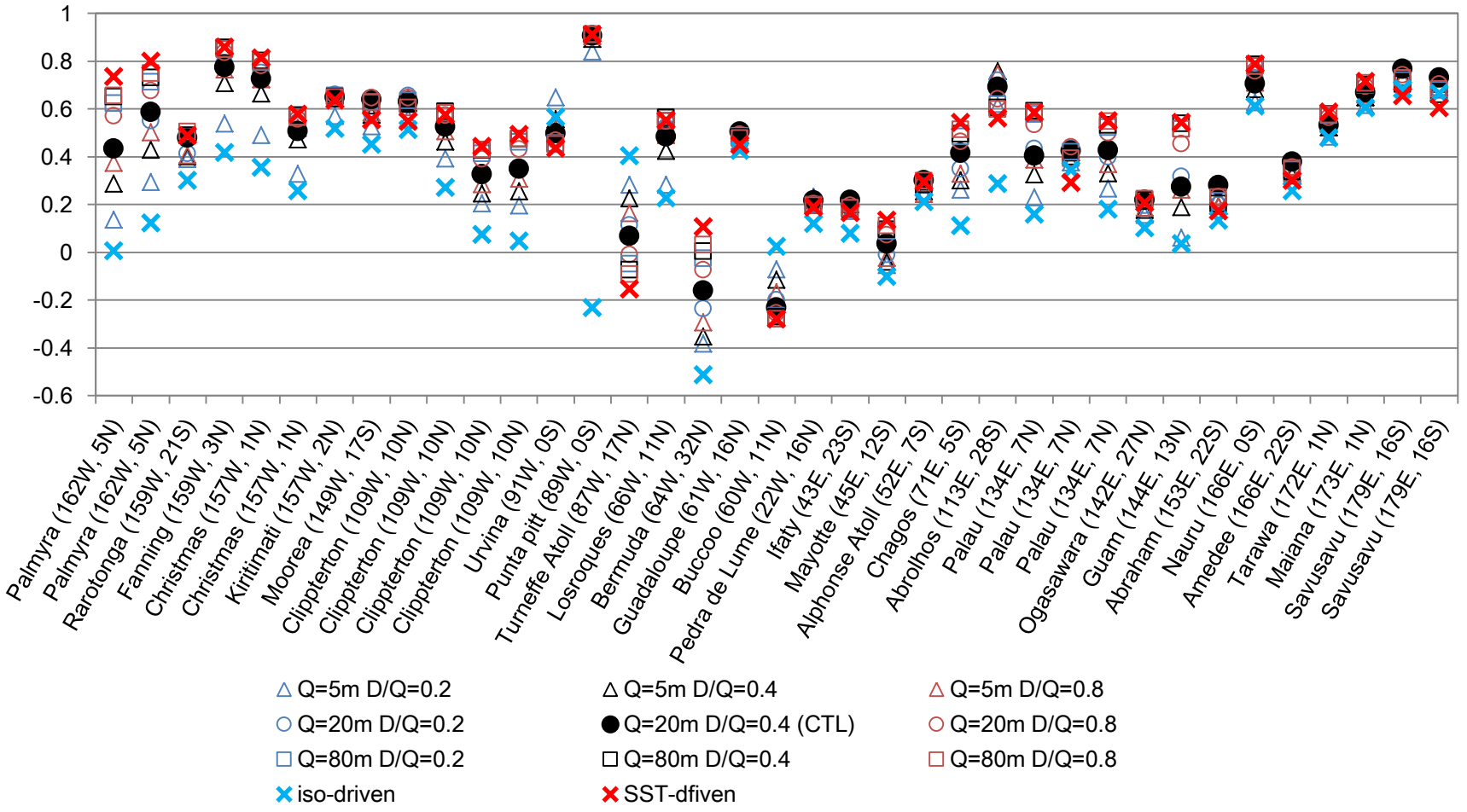

Figure 3-8 Sensitivity of the coral forward model to parameters and forcing.

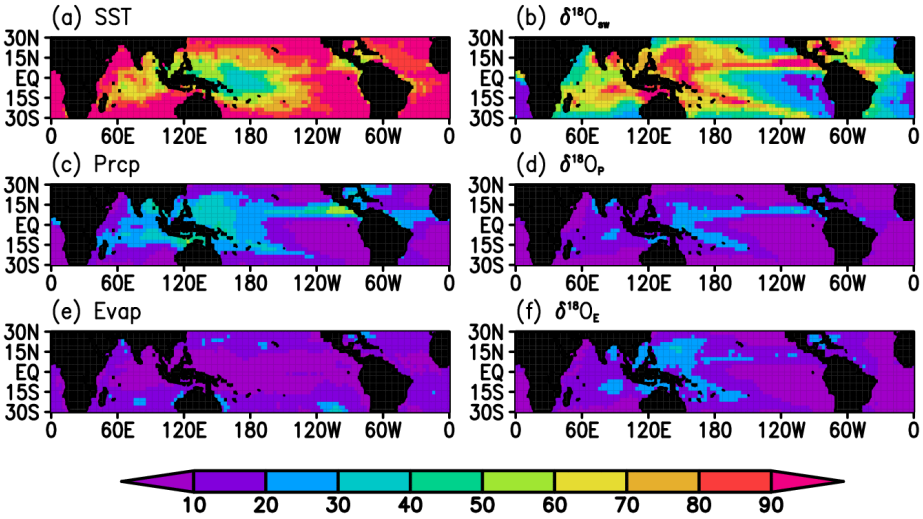

Figure 3-9 Contribution of (a) SST and (b) $\delta^{18}O$ of sea water (c) precipitation (d) $\delta^{18}O$ in precipitation (e) evaporation and (f) $\delta^{18}O$ in evaporation to the variability in $\delta^{18}O$ of coral The unit is %.

3.4.3. Tree ring cellulose

Annual average

Figure 3-10 compares the annual average of $\delta^{18}O$ in tree ring cellulose ($\delta^{18}O_{cell}$) for each site between the observation and the simulation. Some observation data is removed from the figures if the data is reported only in the form of anomaly. The isotopic composition in tree-ring cellulose is high in warm and dry area. This is because $\delta^{18}O$ in precipitation is high in warm area and low in cold area. Besides, in dry area leaf water is enriched in heavy isotopes due to preferential loss of light isotope by transpiration. Figure 3-10 shows that those geographical tendencies are captured by the proxy model, but the figure suggests that the model underestimates $\delta^{18}O_{cell}$ in wet and/or cold area. It is not likely that this discrepancy is due to the underestimation of $\delta^{18}O$ in precipitation, because such a bias is not detected in Figure 2-1 and Figure 2-2. On the other hand, relative humidity may contribute to the bias; the MIROC5 is found to have the tendency to overestimate the relative humidity in cold area and the difference for relative humidity between MIROC5 and ERA-Interim (Dee et al. 2011) is as large as 10% at temperature of 0°C. Another possibility is the misrepresentation of the proxy model. Sternberg and Ellsworth (2011) pointed out that the biochemical oxygen isotope fractionation during cellulose synthesis (ε in Eq. 3.9) is affected by temperature. They showed that the fractionation is around 26‰ at

temperature between 20 and 30°C, which is close to conventionally used value (in this study it is 27‰), but that value increase to 31‰ at lower temperatures. Because the underestimation is the largest in Mackenzie, Hongyuan, and Lhamcoka, where temperature is very low (-2.8, 1.1, 6.7°C respectively for annual mean), the inclusion of the temperature dependency of biochemical fractionation should aid the discrepancy. In this study, the focus is on the temporal variability, and I did not notice any relationship between the temporal reproducibility for $\delta^{18}O_{cell}$ and the annual mean temperature. Hence the constant ε (27‰) will be kept used in this study.

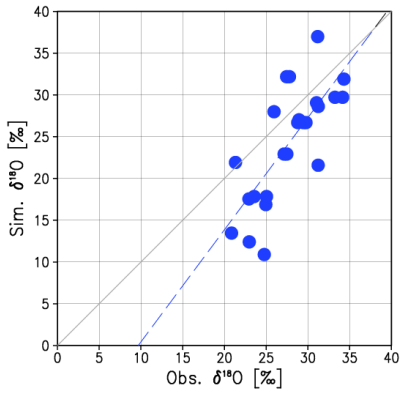

Figure 3-10 Comparison between the observed and the simulated $\delta^{18}O_{cell}$ for annual mean. Each dot represents one sample.

Temporal variability

Figure 3-11 compares the time series of the simulated and the observed isotopic composition in tree-ring cellulose. The time series are expressed as anomaly from the temporal mean because some cellulose isotopes are only anomaly value is available. The observed amplitude of variability and the timings of ups and downs are well captured in the simulation for most of the sites (e.g. HM1, Mapledurham, Braconne, Fujan, etc.). Meanwhile discrepancies are apparent at some other sites. At Wache and Ranwu, the simulation and the observation are in good agreement after 1970s but before then the discrepancies are relatively large. Such a partial agreement can be seen in Puerto Maldonado as well. At the site, the agreement is confined to 1970s to mid-1990s, and they disagreed with each other before- and after that period. The other type of discrepancy is the difference in the timings of peaks. At Reting, the simulation precedes one year faster than the observation. Tree-ring cellulose named Ram-high shows more complex feature. From 1950 to 1960s model precedes faster than the observation but after mid-1970s, the observation and the simulation are synchronous. At Almagre, Jag03 and Jag04 the simulated range of variance are similar to the observation but the peak timings are not. Both the range of variability and the peak timings are largely missed in the simulation at Volcan Granada and Kirijini.

Figure 3-12 maps the global distribution of the correlation coefficients between the simulation and the observation. The reproducibility for $\delta^{18}O$ in tree-ring cellulose is generally satisfactory for East Asia, South East Asia, Europe, and North America. On the other hand the simulation does not capture the variability for South America, South Asia, and Australia.

The possible reasons for the discrepancy are (1) misrepresentation of the input data, (2) averaging procedure in converting monthly data to annual data, and (3) misrepresentation of the forward model. To evaluate the above possibilities, additional experiments are conducted. In the experiment of RH2-20CR, RH2-NNR, and SW-12Mon, the input for the forward model is changed. The experiments of RH2-20CR and RH2-NNR use 2m relative humidity obtained from 20CR (Compo et al. 2011) and by NNR (Kalnay et al. 1996) are used respectively. SW-12Mon uses 12 months averaged $\delta^{18}O_p$ is used as $\delta^{18}O_{sw}$, thus the memory effect in the soil is lengthened in the experiment (originally the averaging duration is set to 3 months). The reason for the selection of only two variables (relative humidity and $\delta^{18}O_p$) is because theoretical and experimental studies find that the model is largely sensitive to those variables (Roden et al. 2000) and many subsequent papers report the relevance between $\delta^{18}O_{sw}$ and the variables (e.g. Brienen et al. 2012; An et al. 2013). Concerning to this point, I also find the moderate correlation between the reproducibility for $\delta^{18}O_{cell}$ and that for relative humidity (the correlation for relative humidity is calculated against NNR), which suggests the reproducibility dependence on relative humidity (Figure 3-13). The experiments named "Jul-Jun" and "NoWgt" test the procedure to calculate the annual mean $\delta^{18}O_{cell}$ from the monthly mean. The growing season is different from site by site, species by species. For instance, Ballantyne et al. (2010) found that *Tachigali myrmecophila* trees in Manaus, Brazil grow in the austral summer by measuring circumferential growth. Cullen & Grierson (2007) define the growth season for *C. clumellaris* in West Australia as October to September by considering climatic condition there. Thus the uniformly defined growing season (January-December) is not the best for some trees especially for trees in the Southern Hemisphere. For that reason the other grow season of July to January is chosen for the experiment of "Jul-Jun". The other experiment, named "NoWgt", do not weight the monthly mean to calculate the annual mean$\delta^{18}O_{cell}$. Since NPP data is estimated by using the satellite image, the estimated value is representative for the gridded scale plants including e.g. grass whose growing season may not be the same as the tree used in this study. Because the alternative global measurements of NPP are not available to the best of my knowledge, I simply assume that the trees grow equally in every month for the experiment (i.e. assume the arithmetic average of monthly mean as the annual mean). In the default experiment (CTL), the effect of the transpirational convection of unenriched water to the evaporating sites opposed by the backward diffusion of $H_2{}^{18}O$ into the leaf (Péclet effect) is not taken into account. The experiment of "Péclet" takes into account this effect following Barbour et al. (2004).

Figure 3-14 shows the correlation coefficients between the observation and the all simulations for all samples. The sensitivity is different sites by sites. In Almagre, located in central Colorado (39N, 105W), the use of NNR relative humidity results in better agreement. Berkelhammer et al. (2012) succeeded in simulating $\delta^{18}O_{cell}$ for that site using the $\delta^{18}O_P$ simulated by isotope enabled AGCM nudged toward

20CR combined with observed value for the other forcing including relative humidity. The combined use of the simulation and the observation may imply that the simulated relative humidity is not satisfactory to reproduce $\delta^{18}O_{cell}$, even though the simulated relative humidity is in reasonable agree with the reanalysis on the interannual timescale (R=0.59, p<0.0001). In the site of Reting (30N, 92E), the reproducibility gets better by extending the soil memory. Grießinger et al. (2011) found that the annual $\delta^{18}O_{cell}$ at that site correlates with precipitation amount which fall in previous summer. This means that the trees use previous year's precipitation. They argue that this can be explained by plant physiological processes and soil water status. As a result of the precipitation maximum during the monsoon season there, soil holds water most in late summer due to the composition of the soils of talus material and loess, some portion of summer precipitation will be stored over winter. Then trees use that water to form early wood in spring. Especially, juniper, which is the sampled tree species, forms the greatest part of a tree ring as early wood. The better agreement not only in the extended the soil memory experiment but also in the experiment of "Jul-Jun", which includes previous year's precipitation, is consistent with the interpretation. On the other hand, the experiment of "NoWgt" does not improve the result and the impact of experiment of "Péclet" is marginal. In fact the NoWgt worsen the skill in most cases. This suggests the importance of the definition of the growing season. The estimation of NPP used in this study covers 14 years more. Even it is not long enough, but with that data seasonality similarity among the years can be estimated. I calculate an index Ω of similarity following Koster et al.(2004). Here the Ω is defined as following:

$$\Omega = (\mathrm{N}\sigma_{\mathrm{clim}}^2 - \sigma^2)/(N-1)\sigma^2 \tag{3.14}$$

where N is the number of years, σ^2 is the intra-year variance of NPP and $\sigma_{clim}{}^2$ is the corresponding variance of the climatological-mean time series. The seasonality of each year would be similar to each other if the index is high, and vice versa. The index is calculated for each grid point and subsequently is compared with the reproducibility of $\delta^{18}O_{cell}$ if $\delta^{18}O_{cell}$ is available within the grid. Figure 3-13c plots the $\delta^{18}O_{cell}$ reproducibility as a function of Ω index. Except for four sites (Almagre, Volcan Granada, Hongyuan, and Kirijini) which are plotted in right-bottom corner of the figure, the reproducibility is moderately correlated with the Ω index. There can be seen weak tendency in which high reproducibility for high Ω and low reproducibility for low Ω. Indeed the lowest Ω corresponds to the lowest reproducibility which is for Jag03 and Jag04. Therefore the nonstationary growing season may explain the low reproducibility for those sites.

The high reproducibility is originally achieved at 21 sites out of 30 in CTL experiment, or the reproducibility gets better by considering site specific condition (Almagre and Reting). Or the low reproducibility is suggested to be because of the averaging procedure in converting monthly data to annual data (Jag03 and Jag04). However none of the experiments reproduce the variability in South America (Puerto Maldonado and Volcan Granada), Australia (Kirijini) and two sites in Tibet (Bomi and

Hongyuan). In South America the simulations do not reproduce the temporal variability regardless of the proxy archive type (Figure 3-2 and Figure 3-12). This may suggest that the quality of the forcing is not good enough to simulate the variability over there. Indeed the reproducibility for precipitation, which is good proxy of $\delta^{18}O_p$ over low latitude, is low both in South America sites (-0.14 and 0.37 respectively for Puerto Maldonado and Volcan Granada) on the interannual timescale. Here the reproducibility is calculated as the interannual correlation with GPCP (Huffman et al. 1997). This tendency can be found in Figure 3-13b. For Bomi, the observed chronology is reported to have some outlier years (Shi et al. 2012). But even after removing those years, the reproducibility remains poor. However, with the atmospheric forcing nudged toward NNR (Kalney et al., 1996), the proxy model can reproduce the temporal variability which agrees well with the observation ($R=0.32$, $p < 0.05$). Thus, the quality of the input data is suspected to limit the reproducibility of the model. On the other hand, the reason for the low reproducibility is not clear for Kirijini and Hongyuan. For both of the sites, the quality of the input data is not especially bad. Besides the links between $\delta^{18}O_{cell}$ and the instrumental observation are found (Cullen & Grierson 2007; Xu et al. 2012) in both sites. That is, the low reproducibility is not owing to non-climatic factors. Given the reproducibility for the other sites, the misrepresentation of the model for $\delta^{18}O$ in tree ring cellulose is not likely. One possible reason for the discrepancy is that they may record very local scale climate. If that is the case, simulation with finer resolution would be required.

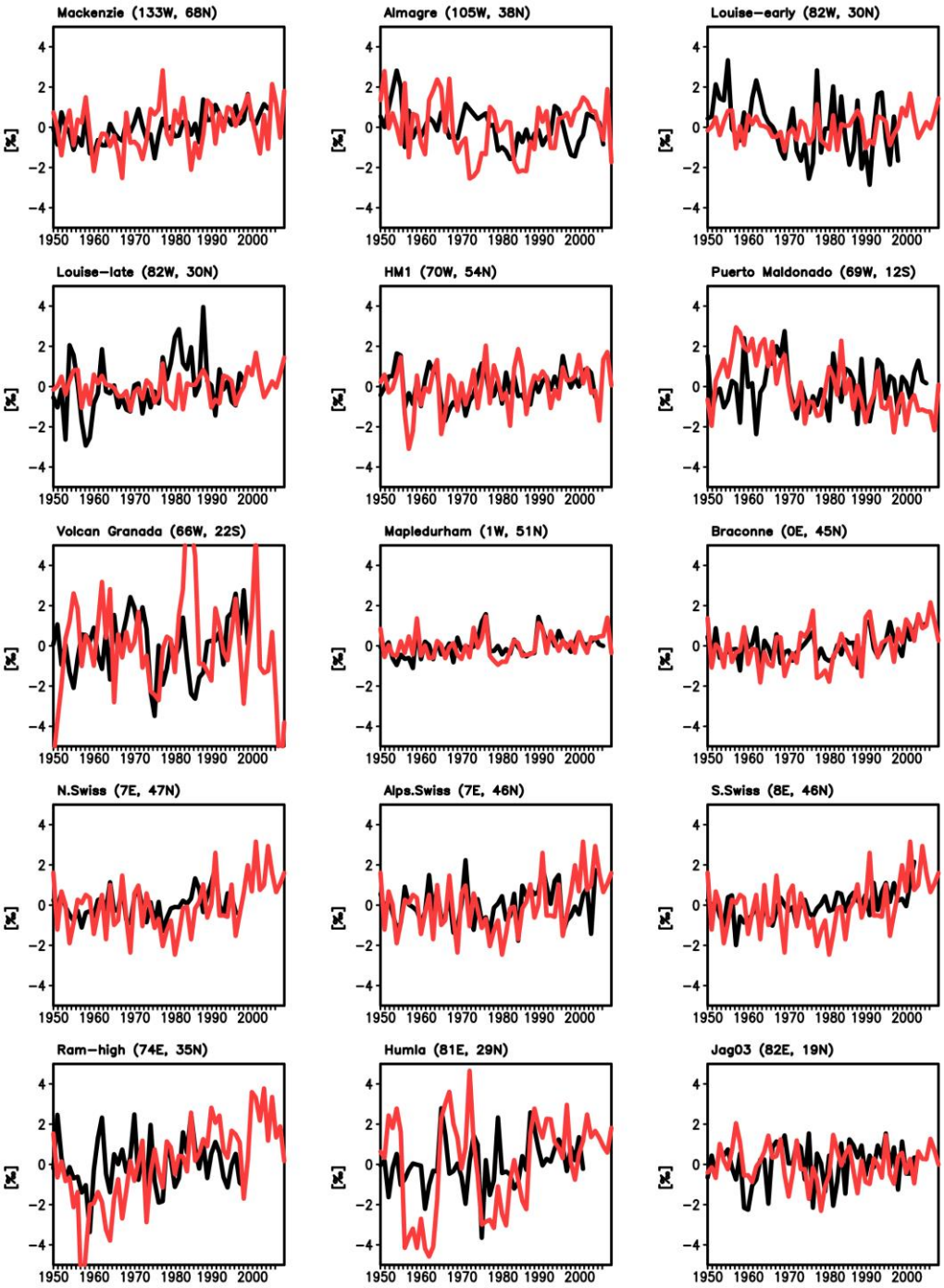

Figure 3-11 Same as in Figure 3-1 but for $\delta^{118}O$ in tree-ring α-cellulose

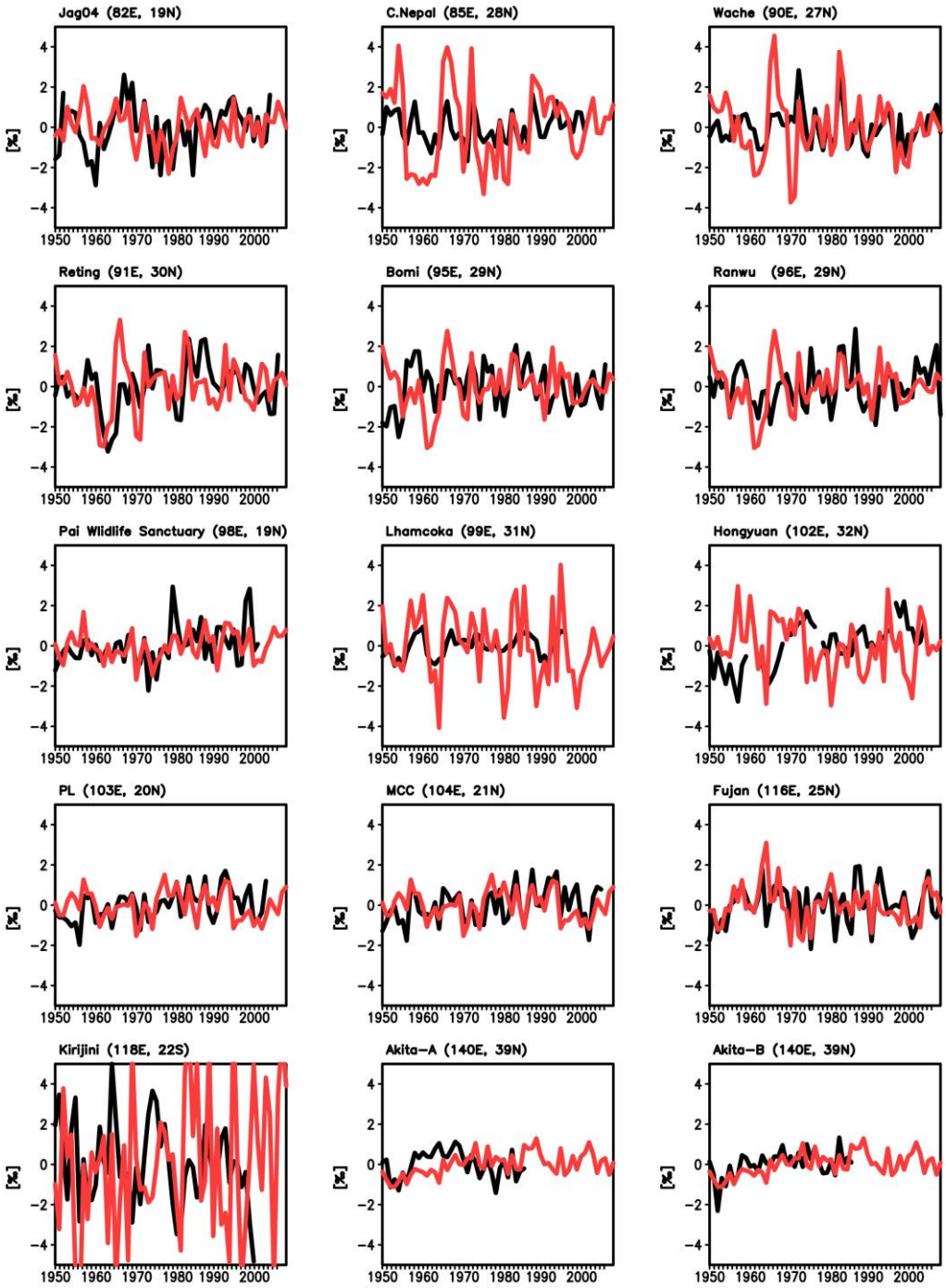

Figure 3-11 (Continued)

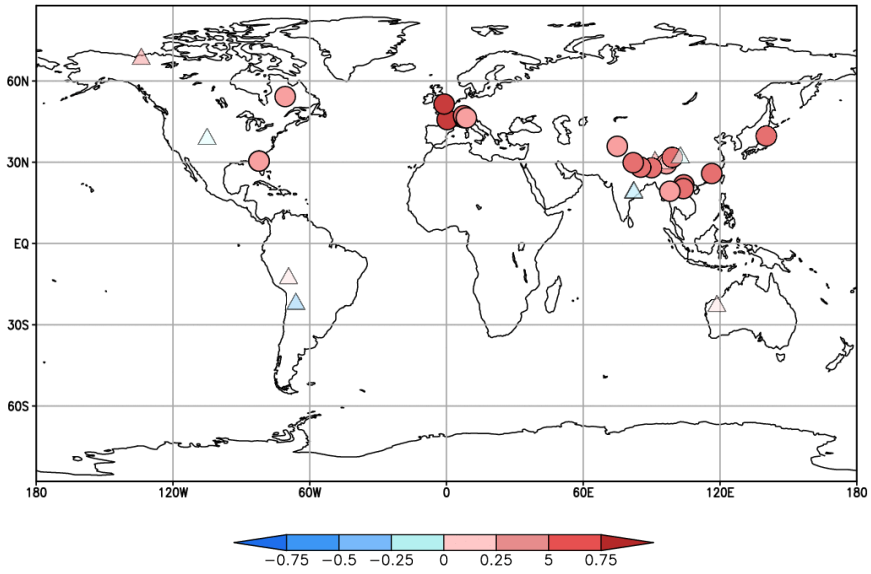

Figure 3-12 Temporal correlation coefficients for $\delta^{18}O$ in cellulose on the interannual timescale between the observation and the simulation

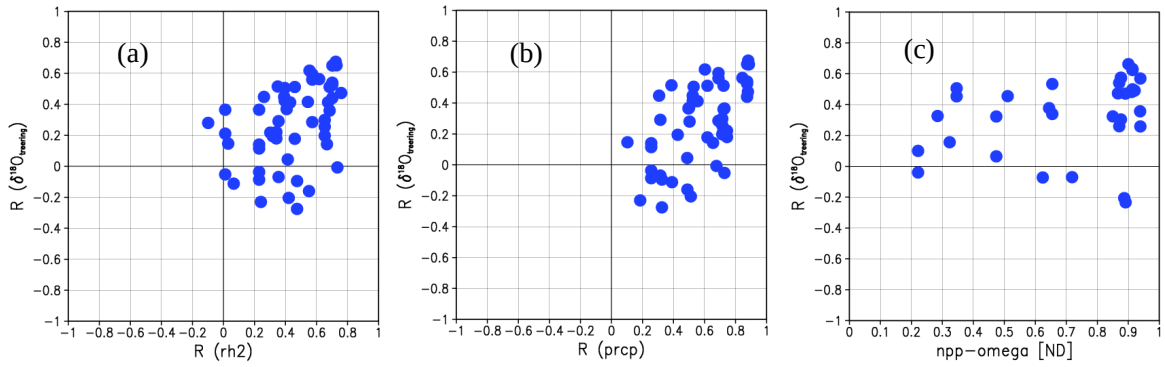

Figure 3-13 Scatterplots show the relationship between the reproducibility of $\delta^{18}O$ in tree cellulose and (a) reproducibility or relative humidity and (b) that of precipitation.

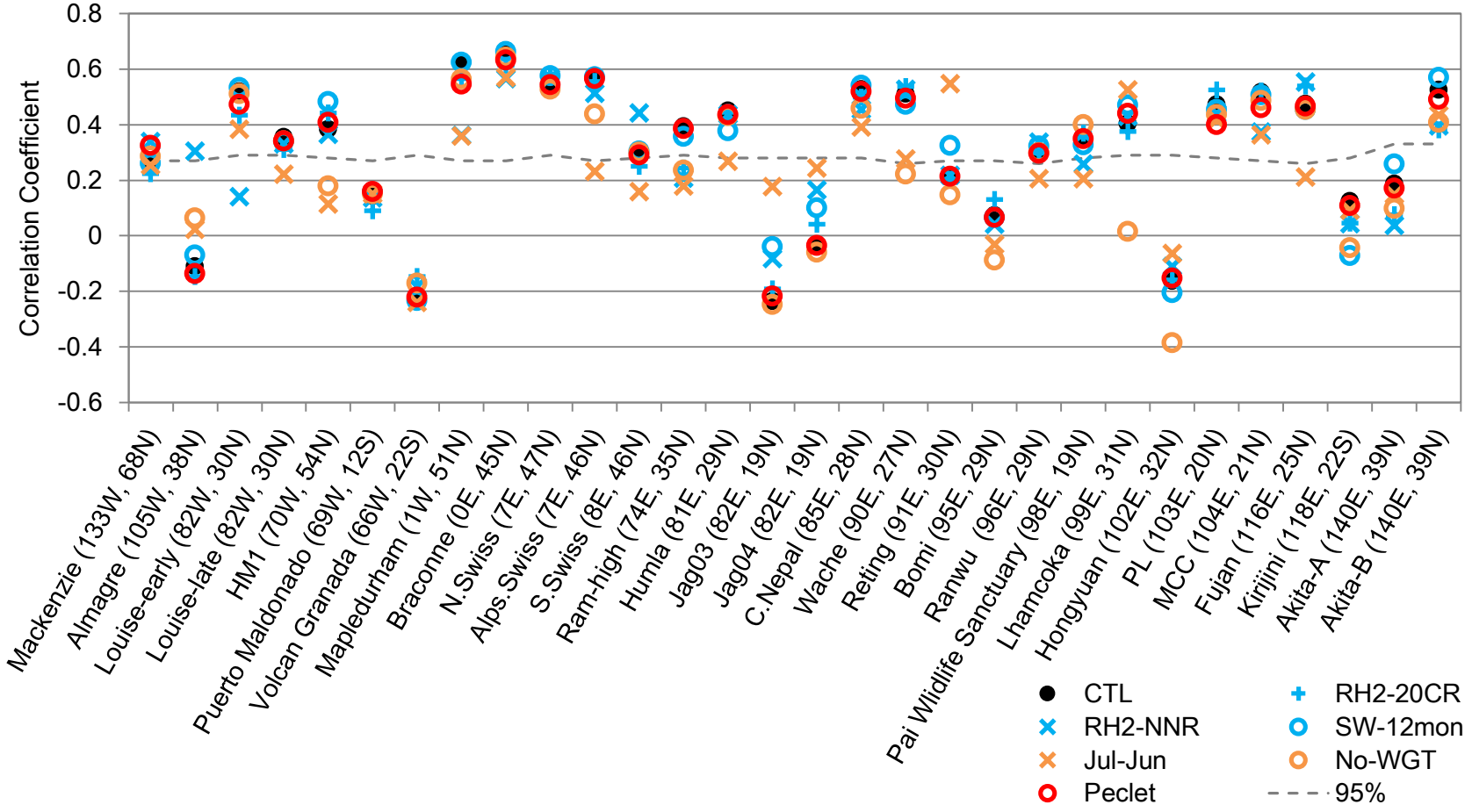

Figure 3-14 Sensitivity of the proxy model to parameters and forcing

The controller of the tree cellulose $\delta^{18}O$

The relative impact of each forcing is investigated to understand the controller of the variability in cellulose isotope ratio. To do so, additional sensitivity tests are conducted in which the forward model is driven by (1) $\delta^{18}O_{sw}$ with the other variables held constant, (2) RH2 with the other variables held constant, (3) temperature with the other variables held constant and (4) surface pressure with the other variables held constant. Here the sensitivity is defined as the ratio of standard deviation of each test to that of CTL. Figure 3-15 shows the result for the sensitivity experiments. As previous studies pointed out, the cellulose isotope is sensitive to the change in isotopic variability in source water and relative humidity (e.g. Berkelhammer et al., 2012) On the other hand, the cellulose isotope is not sensitive to the change in temperature and surface pressure at all. Roden et al. (2000) already noticed that the model is not sensitive to vapor pressure of the leaf surface, which is a function of temperature and surface pressure. Therefore the variability in $\delta^{18}O_{cell}$ can be attributable to $\delta^{18}O_{sw}$ and relative humidity. Here the contribution of $\delta^{18}O_{sw}$ to $\delta^{18}O_{cell}$ is defined as the square of the temporal partial correlation between them. Here the covariant component between $\delta^{18}O_{sw}$ and relative humidity is removed:

$$\delta'_{sw} = \delta_{sw} - \frac{Cov.}{S_{RH}^2} RH \tag{3.15}$$

where Cov. is covariance between the $\delta^{18}O_{sw}$ and relative humidity, and S_{RH}^2 is variance of relative humidity. Thus the contribution of $\delta^{18}O_{sw}$ is the residual of the contribution of relative humidity. Relative humidity can have influence on the $\delta^{18}O_{sw}$ through evaporation but the opposite never occurs. Therefore it is legitimate to attribute the covariance to the change in relative humidity. Figure 3-16 shows the contribution of $\delta^{18}O_{sw}$ to the interannual variability in $\delta^{18}O_{cell}$. The source water contribution is large in the high latitude and in the tropics. The spatial pattern is mainly decided by the balance of the interannual variance magnitude in relative humidity and $\delta^{18}O_{sw}$. Thus the small magnitude of relative humidity in the tropics and large variability in $\delta^{18}O_p$ in the high latitude create the pattern. Globally the isotopic variability in $\delta^{18}O_{sw}$ explains the 42 % of the cellulose isotope variability. Hence in the most of the globe, the $\delta^{18}O_{cell}$ variability is dominated by relative humidity.

For those who want to reconstruct relative humidity from cellulose isotope, variability stem from $\delta^{18}O_{sw}$ is noise. On the other hand for those who want to retrieve climatic information other than relative humidity, the information recorded in $\delta^{18}O_{sw}$ is valuable. The question is, for both groups, how $\delta^{18}O_{cell}$ is interpreted in the end. Accordingly Figure 3-16 is further decomposed into 7 categories in Figure 3-17 as in the interpretation of $\delta^{18}O_p$: precipitation dominant, temperature dominant, relative humidity dominant and the combination of them. The figure colors grids in which the explained variance of a single variable (i.e. not determination coefficient) is greater than 33% (e.g. the grid in which temperature and precipitation both individually explains more than 33% is classified as "temperature and precipitation dominant"). Here the explanatory variables are the same as in the Section 3.4.1, thus precipitation amount include both local and upstream precipitation amount. The figure is largely show resemblance to Köppen

climate classification. The relative humidity is dominant in the subarctic climate. The precipitation dependent area is in the downstream of monsoonal area (West Africa, South Amazon, and Tibet) where the interannual variability in $\delta^{18}O_p$ is dominated by the precipitation (Vuille et al. 2005; Ishizaki et al. 2012; Okazaki et al. 2015). The temperature dominant area is confined to east part of Canada. Both relative humidity and temperature have an influence on Europe and Central USA, Central Africa, and Equatorial South America. In the tropics the climatic signal is not well defined. In Amazon, Central Africa, and Indochina Peninsula, the cellulose $\delta^{18}O$ record temperature and relative humidity, and precipitation in some portion of the area. On the other hand, in Indonesia and New Guinea, precipitation and relative humidity are recorded.

In previous studies, many isotopic signals recorded in tree ring cellulose have shown to be correlated with hydroclimatic variables (relative humidity, precipitation amount, and Palmer Drought Severity Index) over Tibetan Plateau (Grießinger et al. 2011; Sano et al. 2012; Xu et al. 2012; Liu et al. 2013; Sano et al. 2013; Wernicke et al. 2015), South East Asia and East Asia (Xu et al. 2011; Sano et al. 2012; Xu et al. 2013; 2015), Australia (Cullen & Grierson 2007) and Andes (Ballantyne et al. 2010; Brienen et al. 2012). The imprint of temperature have been widely found in central to northern North America (Berkelhammer & Stott 2012; Porter et al. 2014; Bégin et al. 2015). Treydte et al. (2006) also found the correlation with temperature in northern Pakistan. Those signals are widely in consistent with the present study. These classifications must be a good reference for those who want to reconstruct climate from cellulose.

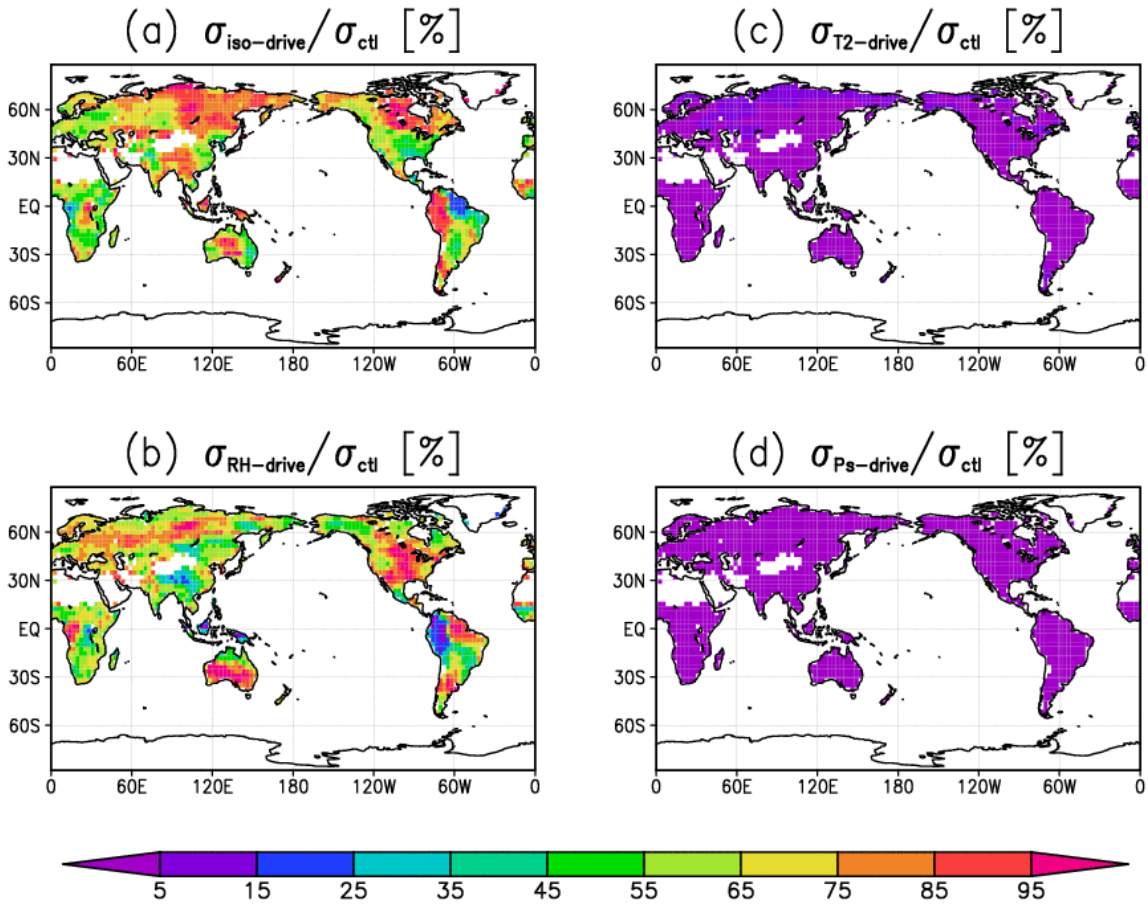

Figure 3-15 $\delta^{18}O_{cell}$ sensitivity to the atmospheric forcings: sensitivity to (a) $\delta^{18}O_P$ and $\delta^{18}O_v$, (b) relative humidity, (c) surface temperature, and (d) surface pressure

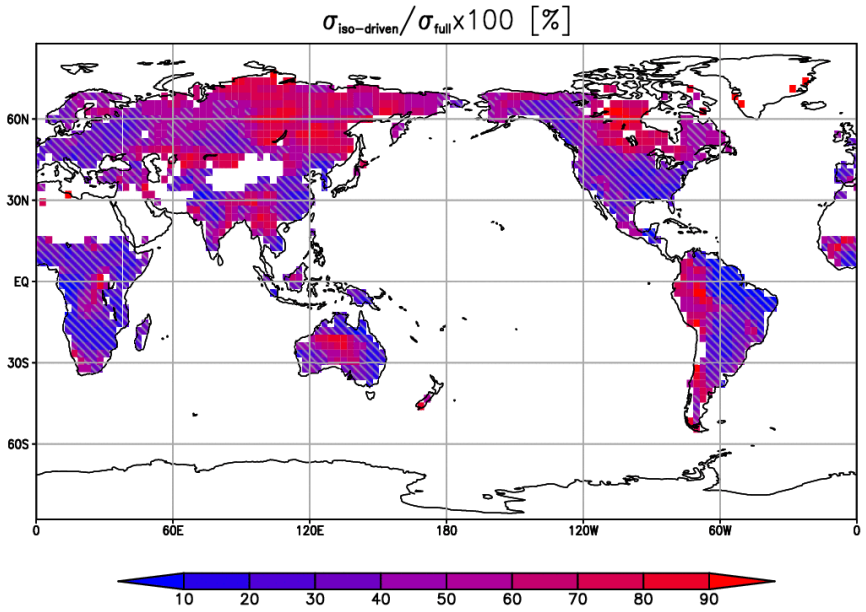

Figure 3-16 Contribution of isotope ratio in tree source water to that in tree ring cellulose (%).

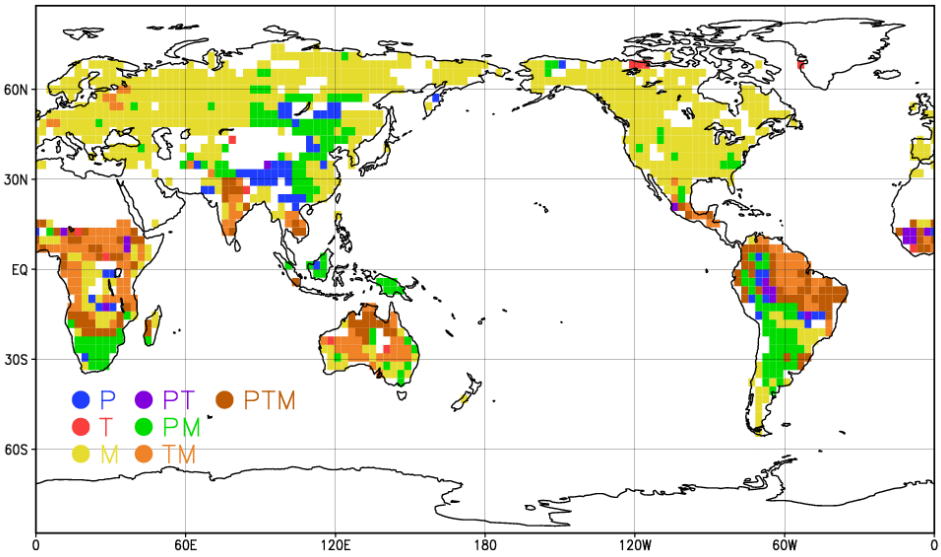

Figure 3-17 Classification of isotopic signal in tree ring cellulose. Categories considered are precipitation (blue), temperature (red), relative humidity (yellow), precipitation and temperature (purple), precipitation and relative humidity (green), temperature and relative humidity (orange), and precipitation, temperature and relative humidity (brown).

3.5. Discussion

3.5.1. **Why the reproducibility for ice core is notably bad?**

Table 3-1 shows the ratio of the number of samples for which the simulation and the observation correlate each other at the 5% level to the all samples. Thus the score can be regarded as how skillful the simulation is. As a reference, the score for $\delta^{18}O$ in precipitation is also listed in the table. In this case, the simulated $\delta^{18}O$ in precipitation is compared with GNIP. It is obvious that the reproducibility for ice core is notably worse than for the other proxies. Given the reproducibility for $\delta^{18}O$ in precipitation, this result is surprising. Here the reason of low reproducibility will be investigated.

The possible reason for the low reproducibility is twofold. One reason is that reproducibility of $\delta^{18}O$ in precipitation is low. The other is that factors which are not included in the simulation have crucial impact on $\delta^{18}O$ in ice core. Those factors include postdepositional processes, sub grid scale circulation, and so on. It is difficult to specify the reason if observation of $\delta^{18}O$ in precipitation is not available at the very site of ice core drilling. Unfortunately, however, this is the case for most of the drilling sites. Thus the best thing I can do is to infer the reason. To do so, the reproducibility for $\delta^{18}O$ in precipitation around the ice core drilling sites is investigated. Next, the reproducibility for the other climate parameters is investigated. Finally the impact of postdepostional processes is assessed.

First of all, whether the reproducibility for $\delta^{18}O$ in precipitation is relatively worse around ice core drilling sites compared to the other area is investigated. In Antarctica, there are only two sites. On the interannual timescale, none of them is simulated significantly for 1960-1980 and one site is simulated significantly for 1981-2007. In the same way, the reproducibility for $\delta^{18}O$ in precipitation is investigated for Greenland, Tibet, and Andes where most of ice cores are drilled. In Greenland two out of two sites are well simulated for 1960-1980. For Tibet four out of seven sites are well simulated for 1981-2007 and one out of six for Andes also for 1981-2007. Though the spatial coverage is too small to conclude, the reproducibility is relatively worse in Andes and Antarctica.

Then, how about the reproducibility of the other variables, such as temperature? Isotopic ratio in precipitation is an integrated and passive tracer of the atmospheric water cycle. It has been widely recognized as the good indicator of temperature over high latitude and precipitation over low latitude (Dansgaard 1964; Rozanski et al. 1993). Therefore one can roughly infer the reproducibility for $\delta^{18}O$ in precipitation by investigating the reproducibility of temperature and/or precipitation. For that purpose, the simulated temperature and precipitation are compared with observation. The meteorological station is sparsely distributed in Greenland and Antarctica. Here, given the performance of ERA-Interim (Dee et al. 2011), the reanalysis will be used as a reference for the validation of temperature. As a reference for the validation of precipitation, GPCP (Adler et al. 2003) are used. In addition to temperature and precipitation, the reproducibility for relative humidity is also considered here, since the variable is known to be important for the reproducibility for $\delta^{18}O$ in tree ring cellulose. Figure 3-18 shows the

correlation coefficient averaged over sampling sites for each proxies. The figure clearly shows that the scores are the lowest at the ice core drilling sites for all the variables. Thus the reason of the low reproducibility for $\delta^{18}O$ in ice core can be deduced that the atmospheric circulation is not well simulated over the ice core sampling sites. As shown in the next section, the quality of reanalysis data to force the atmospheric GCM is partly responsible for the low reproducibility mainly over Antarctica.

Subsequently, the impact of postdepositional processes on $\delta^{18}O$ in ice core is examined. Because the processes are not taken into account in the simulation, the simulation would fail to reproduce the $\delta^{18}O$ in ice core, if it is highly influenced by the processes. It is well known that the depositional noise is inversely related to snow accumulation rate (Jouzel et al. 1997). Thus to estimate the noise, the accumulation rate were calculated. To fairly calculate the accumulation rate, precipitation, evaporation, and melt water are required (Hanna et al. 2011). Here only precipitation data is used to calculate accumulation rate for the first order approximation. The dataset used is GPCP (Adler et al. 2003). Figure 3-19 plots the correlation coefficients for $\delta^{18}O$ in ice cores between the simulation and the observation as a function of the accumulation rate at the drilling sites of ice cores. The figure exhibits the moderate relation between them in which the small correlation corresponds to small accumulation rate and vice versa. This certainly means that it is difficult to simulate the temporal variation of $\delta^{18}O$ in ice cores which are affected by postdepositional effect. Thus the postdeposition processes should significantly distort the isotopic signal imprinted in ice cores for the sites plotted in left-bottom corner of Figure 3-19.

In this section, the two factors (the low reproducibility of atmospheric circulation and the postdeposition processes) are confirmed to be the reason for the small correlation for $\delta^{18}O$ in ice core between the simulation and the observation. To further investigate the relative importance of the factors, observation of $\delta^{18}O$ in precipitation at the very site of ice core drilling site would be necessary. This enables us to clearly separate the impact of two factors. At the same time, models for postdepositional processes must be developed in the future.

Table 3-1 Ratio of the number of samples which the simulation and the observation correlate significantly ($p < 0.05$) to the whole samples.

	Ratio
precipitation	0.58 (192/331)
Ice core	0.16 (6/37)
Coral	0.76 (28/37)
Tree ring cellulose	0.67 (22/33)

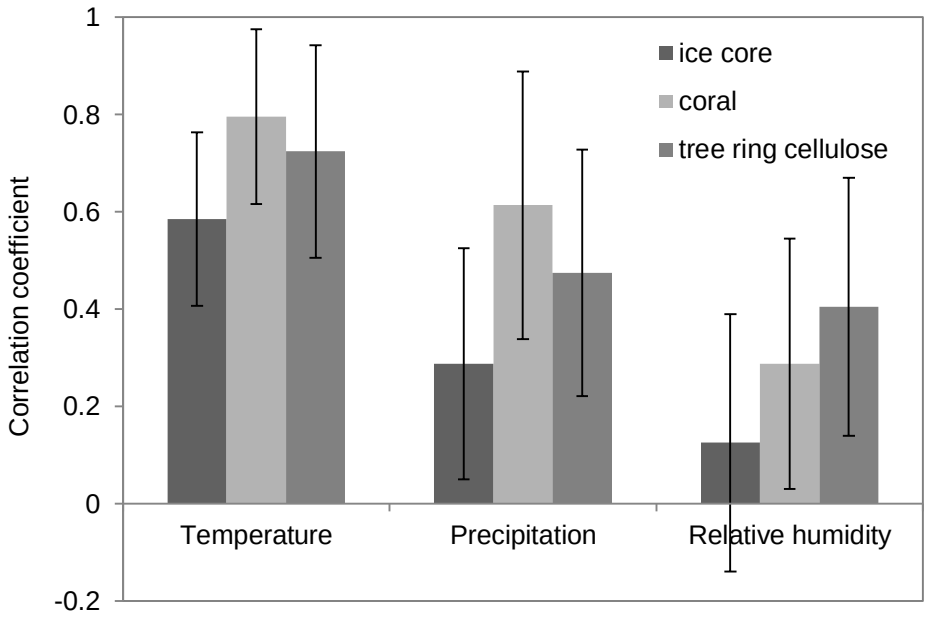

Figure 3-18 Correlation coefficient averaged over sampling sites for each proxies. The color shows the type of archive (dark gray for ice core, light gray for coral, and middle light gray for tree ring cellulose). Bars denote standard deviation.

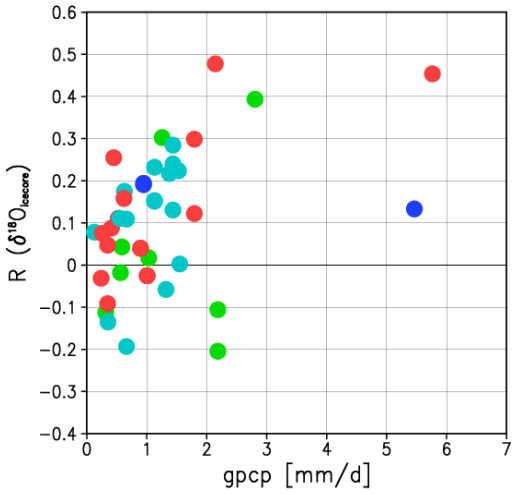

Figure 3-19 Relationship between the model skill for $\delta^{18}O$ in ice core and annual mean precipitation. The skill is measured by the correlation coefficient between the simulation and the observation for 1950-2007. The annual mean precipitation at the ice core drilling site is from GPCP (Adler et al. 2003). Colors show the places at which the ice cores are drilled. Red is for Greenland and high latitudes in Northern Hemisphere, green is for Tibet, blue is for Andes, and light blue is for Antarctica.

3.5.2. **Sensitivity to the quality of forcings**

The reproducibility of the proxy model is inherently limited by the quality of the forcing data to drive the model. As seen in the previous sections (3.4.1and 3.4.3), sometimes replacement of the forcing results in better agreement with the observation. Here I use two additional atmospheric forcing to drive the proxy models. The first atmospheric forcing is from the same GCM but nudged toward the other reanalysis field, NNR (Kalnay et al., 1996). The other is from different GCM (IsoGSM; Yoshimura et al., 2008) nudged toward 20CR (Compo et al. 2011), same as the original simulation. Hence the former tests the impact of difference in the GCM and the latter does the difference in the reanalysis toward which GCMs are nudged.

Figure 3-20 compares the skill of the proxy models driven by three different atmospheric forcing. Here the skill is defined as the ratio of the number of proxies which correlate with observation significantly ($p < 0.05$) to the total number of proxies. The ratio is counted for each proxy. As a reference, the skill for $\delta^{18}O$ in precipitation is also shown in the figure. The most striking feature is that the low reproducibility for ice core as shown in Table 3-1. Although the simulation with NNR results in better agreement with observation, still the reproducibility is the lowest. On the other hand the reproducibility for the coral is the highest among them. This is partly because of the model high sensitivity to SST and the use of observed SST. It is rather surprising to see that the skill for the tree ring $\delta^{18}O_{cell}$ is comparable with that for $\delta^{18}O$ in precipitation. Given the history of isotope enabled GCMs, it is not an overstatement to say that the proxy models for $\delta^{18}O$ in tree ring cellulose and coral are robust enough. At least the result suggests that the model should include essential mechanisms for $\delta^{18}O$ change in those archives.

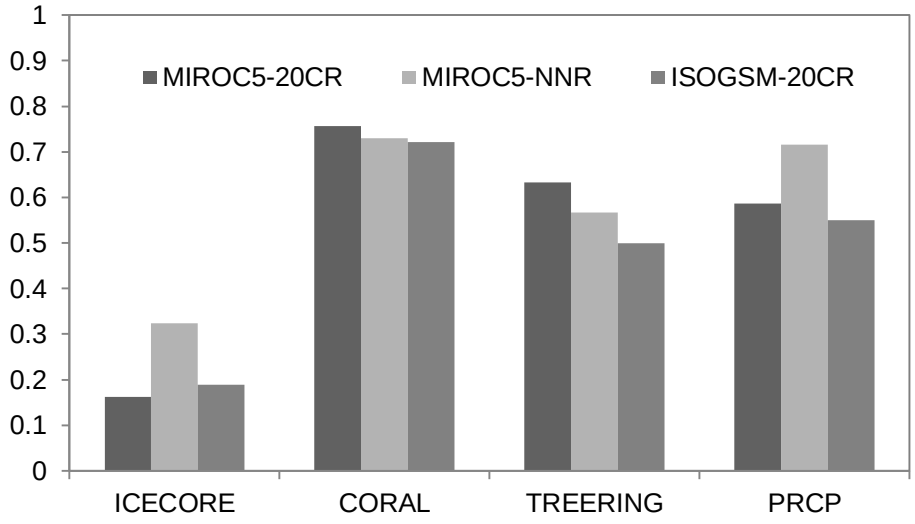

Figure 3-20 Percentage of proxies whose $\delta^{18}O$ chronology is significantly correlated with the simulated one ($p < 0.05$). Ratio of GNIP site whose $\delta^{18}O$ chronology is significantly correlated with the simulation to the number of total observation site is also shown as a reference. Each color represents the

atmospheric forcing used to drive proxy model.

3.6. Conclusion

In this chapter, forward proxy models for oxygen isotope in coral, and tree ring cellulose are evaluated. The models are driven by the output of well-evaluated isotope enabled GCM. The use of GCM simulation nudged toward reanalysis field of 20CR (Compo et al. 2011) makes rigorous comparison with paleoclimate observation possible. The proxy models were evaluated on the interannual timescale for 1950-2007 where the reliability of the forcing is relatively high. Although the reproducibility of the proxy models are inherently limited by the quality of the forcing, the reproducibility is largely satisfactory but with distinctive results for each proxy. The forward proxy models work well for coral and tree ring cellulose. The dominant factor for $\delta^{18}O$ in coral is found to be sea surface temperature in many basins except for tropical Pacific warm pool, where hydrological balance is dominant. On the other hand, the reproducibility for ice core is not as good as that for coral and tree ring cellulose. The reproducibility for ice core becomes better, especially in Antarctica, when the model is nudged toward NNR (Kalnay et al. 1996). This is reasonable because the skill of 20CR is relatively low over Antarctica (Compo et al. 2011). Even though the reproducibility is somewhat limited by the quality of the forcing and/or the poor representation of the forward model, the models seem to represent the key mechanisms in the proxies. Therefore even though they may be too early to be directly compared with proxies in some cases, the forward proxy models and isotope enabled GCMs are skillful enough to be applied to idealized studies like pseudoproxy experiment or paleoclimate observing system simulation experiment.

Chapter 4.
Data Assimilation of isotopic information

4.1. Introduction

Data assimilation involves the combination of information from observations and numerical models. It has played a central role in the improvement of weather forecasts and, through reanalysis, provides gridded datasets for use in climate research (Hakim et al. 2013). Climate proxy data provide noisy and spatially incomplete information on some aspects of past climate states. Meanwhile paleosimulations with climate models provide global, multi-variable states, which may however different from the true states due to unpredictable internal variability not related to climate forcings, as well as due to model deficiencies. Since the proxy based approach and the climate modes based approach are complementary to each other, using data assimilation for combining the two approaches is in principle a promising way to obtain better estimates (Widmann et al. 2010).

Several studies have started applying data assimilation technique to paleoclimate simulations. Goosse et al. (2006) conducted an ensemble of 103 simulations using earth system model of intermediate complexity (EMIC) LOVECLIM for the past millennium and found that the simulation agrees better with the observation with the assimilation of reconstructed temperature from proxies. Bhend et al. (2012) utilized 30 simulations with GCM ECHAM5.4 to assimilate 37 pseudoproxies (noise added temperature generated from one of the simulation) for the last four centuries. They found the simulation improvement not only in temperature field but also in other surface properties, such as precipitation and even upper air circulation. Crespin et al. (2009) conducted an ensemble simulation with LOVECLIM for the past millennium with data assimilation. The Arctic warming in the 15^{th} century was suggested to result from internal variability. Goosse et al. (2012) did the similar experiments and attributed Medieval Climate Anomaly (MCA) to external forcing and internal variability. They concluded that MCA can be explained by a simple thermodynamical response of the climate system to relative weak changes in radiative forcing combined with a modification of the atmospheric circulation. Mathiot et al. (2013) also used LOVECLIM to investigate the causes of Antarctica cooling from 10 to 8 ka BP.

As shown in the above, data assimilation is proven to have a potential to provide better reconstruction not only the locations where proxy observations are available but also locations for no empirical relation exists in consistent way with the proxy observations. Additionally it may be possible to separate the

externally forced variability and the internal variability, or to understand the mechanism of the changes recorded in proxies.

All the previous data assimilation studies in paleoclimate study assimilated reconstructed temperature. This may, however, have several potential problems. First of all, the assimilation of the reconstructed value does not use full information we could have otherwise. Fundamentally, reconstructions assume that the linear relationship between climate proxy and a climate variable, and also that is remained unchanged through time (the assumption of linearity, univariate, and stationarity). These assumptions impose strong limitation on the climate proxies that could be used, and likely led to loss of useful climate information that could not be captured by the linear and univariate empirical models used (Hughes & Ammann 2009). Since any information related to the climate is scarce in the period for paleoclimate study, it is desirable to use as much information as possible. Empirical model based climate reconstruction is accompanied with uncertainty due to the assumptions listed above. The second one is that the uncertainty stems from the reconstruction will be inherited by the assimilation results and degrade the reliability. Indeed, the stationarity between proxies and climate variables do not hold true for many proxies. For instance, tree ring width and density an insensitivity of tree-ring width and density to temperature for many circumpolar northern latitude sites during the last decades of the 20th century, known as "divergence problem" is widely recognized (D'Arrigo et al. 2008 and references therein). Even though this effect may be non-climate influences, the problem can be occur even if the proxy is purely controlled by climate. A number of studies have shown that the regression slope between isotope ratio in precipitation and temperature is time varying (Schmidt et al. 2007; LeGrande & Schmidt 2009; Sime et al. 2009). Therefore, the assimilation of empirically reconstructed temperature would be biased due to the quality of the assimilated variable.

The use of not reconstructed value but measured proxy data itself is one way to make the most of information in paleoclimatology. With process based models which make use of what is already known about the physics, chemistry, and biology of climate and proxy system, the limitation by the assumptions would be cleared away and a lot more proxies could be in use for the assimilation. The relationship between proxies and climate variables would be properly simulated with such models.

This chapter examines the feasibility of the assimilation of isotopic data in precipitation toward proxy data assimilation. Since this study firstly assimilate the isotopic data for the climate reconstruction, the feasibility will be tested in an idealized way by using the isotope enabled GCM developed in Chapter 2. The main goal of the study is twofold. The first is to test whether the assimilation of isotopic information can constrain the climate state. The second is to learn to what extent and under what conditions isotopic information provides sufficient constraints for the assimilation to reconstruct climate.

In the following section, the model and the experimental design are briefly introduced. In Sect. 4-3, DA algorithms previously used are briefly introduced and the algorithm for present study is detailed. The results are presented in Sect. 4-4.

4.2. Data assimilation method and experimental design

4.2.1. **Data assimilation algorithm**

Various data assimilation technique has been used in the field of paleoclimate: (1) pattern nudging (Hans von Storch et al. 2000), (2) forcing singular vectors (van der Schrier & Barkmeijer 2005), (3) selection of the closest simulation among an ensemble to the proxy record (Goosse et al. 2006; Crespin et al. 2009; Goosse et al. 2010), (4) particle filter (Goosse et al. 2012; Mathiot et al. 2013), and (5) ensemble filtering (Bhend et al. 2012; Steiger et al. 2014). Among them, (3) and (5) are called "offline data assimilation". In some cases, offline data assimilation implies non-sequential data assimilation (e.g. 4D-Var, and Adjoint method) in which assimilation is conducted after all the observations are obtained. The offline data assimilation in paleoclimate study is also included in this broad definition, but it has more specific meaning. In a conventional assimilation, the effect of constraining the model with past observation gets propagated by the model and determines to a large extent the current first guess. However, this is not the case in the offline data assimilation. Because temporal resolution of proxy record is much longer than atmospheric model predictability, which is limited by chaotic nature of atmosphere, the effect of the previous update (leading to the new analysis) is lost long before the end of the assimilation cycle (seasonal at best). That is, a forward integration of a constrained simulation and an unconstrained simulation are indistinguishable after six months on average (Bhend et al. 2012). Thus, observed information does not accumulate over time, but only current observed information constrains the model. Therefore, we can assimilate the data non-recursively; in other word, we do not need to feed back the corrected states (the analysis) as new initial conditions for the next simulation cycle. Thus the offline assimilation in paleoclimate more specifically indicates the method which combines existing simulations and observations. Using offline data assimilation technique of ensemble square filtering, Bhend et al. (2012) suggested that we should not refer to those approaches as filtering, instead they suggested to refer to the method as "ensemble square fitting". In this study, however, I keep using the term offline data assimilation. The method used in this study follows Steiger et al. (2014), and will be detailed below.

Data assimilation (DA) estimates the posterior state vector (analysis; x_a) by weighting the prior (forecast; x_b) and the observation (**y**).

$$x_a = x_b + K[y - \mathcal{H}x_b] \tag{4.1}$$

To make the observation and the background comparable, the model forecast is interpolated to the observation location via observation operator$\mathcal{H}$. If they are different, the forecast is further converted from model variables to the observed variables (Kalnay 2003). Note that $\mathcal{H}$ can be non-trivial in a paleoclimatology context, as this operator reflects the complex dependence of climate proxies on climate

(Bhend et al. 2012). To assimilate tree ring width information, for example, the tree ring width dependence on temperature, moisture and other variables has to be well defined. The matrix K is the weighting function, or Kalman gain, which weights the innovation and transforms the innovation into the state space. The matrix is defined to minimize the analysis error covariance. Here I derive K following Kalnay (2003), Miyoshi (2007), and Awaji et al. (2009). Assuming Gaussian distribution, the analysis error (ε_a), the background error (ε_b), and the observation error (ε_y) are defined as follows:

$$\epsilon_{\mathrm{a}} = x_a - x_t \tag{4.2}$$

$$\epsilon_{\mathrm{b}} = x_b - x_t \tag{4.3}$$

$$\epsilon_{\mathrm{y}} = y - \mathcal{H}x_t \tag{4.4}$$

where x_t is the truth. Using Eq. (4.3) and Eq. (4.4), Eq. (4.2) can be reformed into:

$$\begin{aligned} \epsilon_{\mathrm{a}} &\approx \epsilon_b + K\left(\epsilon_y - H\epsilon_b\right) \\ &= (I - KH)\epsilon_b + K\epsilon_y \end{aligned} \tag{4.5}$$

Here the nonlinear observation operator $\mathcal{H}$ is linearized as

$$\mathcal{H}(\mathrm{x_b} - \epsilon_{\mathrm{b}}) \approx \mathcal{H}\mathrm{x_b} - H\epsilon_b \tag{4.6}$$

Then the analysis error covariance (P_a) is written as:

$$\begin{aligned} \mathrm{P_a} &= E\{\epsilon_a \epsilon_a^T\} \\ &\approx E\left\{\left((I - KH)\epsilon_b + K\epsilon_y\right)\left((I - KH)\epsilon_b + K\epsilon_y\right)^T\right\} \\ &= (I - KH)E(\epsilon_b \epsilon_b^T)(I - KH)^T + (I - KH)E(\epsilon_b \epsilon_y^T)K^T \\ &\qquad + KE(\epsilon_y \epsilon_b^T)(I - KH)^T + KE(\epsilon_y \epsilon_y^T)K^T \\ &= (I - KH)B(I - KH)^T + KRK^T \end{aligned} \tag{4.7}$$

where $E(\cdot)$ represents the expected value, B and R are the background error covariance and the observational error covariance. Here the observation and background errors are assumed to be uncorrelated. K minimizes P_a when the sum of the analysis covariance is the minimum:

$$\frac{\partial}{\partial \mathrm{K}}\left(trace(\mathrm{P_a})\right) = 0. \tag{4.8}$$

The above equation can be transformed into the below following Miyoshi (2006):

$$-2(\mathrm{I}-\mathrm{KH})\mathrm{B}H^T+2KR=0. \tag{4.9}$$

Finally K which minimize P_a is obtained

$$\mathrm{K}=\mathrm{BH}^{\mathrm{T}}(HBH^T+R)^{-1} \tag{4.10}$$

Following Whitaker & Hamill (2002), the update equation (Eq. 4.1) is divided into an ensemble mean update and an update of the perturbations from the ensemble mean (denoted by an overbar and prime, respectively):

$$\mathrm{x_a}=\overline{x_a}+x_a' \tag{4.11}$$

$$\overline{\mathrm{x_a}}=\overline{x_b}+K(y-\overline{y_e}) \tag{4.12}$$

$$\mathrm{x_a'}=\mathrm{x_b'}+\widetilde{K}y_e' \tag{4.13}$$

Here the analysis and background ensemble mean states $\overline{\mathrm{x_a}}$ and $\overline{\mathrm{x_b}}$ are column vectors of dimension m x 1, where m is the length of the state vector. The perturbations from the ensemble mean $\mathrm{x_a'}$ and $\mathrm{x_b'}$ have the dimension of m x n, where n is the ensemble size. The observation y is column vector of dimension p x 1. The observation estimates y_e is also split into $\overline{y_e}$ and y_e', and have the dimension of p x 1 and p x n, respectively.

The background error covariance is approximated using the sample covariance from an ensemble of model forecasts. Accordingly the perturbations are equal to the error and the above equation can be expressed as:

$$\mathrm{K}=\mathrm{cov}(\mathrm{x_b'},Hx_b')[cov(Hx_b',Hx_b')+R]^{-1} \tag{4.14}$$

The divided update equations (Eq. 4.12 and 4.13) are solved by processing the observations serially at a time (Houtekamer & Mitchell 2001). Then the equation is simplified to the scalar for a single observation:

$$\mathrm{K}=\frac{\mathrm{cov}(\mathrm{x_b'},\mathrm{y_e'})}{var(y_e')+r} \tag{4.15}$$

where *var* denotes the variance, and *r* is the error variance for the observation. In case the isotope ratio is assimilated, *r* is the measurement error. The weights for the perturbations is given by

$$\widetilde{\mathrm{K}}=\left[1+\sqrt{\frac{r}{var(y_e')+r}}\right]^{-1}K \tag{4.16}$$

To control spurious long-distance correlations due to sampling error, a localization function proposed by Gaspari and Cohn (1999) is used (Figure 4-1). The localization function is as follows.

$$\mathrm{L(l)} = \begin{cases} 1 - \frac{1}{4}l^5 + \frac{1}{2}l^4 + \frac{5}{8}l^3 - \frac{5}{3}l^2 & (l \le 1) \\ \frac{1}{12}l^5 - \frac{1}{2}l^4 + \frac{5}{8}l^3 + \frac{5}{3}l^2 - 5\mathrm{l} + 4 - \frac{2}{3}l^{-1} & (1 < l \le 2) \\ 0, & (2 < \mathrm{l}) \end{cases} \tag{4.17}$$

where l is the ratio of distance between a grid and observation to a length of criteria. Following Steiger et al. (2014), the criteria of 12000 km is used.

The procedure for each reconstruction year is summarized as follows.

1. Construct x_b, y, and r
2. Split x_b into an ensemble mean and perturbations from the mean
3. For each observation:
   i. Compute y_e and split y_e into an ensemble mean and perturbations from the mean
   ii. Compute K from Eq. 4.16 for every grid point
   iii. Apply the localization function
   iv. At each grid point, update the analysis ensemble mean and perturbations from the mean

$$\overline{x_a} = \overline{x_b} + K(y - \overline{y_e}) \tag{4.18}$$

$$\mathrm{x'_a} = x'_b - \tilde{K}y'_e \tag{4.19}$$

   v. Use the updated $\overline{\mathrm{x_a}}$ and $\mathrm{x'_a}$, as $\overline{\mathrm{x_b}}$ and $\mathrm{x'_b}$, respectively, for the next observation

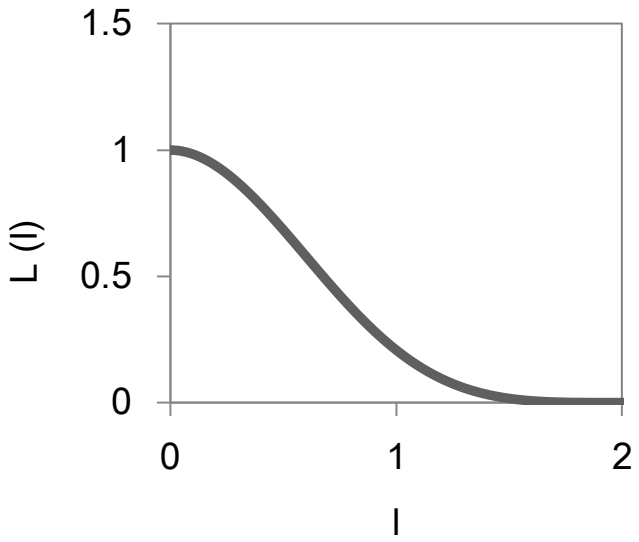

Figure 4-1 Localization factor as a function of distance between grids

4.2.2. **Data assimilation setting**

As DA is conducted in the offline manner in this study, the background ensembles are constructed from existing climate model simulation and the assimilated result (the analysis) is not fed back to the simulation. Thus the offline DA is different from traditional "online" DA as described in the previous section. Furthermore the method is distinctive compared to the other offline DA in the following way. In this study I use the same background ensemble for every reconstruction year. The background ensemble is drawn from part of a single climate model simulation, where ensemble members are individual years instead of independent model simulations (Steiger et al., 2014). This method is taken because the interannual variability in a single run are inherently indistinguishable from the variability in the annual mean within the ensemble of simulations in which initial conditions are perturbed. Thus the background ensemble does not contain year-specific boundary condition and forcing information, and the background error covariance is constant over time. Accordingly K is also constant over time as R is time invariant. Since the analysis error covariance can be written in the following way using Eq. 4.7 and 4.10,

$$\mathrm{P_a} = (I - KH)B \tag{4.20}$$

P^a is also constant over time.

In this study, for the first trial of data assimilation for a new physical property, I adopted the framework of the observation system simulation experiment (OSSE) as in the previous climate data assimilation (Annan and Hargreaves, 2012; Bhend et al., 2012; Steiger et al., 2014). In an OSSE, observations and simulations are both generated from one model. In this study two simulations are conducted for "observation" and "simulation". The model used is a state-of-the-art isotope enabled GCM, MIROC5, described in Chapter 2. The simulation setting is largely similar to that in Chapter 3 but without nudging. The spatial resolution is T42 (around 280km) with 40 vertical layers. The model is driven by sea surface temperature and the sea ice data (HadISST) (Rayner et al., 2003) and historical anthropogenic (carbon dioxide, methane, and ozone) and natural (total solar irradiance) forcing factors. The simulation covers the period of 1871-2007 (137 years). Thus it is assumed to be 137 ensemble members in this study.

Despite of the simulation period, I assume that the only variable we can obtain is the annual mean of $\delta^{18}O$ in precipitation. This assumption is made because my final goal is to do DA in a period when there is no measurement is available other than climate proxies. Therefore, the temporal resolution of "observation" and "simulation" are also annual. I generate 349 observations at different locations in a way that mimics the GNIP observation sites. The generated observation data is assimilated for the whole period (1871-2007). As seen in the Chapter 2 and 3, the interannual variability in $\delta^{18}O_P$ is largely controlled by precipitation amount and temperature. Nevertheless I include the other variables (relative humidity, surface pressure geopotential height, and $\delta^{18}O_v$) in the state vector.

4.3. Results

4.3.1. Temporal variation at a specific grid point

First I focus on temporal variation at single site to understand the characteristics of the method. Figure 4-2 depicts the temporal variation of $\delta^{18}O$ in precipitation at the point where observation is available (53°N, 5°E). Because of the method applied in this chapter, the each of the background ensemble member does not change in time and accordingly the gray lines and the ensemble mean (green line) is drawn as parallel lines (Figure 4-2a). Each member and the ensemble mean are clearly closer to the "truth" (black line) after DA (Figure 4-2b). This confirms the DA worked correctly

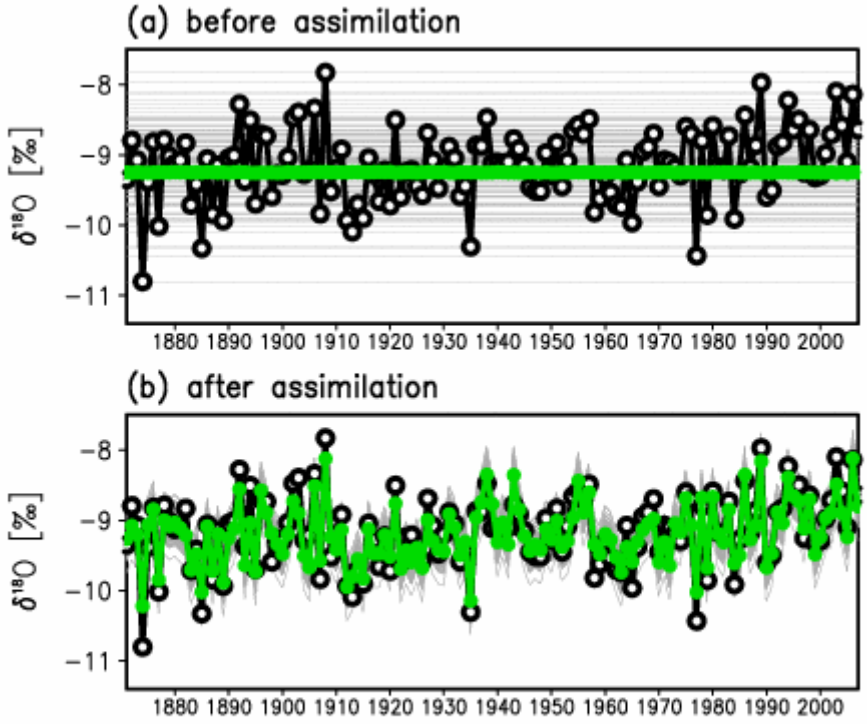

Figure 4-2 Annual mean $\delta^{18}O$ in precipitation for (a) background and (b) analysis. Black line indicates "truth", each of the gray lines indicates an ensemble member and green line indicates the ensemble mean.

4.3.2. Reproducibility of climate

In this section, I focus on the reproducibility of the results. Figure 4-3 shows the temporal correlation for $\delta^{18}O_P$ between the analysis and the truth. The correlation coefficients are high where observations are available. The high correlation is not confined to the observation grid due to the covariance among $\delta^{18}O$ in precipitation. Thanks to that, the areas with scarce observations (e.g. tropical branch of East Pacific, tropical Atlantic, and some part of Antarctica) retain relatively high score. On the other hand, the correlation coefficient is small in southern part of the Indian Ocean to Southern Ocean, subtropical branch

of the Pacific and the Atlantic. In such areas, the coefficient is almost close to zero, which means that DA does not change the background. As most of the land fraction is covered by observation, the correlation is mostly high over land. Figure 4-4 compares the ensemble spread between the background and the analysis and the figure shows their ratio (ensemble spread of the analysis divided by that of the background). Accordingly the figure shows the uncertainty: Dark color means that uncertainty is small and vice versa. The spatial pattern is largely similar to Figure 4-3, and the spreads become smaller in the analysis compared to the background over the globe as can be deduced from Eq. 4.21 but the dark shaded area is confined compared with Figure 4-3.

Figure 4-5 and Figure 4-6 show the correlation coefficient between the truth and the analysis for surface air temperature and precipitation amount, respectively. The correlation coefficients are globally smaller than that for $\delta^{18}O_P$. Indeed, the global mean of the correlation coefficients are 0.52, 0.45, and 0.38 for $\delta^{18}O_P$, surface air temperature, and precipitation, respectively. The spatial patterns are different from each other and are determined by the correlation between $\delta^{18}O_P$ and temperature or precipitation (c.f. Eq. 4.15). As Figure 2-7 shows, the correlation between $\delta^{18}O_P$ and temperature is high over Europe, northern North America, and Antarctica. Accordingly the reproducibility of temperature is high over the area, the area is confined around the grids where observation is available though (Figure 4-5). As for precipitation, as Figure 2-8 shows, the correlation between $\delta^{18}O_P$ and precipitation amount is large over low latitude. Accordingly the reproducibility is high over the area (Figure 4-6).

One of the highest correlation coefficients for temperature between the analysis and the truth can be seen in central to eastern tropical Pacific, where $\delta^{18}O_P$ is supposed to be dominated by precipitation amount. The reason for the good reproducibility is because of the high correlation between $\delta^{18}O_P$ and ENSO (Figure 2-9). ENSO is known as the strongest mode of interannual variability in the global precipitation fields over the land and the ocean (Dai et al., 1997; 2000). For example, the precipitation falls much in the positive phase of ENSO and falls less in the negative phase in central Pacific. Conversely precipitation falls more in West Africa, South- and South East Asia, and Amazon in the negative phase of ENSO, and the amount is small over there in the positive phase. As many studies pointed out, the isotopic composition in precipitation in the tropics is controlled by precipitation amount (Dansgaard 1964; Rozanski et al. 1993; Risi et al. 2008; Lee & Fung 2008) but ENSO modulates that precipitation, hence $\delta^{18}O_P$ is correlated with ENSO. Therefore $\delta^{18}O_P$ is well correlated with temperature over Central to Eastern Pacific and, in turn, that high correlation results in high reproducibility for temperature there.

This reasoning is also confirmed by using empirical orthogonal function (EOF) analysis. Figure 4-7 shows the first mode of EOF and principal component (PC) of simulated $\delta^{18}O_P$ at the observational sites and the PC of the first mode (PC1) regressed on temperature and precipitation field. PC1 explains 9.0% of the total variance. The regressed fields clearly show the features of ENSO (inversed). Indeed the correlation between PC1 and NINO3 index is as high as -0.71 ($p < 0.001$). The EOF1 field shows strong load over South East Asia, equatorial South America and West Africa (Figure 4-7a), which result from

anomalous precipitation there or in upstream regions in the negative phase of ENSO (Vuille and Werner, 2005; Ishizaki et al, 2012; Okazaki et al., 2015), which in turn also clear in Figure 4-7d. Hence it is precipitation amount that directory controls $\delta^{18}O_P$. But still ENSO modulates the precipitation amount over the region. This results in high correlation between $\delta^{18}O$ in precipitation and ENSO index, or temperature over central tropical pacific (Figure 4-5 and see also Figure 2-9). Therefore the pattern in Figure 4-5 largely reflects the teleconnection of ENSO.

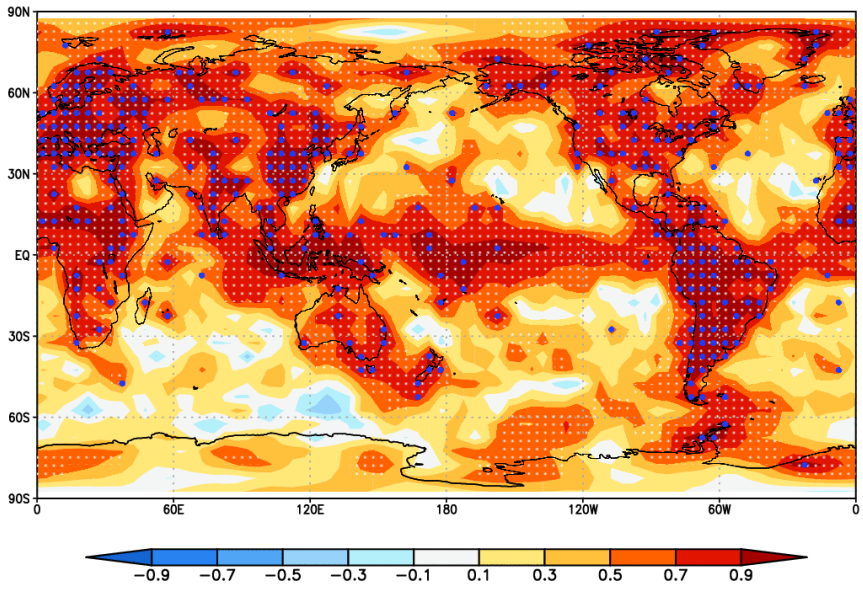

Figure 4-3 Temporal correlation between the analysis and the truth. The blue dot represents the location of GNIP observation site. The stipple means that the correlation is statistically significant ($p < 0.05$).

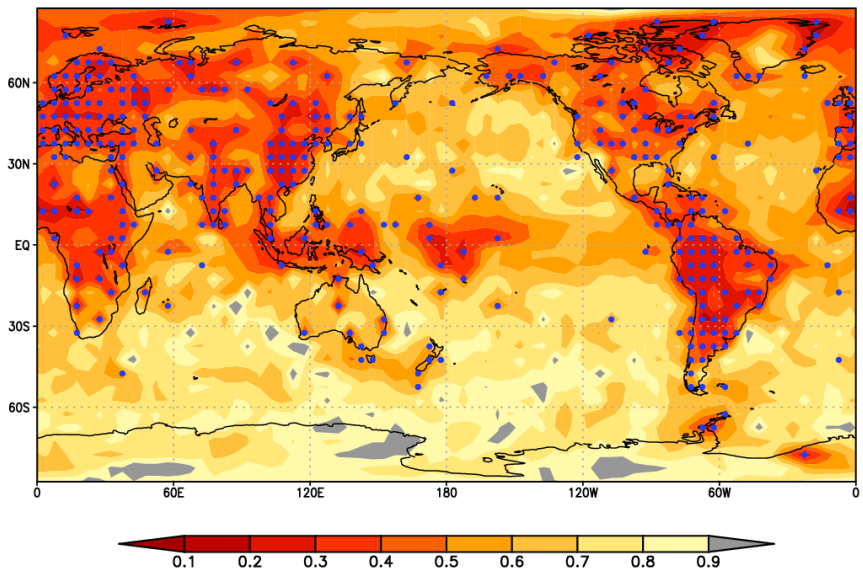

Figure 4-4 The ratio of standard deviation of $\delta^{18}O$ analysis to that of the truth

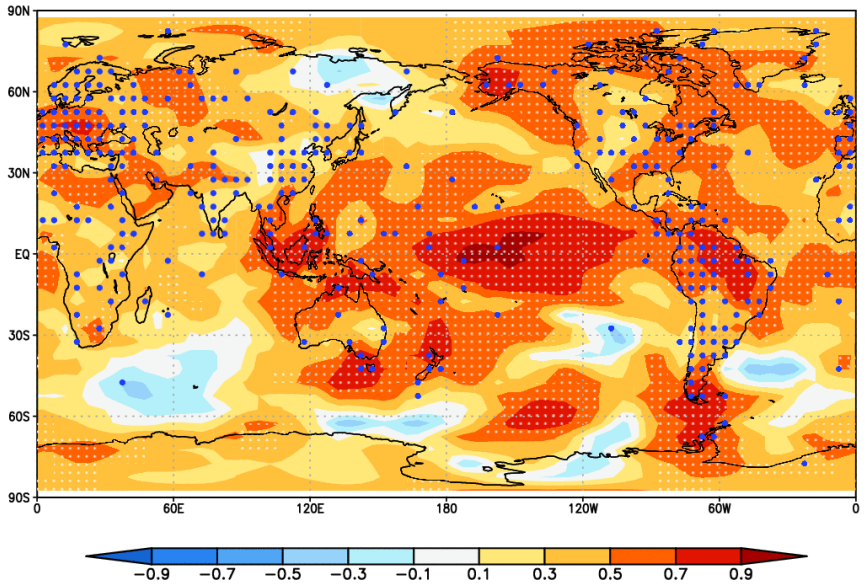

Figure 4-5 Same as in Figure 4-3 but for surface temperature

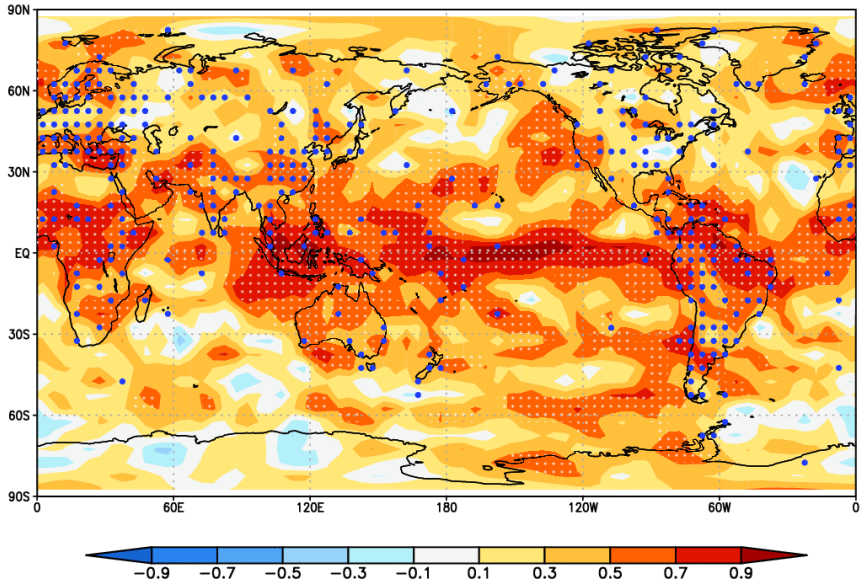

Figure 4-6 Same as in Figure 4-3 but for precipitation

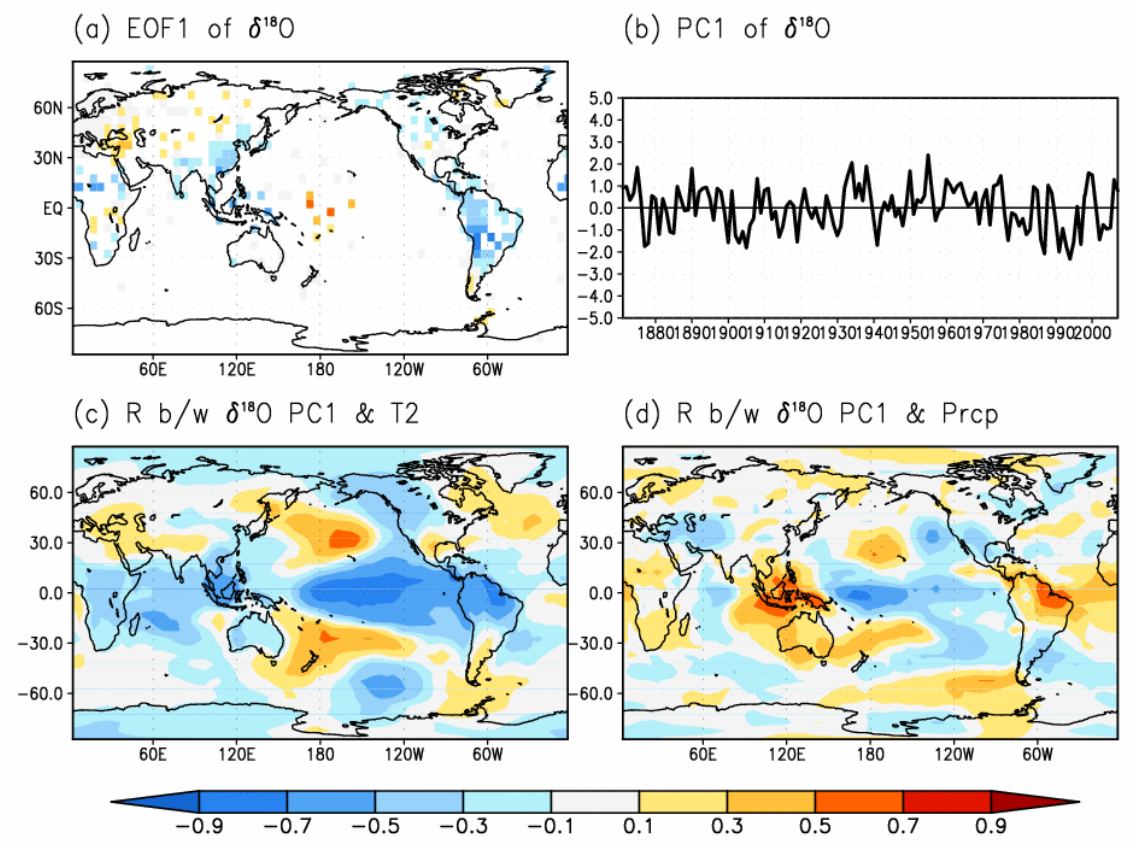

Figure 4-7 The first mode of (a) EOF and (b) PC of $\delta^{18}O$ in precipitation and PC1 correlation with (c) temperature and (d) precipitation

4.3.3. **Reproducibility of climate indices**

Figure 4-8 compares the truth and the analysis for climate indices for ENSO, Southern Annular Mode (SAM), Pacific North American pattern (PNA), North Atlantic Oscillation (NAO), Indian Monsoon, and Sahel rainfall. The definitions of the indices are obtained from Nan and Li (2003) for SAM, and Hurrell (1995) for NAO. The index for Indian Monsoon is calculated simply the areal average of precipitation over 0N-30N, 40E-90E to emulate All Indian Summer Monsson Rainfall index (AISMR; Sontakke et al. 1993). Similarly Sahel rainfall index is calculated the areal average of precipitation over 10N-20N, 20W-10E. The reproducibility is found to be high for all the indices ($p < 0.0001$). The results imply that precipitation isotope ratio is influenced by those phenomena as Figure 4-7 shows the relationship between $\delta^{18}O_P$ and ENSO. This in turn means that $\delta^{18}O$ is rich in climatic information on the interannual scale.

The reason of the high reproducibility for the indices will be discussed. Since the mechanism in which $\delta^{18}O_P$ records ENSO has been already explained above and the reason for high reproducibility

for PNA may be because of deep relationship between ENSO and PNA, the discussion for the rest indices will be presented here.

On the interannual timescales, the variability in stable isotope data from Greenland has been linked to NAO (ref). In the positive (negative) phase of NAO, it is generally cold (warm) in Greenland. Because isotopic ratios in precipitation are largely determined by temperature in Greenland, they correlate with NAO. The relation with NAO has been found not only in $\delta^{18}O$ in precipitation (Sodemann et al. 2008) but also in that in ice cores (Hurrell 1995; Vinther 2003; Ortega et al. 2014). Similarly, NAO is associated with temperature and precipitation change in Atlantic façade of Western Europe (Bladé et al. 2012). Field et al. (2010) have identified the local temperature effect on isotopic ratios in precipitation over central western Europe, even though the effect is weaker in summer due to the effects of continental recycling. Thus isotopic ratios in precipitation are correlated with NAO over Europe (Langebroek et al. 2011). As seen above, NAO exerts large influence on the variability in isotopic composition in precipitation over North Atlantic domain. Indeed NAO is found to be the third leading mode of simulated $\delta^{18}O_P$ at GNIP observation sites with the maximum loading in Greenland (not shown). The explained variance is calculated to be 4.9%, and the correlation coefficient between PC3 and NAO is 0.31 ($p < 0.001$).

On the other hand, the EOF analysis reveals that SAM like pattern is not included in the top 12 leading mode of simulated $\delta^{18}O_P$ at GNIP observation sites, which explains more than half of the variability in total. Thus it is difficult to understand which observation sites are responsible for the reproducibility only from the analysis. According to the previous studies, the positive phase of SAM is associated with cold surface temperatures over most of Antarctica, and a warming on the Antarctic Peninsula (i.e. Thompson & Wallace 2000). Similar results are presented by Gillett et al. (2006), who demonstrated that warming influence extends to the southern tip of South America, Argentina, Tasmania, and south of New Zealand. They also showed that the positive phase of SAM is also associated with anomalously dry conditions over southern South America, New Zealand and Tasmania, and wet conditions over much of Australia and South Africa. Since those factors have impact on the isotopic composition in precipitation and several GNIP observational sites are located in those SAM-influenced regions, it is legitimate that SAM is well resolved by assimilating information of isotopic composition in precipitation.

In low latitude, isotopic composition in precipitation is largely determined by local precipitation amount. Thus it is reasonable that isotopic composition in precipitation is correlated with AISMR and Sahel rainfall. Indeed many previous researches found the relationship between the isotope ratios in precipitation and rainfall activities in the low latitude (Vuille et al. 2005; Ishizaki et al. 2012; Okazaki et al. 2015). Note that distillation processes during moisture transport which provide isotopically depleted vapor contribute to a significant relationship between precipitation amount and isotope ratios in precipitation. The analysis of the mechanism how isotope ratios in precipitation is affected by the upstream precipitation is written in Appendix B.

Next, phenomena which have longer timescale variability than annual are focused. Figure 4-9 compares the time series of the global temperature, Pacific Decadal Oscillation (PDO), and Atlantic Multidecadal Oscillation (AMO). For the all indices, the long term trend is fairly well captured, whereas the absolute change is almost half in the analysis compared with the truth. For the case of the global mean temperature, there are areas where DA shows poor skills and in such areas warming never occurs. Even in the areas where DA shows high skills, the correlation coefficient of 1 is not achieved, which means the variance is not fully captured. The observational error further dampens the variability of the analysis field. Thus the muted variability is understandable. Indeed variance loss is a common problem in the field of paleoclimate reconstruction. Steiger et al. (2014) shows that the problem can be solved by reconstructing temperature anomaly from the global mean in each grid and the global mean separately. This technique can be applicable to the isotopic data assimilation. Furthermore the use of ensemble members which created by perturbed initial condition, parameters, or boundary conditions for the specific year should be remedy for this problem: in such an ensemble, background must be closer to the truth than the fixed background used in this study by responding to the year specific information.

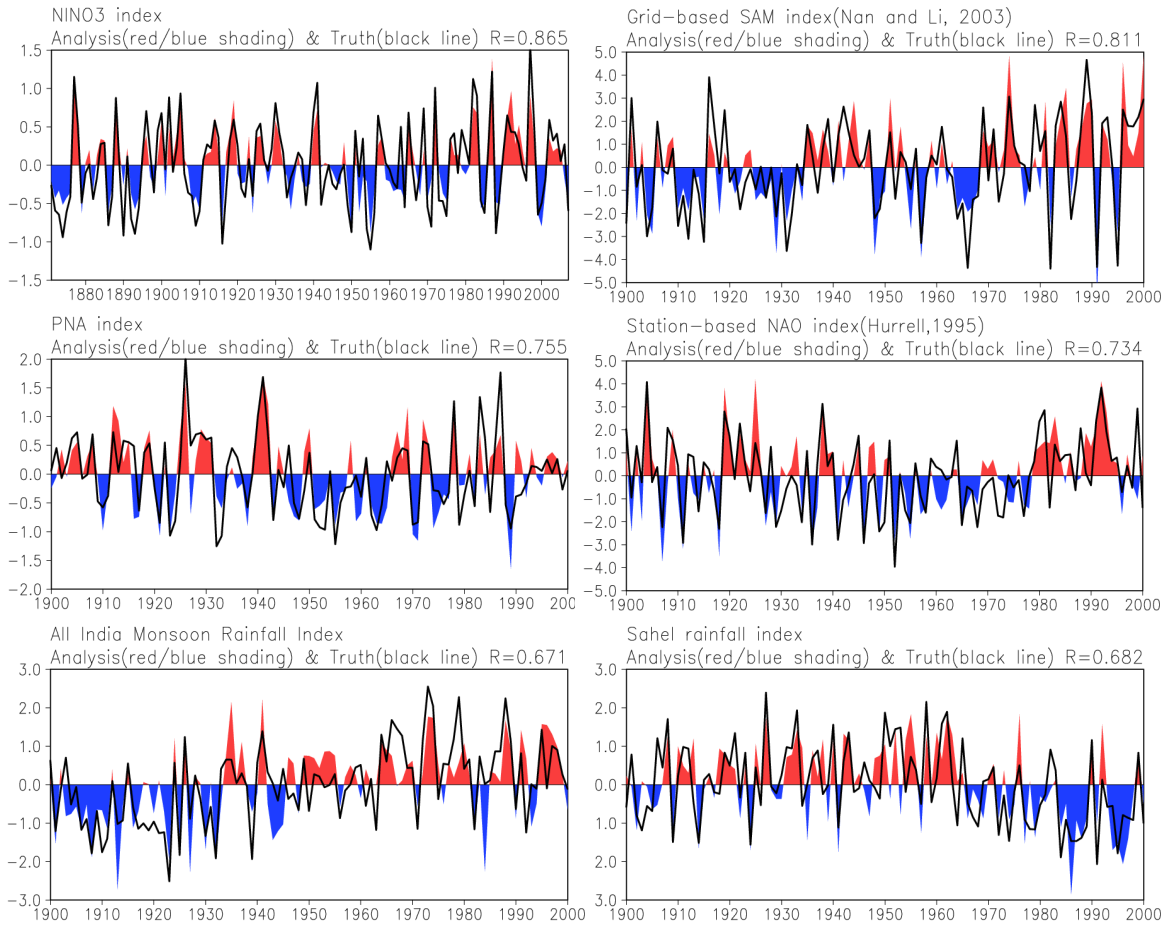

Figure 4-8 Time series of (a) NINO3 (b) SAM index (Nan and Li, 2003), (c) PNA index, (d) station based

NAO index (Hurrell, 1995), (e) All India Rainfall index, and (f) Sahel rainfall index. Black line is for the truth and red and blue shade is for the analysis.

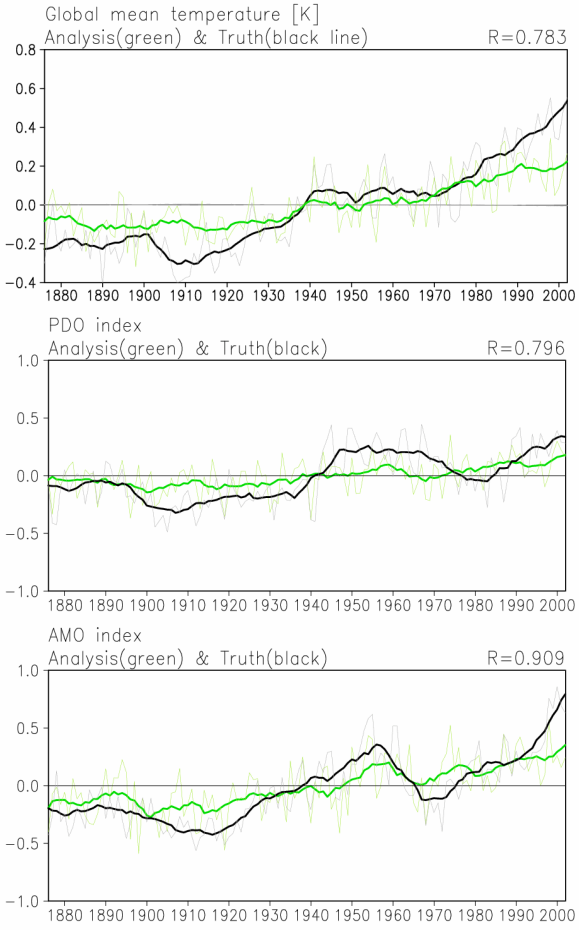

Figure 4-9 Time series of (a) global mean temperature, (b) PDO index, and (c) AMO index. Black line is for the truth and green line is for the analysis. Bold and thin lines represent annual and decadal average, respectively.

4.4. Discussion

4.4.1. **Sensitivity to assumption**

The algorithm used in this study assumes Gaussian error for the background error. However this assumption may not be satisfied due to the global warming. To confirm the possible error due to this unsatisfied assumption, the assimilation is conducted with background from which trend is removed. The effect of detrending is not significant for the reproducibility (Figure 4-10). The figure suggests that the distribution of background may not be significantly different from Gaussian distribution or insensitivity of the algorithm to the assumption. Nevertheless this assumption will be satisfied if the ensemble members are constructed differently.

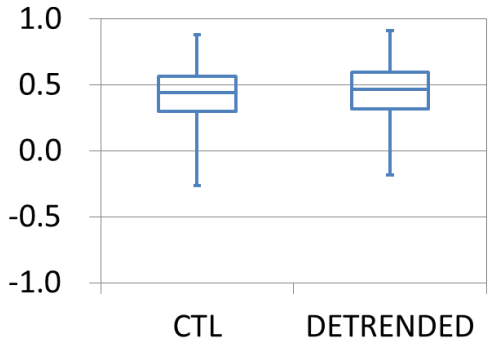

Figure 4-10 Distribution of correlation coefficients between the truth and the analysis for temperature.

4.4.2. **Which is better, raw data assimilation or reconstructed data assimilation?**

Hughes and Ammann (2009) recommended the use of measured proxy data, not reconstructed data from that. This subsection compares the results from three assimilation experiments: the first one assimilates $\delta^{18}O$ in precipitation, and the others assimilate reconstructed surface temperature. The experimental frame work is still OSSE and the observations ($\delta^{18}O_P$) and reconstructed temperature are assumed to be available at GNIP sites (349 grids). Thus the first experiment is the same as the original experiment. For the other experiments, the temperature from the truth run added with noise is assimilated. The noise is added to account for the uncertainty stems from reconstruction. The signal-to-noise ratio of the reconstructed temperature is set to 0.25 and 0.50, which is typical value for proxy records (e.g. Mann et al., 2007).

Figure 4-11 shows the spatial distribution of correlation coefficients for temperature and precipitation between the truth and the analysis obtained from the three experiments. The global areal fraction in which the truth and the analysis correlates significantly ($p < 0.05$) for temperature (precipitation) is 0.60 (0.42), 0.54 (0.17), and 0.70 (0.28) for the experiments with $\delta^{18}O_P$ assimilated, temperature with SNR of 0.25 assimilated, and temperature with SNR of 0.50 assimilated, respectively. The value is higher in $\delta^{18}O_P$ assimilated case than temperature (SNR=0.25) assimilated case for both precipitation and temperature. On the other hand, temperature is well reconstructed by assimilation of temperature with small noise (SNR=0.50) than by assimilation of $\delta^{18}O_P$. But still $\delta^{18}O_P$ assimilation works better for precipitation reconstruction. Accordingly the superiority of assimilation of raw data to assimilation of reconstructed data is not significant for this period. But the superiority is dependent on the magnitude of SNR. In other words, how well we can assimilate the reconstructed value is dependent on the quality of the reconstruction. The quality of reconstruction is in turn dependent on the stationarity between proxy and climate, and the degree to which the proxy is affected by the other factors other than the climate

variable of interest. Isotope enabled GCMs (Schmidt et al. 2007) and the observations and models for tree-ring (D'Arrigo et al. 2008; Evans et al. 2014) have shown the non-stationarity and non-linearity between proxies and climate. Thus we cannot expect high SNR would be maintained along with time. On the other hand, as Hughes and Ammann (2009) pointed out, one does not have to care about the stationarity and the linearity if one has well defined forward proxy model. Therefore the assimilation of raw data is expected to be powerful when one tries to reconstruct paleoclimate in which relationship between proxy and climate constructed with present condition does not hold true.

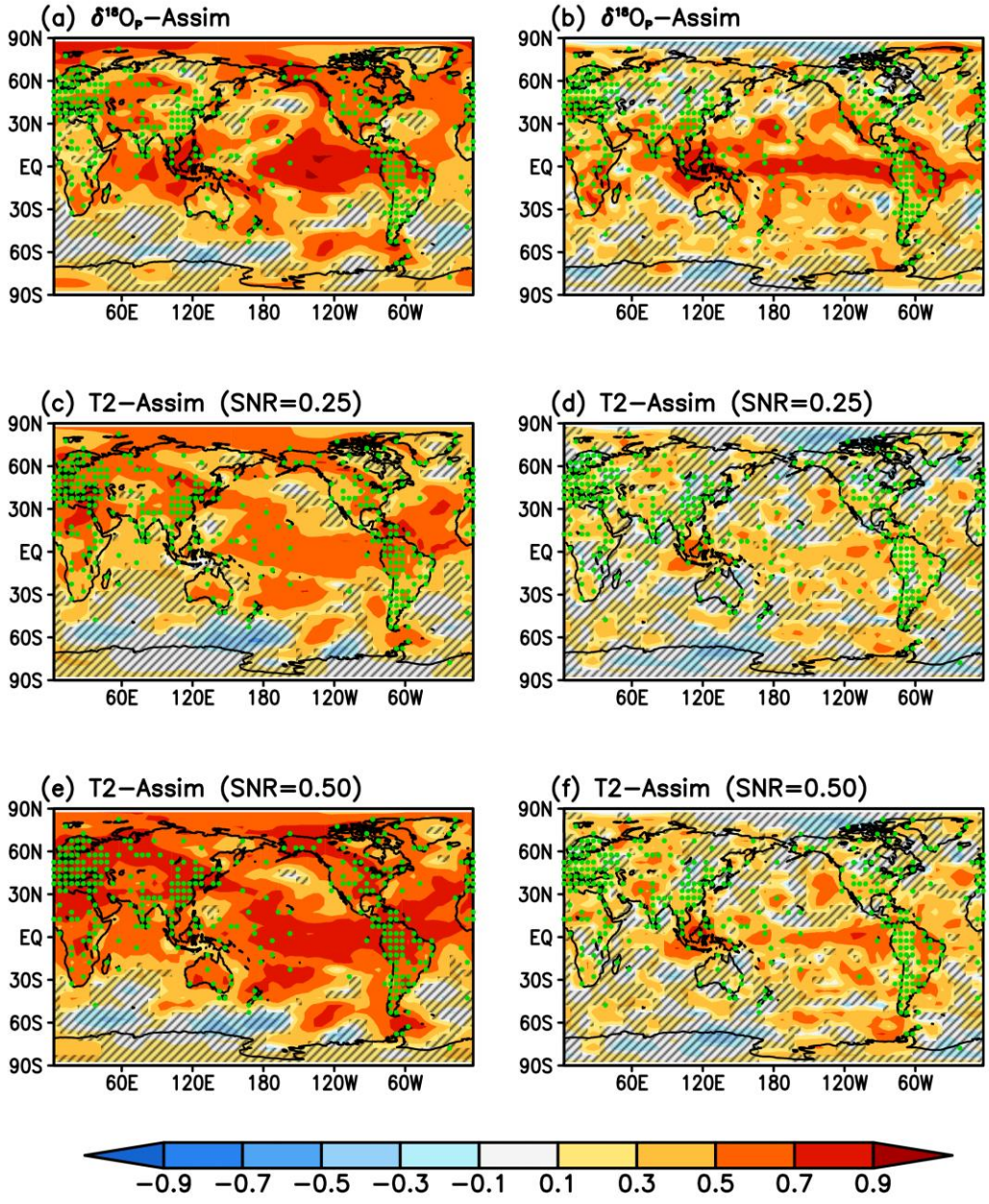

Figure 4-11 Correlation coefficient between truth and the analysis for (a, c, e) surface temperature, and (b, d, f) precipitation. The analysis is made by assimilating (a, b) $\delta^{18}O_p$, (c, d) temperature with noise

(SNR=0.25), and (e, f) temperature with noise (SNR=0.50). Green dots represent the sites where observation is available. The area which does not correlate with the truth is hatched out.

4.5. Conclusion and summary

In this chapter, isotopic information is assimilated into simulation albeit in the idealized way to test the feasibility of isotopic proxy assimilation. The reproducibility is high not only the assimilated variable ($\delta^{18}O$ in precipitation) but also in temperature and precipitation fields. The correlation coefficients are especially high in tropical Pacific due to the leading impact of ENSO on $\delta^{18}O$. Accordingly the reproducibility of ENSO is high. The correlation coefficients are moderate to small over land and high latitudes. On the other hand, the variability of low frequency event or trend in global mean temperature is underestimated because of variance loss. Subsequently some assumptions used in this study are tested. The first one investigates the use of background which does not distribute Gaussian manner. To make the background close to the Gaussian distribution, the trends are removed. This modification does not change the reproducibility significantly. The sensitivity to the variable to be assimilated is also tested. The reproducibility is comparable between $\delta^{18}O_P$ assimilated case and the noise added temperature assimilated case as for temperature reconstruction, but the result is higher for precipitation reconstruction when isotopic information is assimilated. Thus it is expected that the assimilation of isotopic information would provide simulation for wide range of climate information.

In this work the data assimilation of annually averaged isotopic information is shown to be promising. Nonetheless this system cannot gain the information of climate variables finer than the time scale of proxies. Even though the algorithm is suited to draw the picture of past climate change, to investigate the mechanism behind the climate change, one may require temporal resolution finer than annual. For that purpose the other assimilation mechanism (e.g. particle filter) should be used.

In this work, time constant Kalman gain is used for the assimilation. For the timescale of this study (one hundred years), I did not observe severe discrepancy with the constant Kalman gain. But to reconstruct longer timescale in which the relationship between $\delta^{18}O_P$ and climate may not be the same as present, it is better to construct Kalaman gain to be suited for specific period. For example, Kalman gain for a reconstruction year can be constructed before and after several tens of years of that reconstruction year. By doing this, non-stationarity between $\delta^{18}O$ and climate can be dealt with. We have to fully investigate how the impact of non-stationarity is large in the future work. If it is suggested that the impact of non-stationarity is acceptable, it may be possible to utilize a Kalman gain constructed from real proxy data and observed data for present. In this case, we do not have to care about the misrepresentation between proxy and climate. But again, note that previous studies suggest the stationarity is not likely to hold true even for last millennia (Schmidt et al., 2007; LeGrande and

Schmidt, 2009).

The result suggests that the system is applicable to the real observation assimilation. But the uncertainty of data in paleoclimate observation is larger than that of precipitation isotope sampled in modern times. Therein the uncertainty would be larger for both simulation and the observations. This may further dampen the possibility of proxy data assimilation. Therefore further idealized study combining the proxy system models and data assimilation is desirable before the system is applied to the proxy data assimilation.

Chapter 5.

Proxy data assimilation

5.1. Introduction

In the previous chapters, the author evaluates the forward models for isotopic proxies, and tests the feasibility of proxy data assimilation. In Chapter 4, the proxy data is assumed to be isotope ratio in precipitation. However, what we can have about climate in the past prior to the instrumental observation is not isotopic ratio in precipitation but that in proxies ice core, coral, speleothem, tree ring cellulose and so on. Therefore this chapter goes even a little further and examines the feasibility of proxy data assimilation to which isotopic information from ice core, coral, speleothem, and tree ring cellulose is assimilated.

Furthermore, in the previous chapter, the experiments are designed in an idealized way in which simulation run and observation run are constructed from the same model simulation as for the forcing; the only difference between them was the initial condition. Accordingly, the simulation and the truth were designed to be too close. The targeting period of proxy data assimilation is the time when no direct observation is available. In such a period, we do not have observation for SST, and atmospheric model has to be driven by modeled SST, which may result in the simulated pattern not so close to the observed pattern. In that sense, to fairly evaluate the feasibility of proxy data assimilation, the first guess of the data assimilation has to be constructed from modeled SST, not observed SST.

In this chapter, the skill of simulation to which isotopic information recorded in ice core, speleothem, coral, and tree ring cellulose is assimilated is investigated. Additionally the robustness of the result is also investigated by making the condition closer to the real.

5.2. Experimental design

In the first experiment, named control (CTL) experiment, adopts the framework of the observation system simulation experiment (OSSE) as in the previous chapter. That is, the “simulation” and the “truth” are simulated by the same model (isotope equipped version of MIROC5) with the same forcing (SST, sea ice, carbon dioxide, methane, ozone, and total solar irradiance) but with different initial condition. The assimilation algorithm is also the same as that in the previous chapter. The spatial resolution is T42 (around 280km) with 40 vertical layers. The both simulation periods are from 1871 to 2007 (137 years). The difference from the previous chapter is the variable to be assimilated. In the

previous chapter it was $\delta^{18}O$ in precipitation, but in the present chapter the variables are $\delta^{18}O$ in ice core, speleothem, coral and tree ring cellulose. They are simulated by using the proxy models which are evaluated in Chapter 3. For $\delta^{18}O$ in ice core and speleothem, they are assumed to be the same as the $\delta^{18}O$ in precipitation. The measurement error is assumed to be 0.1‰ for the whole proxies. The spatial distributions for various periods of each proxy are mapped in Figure 5-1. In reality, the distributions are changing along with time (Figure 5-1 c-h), and consequently the number of proxies is not constant over time (Figure 5-1 b). For the sake of simplicity, however, the distributions of the proxies are assumed to be constant over time in the CTL experiment (Figure 5-1 a).

Three additional experiments will be conducted to test the robustness of the result of proxy data assimilation. In the experiment 1 (Exp.1), the simulation run is constructed from the simulation forced by modeled SST. The SST is simulated by atmosphere-ocean coupled version of MIROC5 (Watanabe et al. 2010). The simulation is so-called historical run in Coupled Model Intercomparison Project Phase 5 (CMIP5; Taylor et al. 2007). The simulated SST and sea ice concentration are obtained from CMIP5 data server (https://pcmdi.llnl.gov/search/cmip5/). The settings for simulation run other than SST and sea ice are the same as that for CTL simulation. The truth run is the same as that for CTL experiment. Thus this experiment is aimed at investigating how the result will be degraded by using the simulated SST.

In the experiment 2 (Exp.2), the experimental design is almost the same as that in Exp.1. The only one difference is the number of proxies. In the Exp.1, the distribution of proxies and the number of proxies are set to be constant over time as in CTL experiment. In the Exp.2, the distribution and the number of proxies are time different in the same manner as the real to fairly evaluate the result of experiment 3 which is written in below.

In the experiment 3 (Exp.3), the simulation run is constructed from the simulation forced by modeled SST, and assimilated variables are the real proxy data. Hence, the Exp.3 is not the idealized experiment anymore; it is real proxy data assimilation. All proxy records are firstly normalized and then averaged onto T42 grid box to ignore the model bias and to produce a regional grid box composite following Crespin et al. (2009) and Goosse et al. (2010). To fairly compare the results from each experiment, the assimilated variables are all normalized in all the simulation and truth runs and observation in the all experiments. The experimental designs are summarized in Table 5-1.

Table 5-1 Summary for the experimental design of proxy data assimilation.

	SST data to drive simulation run	SST data to drive truth run	Assimilated variable	Observation network
CTL	HadISST	HadISST	Simulated $\delta^{18}O$	w/o missing
Exp.1	Modeled SST	HadISST	Simulated $\delta^{18}O$	w/o missing
Exp.2	Modeled SST	HadISST	Simulated $\delta^{18}O$	w/ missing
Exp.3	Modeled SST	-	Observed $\delta^{18}O$	w/ missing

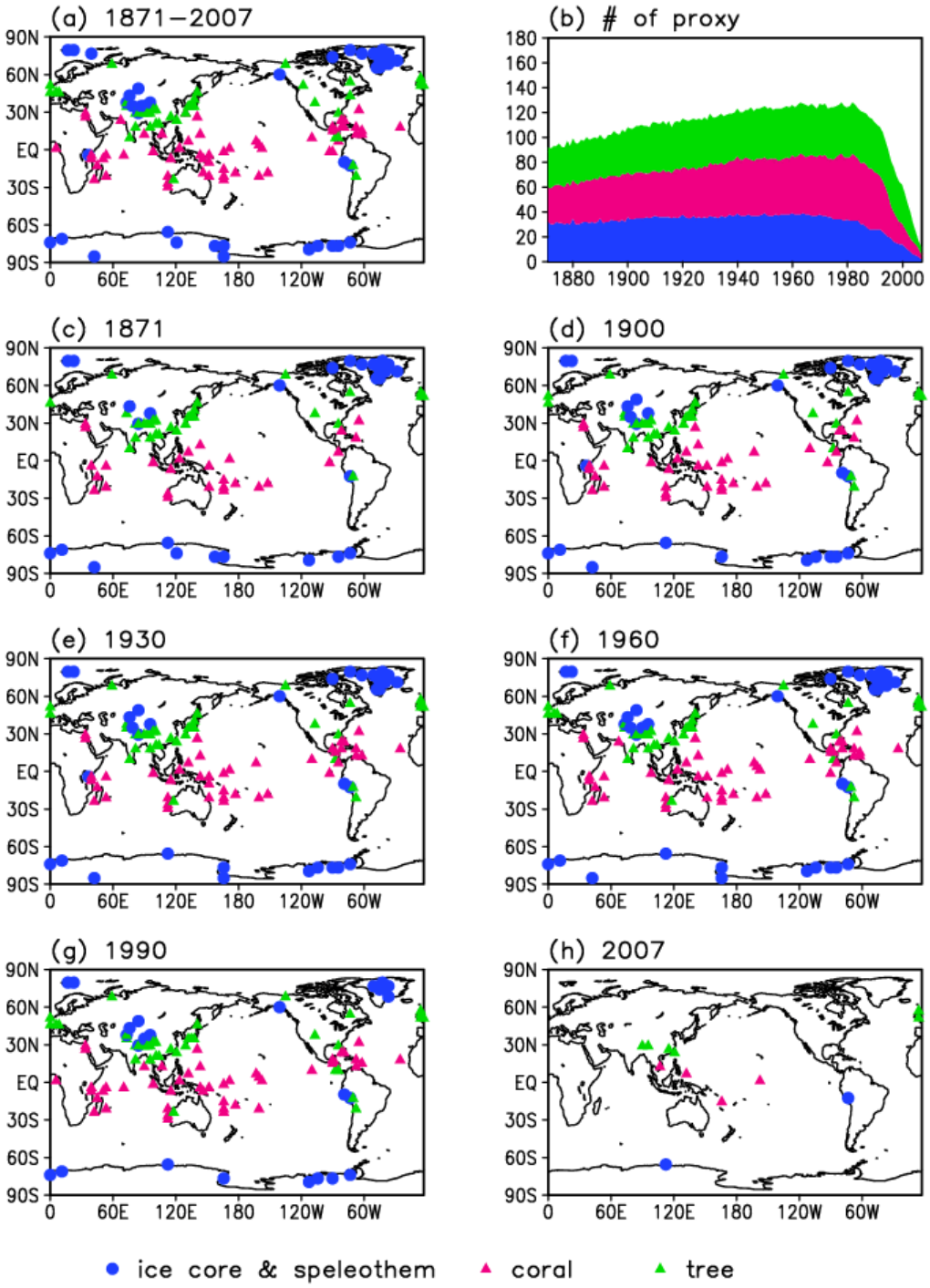

Figure 5-1 Distribution of the proxies (ice core, speleothem, coral, and tree ring). Ice cores and speleothems are drawn in blue. Pink triangle is for coral. Green triangle is for tree ring cellulose. (a) Proxy which covers at least one year of 1871-2000 are mapped (b) The number of proxies is depicted as a function of time. (c-h) The spatial distribution of proxies are mapped for (c) 1871, (d) 1900, (e) 1930, (f) 1960, (g) 1990, and (h) 2007.

5.3. Results

5.3.1. Control experiment

The temporal correlations between the analysis of CTL and the truth for temperature and precipitation are shown in Figure 5-2 (a) and (e). The correlation is calculated for the period of 1970-2000. As explained in the previous chapter, the first guess is the climatology for every reconstruction year. Hence the any positive correlation means that the assimilation works well. For temperature, the correlation is high over the low latitudes, the same as the result of assimilation of $\delta^{18}O$ in precipitation shown in previous chapter. In this chapter the high correlation is due to the coral records. $\delta^{18}O$ in coral is largely determined by temperature as shown in Figure 3-9 and in the past studies (Epstein & Mayeda 1953). Therefore by assimilating isotopic information imprinted in corals, temperature field over low latitudes, especially over the ocean, are skillfully reconstructed. On the other hand, the coral records are determined both by temperature and precipitation over the Pacific Warm pool (Figure 3-9). Reflecting that, the reproducibility is relatively low there compared with central to east Pacific. In high latitudes, the temperature is also relatively well reconstructed. This is because of the ice core records. The isotope ratio in precipitation and ice core is largely determined by temperature over high latitudes (Figure 3-4). Therefore by assimilating isotopic information imprinted in ice cores, temperature field over high latitudes, are well reconstructed. The reason of the relatively small correlation is because the annual $\delta^{18}O$ in ice core is biased toward rainy day condition and not representative for annual mean temperature (e.g. Noone & Simmonds 2002).

For precipitation, the correlation is high over the low latitudes, again the same as the result of assimilation of $\delta^{18}O$ in precipitation which is shown in previous chapter. This is also due to the coral records. Since $\delta^{18}O$ in coral in Pacific warm pool records the signal of precipitation (Figure 3-9), it is reasonable that precipitation amount is reconstructed around the sites by assimilating the data. Although $\delta^{18}O$ in coral in central to east Pacific records the signal of temperature, precipitation amount is well reconstructed due to covariation between precipitation and temperature on the interannual timescale over there. $\delta^{18}O$ in tree ring cellulose also contributes to the reconstruction of precipitation field. As shown in Figure 3-17, $\delta^{18}O$ in tree ring cellulose is good indicator of hydroclimate globally. Accordingly, the correlation is relatively high around the sampling sites of tree ring cellulose, such as in Europe, Tibet, and western North America.

As did in the previous chapter, the responsible proxy for the reproduced pattern can be found by EOF analysis. Here the EOF analysis for $\delta^{18}O$ in ice core, speleothem, coral, and tree ring cellulose is conducted. Since $\delta^{18}O$ in ice core and speleothem are assumed to be equal to $\delta^{18}O$ in precipitation in this chapter, the analysis is conducted for them together.

The principal mode of $\delta^{18}O$ in ice core and speleothem explains 12.6% of the total variance and it is the only significant mode according to the Rule of Thumb (North et al. 1982). The maximum loading is

in Greenland and East Antarctica where temperature has been increasing significantly for the past hundred years. Actually the PC1 shows the significant trend and is correlated with global mean surface temperature (R=0.65). Therefore ice core data represents global warming pattern and is responsible for the temperature in high latitudes.

The first mode of $\delta^{18}O$ in coral and tree ring cellulose are both ENSO. The explained variance of the first mode is 19.1% and 15.3% for $\delta^{18}O$ in coral and tree ring cellulose, respectively. The maximum loadings are in central Pacific for coral, and Tibet for tree ring cellulose. The temporal correlation between PC1 and NINO3 index is 0.74 and 0.50, respectively. Since isotopic composition in coral is influenced by sea temperature, it is not surprising that $\delta^{18}O$ in coral in central Pacific has a link to ENSO. Interestingly, this analysis reveals that $\delta^{18}O$ in tree ring cellulose is influenced by ENSO and hence contributes to the reconstruction of temperature and precipitation over tropical Pacific. Indeed many previous researches found the link between $\delta^{18}O$ in tree ring cellulose and ENSO (Xu et al. 2011; M. Sano et al. 2012; Masaki Sano et al. 2012; Xu, Sano, et al. 2013; Xu, Zheng, et al. 2013; Xu et al. 2015). The link between them is explained following way by Xu et al. (2011). Although the relation is found to be non-stationary over time (Kumar 1999), plentiful numbers of article have associated with the Indian monsoon rainfall and ENSO (e.g. Rasmusson & Carpenter 1983). The positive phase of ENSO results in a reduction of summer monsoon rainfall there, and the decrease in rainfall leads to a dry condition in summer. The decrease in precipitation leads isotopically enriched precipitation, and dry condition enhances the enrichment of water in the leaf. Accordingly $\delta^{18}O$ in tree ring cellulose becomes heavier than usual in the positive phase of ENSO. Thanks to coral and tree ring cellulose data, the correlation coefficient between the analysis and the truth for NINO3 index is as high as 0.97.

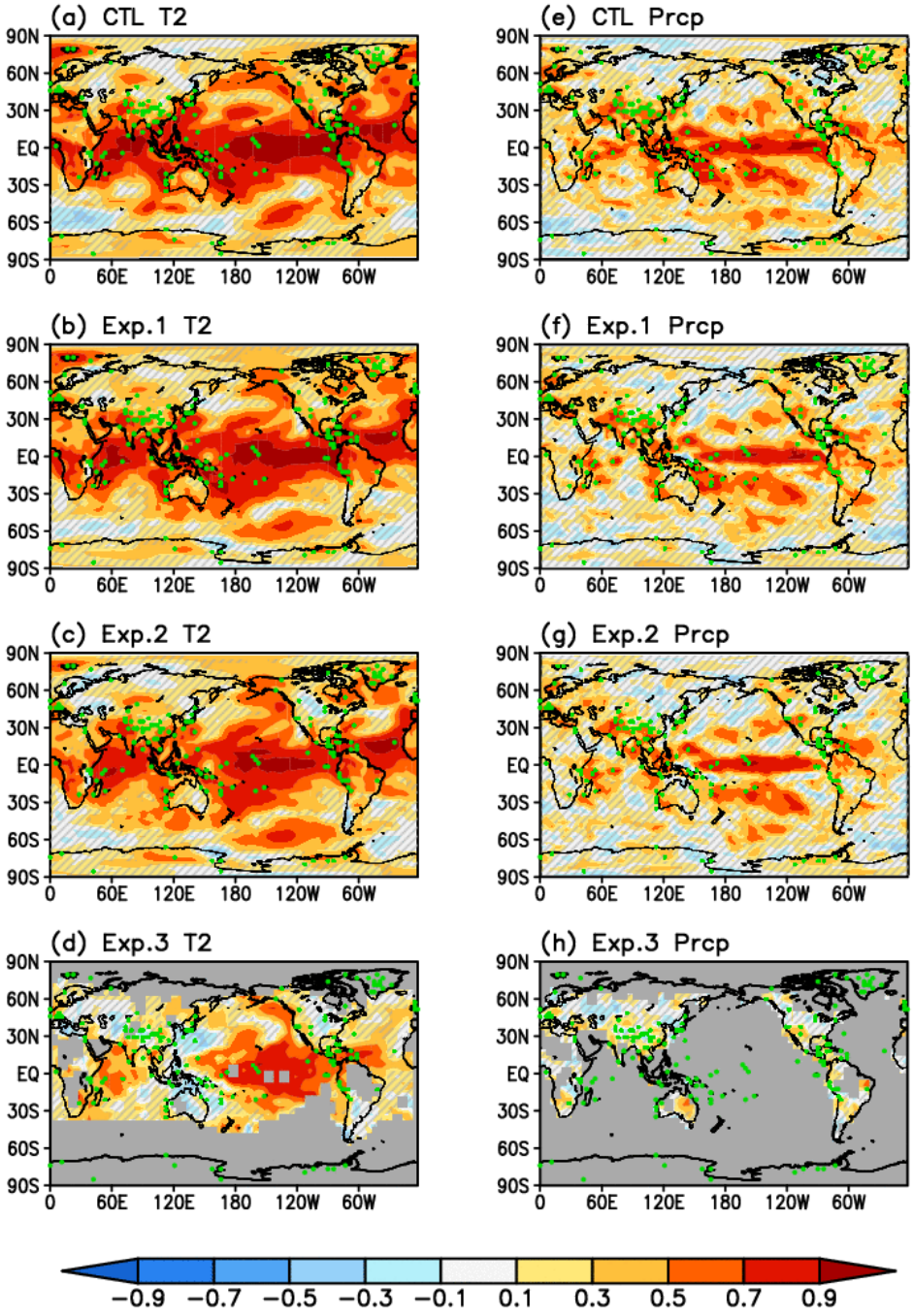

Figure 5-2 Temporal correlation between the analysis and the truth or observation for surface air temperature (a) and precipitation amount (b). The period considered is from 1970 to 2000. Green dots represent the sites where observation is available. The area which does not correlate with the truth significantly at the 5% level is hatched out. The areas where the observation covers less than 50% of the period are left blank.

5.3.2. **Sensitivity experiment**

As shown in the previous section, proxy data assimilation shows the reasonable skill. From here, how the results will change when the experimental design is changed toward more realistic condition of proxy data assimilation. In the "realistic" condition, observed SST data to drive atmospheric GCM is not available. Furthermore, the local relation and teleconnection between $\delta^{18}O$ in proxy and climate variables may be different in the simulation and in the real world.

In Exp.1, the temporal correlation between the analysis and the truth is not so much degraded from CTL experiment both for temperature and precipitation (Figure 5-2 (b) and (e)). This should be because ENSO is well represented in the modeled SST which is used to construct "simulation". Indeed Watanabe et al. (2010) showed that the modeled SST and the observation are very similar for the amplitude of ENSO measured by NINO3 index and the spatial pattern of temperature and precipitation field regressed on the NINO3 time series (see Figure 13 and 14 in their article).

The Exp.3 is not the idealized case anymore; it is real proxy data assimilation. In this experiment, the "simulation" is constructed from the simulation forced by modeled SST, and real proxy data is assimilated into the simulation. The temporal correlation between the analysis and the observation for temperature and precipitation are shown in Figure 5-2 (d) and (h). Here the observations are obtained from HadCRUT3 (Brohan et al. 2006) for temperature and GHCN-Monthly Version 3 (Peterson & Vose 1997). Since the number of proxies to be assimilated is not equal to that in Exp.1, to compare the result of Exp.3 with that of Exp.1 is not straightforward. To fairly compare the results, the Exp.2 assimilates the same number of proxies as Exp.3 with the same setting as Exp.1 for the other points. The correlation coefficients are notably decreased over Indian Ocean, east Pacific and the Atlantic Ocean for temperature. These areas match with the area where the reproducibility of coral model is relatively worse. In those areas, the impact of sea current and river flow which is not included in the coral model are thought to be large. To enhance the skill of assimilation, the reproducibility of $\delta^{18}O$ in coral over those areas must be improved.

The global mean correlation coefficient for temperature and precipitation in Exp.3 is almost as half as that in Exp.2 (Table 5-2). Note that the correlation is averaged in the same domain for the all experiments to take into the difference of representativeness. The correlation for NINO3 is also decreased to 0.60 but it is still statistically significant at 0.01% level.

Table 5-2 Temporal correlation between the analysis and the truth (observation) for each experiment. The values for temperature and precipitation are the global mean of temporal correlation.

	CTL	Exp.1	Exp.2	Exp.3
T2	0.61	0.56	0.52	0.28
Precip.	0.32	0.30	0.26	0.10
NINO3	0.97	0.98	0.96	0.60

5.4. Discussion

The skill of proxy data assimilation is relatively low over Eurasia and North America even in the idealized experiment. Is this because of the limitation of the proxy data assimilation or the scarce distribution of proxy? This section investigates the reason for the relatively low reproducibility in the area by changing the spatial distribution of proxy.

The experimental design other than the spatial distribution of proxy is the same as the CTL experiment. The proxy network used in this section mimics that of Mann et al. (2008) (Figure 5-3). Here I assume that isotopic information is available for all the sites even if this is not the case. For instance, even if only tree ring width data is available at some site in Mann et al. (2008), this section assumes that the isotopic data recorded in tree ring cellulose is available at that site. The number of grids in which proxy is available over the North America is 8 and 91 respectively for CTL experiment and Mann et al. (2008).

The result for North America is shown in Figure 5-4. The figure shows the temporal correlation coefficients between the analysis and the truth for surface air temperature, precipitation, surface relative humidity, and 500hPa geopotential height. The correlation coefficient is calculated for the period of 1970-2000. The skill is especially high around the area in which proxies are densely distributed for all the variables. The coefficients averaged over the United States (30N-50N, 120W-80W) are 0.58 and 0.52 for temperature and precipitation. Compared from Figure 5-2 (a) and (e), the skill is apparently improved for both variables; the coefficients are originally 0.32 and 0.31 in the CTL experiment. The result implies that the reconstruction skill is heavily dependent on the distribution of proxy data.

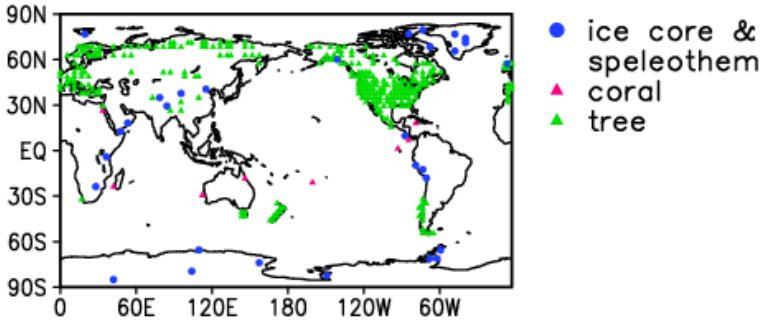

Figure 5-3 Distribution of the proxies (ice core, speleothem, coral, and tree ring) which mimics that of Mann et al. (2008). Ice cores and speleothems are drawn in blue. Pink triangle is for coral. Green triangle is for tree ring cellulose.

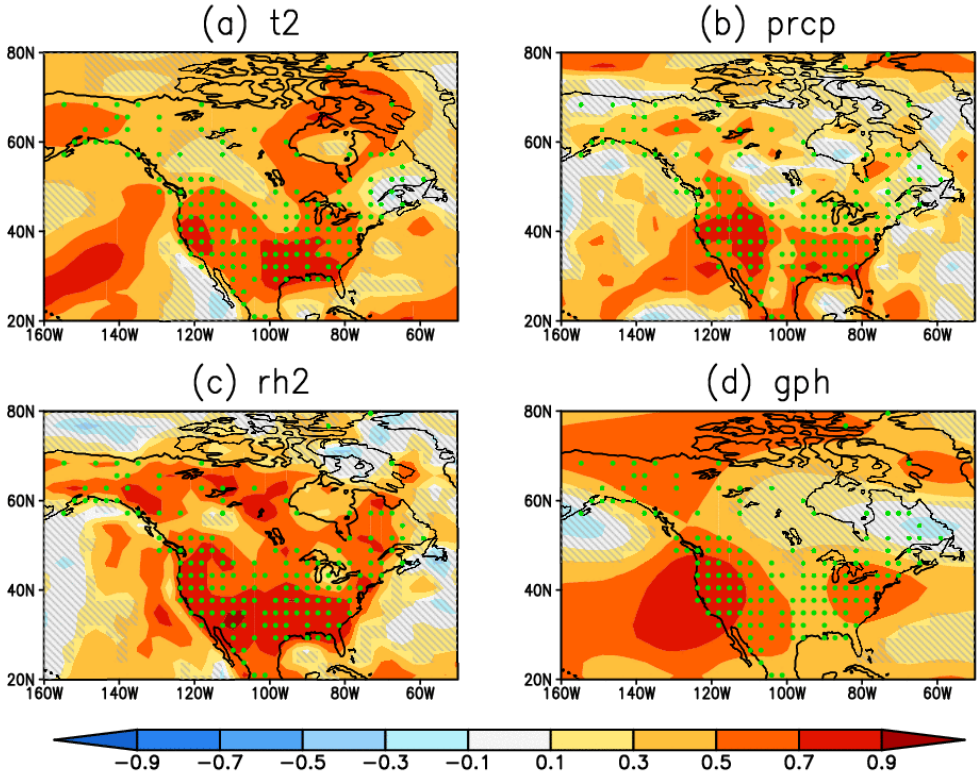

Figure 5-4 Temporal correlation between the analysis and the truth for surface air temperature (a), precipitation amount (b), relative humidity (c), and 500hPa geopotential height (d). The period considered is from 1970 to 2000. Green dots represent the sites where observation is available. The area which does not correlate with the truth significantly at the 5% level is hatched out. The areas where the observation covers less than 50% of the period are left blank.

5.5. Conclusion and summary

The feasibility of proxy data assimilation is examined subsequently to chapter 4. In this chapter, however, more realistic proxy data is assimilated than in the previous chapter. In other words, $\delta^{18}O$ in ice core, speleothem, coral, and tree ring cellulose are assimilated into the simulation instead of $\delta^{18}O$ in precipitation.

The result of proxy data assimilation remains the same level as that of precipitation isotope data assimilation. The skill is good in low latitudes because of temperature dependency of coral data over there and correlation between ENSO and tree ring cellulose data in Tibet.

To test the robustness of the result of proxy data assimilation, the additional experiments are conducted. In the first experiment, the simulation run is constructed from the simulation forced by modeled SST (Exp.1). The experiment tests how the result will be degraded by using the simulated SST. The result shows little difference for the reconstruction skill both for temperature and precipitation field. This is because ENSO, which is the most important mode for the reconstruction, is well represented in the modeled SST.

Finally, the real proxy data assimilation is conducted, where the simulation run is constructed from the simulation forced by modeled SST, and the real (observed) proxy data is assimilated into the simulation (Exp.3). The reconstruction skill decreased over Indian Ocean, east Pacific and the Atlantic Ocean where the reproducibility of proxy model is relatively worse. To enhance the skill of assimilation, the reproducibility of $\delta^{18}O$ in coral over those areas must be improved. The global means of the correlation for temperature and precipitation are as half as that of idealized experiment. Though the correlation for NINO3 is also decreased from the idealized experiment, the coefficient is still as high as 0.60.

From the results, it is clear that isotope enabled atmospheric GCM and proxy models must be improved more. The difference between the CTL and Exp.1 is because of misrepresentation of SST by the coupled GCM. The difference between the Exp.1 and Exp.2 is because of the number of observation to be assimilated. Finally, the difference between the Exp.2 and Exp.3 is because of misrepresentation of atmospheric GCM equipped with isotope and proxy models. The difference is the largest in the Exp.2 and Exp.3 (Table 5-2). Therefore the reproducibility is degraded because of the misrepresentation of atmospheric GCM equipped with isotope and proxy models. Though it is too early to conclude which is the cause of the degradation at this stage, the models for ice core which take into account whole post depositional processes and for speleothem must be developed to utilize all the data more effectively.

In this chapter, I investigated the feasibility of proxy data assimilation and showed that, at least, it may be possible to reconstruct ENSO and ENSO related temperature and precipitation variation with this proxy network. Since the reproducibility is heavily depends on the spatial distribution, we can expect that the reproducibility will be better and better with more proxy data.

Chapter 6.

General Conclusion

The goal of this study is to develop a solid base of proxy data assimilation to provide the best estimate for the past millennium. For that goal, following sub-studies were conducted to build a proxy data assimilation system: development of a new isotope enabled GCM to create realistic atmospheric variables including isotopic information; evaluation of forward proxy models; and evaluation of isotopic data assimilation.

In Chapter 2, stable water isotopes have been successfully implemented into state-of-the-art GCM; MIROC5. The reproducibility of $\delta^{18}O_P$ in mean field, seasonality, spatial relationship with temperature and precipitation are evaluated by means of correlation coefficients, and RMSE, and are found to be comparable with previous isotope enabled GCMs. On the other hand, the reproducibility of $\delta^{18}O_P$ on the interannual timescale is found to be the best among the GCMs when the models are nudged toward reanalysis field.

Chapter 2 also investigates the impact of isotopic fractionation over land. The impact is found to be significantly large for the mean field and the seasonal difference in $\delta^{18}O_p$ over Siberia and North America as Jouzel et al. (1991) have shown before. Since the simulation with the isotopic fractionation over land is more realistic, the continental effect is more realistically reproduced with the process. The isotope ratio in surface vapor and soil water are also better simulated by the model with the process. On the other hand, the interannual variability of the isotope ratio in precipitation or in vapor is not significantly affected by the process. Thus the conventional assumption in which all the land surface fluxes are not accompanied by isotopic fractionation may be legitimate to some extent. However, if one use isotope enabled models to investigate processes close to land surface, or isotopic variability in terrestrial archives, the process has to be taken into account.

The isotope enabled GCMs have been used to disentangle the isotopic variability from daily (Tremoy et al. 2012; Tremoy et al. 2014) to glacial-interglacial (Werner et al. 2000; Lee et al. 2008) timescale. Recently the other direction have emerged in which the simulated isotope-climate relationship is used to reconstruct paleoclimate (Sime et al. 2009; Risi et al. 2010) or use of the isotope ratio to constrain model physical parameters (Risi et al. 2012; 2013). For such studies, the relationships between isotopes and variables have to be well simulated in the model. On the interannual scale, however, large differences in the linear slope between $\delta^{18}O_p$ and temperature and precipitation among models are found. Although this is far beyond the scope of this study, the reason of the difference should be investigated as Conroy et al. (2013) did for the relationship between $\delta^{18}O_P$ and precipitation.

In Chapter 3, forward models for isotopic proxies are evaluated. The proxy models used are Roden et

al. (2000) for $\delta^{18}O$ in tree ring cellulose and Liu et al. (2013; 2014) for that in coral. The forward models were driven by the output of atmospheric GCM equipped with isotopes. As for ice core, the GCM simulated isotope ratio in precipitation is directly compared against observation data. The use of atmospheric GCM simulation nudged toward reanalysis field of 20CR (Compo et al., 2011) makes direct comparison of the simulation with paleoclimate observation possible. The simulation was evaluated on the interannual timescale for 1950-2007 where the reliability of the atmospheric forcing is relatively high. The result shows that the reproducibility for tree-ring cellulose and coral is comparable with that of isotope ratio in precipitation with the metrics of temporal correlation; around 70% of the proxies are well reproduced by the models. Meanwhile, with less than 20% of the proxies reproduced, ice cores exhibited the lowest reproducibility. The reasons for this may be due to relatively poor skill of the GCM over the sampling sites (e.g. Antarctica, Greenland, and Tibet) and deposition noise included in ice core data. Even though the reproducibility is somewhat limited by the quality of the input and/or the poor representation of the proxy models, the models seem to represent the key mechanisms in the proxies, especially for tree-ring cellulose and coral.

Given the reproducibility, the dominant factor for the interannual variability in $\delta^{18}O$ of ice core, coral, and tree-ring cellulose is also investigated using the models. The variability in $\delta^{18}O$ in ice core is found to be modulated by temperature over high latitude and precipitation amount over low latitude. The variability in $\delta^{18}O$ in coral is found to be dominated by sea surface temperature in many basins except for tropical Pacific warm pool, where hydrological balance is dominant. These results are consistent with the previous studies (e.g. Liu et al. 2014). The driver of the variability of $\delta^{18}O$ in tree ring cellulose is investigated globally for the first time in this study. The interannual variability of $\delta^{18}O$ in tree ring cellulose is mainly controlled by relative humidity in mid- to high latitudes, whereas the variability is controlled by multiple factors in low latitudes. This work would work as a reference to look for new sampling site.

In Chapter 4, the feasibility of isotopic data assimilation for paleoclimate reconstruction is examined. Since this is the first challenge to assimilate temporally averaged isotopic information, the isotope ratio in precipitation is assimilated in an idealized way for the sake of simplicity. A data assimilation algorithm based on ensemble Kalman filtering with the modification to assimilate time average data proposed by Steiger et al. (2014) is applied in this study. The results shown are quite promising. By assimilating the isotopic information, the analysis fields of temperature, precipitation, and pressure as well as isotope ratio in precipitation become closer to the truth than the first guess over almost all the globe. The skills for temperature, precipitation, and pressure are especially high over low latitude. The reason is because the isotope ratio in precipitation is largely affected by El Niño-Southern Oscillation (ENSO); indeed the first mode of the isotope ratio in precipitation is confirmed to be ENSO by empirical orthogonal function (EOF) analysis. Although the leading modes confirmed by the EOF analysis are only ENSO and North Atlantic Oscillation (NAO), the analysis reproduced the interannual variability in major climate indices e.g. Southern Annular Mode (SAM), Pacific North American (PNA)

pattern, All Indian Summer Monsoon Rainfall and Sahel Rainfall. Moreover, the results of isotopic data assimilation show comparable or higher performance than the case in which reconstructed temperature is assimilated. Thus, proxy data assimilation is confirmed to work well, and the performance is better than the previous studies of paleoclimate data assimilation.

In Chapter 5, using the models and the assimilation technique developed and evaluated in the previous chapters, the feasibility of proxy data assimilation is examined as a conclusive part of this study. In this chapter, $\delta^{18}O$ in ice core, speleothem, coral, and tree ring cellulose are assimilated into the simulation instead of $\delta^{18}O$ in precipitation. The result of proxy data assimilation remains the same level as that of precipitation isotope data assimilation. The skill is good in low latitudes because of temperature dependency of coral data over there and correlation between ENSO and tree ring cellulose data in Tibet. Given the performance, the real proxy data assimilation is conducted, where the simulation run is constructed from the simulation forced by modeled SST, and the real (observed) proxy data is assimilated into the simulation. Compared with the idealized experiment, the reconstruction skill decreased over Indian Ocean, east Pacific and the Atlantic Ocean where the reproducibility of proxy model is relatively worse. From the results, it is clear that isotope enabled atmospheric GCM and proxy models must be improved more to improve the assimilation skill. Furthermore, since the skill of proxy data assimilation is heavily dependent on the spatial distribution of the proxy data, the skill and the reliability of the product will be improved with more proxies.

The data assimilation algorithm used in this study constructs the ensemble member in a distinct way from the ordinal ensemble Kalman filtering; the ensemble members constitute for individual years from a serial run instead of independent simulations. With this setting, Kalman gain is identical for each year of reconstruction. This may contain two potential problems. The simulation used in the study was the historical simulation for the past 140 years, in which global warming proceeds. Therefore the assumption in the algorithm that the ensemble members distribute Gaussian around the truth may not be satisfied. Secondly the constant Kalman gain cannot describe non-stationarity of the relationship between climate variables and proxies as in the empirical climate reconstructions. Though I noted these points, they are intentionally neglected because the aim of this study is to investigate the feasibility of isotopic data assimilation and for that purpose it is desirable to conduct the test with small computational cost. The ultimate goal of the development of this assimilation system is to provide the best estimate for the past millennium. For that goal, however, these issues should be cleared away. One way to solve those issues is to construct the Kalman in the other way in which the Kalman gain for a reconstruction year is constructed from before and after several tens of years of that reconstruction year. By doing this, conditional change in proxy-climate relation can be considered. Furthermore this construction of ensemble members should assure the normal distribution around the truth (assuming that climate change is not so drastic within the period of ensemble selection).

With improved assimilation algorithm, models and spatiotemporally denser proxies, the proxy data assimilation will provide the best estimate for annually resolved various variables covering the globe

based on both the real information recorded in proxies and the physics represented by model. The reconstructed long-term “reanalysis” will contribute the separation of the forcing induced variability and the internal variability within the period. This will further contribute to constrain the model response to the given forcing, or inversely to get better estimates of past forcing. Furthermore by obtaining the long term internal variability it may be possible to refine the estimate of low frequency disasters.

Appendix A.

Evaluation of MIROC5

The precipitation and river discharge reproducibility of MIROC5 is presented here. The model validated here is a coupled version of MIROC5. The spatial resolution is set to T85.

A.1. Precipitation

The agreement of global mean annual precipitation between the MIROC5 simulation and GPCP precipitation data between 1980 and 1999 was evaluated by the root-mean-square error (RMSE) and the pattern correlation coefficient (R). Global average precipitation was 2.67 mm/day from the GPCP data and 3.20 mm/day from MIROC5. Meanwhile the values produced by the high-resolution (hires) and medium-resolution (medres) versions of MIROC3.2 were 3.10 mm/day and 2.83 mm/day, respectively. The global average RMSE for monthly precipitation compared with GPCP was 1.25 mm/day, which represents an improvement over the RMSE of 1.50 mm/day, which was derived as the multi-model average in the CMIP3 Project (ranging from 1.10–1.99 mm/day, see Nohara et al., 2006). The global land-only RMSE was 1.42 mm/day. MIROC3.2 (hires) and MIROC3.2 (medres) produced values of 1.30 mm/day and 1.17 mm/day respectively. The R value of 0.86 is better than any of the global values obtained by the 19 GCMs used by Nohara et al. (2006, Table 2). The global land-only R values were 0.76, 0.71, and 0.68 by MIROC5, MIROC3.2 (hires), and MIROC3.2 (medres), respectively. Figure A-2 shows (a) the global pattern of the difference in 1980–1999 mean precipitation between the MIROC5 and GPCP values and (b) the corresponding global zonal mean precipitation comparison. Values produced by MIROC3.2 (hires) and MIROC3.2 (medres) are also shown in Figure 2 (b) by dotted and short dashed lines, respectively. These results indicate that MIROC5 overestimated precipitation in central and southern Africa, most of Asia, western and central North America, and western South America. By contrast, MIROC5 underestimated precipitation in the north and west of Europe, southern Asia, and most of the Mississippi and Amazon river basins. Overall the reproducibility of the MIROC5 precipitation is fair to good with the exception of locations close to the equator (north and south of 15 degrees) where large biases can be noted. In addition, compared to MIROC3.2, MIROC5 showed similar or slightly poorer reproducibility of absolute values for the mean state of precipitation. As mentioned by Watanabe et al. (2010), the hydrological cycle simulation appears to be too active in MIROC5. However, spatial variability was better simulated by MIROC5 than by MIROC3.2. Also it should be worthwhile to note that GPCP may include some errors particularly at high-latitudes over land (Adler et al., 2011).

A.2. River discharge

The mean seasonal cycles of simulated 1980–1999 river discharges over the selected 15 large river basins are compared with the corresponding GRDC observations in Figure A-3, with all three ensemble simulations. Discharges were well simulated for the Changjiang and Yenisey River basins. Discharges of the Mekong and Mississippi also appeared to be well simulated, but this may be because biases were cancelled out by the spatial average over a whole basin, considering Figure A-2 (a). Although the simulated peak discharges in the Ganges and Volga basins did not match local observations, the timing of the seasonal cycle of discharge was accurately reproduced. For the Amazon, Columbia, Danube, Ob, and Yukon river basins, however, the timing of simulated peak discharge was shifted forward by one or two months. In addition, the simulated discharge in the Congo, Murray, Nile, and Parana basins showed relatively low reproducibility. Comparison of simulated precipitation with GPCP data (not shown) indicated that the seasonal cycle of precipitation was generally well simulated by MIROC5, and the precipitation simulation had a better quality in general than the corresponding discharge simulation (particularly for the Parana and Murray basins). This suggests that factors other than precipitation (e.g., human activities of water regulation and evaporation from river surface in arid basins) may be the main contributors to the simulation biases of river discharge.

Figure A-4 plots the coefficient of variance (CV) of observed and simulated monthly river discharges (1980–1999). CV is defined as the ratio of the standard deviation to the mean, indicating the model's ability to reproduce the observed interannual variability of streamflow. The CV of simulated discharge agreed well with that produced by the GRDC in the Changjiang, Ganges, Mekong, Yenisey, and Yukon basins, whereas the agreement was relatively poor in the Murray, Nile, and Parana basins.

Table A-1 summarizes the observed and simulated mean river discharge for the 15 river basins and the corresponding relative RMSE (RRMS) between the simulated discharge and observation. The RRMS indicates the extent to which the simulated river discharge deviates from the observed value and is an index of reproducibility, as used by Nohara et al. (2006, Eq. 5). The magnitude of RRMS in Table 1 is very close to that of the multi-model average presented by Nohara et al. (2006, Table 4). Considering that it was not constrained by observed precipitation, the quality of the MIROC5 simulation of global hydrology in this study was considered acceptable for the purpose of evaluating future hydrologic changes following global warming.

Table A-1 Summary of observed and simulated river discharge in 15 global large river basins and the corresponding relative root-mean-square error (RRMS).

River basin	Station	Observation (m^3/s)	Simulation (m^3/s)	RRMS (%)
Amazon	Obidos	169987	111248	50.7
Changjiang	Hankou	22115	27741	50.5
Columbia	Dalles	5252	5294	66.7
Congo	Kinshasa	44931	82117	124.7
Danube	Ceatal Izmail	7894	5819	42.6
Ganges	Farraka	12085	16194	88.3
Mekong	Stung Treng	13239	11703	33.4
Mississippi	Vicksburg	18944	17861	21.3
Murray	Lock 9 upstream	295	2363	763.1
Nile	El Ekhasa	1276	40616	3390.4
Ob	Salekharad	12729	12686	135
Parana	Timbues	17328	34190	220.5
Volga	Volgograd Power Plant	8243	6798	94.6
Yenisey	Igarka	18964	12276	55.3
Yukon	Pilat station	6608	11022	177.1

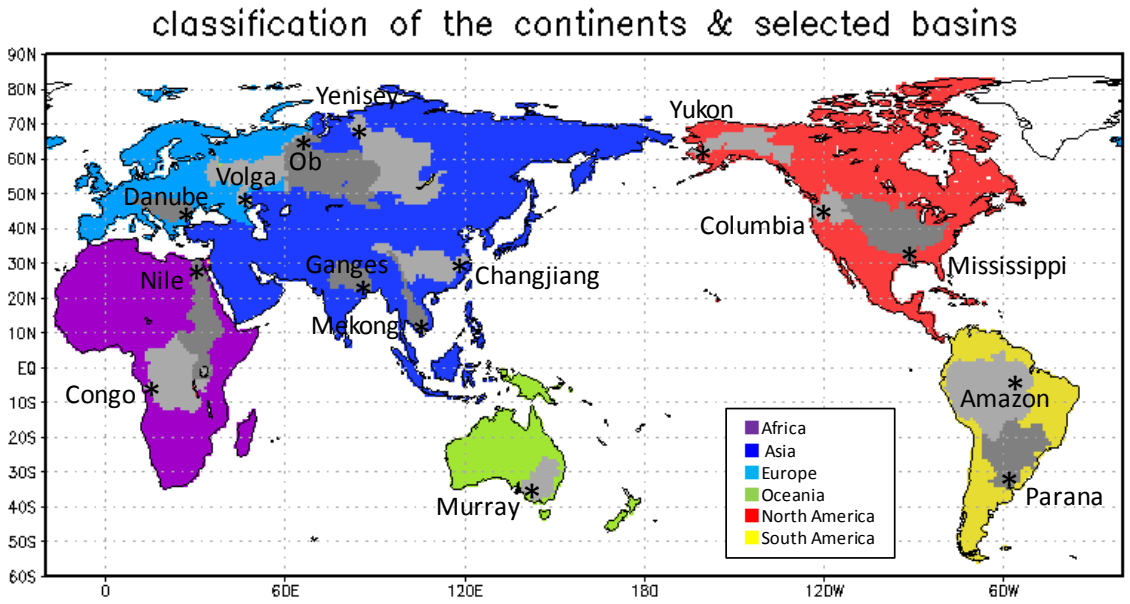

Figure A-1 Classification map of the selected 15 major river basins and continents. The Ob basin belongs to Asia and Volga belongs to Europe. Asterisks indicate the location of the discharge observation.

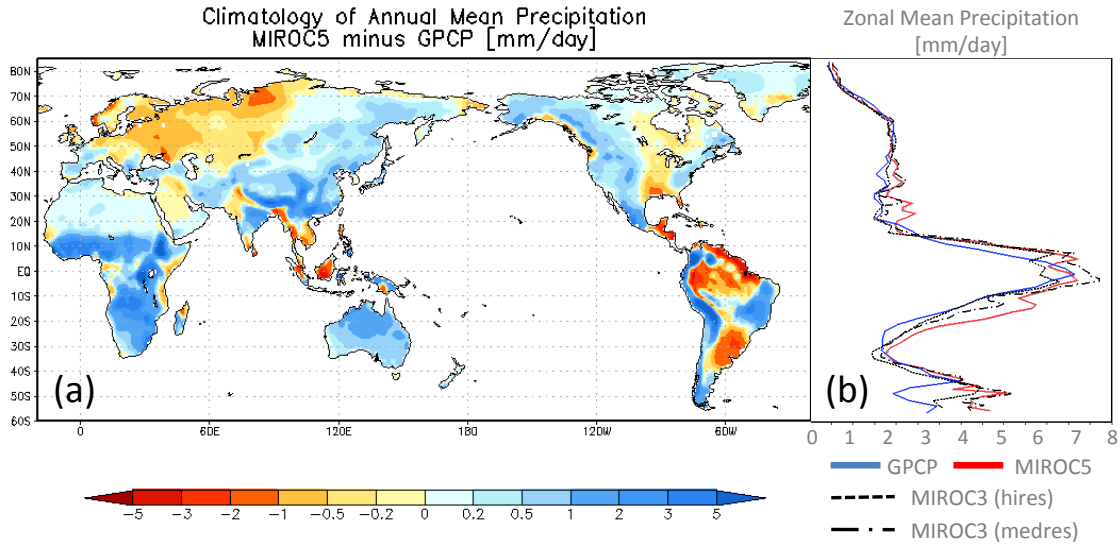

Figure A-2 Climatology of annual mean precipitation (mm/day). (a) Difference between simulated mean precipitation and observed GPCP data. (b) Zonal-mean precipitation simulated by MIROC5 (red) and two versions of MIROC3 (black) simulations and from the GPCP observations (blue).

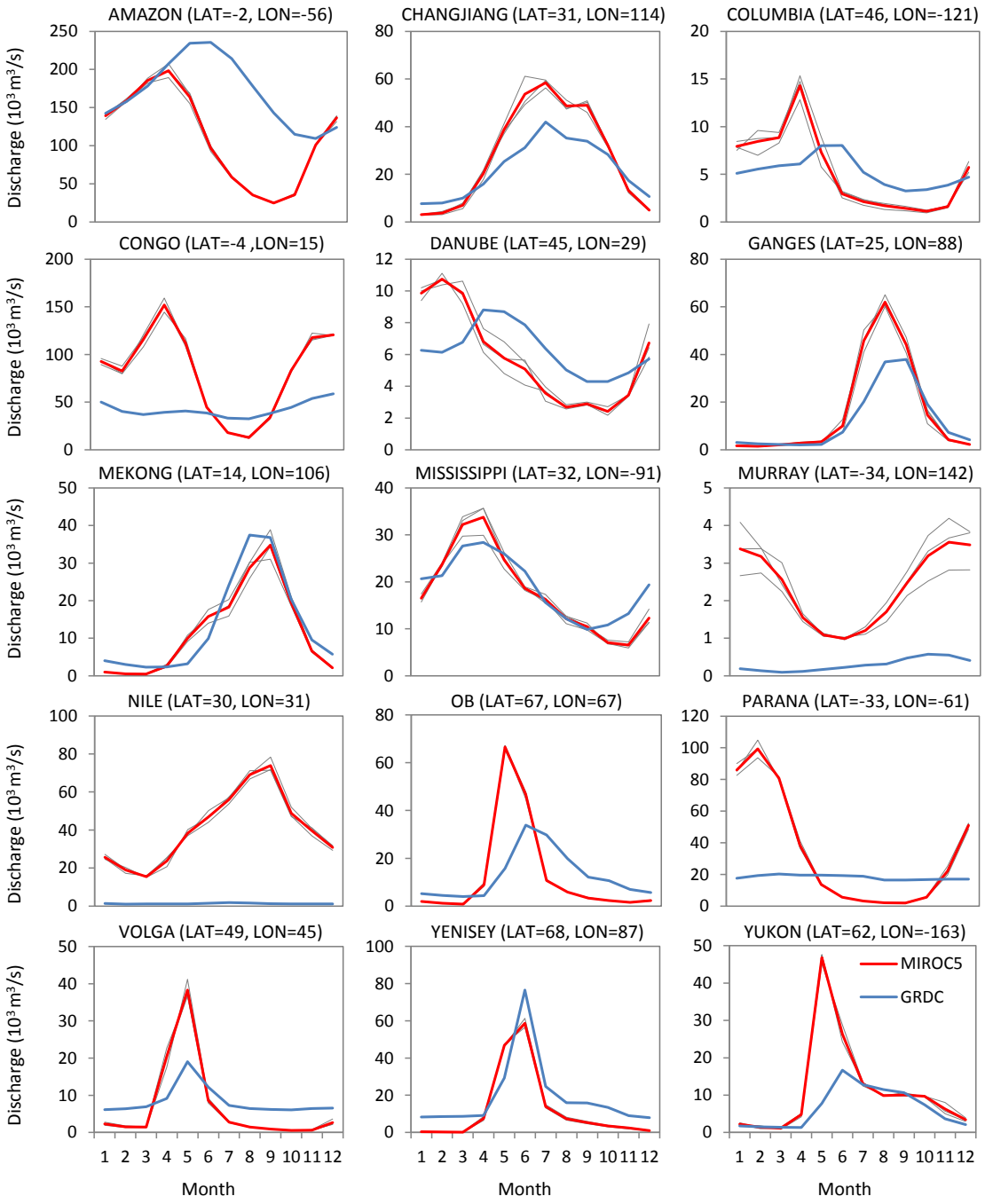

Figure A-3 Comparison of simulated (red) and observed (blue) long-term 1980–1999 average monthly river discharges for the selected 15 large river basins (10^3 m^3/s). Simulations include three ensembles plotted in gray and the ensemble average in red.

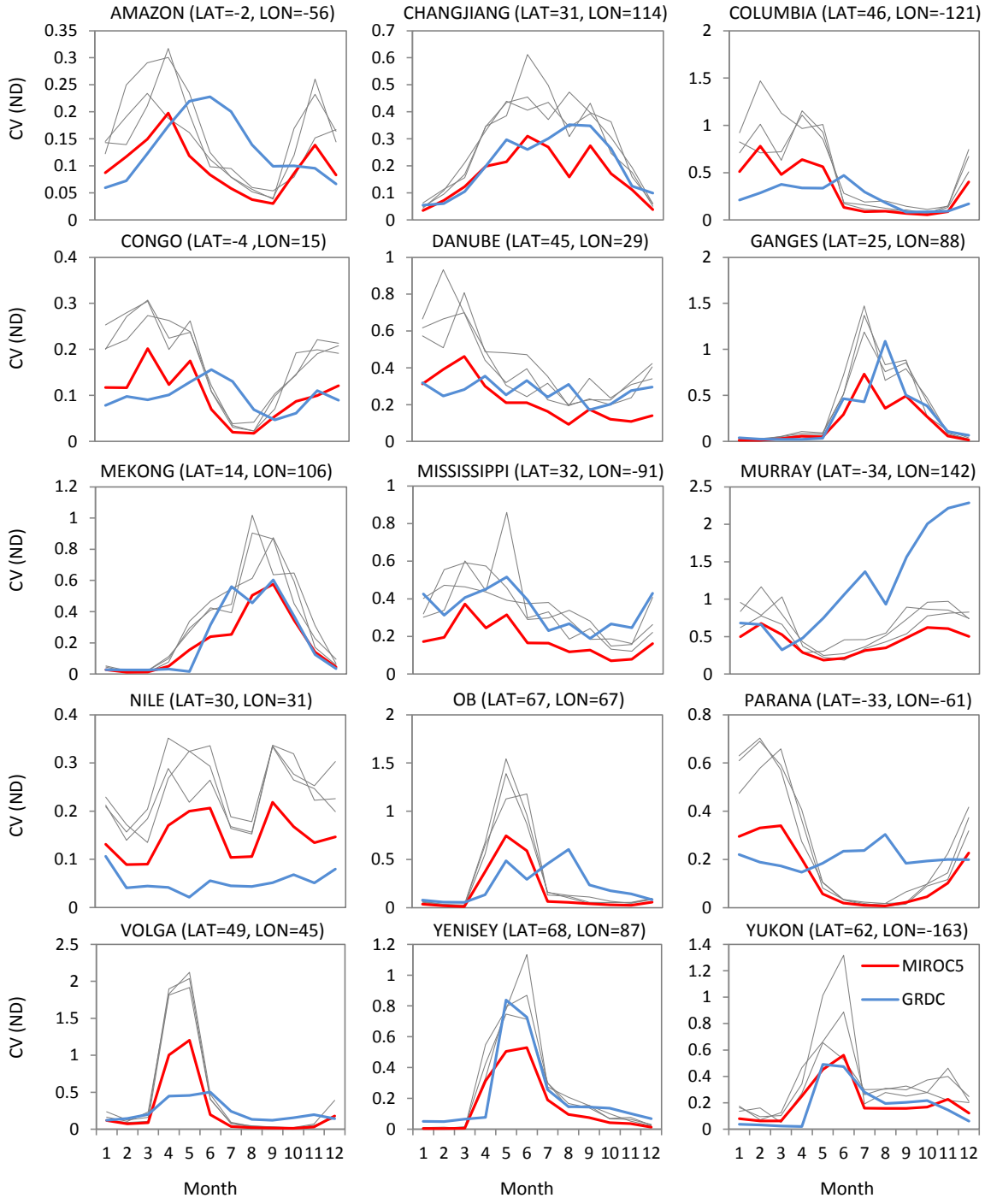

Figure A-4 Comparison of the coefficient of variance (CV) of simulated (red) and observed (blue) long-term (1980–1999) river discharges for the selected 15 large river basins (non-dimensional). Simulations include three ensembles plotted in gray and the ensemble average in red.

Appendix B.

A case study of interannual variability of $\delta^{18}O$ in precipitation over West Africa

B.1. Introduction

The El Niño-Southern Oscillation (ENSO) is the strongest mode of interannual variability in the tropics (Dai et al., 1997) and plays an important role in variability of precipitation, temperature, and circulation patterns on this timescale. El Niño can cause catastrophic floods and droughts (Philander, 1983) and damage to ecosystems (Aronson et al., 2000). A recent study projected an increase in the frequency of extreme El Niño events due to global warming (Cai et al., 2014). Therefore, it is essential to understand the natural variability of ENSO. Stable water isotopes (D, ^{18}O) have been used to infer past and present climate since the work of Dansgaard (1964). Several studies have linked ENSO with isotopic variation in precipitation or in seawater under the present climate (e.g., Schmidt et al., 2007; Yoshimura et al., 2008; Tindall et al., 2009). For example, tropical South America (Vuille and Werner, 2005), Western and Central Pacific (Brown et al., 2006), and the Asian monsoon region (Ishizaki et al., 2012) are identified as having a connection with ENSO, basically through changes in local rainfall or integrated rainfall along the trajectory. However, other regions, such as West Africa, have not yet been investigated in detail.

West Africa receives most precipitation in the monsoon season (July – September; JAS) and is known for its high variability at interannual or longer timescales. The severe drought that hit West Africa during the 1970s and 1980s prompted researchers to study the factors controlling West African rainfall variability at interannual to multidecadal timescales (e.g., Folland et al., 1986; Palmer, 1986; Janicot et al., 1996; Giannni et al., 2003; Shanahan et al., 2009; Mohino et al., 2011a, b). At present, the major role of sea surface temperatures (SST) in driving the variability with land–atmosphere interactions as an amplifier (Giannni et al., 2003) is widely recognized. However, there is still debate regarding the relative importance of the various basins and mechanistic timescales involved (Nicholson, 2013). The Atlantic (Lamb, 1978; Joly and Voldoire, 2010; Mohino et al., 2011a), Pacific (Janicot et al., 2001; Mohino et al., 2011b), Indian Ocean (Palmer et al., 1986), and Mediterranean (Rowell, 2003; Polo et al., 2008) are all

candidates. Among them, the ENSO is thought to modulate the high-frequency component (interannual) of the variability (Ward, 1998; Joly et al., 2007). However, the relationships are not stationary over time; the West African rainfall is correlated with ENSO only after the 1970s (Janicot et al., 2001; Losada et al., 2012), indicating the existence of multiple competing physical mechanisms. How the impact has changed remains an open question.

Several studies used isotopes to understand the water cycle over West Africa at the intraseasonal timescale. Risi et al. (2008b) and Tremoy et al. (2012; 2014) examined the isotopic compositions of precipitation ($\delta^{18}O_P$) and vapor ($\delta^{18}O_v$), respectively, and both found that $\delta^{18}O$ records the spatially and temporally integrated convective activity during the monsoon season. Here δ in per mil units is defined as $(R_{sample}/R_{std}-1) \times 1000$, where R_{std} is VSMOW: Vienna Standard Mean Ocean Water. Risi et al. (2010) confirmed the relation using the LMDZ-iso model and suggested that $\delta^{18}O$ is controlled by convection through rain re-evaporation and the progressive depletion of the vapor by convective mixing along air mass trajectories. The relation between $\delta^{18}O$ and convective activity suggests the possibility of reconstructing the convective activity using a climate proxy, if the relation holds at the interannual timescale. The long record of precipitation should help in determining how SSTs influence precipitation variability. Some studies reconstructed precipitation over West Africa (Lézine and Casanova, 1989; Shanahan et al., 2009). Shanahan et al. (2009) directly tied isotopic composition with the local precipitation. However it is possible that the amount of rainfall along the trajectory has more impact rather than local information, as mentioned above. Therefore it is still necessary to estimate the relative contributions of the main controls on interannual variability of the isotopic composition in more comprehensive way.

In this paper, we explore the factors governing the interannual variability of monsoon season $\delta^{18}O_v$, which is the source of precipitation and controls $\delta^{18}O_p$ variability (Risi et al., 2008a), over West Africa and how the ENSO signal is imprinted. As the observations cover relatively short periods to look into the interannual variability and available variables are limited, we use an isotope-enabled general circulation model (GCM) to complement the observations.

In the following section, the model simulations and the observations are described. In Sect. 3, we compare the simulated and observed variability of $\delta^{18}O$ at daily to interannual timescale. Section 4 investigates the factors controlling $\delta^{18}O_v$ at the interannual timescale by analyzing the simulation results and confirms the role of the identified factors by sensitivity experiments. Finally, we examine the relation between $\delta^{18}O$ and ENSO in Sect. 5.

B.2. Data and methods

B.2.1. Observations

Observation of HDO in vapor from space

Frankenberg et al. (2009) measured column-averaged isotopologue ratio (δD) values in water vapor using the SCanning Imaging Absorption spectroMeter for Atmospheric CHartographY (SCIAMACHY) onboard the European research satellite ENVISAT. We used the updated and extended version of this dataset from Scheepmaker et al. (2014), covering the years 2003 – 2007. As measured δD is weighted by the H_2O concentration at all heights, it is largely determined by the isotopic abundance in the lowest tropospheric layers, where most water vapor resides. The footprint of each measurement is 120 km (across-track) × 30 km (along-track). We apply the following selection criteria concerning the retrievals (Scheepmaker et al., 2014):

- Retrieved H_2O total column must be at least 70% of the a priori value.
- The CH_4 column in the same retrieval window must be at least within 10% of the a priori value.
- Root-mean-square variation of the spectral residuals must be below 5%.
- Convergence achieved in a maximum of four iteration steps.

Here, the first two criteria restrict large deviations from the a priori H_2O and CH_4 columns, which are normally the result of light scattering by clouds. Therefore, these two criteria function as a simple cloud filter. Due to high detector noise of SCIAMACHY in the short-wave infrared channels, the single measurement noise (1-sigma) is typically 40‰ – 100‰, depending on total water column, surface albedo, and viewing geometry. For the region of our study, however, the mean single measurement noise is of the order of 20‰ – 50‰, due to the high albedo and optimal viewing geometry of West Africa. This random error can be further reduced by averaging multiple measurements. Therefore, we average the measurements according to the procedure of Yoshimura et al. (2011); we averaged multiple measurements that were collected in a grid of 2.5° × 2.5° in 6 h. We set the threshold value for averaging to 10, meaning that the average of the SCIAMACHY measurements in every grid cell is based on at least 10 measurements taken within 6 h. From the IsoGSM simulation results, the times of the nearest satellite measurements were extracted (hereafter the process is called "collocation"). Thus, there was no difference in representativeness between the model and the satellite data.

In situ measurement of water isotopologues in vapor

To assess the performance of the model at shorter timescales, daily $\delta^{18}O_v$ from Tremoy et al. (2012)

was used in this study. The $\delta^{18}O_v$ was observed at about 8 m above the ground using a Picarro laser instrument (L1102-i model) with an accuracy of ± 0.25‰ at the Institut des Radio-Isotopes in Niamey, Niger (IRI, 13.31°N 2.06°E, 218 m.a.s.l) from 2 July 2010 to 12 May 2011.

In situ measurement of isotopes in precipitation (GNIP)

Observations of the monthly isotope ratio in precipitation over West Africa were obtained from the Global Network for Isotopes in Precipitation (GNIP) observational database (IAEA/WMO, 2014). We chose 28 GNIP stations in Africa that have full annual data spanning more than 10 years. The observatory location and its operation period are summarized in Table B-1.

B.2.2. Isotope-enabled General Circulation Model simulation

The Isotope-incorporated Global Spectral Model (IsoGSM) is an atmospheric GCM, into which stable water isotopes are incorporated. The model uses T62 horizontal resolution (about 200 km) and 28 vertical levels, and temporal resolution of the output is 6h. The convection scheme is the Relaxed Arakawa-Schubert Scheme (Moorthi and Suarez, 1992). The main time integration scheme is leapfrog scheme. The model is spectrally nudged toward wind and temperature fields from the National Centers for Environmental Prediction (NCEP)/Department of Energy (DOE) Reanalysis 2 (R2) (Kanamitsu et al., 2002) in addition to being forced with prescribed SST and sea ice from NCEP analysis, which are the same as the one used in NCEP/DOE R2 (Kanamitsu et al., 2002). After a spin-up period of about 10 years with the constant 1979 forcing, the simulation was run from 1979 to 2012 as in Yoshimura et al. (2008). Isotope processes were incorporated following Joussaume et al. (1984): Isotopic fractionation takes place whenever phase transition occurs. Most fractionation can be assumed to occur at thermodynamic equilibrium, except for three particular cases; surface evaporation form open water; condensation from vapor to ice in supersaturation conditions under -20 deg-C; and evaporation and isotopic exchange from liquid raindrop into unsaturated air. IsoGSM assumes no fractionation when water evapotranspires over land. More details of the model configurations were described previously (Yoshimura et al., 2008). The general reproducibility of the model for daily to interannual time scales is well evaluated by comparing with precipitation isotope ratio (Yoshimura et al., 2008) and vapor isotopologue ratio from satellite measurements (Yoshimura et al., 2011), and showed sufficiently accurate results for various process studies (e.g., Berkelhammer et al., 2012; Liu et al., 2013; Liu et al., 2014).

In addition to the standard experiment (Std) mentioned above, we carried out two sensitivity experiments. The first of these experiments examined the sensitivity of the results to the "equilibrium fraction ε," which is the degree to which falling rain droplets equilibrate with the surroundings. Risi et al. (2010) reported the importance of re-evaporation for $\delta^{18}O_v$ over West Africa, and Yoshimura et al. (2011) found an improved simulation result with the changed parameter. Following Yoshimura et al. (2011), we set this value to 10%, while in the standard simulation it was set to 45%. The other sensitivity experiment

was to estimate the contributions to interannual variability in $\delta^{18}O_v$ of the distillation effect during transportation from the source regions. In this experiment, we removed the influences of the distillation processes by turning off isotopic fractionation during condensation and re-evaporation from raindrops and preventing isotopic exchange between falling raindrops and the surrounding vapor. Note that these effects were switched off only in a certain region in the simulation. For a similar purpose, Ishizaki et al. (2012) specified transport pathways and then removed these effects along the pathway. We chose a different means of removing the effects in a certain domain, as we wished to specify the area that plays an important role in controlling the isotopic variation at a point. Hereafter, we refer to the former sensitivity experiment as the "E10" experiment and the latter as the "NoFrac" experiment. Std and NoFrac cover the 1979 – 2012 period, and E10 covers the 2010 – 2011 period. The simulation results used in this study are basically from Std unless otherwise noted.

We use both δD and $\delta^{18}O$ in the evaluation of the model, since SCIAMACHY observes δD whereas Tremoy et al. (2012) observes $\delta^{18}O$. As δD and $\delta^{18}O$ basically respond to meteorological factors in the same way, there are no differences in underlying mechanisms to produce changes. Therefore, there is no problem using the combination of δD and $\delta^{18}O$ to evaluate model performance. In the other section we consistently use $\delta^{18}O$.

B.2.3. **Isoflux analysis**

Isoflux analysis specifies the contributions of advection, evapotranspiration, and precipitation to the changes in the isotopic composition of precipitable water in an atmospheric column. The concept of the analysis is based on budget analysis. Using such analysis, Lai et al. (2006) specifies the factors controlling $\delta^{18}O_v$ in a canopy layer. Worden et al. (2007) found the importance of re-evaporation from raindrops. Here, we developed the mass balance equation for ^{18}O in the atmospheric column. The mass balance for total precipitable water inside the atmospheric column can be written as:

$$\frac{dW}{dt} = -\nabla \cdot Q + E - P \quad (1)$$

where W represents the total precipitable water, Q is the vertically integrated two-dimensional vapor flux vector, E is evapotranspiration, and P is precipitation. The term $\nabla \cdot Q$ denotes the horizontal divergence of vapor flux. Here, we refer to this term as advection. A mass balance equation can also be written for ^{18}O in the same manner as Eq. (1).

$$\frac{dR_W W}{dt} = -\nabla \cdot R_W Q + R_E E - R_P P \quad (2)$$

where R_W, R_E, and R_P represent the isotope ratio ($^{18}O/^{16}O$) of precipitable water, evapotranspiration, and precipitation, respectively. Multiplying Eq. (1) by R_W, and subtracting that from Eq. (2) we obtain:

$$\frac{dR_W}{dt} W = -\nabla R_W \cdot Q + (R_E - R_W)E - (R_P - R_W)P . \quad (3)$$

Dividing by the R_{std}, we can rewrite Eq. (3) in δ notation as:

$$\frac{d\delta_W}{dt}W = -\nabla\delta_W \cdot Q + (\delta_E - \delta_W)E - (\delta_P - \delta_W)P \,. \quad (4)$$

Starting from the left, the terms represent the temporal derivative of the isotopic composition of precipitable water, the effect of advection, evapotranspiration, and precipitation to deplete or enrich the precipitable water, respectively. As the analysis specifies the contribution of each factor to the change in isotopic composition of precipitable water, the analysis period should start before initiation of isotopic depletion and end at the most depleted point. We use the 6h output of IsoGSM to calculate each term in Eq. (4), then each term is averaged over the targeting period and compared.

B.3. Evaluation of IsoGSM

B.3.1. Evaluation of IsoGSM at the mean state and seasonal climatology

The annual mean climatology of the SCIAMACHY data and the collocated IsoGSM fields together with precipitable water by JRA25 (Onogi et al., 2007) and the model are shown in Figure B-1. In the SCIAMACHY data, the meridional gradient over West Africa is notable; the lowest values of δD were found in the Sahara and the highest in the Guinea coast. This is due to the dry and therefore HDO-depleted air mass from the subsiding branch of the Hadley circulation in the dry season over the Sahara and strong evaporation and/or recycling of water in the Tropics (Frankenberg et al., 2009). IsoGSM simulates this spatial pattern qualitatively well. Although the average is negatively biased (about 20‰) (Yoshimura et al., 2011) and the latitudinal gradient is weaker in IsoGSM, bias and overestimated gradient is found in SCIAMACHY when compared with ground-based Fourier-Transform Spectrometers (Scheepmaker et al., 2014). Accordingly we cannot conclude such differences from the satellite is indeed problematic or not at this stage.

Figure B-2 shows time–latitude diagrams of δD and precipitable water averaged on 5°W – 5°E from 2003 to 2007. Over the region, vapor δD is high and wet in the monsoon season and low in the dry season. In the monsoon season, the wet and isotopically heavy vapor comes from the south along with the monsoon flow. The northern end of the flow coincides with the location of the Inter-Tropical Discontinuity (ITD), which limits the extension of the monsoon flow (Janicot et al., 2008). In the dry season, the subsiding branch of the Hadley cell brings a dry and depleted air mass to the north of the area (Frankenberg et al., 2009). Around 10°N, δD has two minima; one in winter reflecting the depleting effect of subsidence, and the other in summer reflecting the depleting effect of convective activity (Risi et al., 2010). The model captures these two regimes and the depleting effect of convective activity around 10°N in the monsoon season. Pearson product moment correlation coefficient (hereafter we use the term "correlation" unless otherwise noted) between the observed and simulated zonally averaged δD (5°W-5°E) is 0.77 (significance level: $P < 0.001$). Note that the range is widely different between them (–

300‰ – 0‰ for SCIAMACHY; –190‰ – 90‰ for IsoGSM). This may be because IsoGSM misses the enrichment in boreal summer over tropical Africa, as suggested in previous studies (Frankenberg et al., 2009; Yoshimura et al., 2011). The bias in the mean field (Risi et al., 2010; Werner et al., 2011; Lee et al., 2012) and the underestimated seasonality (Risi et al., 2010) are also common in other GCMs. Again, the bias in SCIAMACHY has been indicated as well (Scheepmaker et al., 2014), and Risi et al. (2010) pointed out the possibility that SCIAMACHY may overestimate the variability by preferentially sampling high altitudes.

Then we compared the simulated $\delta^{18}O_v$ with in situ measurement from Tremoy et al. (2012) in Niamey grid point over the 2010 – 2011 period. Figure B-3 shows the time series of near surface daily $\delta^{18}O_v$ from the observation and IsoGSM, and the statistics are summarized in Table B-2. Note that only the days for which observations were available were used to calculate the statistics. These measurements also showed the two isotopic minima of the year (W-shape); the first in August and September, and the second in January associated with the convective activity and large scale subsidence respectively. The model nicely captures the two minima and simulates well the average and variability, especially in the dry season. On the other hand, the model reveals rather poor reproducibility of day-to-day variation during the monsoon season; the depletion and variability were both overestimated. In the sensitivity experiment E10, the average and standard deviation (-14.9‰ and 1.8‰ respectively for monsoon season) were comparable with the observation (-15.2‰ and 1.8‰), and the correlation was slightly improved. Although this does not fully explain the discrepancy, it implies that the parameter controlling the equilibrium fraction ε can be problematic. The positive points are that the $\delta^{18}O_v$ and precipitation averaged over previous days showed a strong correlation ($R < 0.6$) southwest of Niamey as in the observation (Fig. S3 in Tremoy et al., 2012), which means that the relation between convective activity and the $\delta^{18}O_v$ is well represented, and that the comparable time evolution at the monthly scale (thick lines in Figure B-3). The seasonal differences were similar, suggesting that SCIAMACHY may overestimate the seasonal variability.

B.3.2. **Evaluation of IsoGSM at the interannual scale**

Finally we evaluate the reproducibility of IsoGSM at the interannual scale. Although our target is the isotope ratio of near-surface water vapor, we use the isotope ratio of precipitation to validate the model reproducibility of surface vapor isotope at the interannual timescale. The reason is twofold; one is the lack of observations of vapor isotope covering several years. The other one is the fact that the isotopic composition of the precipitation is strongly constrained by that of the local lower tropospheric vapor (Risi et al., 2008a). Hence the precipitation isotope somewhat represents surface vapor isotope, and can be used to evaluate the reproducibility of vapor isotope, even though they are not identical.

Figure B-4 compares the modeled and observed time series of annual mean $\delta^{18}O_P$ at Niamey. Note that there are missing observations from 2000 to 2008, and after 2010. The correlation between them is 0.74 ($P < 0.05$). The simulated (observed) annual average is –4.6‰ (–4.1‰) and standard deviation is 1.2‰

(1.1‰). The factors controlling the variability will be discussed in Sect. 4.

B.3.3. **Overview of IsoGSM evaluation**

To summarize the evaluation results, the spatial pattern in the mean state, and the seasonal pattern driven by the Hadley circulation, monsoon flow, and convective activity are qualitatively well simulated with an emphasis on reproducibility of the interannual variability. When compared with SCIAMACHY measurements of δD, there is a slight bias in the mean state, and IsoGSM largely underestimates the seasonal δD variations. When compared with the in situ measurements, the bias and variation difference are not as large as when compared with SCIAMACHY. Although the results of the simulation in the monsoon season are not as good as those of the dry season at the daily scale, IsoGSM captures the monthly scale variability fairly well. These results suggest that the model is applicable to study the interannual variability of $\delta^{18}O$ during the monsoon season.

B.4. Simulated interannual variability of vapor isotope

B.4.1. **General features of interannual variability**

In this section, we explore the interannual variability of $\delta^{18}O_v$ over Niamey by the standard experiment. The simulation period is from 1979 to 2012. The most striking feature of the interannual variability is that the depletion in the monsoon season does not appear every year in the model (Figure B-4 and Figure B-5). In contrast, $\delta^{18}O_v$ depletion occurs each winter. We term the years with isotopic depletion in the monsoon season the "W-shape year" following Tremoy et al. (2012). To understand the factors controlling the interannual variability of $\delta^{18}O_v$, it is necessary to investigate the differences between the years with and without depletion. For the purpose of comparison, we set the criteria and made two composite fields: W-shape year composite and non-W-shape (NW-shape) year composite. The quantitative definition of a W-shape year is a year in which the surface vapor isotope value averaged over JAS in Niamey is 1σ (1.1‰) less than that of the climatological average (–12.9‰). We picked out six W-shape years (1988, 1999, 2009, 2010, 2011, and 2012) in the period, and the rest are appointed to the NW-shape composite. The seasonal variations in surface $\delta^{18}O_v$ in the two composite fields are shown in Figure B-5.

Here, we briefly discuss the features of the W-shape years. Figure B-6 and Figure B-7 show the two composite fields and their differences (W-shape years minus NW-shape years) in the monsoon season. W-shape years are characterized by enhanced monsoon activity; the velocities of southwesterly winds over West Africa are higher (Figure B-6l), and latitudes south of 10°N receive a larger amount of precipitation, especially on the Guinean coast and the West and East Sahel (Figure B-6f). Due to the larger amount of precipitation, the level of evapotranspiration is also higher (Figure B-6i), and hence wetter conditions prevail (Figure B-6c) in W-shape years. The $\delta^{18}O_v$ is more depleted, as expected, centering on Niamey (Figure B-7c). The isotopic compositions of precipitation and evapotranspiration

are also more depleted south of Niamey (Figure B-7f, i).

B.4.2. **Factors controlling $\delta^{18}O_v$ at interannual timescales**

To identify the mechanism responsible for the difference in isotopic variability between W shape and NW shape years, isoflux analysis was applied to both composite fields. Here we analyze precipitable water instead of surface vapor for two reasons: first is for the sake of simplicity. By analyzing precipitable water, we do not have to consider at what height condensation and re-evaporation take place, or the effect of vertical advection; and second, most of the atmospheric water resides near the surface, and therefore the isotopic composition of precipitable water should be useful as a proxy for surface $\delta^{18}O_v$. This kind of alternation is also seen is Tremoy et al. (2012). As the analysis specifies the contribution of each factor to the change in isotopic composition of precipitable water, the analysis period should start before the initiation of isotopic depletion and end at the most depleted point. Since the seasonal variation in the isotopic composition of precipitable water is almost the same as the surface $\delta^{18}O_v$ (Figure B-5), the analysis period was June-August to capture the decrease in isotopic composition of precipitable water.

Figure B-8 shows the results for the two composite fields at the Niamey gridcell. First, we discuss how each factor contributes to the δ_W variation in general. Precipitation lowers δ_W, which is reasonable when considering the Rayleigh distillation model. That is, δ_P is greater than δ_W; therefore, the effect of precipitation is always negative, and contributes to lowering δ_W. Evapotranspiration works in the opposite way. As the model does not take fractionation into account on the land surface, δ_E can be assumed to be a mixture of all precipitation (Yoshimura et al., 2008). Hence, δ_E is presumably larger than δ_W by the same analogy used to explain the effect of precipitation, and contributes to the increase in δ_W. The impact of advection in this form in Eq. (4) seems weaker compared with the other terms. However, the impact is the temporally averaged value. Given that the advection sometimes lowers the δ_W and sometimes enriches δ_W, the fact that the averaged value is very low does not readily imply that the impact itself is small. Therefore we further decompose the effect of advection in Eq. (4) into:

$$\nabla \delta_W \cdot Q = \frac{\partial \delta_W}{\partial y} Q_N + \frac{\partial \delta_W}{\partial y} Q_S + \frac{\partial \delta_W}{\partial x} Q_E + \frac{\partial \delta_W}{\partial x} Q_W \quad (5)$$

where Q_N, Q_S, Q_E, and Q_W, represent the vertically integrated two-dimensional vapor flux vector from the north, south, east, and west, respectively. In this form, the impact of advection becomes clearer (Figure B-8b); southerly flow decreases δ_W, and easterly flow increases δ_W. The precipitation area in the south of Niamey which produces isotopically light moisture is considered to contribute decreases δ_W. While there is relatively less precipitated area in the east of Niamey, which should produce isotopically heavier moisture compared with the southern part, contributing to increase δ_W (Figure B-6). The impacts of the westerly flow and northerly flow are ambiguous and negligible.

The $(d\delta_W/dt)W$ is low in W-shape years ($P < 0.05$). Precipitation further lowers δ_W and evapotranspiration further increases δ_W in W-shape years reflecting the larger amounts of precipitation

and evapotranspiration. Although the differences between the impacts of the two composite fields are large, they are not significant because of the high degree of variation. The only term significantly different at 5% significance level other than $(d\delta_W/dt)W$ is the impact of the southerly flow. When regressed with JAS averaged surface $\delta^{18}O_v$ at the interannual timescale, the term that shows a strong correlation ($P < 0.05$) is the southerly flow alone. This suggests that the monsoon flow brings depleted moisture produced by heavier precipitation to the Niamey area, controlling the interannual variability of $\delta^{18}O_v$. The interannual regression field of JAS averaged precipitation against Niamey surface $\delta^{18}O_v$ shows the correlation at the Guinea Coast (10°W – 10°E, EQ – 10°N; Figure B-9). This indicates the relative importance of the distillation process during transport, as compared to local precipitation for the interannual variability of $\delta^{18}O_v$ in West Africa.

In this regard, the correlation between $\delta^{18}O_v$ and precipitation east of Niamey, which is also located in the upstream region of Niamey, is expected to be strong, because heavier precipitation falls in the East Sahel in W-shape years and the African Easterly Jet (AEJ) flows toward the Niamey region at heights above 800 hPa. The correlation for this region east of Niamey, however, is relatively weak ($|R| < 0.4$). As the southerly flow is dominant in the lower atmosphere (1000 – 800 hPa) in the monsoon season, the relatively weak connection between surface $\delta^{18}O_v$ and precipitation east of Niamey is reasonable.

B.4.3. **Sensitivity experiment**

To confirm the contributions of the amount of precipitation that falls at the Guinea Coast to the interannual variability in $\delta^{18}O_v$ at Niamey, we carried out the sensitivity experiment, NoFrac, in which we removed the influence of the distillation process in the Guinea Coast (10°W – 10°E, EQ – 10°N). As shown in Figure B-4, most of the interannual variability in $\delta^{18}O_v$ at Niamey was removed. In the standard experiment, the average $\delta^{18}O_v$ and the variance at Niamey are –12.9‰ and 1.16, respectively, whereas they are –11.7‰ and 0.15, respectively, in NoFrac. The enriched average and considerably smaller variance in NoFrac confirm the key role of the Guinea Coast precipitation in controlling the interannual variability of $\delta^{18}O_v$ at Niamey. In addition, we conducted other sensitivity experiments that were the same as the sensitivity experiment NoFrac but for East Sahel (10°E – 30°E, 10°N – 20°N) and Niamey (10°E – 14°E, 11°N – 15°N). Neither of these experiments showed a significant difference from the standard experiment (data not shown): the average and variance were –12.8‰ (–12.8‰) and 1.07 (1.15), respectively, for East Sahel (Niamey). These results exclude the impact of precipitation in East Sahel or Niamey in controlling the interannual variability, and enhance the robustness of our hypothesis.

B.5. Relationship with ENSO

West African rainfall in the monsoon season has been connected to ENSO (e.g., Janicot et al., 2001; Joly et al., 2007; Losada et al., 2012); i.e., less precipitation during El Niño and more precipitation during

La Niña. Given this connection, a relation between $\delta^{18}O_v$ and ENSO through precipitation change is expected. Indeed, three of six W-shape years (1988, 1999, and 2010) fell during a La Niña period. Therefore, we regressed JAS $\delta^{18}O_v$ from the model and annually averaged the NINO3 index calculated from the NCEP SST analysis, which was used to force the model. High positive correlations were found in all of West Africa (Figure B-10a). The spatial distribution of the correlation between the annual average of $\delta^{18}O_p$ weighted by monthly precipitation, and the annual averaged NINO3 index was almost identical to the former, but the correlated area over West Africa was confined to south of 15°N (Figure B-10b). To validate this relation, we also show the relation between observed $\delta^{18}O_p$ from GNIP and the NINO3 index. The correlation pattern agreed well with GNIP over most of Africa; the highest positive correlation was in West Africa, a weak negative correlation was seen in the south of Central and East Africa, and a weak positive correlation was found in South Africa (Figure B-10c). All of the figures indicate that $\delta^{18}O$ is significantly lower (higher) during the cold (warm) phase of ENSO over West Africa. The relation between $\delta^{18}O$ in West Africa and ENSO is evident from the figures. The relation results from the relation between $\delta^{18}O$ and West African precipitation, as discussed in Sect. 4, and between the precipitation and ENSO. This mechanism is also found in the Asian and South American monsoon regions: ENSO governs precipitation and the precipitation determines the interannual variability of the isotopic composition over the downstream regions (Vuille and Werner, 2005; Ishizaki et al., 2012).

ENSO is not the only mode affecting West African rainfall (Janicot et al., 2001); Global Warming, inter-decadal Pacific Oscillation (IPO), and Atlantic Multidecadal Oscillation (AMO) are found to have significant impact (Mohino et al., 2011a) as well. Therefore, a non-stationary relation between West African rainfall and ENSO (Janicot et al., 1996; Losada et al. 2012) has been reported, but this lies beyond the scope of the present study. Here, we wish to emphasize that we confirmed the statistical relation between rainfall at the Guinea Coast and ENSO, in both observations (Global Precipitation Climatology Project: GPCP (Huffman et al., 2009)) ($R = –0.43$, $P < 0.05$) and the model ($R = –0.45$, $P < 0.05$) during the period 1979 – 2012. Losada et al. (2012) also showed that this relation became significant after the 1970s. Hence, we ensured the robustness of the relation between the isotope ratio in surface vapor, precipitation, and ENSO over West Africa.

B.6. Conclusion and perspective

Here, we presented the interannual variability of $\delta^{18}O_v$ in West Africa and its relation to ENSO using the nudged IsoGSM model (Yoshimura et al., 2008). Our simulation indicated that the isotopic depletion in the monsoon season, which was reported by Risi et al. (2010) and Tremoy et al. (2012), does not occur every year. The main driver of the depletion was found to be precipitation at the Guinea Coast. Second, we found a relation between $\delta^{18}O$ over West Africa and ENSO; ENSO modulates the interannual variability of $\delta^{18}O$ via precipitation at the Guinea Coast.

We showed the ability of the model to simulate intraseasonal to interannual time scale variability, but

the model performed relatively poorly on the daily scale. The parameter controlling the equilibrium fraction ε is suggested to be problematic. Another possibility is the lack of isotopic fractionation over the land surface. Risi et al. (2013) demonstrated the importance of continental recycling and sensitivity to model parameters that modulate evapotranspiration over West Africa. They indicated the importance of taking land surface fractionation into account. As IsoGSM assumes that isotopic fractionation does not occur over the land surface, coupling with more sophisticated land surface models would allow more accurate simulations. Similarly, an atmosphere–ocean-coupled model with stable isotopes is desirable to determine how ENSO impacts isotope ratio above water more clearly.

One of the expected roles of isotope-enabled GCMs is to find "hot spots"; i.e., places at which a climate proxy is sensitive to climate change, for climate reconstruction. Here, we propose that $\delta^{18}O$ at Niamey may be a good proxy of West African rainfall and its relation to ENSO. Indeed, we found a good correlation between the simulated $\delta^{18}O$ and a climate proxy from Ghana, which has a signal of ENSO (Shanahan et al., 2009) for their overlapping period ($R = 0.65$, $P < 0.01$). Despite the strong correlation, however, ENSO is certainly not the single mode modulating $\delta^{18}O$ in the area. In our simulation, the last four years were counted as W-shape years in which surface $\delta^{18}O_v$ was lower at Niamey and precipitation over West Africa was higher, even though not all of these were La Niña years. This may reflect the recent La Niña-like trend associated with the hiatus (Kosaka and Xie, 2013; England et al., 2014), supporting the impact of Interdecadal Pacific Oscillation (IPO) on West African rainfall on a multidecadal timescale (Mohino et al., 2011a). On the other hand, Shanahan et al. (2009) reconstructed West African rainfall variability from the sediments of a lake in Ghana, supporting the suggestion that Atlantic SST controls the multidecadal variability. Further comparisons with in situ observations and climate proxies would be of interest.

This study confirms the relation between West African rainfall and isotopic variability at the interannual time scale, which enables us to reconstruct detailed West African rainfall and, this should help disentangle the non-stationarity of the impact of various SST basins on West Africa rainfall.

Table B-1 Locations and operational periods of the GNIP observatories used in this study

Station Name	Latitude	Longitude	Operation Period
Tunis	36°50'N	10°14'E	1967-2006
Algiers	36°47'N	3°03'E	1998-2006
Sfax	34°43'N	10°41'E	1992-2008
Fes Sais	33°58'N	4°59'W	1994-2008
Sidi Barrani	31°38'N	25°57'E	1978-2003
Bamako	13°42'N	8°00'W	1962-2007
Niamey	13°29'N	2°05'E	1992-2009
N'djamena	12°08'N	15°02'E	1960-1995
Addis Ababa	9°00'N	38°44'E	1961-2009
Sao Tome	0°23'N	6°43'E	1962-1976
Entebbe	0°03'N	32°27'E	1960-2006
Kinshasa	4°22'S	15°15'E	1961-1972
Diego Garcia Island	7°19'S	72°26'E	1962-2003
Dar Es Salaam	6°53'S	39°12'E	1960-1976
Ascension Island	7°55'S	14°25'W	1961-2009
Malange	9°33'S	16°22'E	1969-1983
Ndola	13°00'S	28°39'E	1968-2009
Menongue	14°40'S	17°42'E	1969-1983
St. Helena	15°58'S	5°42'E	1962-1975
Harare	17°48'S	31°01'W	1960-2003
Antananarivo	18°54'S	47°32'E	1961-1975
Saint Denis	20°54'S	55°29'E	2001-2009
Windhoek	22°57'S	17°09'E	1961-2001
Pretoria	25°43'S	28°10'E	1958-2001
Malan	33°58'S	18°36'E	1961-2009
Cape Town	33°57'S	18°28'E	1995-2008
Gough Island	40°21'S	9°53'W	1960-2009
Marion Island	46°53'S	37°52'E	1961-2009

Table B-2 Averages, standard deviations, their differences (simulations minus observations) and correlation coefficients for the simulations and observations from the 2010 to 2011 time series. *P < 0.05.

		Ave. [‰]			S.D. [‰]			Cor.
		Sim.	Obs.	Diff.	Sim.	Obs.	Diff.	
Std.	whole period	-14.6	-13.7	0.9	2.2	2.1	0.1	0.46*
	monsoon season	-16.1	-15.2	0.9	2.3	1.8	0.5	0.16
	dry season	-14.7	-15.0	-0.3	1.7	1.6	0.1	0.63*
E10	whole period	-13.9		-0.2	1.7		-0.4	0.46*
	monsoon season	-14.9		-0.3	1.8		0.0	0.20
	dry season	-15.2		-0.2	1.7		0.1	0.64*

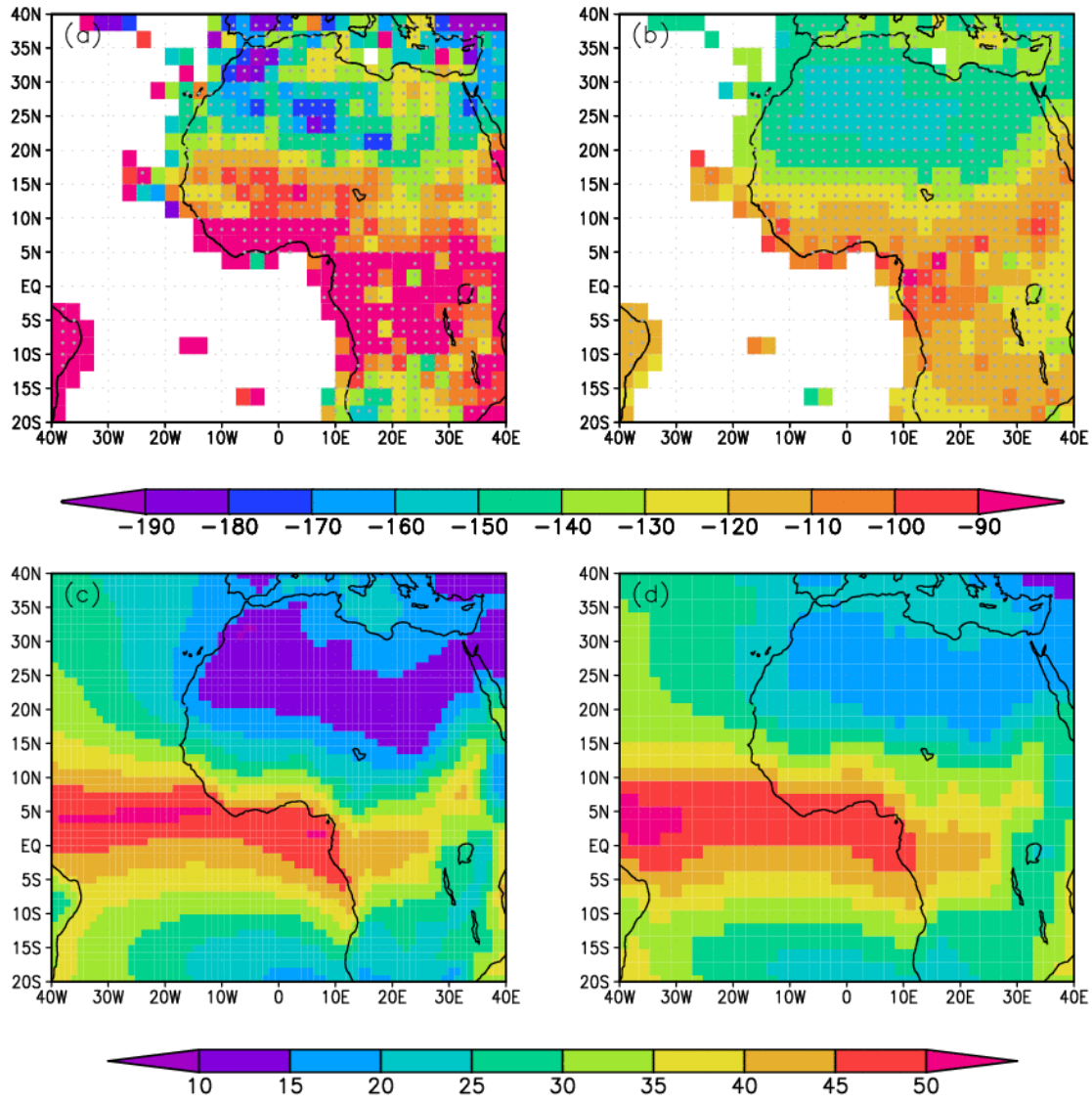

Figure B-1 Annual mean δD (‰) in column vapor by (a) SCIAMACHY and (b) collocated IsoGSM. Regions in which the measurements did not pass the retrieval criteria were left blank. The shaded grid with dots represents the mean value of the average, which consists of at least 10 measurements within every 6h. Annual mean precipitable water (kg/m2) by (c) JRA25 and (d) IsoGSM is also shown.

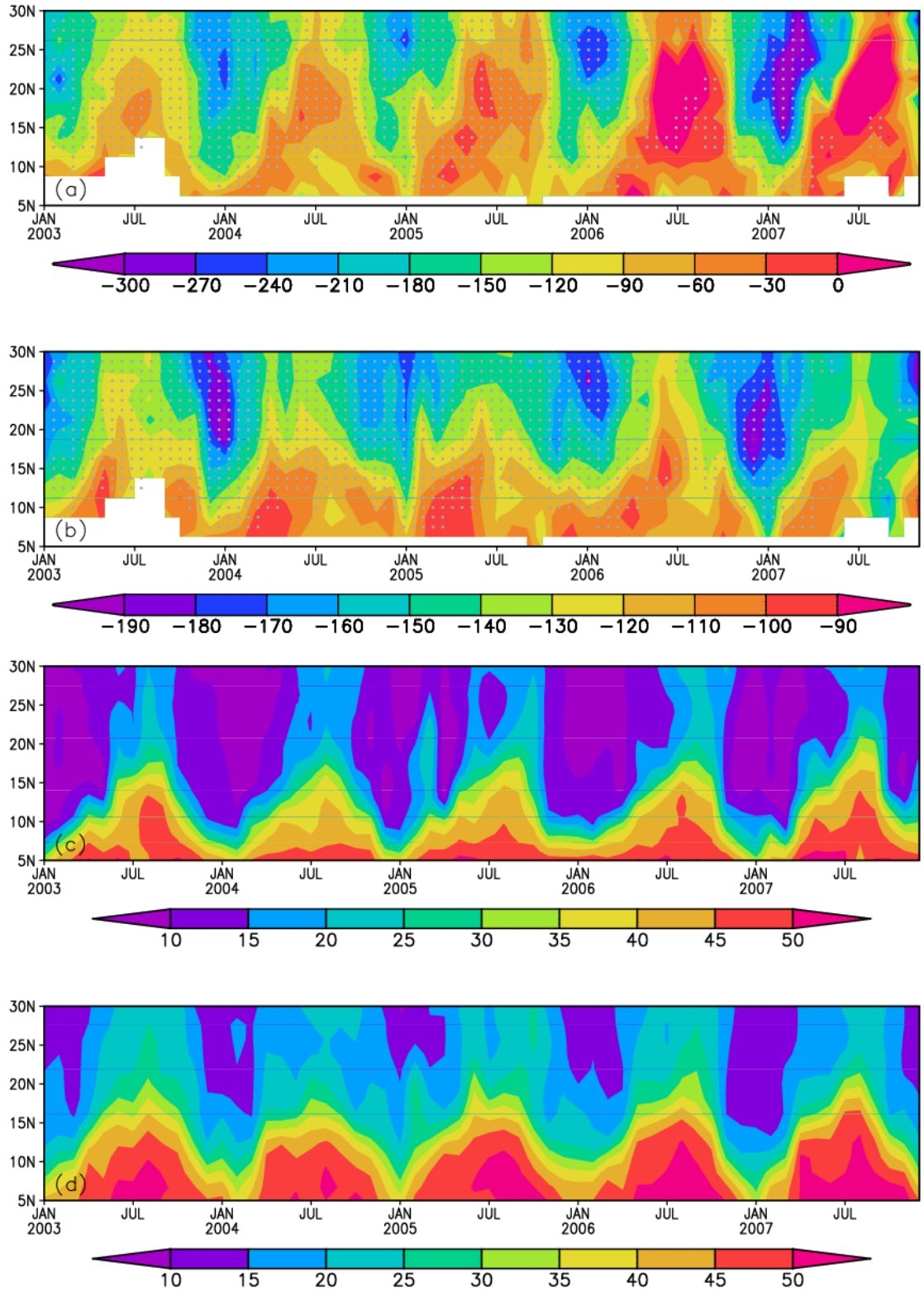

Figure B-2 Time–latitude diagrams of δD (‰) in column vapor averaged over 5°W – 5°E from 2003 to 2007 by (a) SCIAMACHY and (b) collocated IsoGSM. Regions in which the measurements did not pass the retrieval criteria are left blank. The shaded grid with dots represents the mean value of the average,

which consists of at least 10 measurements within every 6h. Same as in (a-b) but for precipitable water (kg/m2) by (c) JRA25 and (d) IsoGSM is also shown.

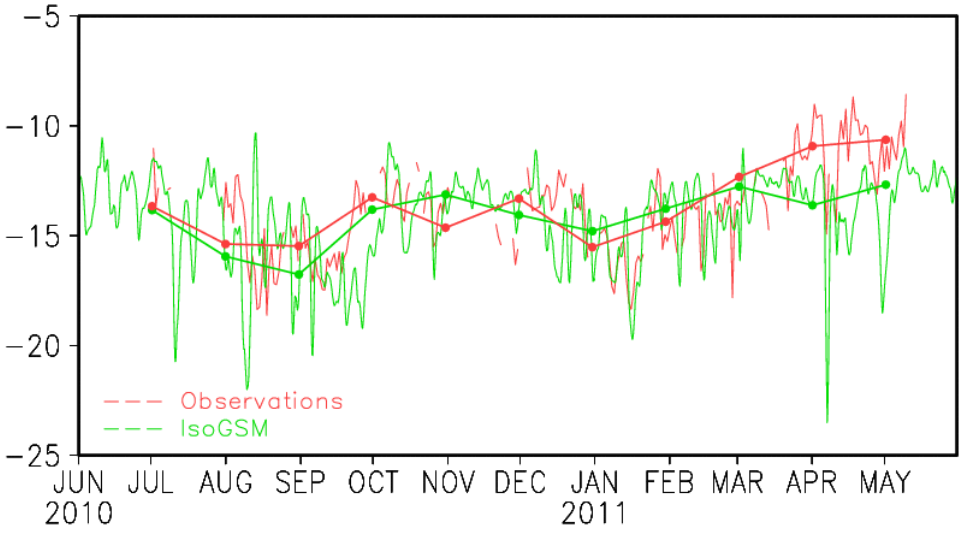

Figure B-3 Temporal evolution from June 2010 to May 2011 of near-surface δ^{18}Ov (‰): the thin red and green lines are the daily averaged observations and model values, respectively. The thick red and green lines connected by dots are the monthly averaged observations and model values, respectively.

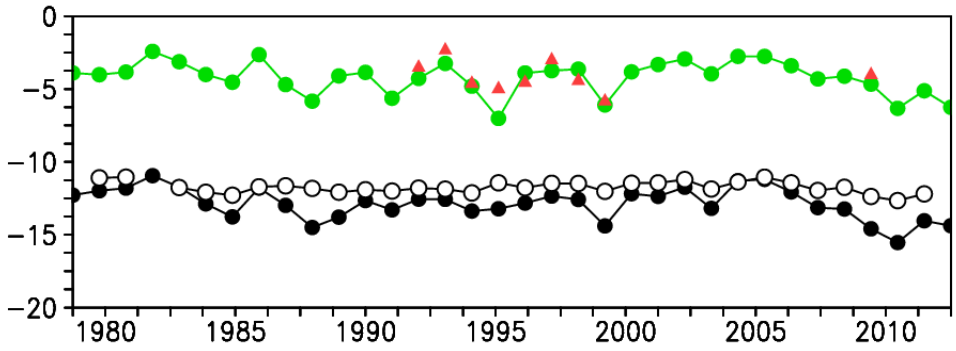

Figure B-4 Interannual variability of annual mean δ^{18}Op (‰) at Niamey by the standard experiment (green) and by GNIP observation (red), together with that of near-surface δ^{18}Ov (‰) during JAS at Niamey by the standard experiment (black) and the sensitivity experiment NoFrac (white).

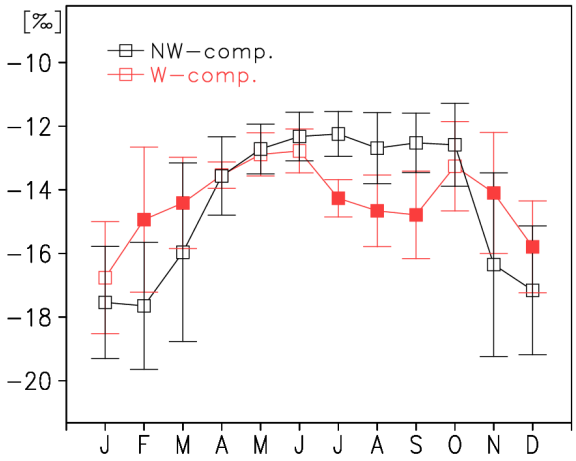

Figure B-5 Seasonal variation of surface δ^{18}Ov (‰) in W-shape years (red) and NW-shape years (black). Bars denote the interannual standard deviations for each month of the two composite fields. Closed red squares indicate that the monthly δ^{18}Ov in the W-shape year differs significantly from NW-shape year ($P < 0.05$).

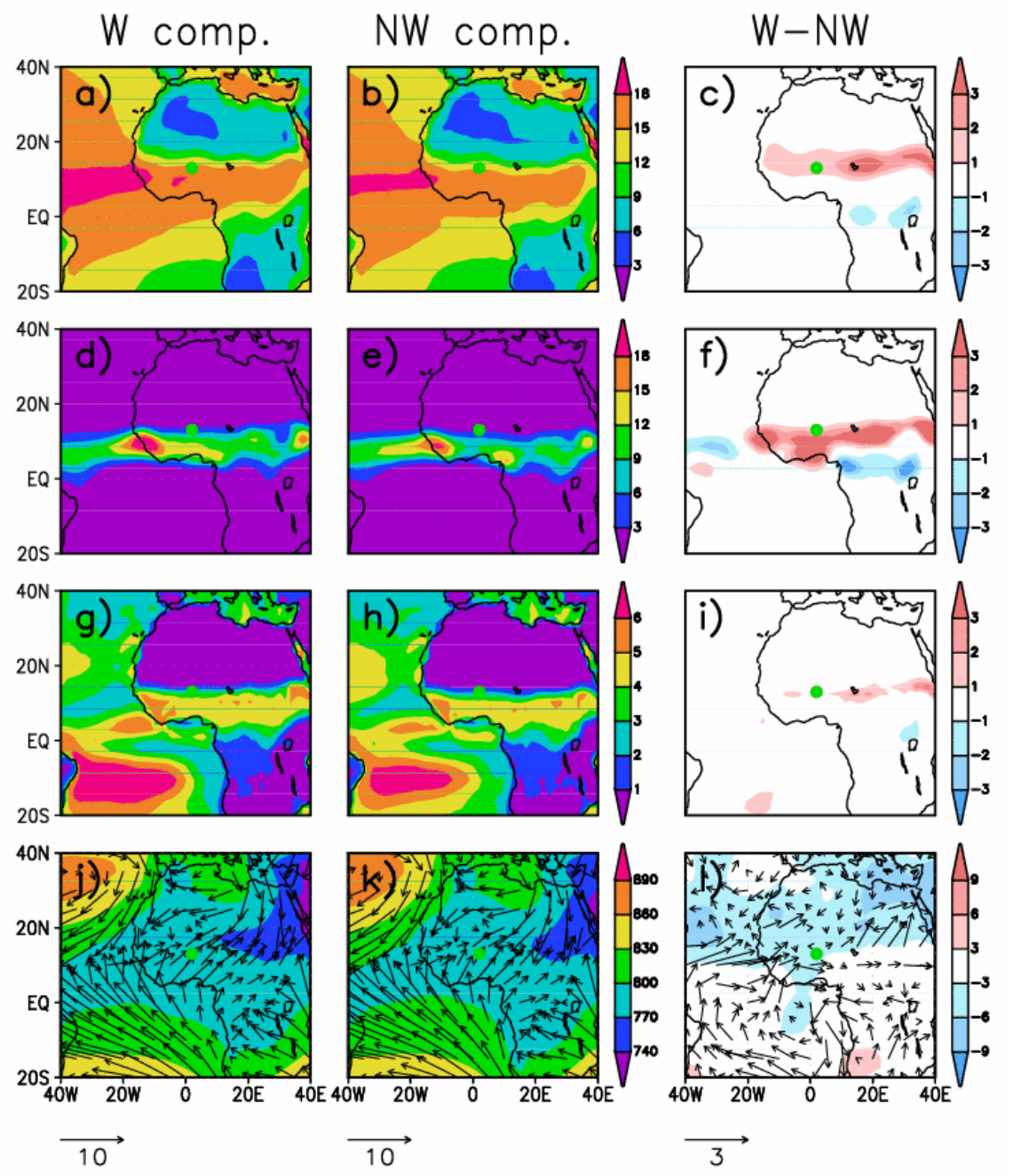

Figure B-6 JAS average of 2 m height specific humidity (g/kg) (a) in W-shape years, (b) in NW-shape years, and (c) the difference between them. (d – f) Same as in (a – c) but for precipitation (mm/day). (g – i) Same as in (a – c) but for evapotranspiration (mm/day). (j – l) Same as in (a-c) but for geopotential height at 925 hPa (gpm). Vectors denote wind at 925 hPa.

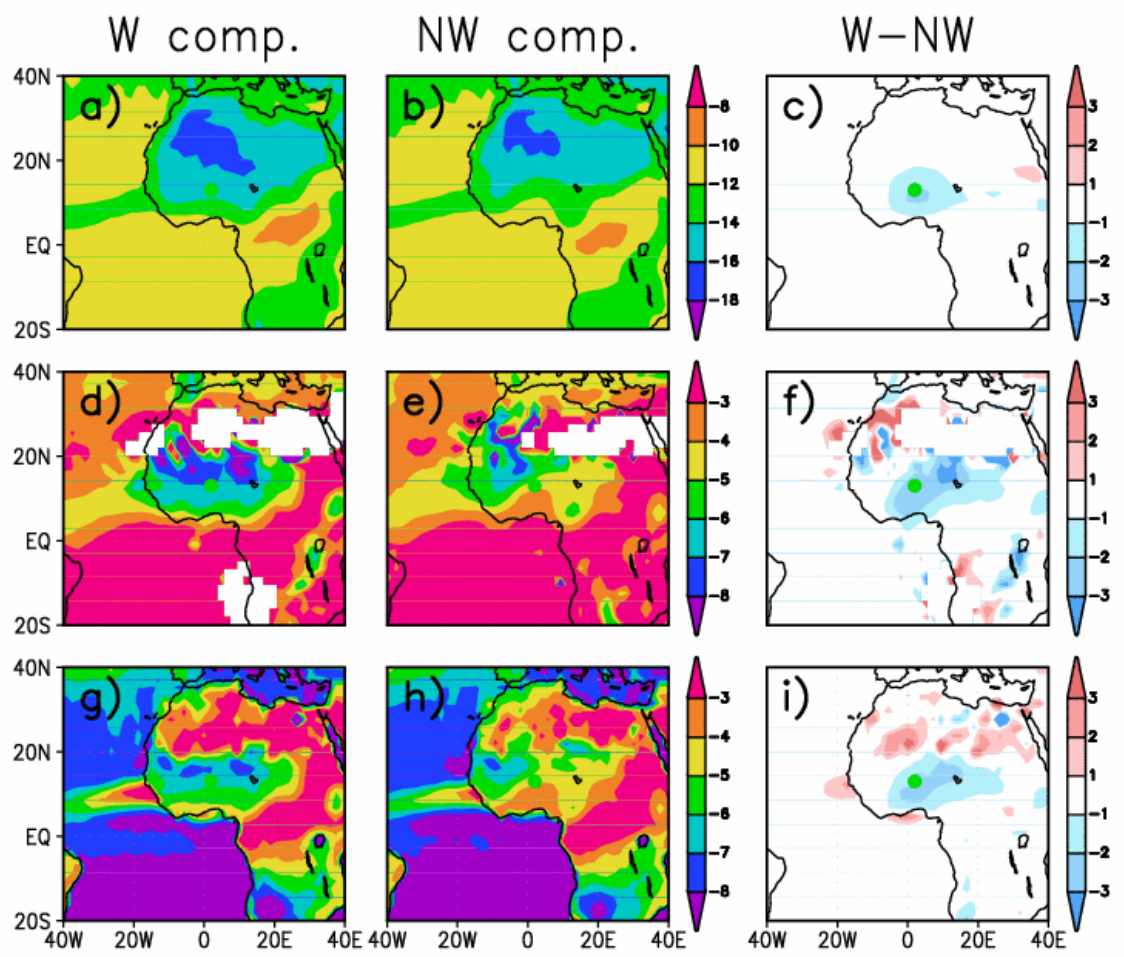

Figure B-7 JAS average of isotopic composition of 2 m height vapor (‰) (a) in W-shape years, (b) in NW-shape years, and (c) the difference between them. (d – f) Same as in (a – c) but for isotopic composition of precipitation (‰). (g – i) Same as in (a – c) but for isotopic composition in evapotranspiration (‰).

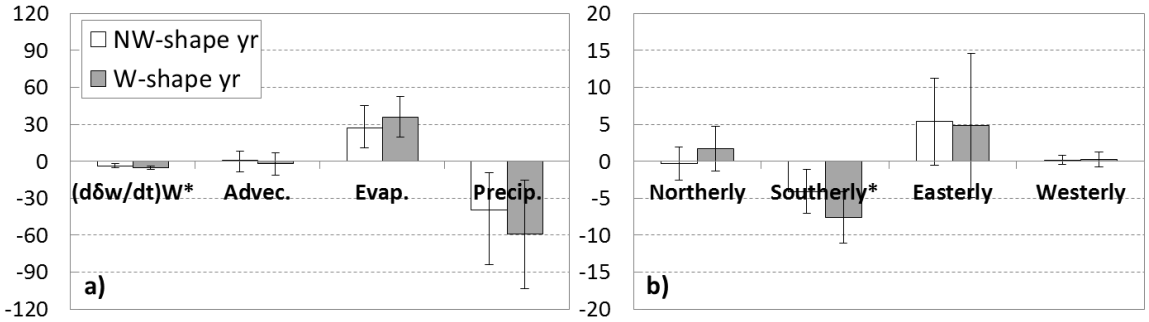

Figure B-8 (a) Temporal derivative of isotopic composition in precipitable water during JJA and the contributions of advection, evapotranspiration, and precipitation to the vapor isotope change in NW-shape years (white) and W-shape years (gray) (‰ mm/day). (b) Same as in (a), but for the decomposed terms of the advection isoflux (‰ mm/day). *P < 0.05 between two composites.

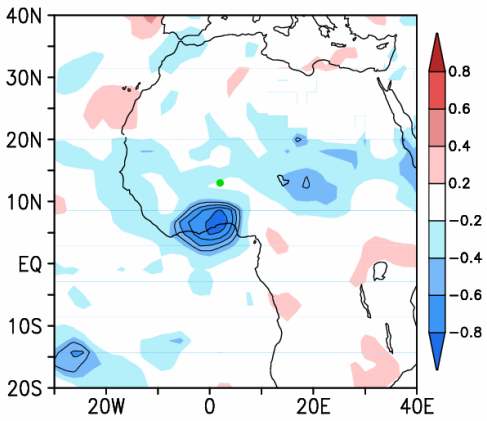

Figure B-9 Correlation coefficient between JAS averaged δ^{18}Ov at Niamey (green dot) and precipitation. The contoured area represents statistical significance (P < 0.01).

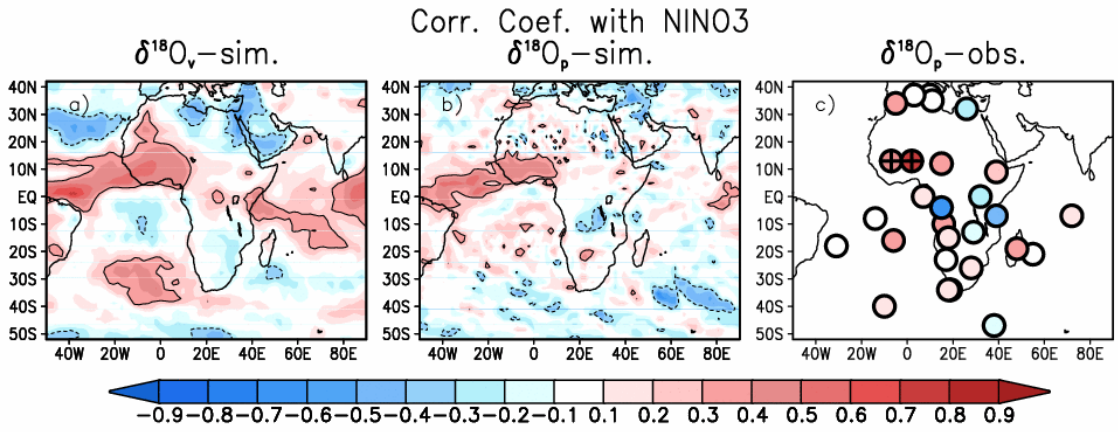

Figure B-10 Correlation coefficient between annual averaged NINO3 index and a) simulated July – September averaged vapor isotope, b) annual averaged simulated precipitation isotope weighted by monthly precipitation, and c) annual averaged observed precipitation isotope weighted by monthly precipitation. Regions with significant positive (negative) correlations at the 90% confidence level are circled with solid (dotted) lines in a) and b). Sites with significant correlations at the 90% confidence level are indicated by crosses in c).

Appendix C.

List of proxies

Latitude	Longitude	Site	Archive	Reference
80.7	-73.1	Agassiz	ice core	Fisher, et al. (1995)
80.7	-73.1	Agassiz	ice core	Fisher, et al. (1995)
80.7	-73.1	Agassiz	ice core	Fisher, et al. (1995)
80.7	-73.1	Agassiz	ice core	Fisher, et al. (1995)
80.7	-73.1	Agassiz	ice core	Vinther et al. (2008)
80	-41.1374	B21	ice core	Schwater and Matthias (2000)
79.8333	24.0167	Austfonna	ice core	Isaksson et al., (2005)
78.8647	17.425	Lomonosovfonna	ice core	Isaksson et al., (2005)
77.17	-61.13	CampCentury	ice core	Johnsen et al. (1972)
76.617	-36.4033	B18	ice core	Schwater and Matthias (2000)
75.1	-42.32	NGRIP	ice core	Vinther et al. (2006)
75	-89	Devon	ice core	Fisher, et al. (1983)
73.9402	-37.6299	B16	ice core	Schwager, Matthias (2000):
72.58	-37.64	GRIP 89-2	ice core	Vinther et al. (2010)
72.1	-38.08	GISP2	ice core	Grootes and Stuiver (1997)
71.28	-37.93	Summit	ice core	Langway et al. (1985)
71	-40	crete	ice core	Clausen et al. (1988)
71	-40	site A	ice core	Clausen et al. (1988)
71	-40	site B	ice core	Clausen et al. (1988)
71	-40	site C	ice core	Clausen et al. (1988)
71	-40	site D	ice core	Clausen et al. (1988)
71	-40	site E	ice core	Clausen et al. (1988)
71	-40	site F	ice core	Clausen et al. (1988)
71	-40	site G	ice core	Clausen et al. (1988)
71	-40	site H	ice core	Clausen et al. (1988)
71	-40	site I	ice core	Clausen et al. (1988)
71	-40	site J	ice core	Clausen et al. (1988)
71	-40	site K	ice core	Clausen et al. (1988)
71	-40	site L	ice core	Clausen et al. (1988)
68.4	-133.8	Mackenzie	tree-ring cellulose	Porter et al. (2014)
67.5273	-36.0615	Das2	ice core	Pedro et al. (2012)
65.18	-43.83	DYE-3 79	ice core	Vinther et al. (2010)
60.615	-140.515	Mt.Logan	ice core	Moore et al. (2002)
60.52	-139.47	Eclipse	ice core	Yalcin et al. (2003)
54.25	-70.77	HM1	tree-ring cellulose	Begin et al. (2015)
51.49	-1.04	Mapledurham	tree-ring cellulose	Young et al. (2015)
49.8167	86.5667	Blukha	ice core	Okamoto et al. (2011)

47.2	7.5	N.Swiss	tree-ring cellulose	Saurer et al. (2012)
46.4	7.8	Alps.Swiss	tree-ring cellulose	Saurer et al. (2012)
46.4	8.7	S.Swiss	tree-ring cellulose	Saurer et al. (2012)
45.7333	0.3	Braconne	tree-ring cellulose	Labuhn et al. (2014)
41.9667	77.9167	Gregoriev	ice core	Takeuchi et al. (2014)
39.7	140.3	Akita-A	tree-ring cellulose	Nakatsuka (in prep)
39.7	140.3	Akita-B	tree-ring cellulose	Nakatsuka (in prep)
38.8	-105	Almagre	tree-ring cellulose	Berkelhammer et al. (2012)
38.2833	75.1	Muztagata	ice core	Tian et al. (2006)
38.1	96.4083	Dunde	ice core	Takeuchi et al. (2009)
35.9	74.9333	Ram-high	tree-ring cellulose	Treydte et al. (2006)
33.5772	91.1765	Galadaindong	ice core	ShiChang et al. (2007)
32.0167	102.617	Hongyuan	tree-ring cellulose	Xu et al. (2012)
32	-64	Bermuda	coral	Goodkin et al. (2008)
31.8167	99.1	Lhamcoka	tree-ring cellulose	Wernicke et al. (2015)
30.43	-82.25	Louise-early	tree-ring cellulose	Labotka et al. (2015)
30.43	-82.25	Louise-late	tree-ring cellulose	Labotka et al. (2015)
30.3083	91.5167	Reting	tree-ring cellulose	Griesinger et al. (2011)
29.87	95.55	Bomi	tree-ring cellulose	Shi et al. (2012)
29.85	81.9333	Humla	tree-ring cellulose	Sano et al. (2012)
29.4333	96.4833	Ranwu	tree-ring cellulose	Liu et al. (2013)
28.3833	85.7167	Dasuopu	ice core	Thompson et al. (2000)
28.1667	85.1833	C.Nepal	tree-ring cellulose	Sano et al. (in prep)
28.0167	86.95	Rongbuk	ice core	Ming et al. (2008)
27.9833	90	Wache	tree-ring cellulose	Sano et al. (2013)
27.9833	86.9167	Rongbuk	ice core	Shugui et al. (2003)
27.1059	142.194	ogasawara	coral	Felis et al. (2009)
25.85	116.37	Fujan	tree-ring cellulose	Xu et al. (2013)
21.6667	104.1	MCC	tree-ring cellulose	Sano et al. (2012)
20.2833	103.917	PL	tree-ring cellulose	Xu et al. (2013)
19.3	98	Pai Wlidlife Sanctuary	tree-ring cellulose	Xu et al. (2015)
19.0833	82.3333	Jag04	tree-ring	Managave et al. (2011)

			cellulose	
19.05	82.05	Jag03	tree-ring cellulose	Managave et al. (2011)
17.3069	-87.8011	Turneffe Atoll	coral	Carilli et al. (2013)
16.76	-22.8883	Pedra de Lume	coral	Moses et al. (2006)
16.2	-61.49	guadaloupe	coral	Linsley et al. (2000)
13.5982	144.836	guam	coral	Asami et al. (2004)
11.77	-66.75	losroques	coral	Hetzinger et al. (2008)
11.1667	-60.85	Buccoo	coral	Moses and Swart (2006)
10.3	-109.22	clipperton	coral	Linsley et al. (2000)
10.3	-109.22	clippterton	coral	Linsley et al. (2000)
10.3	-109.22	clippterton	coral	Linsley et al. (2000)
10.3	-109.22	clippterton	coral	Linsley et al. (2000)
7.4064	134.435	palau	coral	Osborne et al. (2013)
7.2859	134.25	palau	coral	Osborne et al. (2013)
7.2859	134.25	palau	coral	Osborne et al. (2013)
7.2708	134.384	palau	coral	Osborne et al. (2013)
7.2708	134.384	palau	coral	Osborne et al. (2013)
5.88333	-162.083	palmyra	coral	Cobb et al. (2001)
5.88333	-162.833	palmyra	coral	Nurhati et al. (2011)
5.87	-162.13	palmyra	coral	Cobb et al. (2003)
5.87	-162.13	palmyra	coral	Cobb et al. (2001)
3.85	-159.35	fanning	coral	Cobb et al. (2001)
2	-157.3	kiritimati	coral	Evans et al. (1998)
1.86667	-157.4	christmas	coral	Cobb et al. (2001)
1.86667	-157.4	christmas	coral	Cobb et al. (2013)
1	173	maiana	coral	Urban et al. (2000)
1	172	Tarawa	coral	Cole et al. (1993)
1	172	Tarawa	coral	Cole et al. (1993)
-0.40867	-91.234	urvina	coral	Dunbar et al. (1994)
-0.5	166	nauru	coral	Guilderson and Schrag (1999)
-0.66667	-89.1667	punta pitt	coral	Shen et al. (1992)
-5.44	71.7643	chagos	coral	Pfeiffer et al. (2004)
-7	52.75	Alphonse Atoll	coral	Levy et al. (2006)
-9	-77.5	Huascaran	ice core	Thompson et al. (1995)
-12.6	-69.2	Puerto Maldonado	tree-ring cellulose	Ballantyne et al. (2011)
-12.65	45.1	mayotte	coral	Zinke et al. (2008)
-12.65	45.1	mayotte	coral	Zinke et al. (2009)
-13.9333	-70.8333	Quelccaya	ice core	Thompson et al. (2013)
-16.8167	179.233	Savusavu	coral	Bagnato et al. (2004)
-16.8167	179.233	Savusavu	coral	Bagnato et al. (2004)
-17.5	-149.833	moorea	coral	Boiseau et al. (1999)
-21.23	-159.82	Rarotonga	coral	Linsley et al. (2006)
-22	-66	Volcan Granada	tree-ring cellulose	Ballantyne et al. (2011)
-22.1	153	abraham	coral	Druffel et al. (1993)
-22.48	166.47	Amedee	coral	Quin et al. (1998)
-22.85	118.617	Kirijini	tree-ring cellulose	Cullen et al. (2007)

-23.143	43.583	ifaty	coral	Zinke et al. (2004)
-28.4617	113.768	abrolhos	coral	Kuhnert et al. (1999)
-66.7667	112.8	Law Dome	ice core	Pedro et al. (2012)
-66.78	112.82	Law Dome	ice core	Schneider et al. (2006)
-70.86	11.54	DML	ice core	Thamban et al. (2006)
-73.59	-70.36	Gomez	ice core	Thomas et al. (2009)
-75.92	-84.25	Siple	ice core	Schneider et al. (2006)
-77.06	-89.14	ITASE 01-5	ice core	Schneider et al. (2008)
-77.515	167.676	Erebus	ice core	Rhodes et al. (2012)
-77.84	-102.91	ITASE 01-2	ice core	Schneider et al. (2008)
-79.38	-111.24	ITASE 00-1	ice core	Schneider et al. (2006)
-79.46	-112.09	WDC	ice core	Mitchell et al. (2011)
-84	43	Plateau Remote	ice core	Cole-Dai et al. (2000)

Reference

Adler, R.F. et al., 2003. The Version-2 Global Precipitation Climatology Project (GPCP) Monthly Precipitation Analysis (1979–Present). *Journal of Hydrometeorology*, 4(6), pp.1147–1167.

Ahmed, M. et al., 2013. Continental-scale temperature variability during the past two millennia. *Nature Geoscience*, 6(6), pp.503–503.

Aleinov, I. & Schmidt, G. a., 2006. Water isotopes in the GISS ModelE land surface scheme. *Global and Planetary Change*, 51, pp.108–120.

Allison, G.B. & Hughes, M.W., 1983. The use of natural tracers as indicators of soil-water movement in a temperate semi-arid region. *Journal of Hydrology*, 60(1-4), pp.157–173.

Ammann, C.M. et al., 2007. Solar influence on climate during the past millennium: results from transient simulations with the NCAR Climate System Model. *Proceedings of the National Academy of Sciences of the United States of America*, 104(10), pp.3713–8.

An, W. et al., 2013. Relative humidity history on the Batang–Litang Plateau of western China since 1755 reconstructed from tree-ring δ18O and δD. *Climate Dynamics*, 42(9-10), pp.2639–2654.

Ball, T., 1987. *Calculations Related to Gas Exchange* E. Zeiger, G. D. Farquhar, & I. Cowan, eds., Stanford University Press.

Ballantyne, A.P. et al., 2010. Regional Differences in South American Monsoon Precipitation Inferred from the Growth and Isotopic Composition of Tropical Trees*. *Earth Interactions*, 15(5), pp.1–35.

Barbour, M.M. et al., 2004. Expressing leaf water and cellulose oxygen isotope ratios as enrichment above source water reveals evidence of a Péclet effect. *Oecologia*, 138(3), pp.426–435.

Bégin, C. et al., 2015. Assessing tree-ring carbon and oxygen stable isotopes for climate reconstruction in the Canadian northeastern boreal forest. *Palaeogeography, Palaeoclimatology, Palaeoecology*, 423, pp.91–101.

Berkelhammer, M. & Stott, L.D., 2012. Secular temperature trends for the southern Rocky Mountains over the last five centuries. *Geophysical Research Letters*, 39(17), pp.1–6.

Bhend, J. et al., 2012. An ensemble-based approach to climate reconstructions. *Climate of the Past*, 8(3), pp.963–976.

Bladé, I. et al., 2012. Observed and simulated impacts of the summer NAO in Europe: Implications for projected drying in the Mediterranean region. *Climate Dynamics*, 39(3), pp.709–727.

Blossey, P.N., Kuang, Z. & Romps, D.M., 2010. Isotopic composition of water in the tropical tropopause layer in cloud-resolving simulations of an idealized tropical circulation. *Journal of Geophysical Research: Atmospheres*, 115(24), pp.1–23.

Bohleber, P. et al., 2013. To what extent do water isotope records from low accumulation Alpine ice cores reproduce instrumental temperature series? *Tellus, Series B: Chemical and Physical Meteorology*, 65(1), pp.1–17.

Brienen, R.J.W. et al., 2012. Oxygen isotopes in tree rings are a good proxy for Amazon precipitation and El Nino-Southern Oscillation variability. *Proceedings of the National Academy of Sciences*, 109(42), pp.16957–16962.

Brohan, P. et al., 2006. Uncertainty estimates in regional and global observed temperature changes: A new data set from 1850. *Journal of Geophysical Research Atmospheres*, 111(12), pp.1–21.

Brown, J., Simmonds, I. & Noone, D., 2006. Modeling δ^{18}O in tropical precipitation and the surface ocean for present-day climate. *Journal of Geophysical Research*, 111(D5), p.D05105.

Caley, T., Roche, D.M. & Renssen, H., 2014. using an isotope-enabled global climate model. *Nature Communications*, 5, pp.1–6.

Clausen, H.B. et al., 1988. Glaciological investigation in the Crête area, Central Greenland: A research for a new deep-drilling site. *Annals of Glaciology*, 10, pp.10 – 15.

Cobb, K.M. et al., 2013. Highly Variable El Nino-Southern Oscillation Throughout the Holocene. *Science*, 339(6115), pp.67–70.

Compo, G.P. et al., 2011. The Twentieth Century Reanalysis Project. , (January), pp.1–28.

Conroy, J.L., Cobb, K.M. & Noone, D., 2013. Comparison of precipitation isotope variability across the tropical Paci fi c in observations and SWING2 model simulations. , 118(April), pp.5867–5892.

Craig, H. & Gordon, L., 1965. *Deuterium and oxygen 18 variations in the ocean and the marine atmosphere*,

Crespin, E. et al., 2009. of the Past The 15th century Arctic warming in coupled model simulations with data assimilation. , pp.389–401.

Cullen, L.E. & Grierson, P.F., 2007. A stable oxygen , but not carbon , isotope chronology of Callitris columellaris reflects recent climate change in north-western Australia. , pp.213–229.

D'Arrigo, R. et al., 2008. On the "Divergence Problem" in Northern Forests: A review of the tree-ring evidence and possible causes. *Global and Planetary Change*, 60(3-4), pp.289–305.

Dansgaard, W., 1964. Stable isotope in precipitation. *Tellus*, 16, pp.436–468.

Dansgaard, W., 1954. The O18-abundance in fresh water. *Geochimica et Cosmochimica Acta*, 6(5-6), pp.241–260.

Dee, D.P. et al., 2011. The ERA-Interim reanalysis: Configuration and performance of the data assimilation system. *Quarterly Journal of the Royal Meteorological Society*, 137(656), pp.553–597.

Dee, S. et al., 2015. PRYSM: An open-source framework for PRoxY System Modeling, with applications to oxygen-isotope systems. *Journal of Advances in Modeling Earth Systems*, 7(3), pp.1220–1247.

Dee, S. et al., 2015. SPEEDY-IER: A fast atmospheric GCM with water isotope physics. *Journal of Geophysical Research: Atmospheres*, 120(1), pp.73–91.

Epstein, S. et al., 1951. CARBONATE-WATER ISOTOPIC TEMPERATURE SCALE. *Geological Society of America Bulletin*, 62(4), p.417.

Epstein, S. & Mayeda, T., 1953. S. epstein*.

Evans, M.N. et al., 2013. Applications of proxy system modeling in high resolution paleoclimatology.

Quaternary Science Reviews, 76, pp.16–28.

Evans, M.N., Smerdon, J.E. & Kaplan, A., 2014. Climate field reconstruction uncertainty arising from multivariate and nonlinear properties of predictors. , pp.1–8.

Federer, B., Brichet, N. & Jouzel, J., 1982. Stable Isotopes in Hailstones. Part I: The Isotopic Cloud Model. *Journal of the Atmospheric Sciences*, 39(6), pp.1323–1335.

Fernández-Donado, L. et al., 2013. Large-scale temperature response to external forcing in simulations and reconstructions of the last millennium. *Climate of the Past*, 9(1), pp.393–421.

Field, R.D., 2010. Observed and modeled controls on precipitation $\delta^{18}O$ over Europe: From local temperature to the Northern Annular Mode. *Journal of Geophysical Research Atmospheres*, 115(12), pp.1–14.

Fisher, D.A. et al., 1983. Effect of wind scouring on climatic records from ice-core oxygen-isotope profiles. *Nature*, 301, pp.205–209.

Flanagan, L.B., Comstock, J.P. & Ehieringer, J.R., 1991. Comparison of Modeled and Observed Environmental Influences on the Stable Oxygen and Hydrogen Isotope Composition of Leaf Water in Phaseolus vulgaris L .'. , pp.588–596.

Gat, J.R., 2000. Atmospheric water balance-the isotopic perspective. *Hydrological Processes*, 14(8), pp.1357–1369.

Gillett, N.P., Kell, T.D. & Jones, P.D., 2006. Regional climate impacts of the Southern Annular Mode. *Geophysical Research Letters*, 33(23), pp.1–4.

Goosse, H. et al., 2010. Reconstructing surface temperature changes over the past 600 years using climate model simulations with data assimilation. , 115, pp.1–17.

Goosse, H. et al., 2006. Using paleoclimate proxy-data to select optimal realisations in an ensemble of simulations of the climate of the past millennium. *Climate Dynamics*, 27(2-3), pp.165–184.

Goosse, H., Crespin, E. & Dubinkina, S., 2012. The role of forcing and internal dynamics in explaining the "' Medieval Climate Anomaly ."" , pp.2847–2866.

Grießinger, J. et al., 2011. Late Holocene Asian summer monsoon variability reflected by δ^{18}O in tree-rings from Tibetan junipers. *Geophysical Research Letters*, 38(3), p.n/a–n/a.

Haese, B., Werner, M. & Lohmann, G., 2013. Stable water isotopes in the coupled atmosphere-land surface model ECHAM5-JSBACH. *Geoscientific Model Development*, 6, pp.1463–1480.

Hakim, G.J. et al., 2013. Overview of data assimilation methods. , 21(2), pp.5–6.

Hanna, E. et al., 2011. Greenland Ice Sheet surface mass balance 1870 to 2010 based on Twentieth Century Reanalysis, and links with global climate forcing. *Journal of Geophysical Research Atmospheres*, 116(24), pp.1–20.

Hardy, D.R., 2003. Variability of snow accumulation and isotopic composition on Nevado Sajama, Bolivia. *Journal of Geophysical Research*, 108, pp.1–10.

Hasumi, H. & EMORI, S., 2004. *K-1 coupled model (MIROC) description*,

Hoffmann, G., Werner, M. & Heimann, M., 1998. Water isotope module of the ECHAM atmospheric

general circulation model: A study on timescales from days to several years. *Journal of Geophysical Research*, 103(D14), p.16871.

Houtekamer, P.L. & Mitchell, H.L., 2001. A Sequential Ensemble Kalman Filter for Atmospheric Data Assimilation. *Monthly Weather Review*, 129(1), pp.123–137.

Huffman, G.J. et al., 1997. The Global Precipitation Climatology Project (GPCP) Combined Precipitation Dataset. *Bulletin of the American Meteorological Society*, 78(1), pp.5–20.

Hughes, M.K. & Ammann, C.M., 2009. The future of the past-an earth system framework for high resolution paleoclimatology: Editorial essay. *Climatic Change*, 94(3-4), pp.247–259.

Hurrell, J.W., 1995. Decadal Trends in the North Atlantic Oscillation: Regional Temperatures and Precipitation. *Science*, 269(5224), pp.676–679.

IPCC, 2013. Climate Change 2013: The Physical Science Basis. Summary for Policymakers. *Ipcc*, pp.1–29.

Ishizaki, Y. et al., 2012. Interannual variability of $H_2{}^{18}O$ in precipitation over the Asian monsoon region. *Journal of Geophysical Research*, 117(D16), p.D16308.

Joussaume, S. & Jouzel, J., 1993. Paleoclimatic tracers: an investigation using an atmospheric General Circulation Model under ice age conditions 2. Water isotopes. *Journal of Geophysical Research*, 98(D2), pp.2807–2830.

Joussaume, S., Sadourny, R. & Jouzel, J., 1984. A general circulation model of water isotope cycles in the atmosphere. *Nature*, 311(5981), pp.24–29.

Jouzel, J. et al., 1987. Simulations of the HDO and H 2 18 O atmospheric cycles using the NASA GISS general circulation model: The seasonal cycle for present-day conditions. *Journal of Geophysical Research*, 92(D12), p.14739.

Jouzel, J. et al., 1997. Validity of the Temperature Reconstruction from Water Isotopes in Ice Cores. *J. Geophys. Res.*, 102(C12), pp.26471–26487.

Jouzel, J. et al., 1991. XLaboratoire de Geochimie Centre National de la Re- cherche precipitation events able characteristics . In short , the GCM is a complete Sciences New GCM distributions might 5NASA / Goddard Space Flight Center , Institute point to specific deficiencies in. , 96(90), pp.7495–7507.

Jouzel, J. & Merlivat, L., 1984. Deuterium and oxygen 18 in precipitation: Modeling of the isotopic effects during snow formation. *Journal of Geophysical Research*, 89(D7), p.11749.

Jouzel, J., Merlivat, L. & Roth, E., 1975. Isotopic study of hail. *Journal of Geophysical Research*, 80(36), p.5015.

Juillet--Leclerc, A. & Schmidt, G., 2001. A calibration of the oxygen isotope paleothermometer of coral aragonite from Porites. *Geophysical Research Letters*, 28(21), pp.4135–4138.

Kalnay, E. et al., 1996. The NCEP/NCAR 40-year reanalysis project. *Bulletin of the American Meteorological Society*, 77(3), pp.437–471.

Kanner, L. et al., 2013. Climatologic and hydrologic influences on the oxygen isotope ratio of tree

cellulose in coastal southern California during the late 20th century. *Geochemistry, Geophysics, Geosystems*, 14(10), pp.4488–4503.

Kubota, T., Tsuboyama, Y. & Kabeya, N., 2012. Kubota Application of seasonal variations of deuterium excess to the estimation of water sources of trees in humid areas like Japan. *Hydrological Research Letters*, 6(0), pp.65–69.

Kumar, K.K., 1999. On the Weakening Relationship Between the Indian Monsoon and ENSO. *Science*, 284(5423), pp.2156–2159.

Langebroek, P.M., Werner, M. & Lohmann, G., 2011. Climate information imprinted in oxygen-isotopic composition of precipitation in Europe. *Earth and Planetary Science Letters*, 311(1-2), pp.144–154.

Lee, J.-E. et al., 2007. Analysis of the global distribution of water isotopes using the NCAR atmospheric general circulation model. *Journal of Geophysical Research*, 112(D16), p.D16306.

Lee, J.-E. et al., 2008. Water isotopes during the Last Glacial Maximum: New general circulation model calculations. *Journal of Geophysical Research*, 113(D19), p.D19109.

Lee, J.-E. & Fung, I., 2008. "Amount effect" of water isotopes and quantitative analysis of post-condensation processes. *Hydrological Processes*, 22(1), pp.1–8.

LeGrande, A.N. & Schmidt, G.A., 2006. Global gridded data set of the oxygen isotopic composition in seawater. *Geophysical Research Letters*, 33(12), p.L12604.

LeGrande, A.N. & Schmidt, G.A., 2009. Sources of holocene variability of oxygen isotopes in paleoclimate archives. *Climate of the Past Discussions*, 5(2), pp.1133–1162.

Liu, G. et al., 2013. A model-based test of accuracy of seawater oxygen isotope ratio record derived from a coral dual proxy method at southeastern Luzon Island, the Philippines. *Journal of Geophysical Research: Biogeosciences*, 118(2), pp.853–859.

Liu, G. et al., 2014. Journal of Geophysical Research : Atmospheres. , pp.21–33.

Liu, X. et al., 2013. A 400-year tree-ring δ18O chronology for the southeastern Tibetan Plateau: implications for inferring variations of the regional hydroclimate. *Global and Planetary Change*, 104(0), pp.23–33.

Liu, Z. et al., 2012. Younger Dryas cooling and the Greenland climate response to CO2. *Proceedings of the National Academy of Sciences*, 109(28), pp.11101–11104.

Mann, M.E. et al., 2008. Proxy-based reconstructions of hemispheric and global surface temperature variations over the past two millennia. *Proceedings of the National Academy of Sciences of the United States of America*, 105(36), pp.13252–13257.

Mann, M.E., Bradley, R.S. & Hughes, M.K., 1998. Global-scale temperature patterns and climate forcing over the past six centuries. *Nature*, 392(6678), pp.779–787.

Masson-Delmotte, V. et al., 2008. A Review of Antarctic Surface Snow Isotopic Composition: Observations, Atmospheric Circulation, and Isotopic Modeling*. *Journal of Climate*, 21(13), pp.3359–3387.

Masson-Delmotte, V., M. et al., 2013. Information from Paleoclimate Archives. *Climate Change 2013:*

The Physical Science Basis. Contribution of Working Group I to the Fifth Assessment Report of the Intergovernmental Panel on Climate Change, pp.383–464.

Mathieu, R., 2002. Simulation of stable water isotope variations by the GENESIS GCM for modern conditions. *Journal of Geophysical Research*, 107(D4).

Mathiot, P. et al., 2013. Using data assimilation to investigate the causes of Southern Hemisphere high latitude cooling from 10 to 8 ka BP. *Climate of the Past*, 9(2), pp.887–901.

Merlivat, L. & Jouzel, J., 1979. Global climatic interpretation of the deuterium-oxygen 18 relationship for precipitation. *Journal of Geophysical Research*, 84(C8), p.5029.

Moses, C.S. & Swart, P.K., 2006. Stable isotope and growth records in corals from the island of Tobago : Not simply a record of the Orinoco. *Proceedings 10th International Coral Reef Symposium*, 587, pp.580–587.

Murakami, S., 2002. Dependency of LAI and evapotranspiration on stand age at planted stands of Japanese cypress and cedar and its potential for the application to the management of water conservation forest. *Journal of Japan Society of Hydrology and water resources*, 15(5), pp.461–472.

Nan, S. & Li, J., 2003. The relationship between the summer precipitation in the Yangtze River valley and the boreal spring Southern Hemisphere annular mode. *Geophysical Research Letters*, 30(24), pp.1–4.

Nitta, T. et al., 2014. Representing variability in subgrid snow cover and snow depth in a global land model: Offline validation. *Journal of Climate*, 27(9), pp.3318–3330.

Noone, D. & Simmonds, I., 2002. Associations between delta O-18 of water and climate parameters in a simulation of atmospheric circulation for 1979-95. *Journal of Climate*, 15(22), pp.3150–3169.

North, G.R., Bell, T.L. & Cahalan, R.F., 1982. Sampling Errors in the Estimation of Empirical Orthogonal Funtions. *Monthly Weather Review*, 110(7), pp.699–706.

Okazaki, A. et al., 2015. Interannual variability of isotopic composition in water vapor over western Africa and its relationship to ENSO. *Atmospheric Chemistry and Physics*, 15(6), pp.3193–3204.

Onogi, K. et al., 2007. The JRA-25 Reanalysis. *Journal of the Meteorological Society of Japan*, 85(3), pp.369–432.

Ortega, P. et al., 2014. Characterizing atmospheric circulation signals in Greenland ice cores: insights from a weather regime approach. *Climate Dynamics*, 43(9-10), pp.2585–2605.

Pausata, F.S.R. et al., 2011. Chinese stalagmite δ18O controlled by changes in the Indian monsoon during a simulated Heinrich event. *Nature Geoscience*, 4(7), pp.474–480.

Peterson, T.C. & Vose, R.S., 1997. An Overview of the Global Historical Climatology Network Temperature Database. *Bulletin of the American Meteorological Society*, 78(12), pp.2837–2849.

Porter, T.J. et al., 2014. Spring-summer temperatures since AD 1780 reconstructed from stable oxygen isotope ratios in white spruce tree-rings from the Mackenzie Delta, northwestern Canada. *Climate Dynamics*, 42(3-4), pp.771–785.

Rasmusson, E.M. & Carpenter, T.H., 1983. The Relationship Between Eastern Equatorial Pacific Sea

Surface Temperatures and Rainfall over India and Sri Lanka. *Monthly Weather Review*, 111, pp.517–258.

Rayner, N.A., 2003. Global analyses of sea surface temperature, sea ice, and night marine air temperature since the late nineteenth century. *Journal of Geophysical Research*, 108(D14), p.4407.

Risi, C., Noone, D., Worden, J., Frankenberg, C., Stiller, G., Kiefer, M., Funke, B., Walker, K., Bernath, P., Schneider, M., Bony, S., et al., 2012. Process-evaluation of tropospheric humidity simulated by general circulation models using water vapor isotopic observations: 2. Using isotopic diagnostics to understand the mid and upper tropospheric moist bias in the tropics and subtropics. *Journal of Geophysical Research: Atmospheres*, 117(5), pp.1–25.

Risi, C., Noone, D., Worden, J., Frankenberg, C., Stiller, G., Kiefer, M., Funke, B., Walker, K., Bernath, P., Schneider, M., Wunch, D., et al., 2012. Process-evaluation of tropospheric humidity simulated by general circulation models using water vapor isotopologues: 1. Comparison between models and observations. *Journal of Geophysical Research*, 117, pp.1–26.

Risi, C. et al., 2013. Role of continental recycling in intraseasonal variations of continental moisture as deduced from model simulations and water vapor isotopic measurements. *Water Resources Research*, 49(7), pp.4136–4156.

Risi, C. et al., 2010. Water-stable isotopes in the LMDZ4 general circulation model: Model evaluation for present-day and past climates and applications to climatic interpretations of tropical isotopic records. *Journal of Geophysical Research: Atmospheres*, 115, pp.1–27.

Risi, C., Bony, S. & Vimeux, F., 2008. Influence of convective processes on the isotopic composition (δ^{18}O and δD) of precipitation and water vapor in the tropics: 2. Physical interpretation of the amount effect. *Journal of Geophysical Research*, 113(D19), p.D19306.

Roche, D.M., 2013. δ^{18}O water isotope in the *i*LOVECLIM model (version 1.0) – Part 1: Implementation and verification. *Geoscientific Model Development*, 6(5), pp.1481–1491.

Roden, J.S., Lin, G. & Ehleringer, J.R., 2000. A mechanistic model for interpretation of hydrogen and oxygen isotope ratios in tree-ring cellulose. *Geochimica et Cosmochimica Acta*, 64(1), pp.21–35.

Rozanski, K., Araguás-Araguás, L. & Gonfiantini, R., 1993. Isotopic Patterns in Modern Global Precipitation. *Climate Change in COntinental Isotopic Records*, 78, pp.1–36.

Sano, M. et al., 2012. Increasing aridity over the past 223 years in the Nepal Himalaya inferred from a tree-ring 18O chronology. *The Holocene*, 22, pp.809–817.

Sano, M. et al., 2013. May–September precipitation in the Bhutan Himalaya since 1743 as reconstructed from tree ring cellulose δ18O. *Journal of Geophysical Research: Atmospheres*, 118(15), pp.8399–8410.

Sano, M., Xu, C. & Nakatsuka, T., 2012. A 300-year Vietnam hydroclimate and ENSO variability record reconstructed from tree ring δ18O. *Journal of Geophysical Research: Atmospheres*, 117(12), pp.1–11.

Scheepmaker, R. a. et al., 2015. Validation of SCIAMACHY HDO/H₂O

measurements using the TCCON and NDACC-MUSICA networks. *Atmospheric Measurement Techniques*, 8(4), pp.1799–1818.

Schmidt, G. a. et al., 2005. Modeling atmospheric stable water isotopes and the potential for constraining cloud processes and stratosphere-troposphere water exchange. *Journal of Geophysical Research: Atmospheres*, 110(21), pp.1–15.

Schmidt, G.A., LeGrande, A.N. & Hoffmann, G., 2007. Water isotope expressions of intrinsic and forced variability in a coupled ocean-atmosphere model. *Journal of Geophysical Research*, 112(D10), p.D10103.

Schotterer, U., Stichler, W. & Ginot, P., 2004. the Influence of Post-Depositional Effects on Ice Core Studies : Examples From the Alps , Andes , and Altai. *Plateau*, pp.39–59.

van der Schrier, G. & Barkmeijer, J., 2005. Bjerknes' hypothesis on the coldness during AD 1790–1820 revisited. *Climate Dynamics*, 25(5), pp.537–553.

Schurer, A.P. et al., 2013. Separating forced from chaotic climate variability over the past millennium. *Journal of Climate*, 26, pp.6954–6973.

Shanahan, T.M. et al. et al., 2009. Atlantic forcing of persistent drought in West Africa. *Science (New York, N.Y.)*, 324(5925), pp.377–80.

Shi, C. et al., 2012. Reconstruction of southeast Tibetan Plateau summer climate using tree ring δ18O: Moisture variability over the past two centuries. *Climate of the Past*, 8(1), pp.205–213.

Sime, L.C. et al., 2009. Evidence for warmer interglacials in East Antarctic ice cores. *Nature*, 462(7271), pp.342–345.

Sinha, A. et al., 2015. Trends and oscillations in the Indian summer monsoon rainfall over the last two millennia. *Nature Communications*, 6, p.6309.

Sodemann, H., Masson-Delmotte, V., et al., 2008. Interannual variability of Greenland winter precipitation sources: 2. Effects of North Atlantic Oscillation variability on stable isotopes in precipitation. *Journal of Geophysical Research*, 113(D12), p.D12111.

Sodemann, H., Schwierz, C. & Wernli, H., 2008. Interannual variability of Greenland winter precipitation sources: Lagrangian moisture diagnostic and North Atlantic Oscillation influence. *Journal of Geophysical Research*, 113(D3), p.D03107.

Sontakke, N. a., Pant, G.B. & Singh, N., 1993. Construction of All-India Summer Monsoon Rainfall Series for the Period 1844–1991. *Journal of Climate*, 6, pp.1807–1811.

Steiger, N.J. et al., 2014. Assimilation of Time-Averaged Pseudoproxies for Climate Reconstruction. *Journal of Climate*, 27(1), pp.426–441.

Sternberg, L. & Ellsworth, P.F.V., 2011. Divergent Biochemical Fractionation, Not Convergent Temperature, Explains Cellulose Oxygen Isotope Enrichment across Latitudes. *PLoS ONE*, 6(11), p.e28040.

Stewart, M.K., 1975. Stable isotope fractionation due to evaporation and isotopic exchange of falling waterdrops: Applications to atmospheric processes and evaporation of lakes. *Journal of Geophysical*

Research, 80(9), pp.1133–1146.

von Storch, H. et al., 2000. Combining paleoclimatic evidence and GCMs by means of Data Assimilation Through Upscaling and Nudging,. *Proc. 11th Symposium on Global Climate Change Studies*, pp.28–31.

von Storch, H., Langenberg, H. & Feser, F., 2000. A Spectral Nudging Technique for Dynamical Downscaling Purposes. *Monthly Weather Review*, 128(10), pp.3664–3673.

Takata, K., Emori, S. & Watanabe, T., 2003. Development of the minimal advanced treatments of surface interaction and runoff. *Global and Planetary Change*, 38(1-2), pp.209–222.

Taylor, K.E., Stouffer, R.J. & Meehl, G. a, 2007. A Summary of the CMIP5 Experiment Design. *World*, 4(January 2011), pp.1–33.

Thompson, D.M. et al., 2011. Comparison of observed and simulated tropical climate trends using a forward model of coral δ18O. *Geophysical Research Letters*, 38(L14706), p.doi:10.1029/2011GL048224.

Thompson, D.W.J. & Wallace, J.M., 2000. Annular Mode in the Extratropical Circulation. Part I : Month-to-Month Variability. *Journal of Climate*, 13(1999), pp.1000–1016.

Tindall, J.C., Valdes, P.J. & Sime, L.C., 2009. Stable water isotopes in HadCM3: Isotopic signature of El Niño-Southern Oscillation and the tropical amount effect. *Journal of Geophysical Research: Atmospheres*, 114(4), pp.1–12.

Tremoy, G. et al., 2012. A 1-year long δ ¥n 18O record of water vapor in Niamey (Niger) reveals insightful atmospheric processes at different timescales. *Geophysical Research Letters*, 39, pp.1–5.

Tremoy, G. et al., 2014. Journal of Geophysical Research : Atmospheres. , pp.1–25.

Treydte, K.S. et al., 2006. The twentieth century was the wettest period in northern Pakistan over the past millennium. *Nature*, 440(7088), pp.1179–1182.

Urey, H., 1935. Isotopic exchange. *J. Am. Chem. Soc.*, 57(2), pp.321–327.

Urey, H.C. et al., 1951. Measurement of Paleotemperatures and Temperatures and the Southeastern United States. *Bulletin of the geological society of America*, 62(April), pp.399–416.

Vinther, B.M. et al., 2010. Climatic signals in multiple highly resolved stable isotope records from Greenland. *Quaternary Science Reviews*, 29(3-4), pp.522–538.

Vinther, B.M., 2003. NAO signal recorded in the stable isotopes of Greenland ice cores. *Geophysical Research Letters*, 30(7), p.1387.

Vuille, M., 2003. Modeling δ^{18}O in precipitation over the tropical Americas: 1. Interannual variability and climatic controls. *Journal of Geophysical Research*, 108(D6), p.4174.

Vuille, M. et al., 2005. Stable isotopes in precipitation in the Asian monsoon region. *Journal of Geophysical Research: Atmospheres*, 110, pp.1–15.

Vuille, M. & Werner, M., 2005. Stable isotopes in precipitation recording South American summer monsoon and ENSO variability: Observations and model results. *Climate Dynamics*, 25(4), pp.401–

413.

Watanabe, M. et al., 2010. Improved climate simulation by MIROC5: Mean states, variability, and climate sensitivity. *Journal of Climate*, 23(23), pp.6312–6335.

Werner, M. et al., 2000. Borehole versus isotope temperatures on Greenland : Seasonality does matter The disagreement in ice cores are biased by a substantially temperature (Ts) and the isotopic composition of precipitation were defined for tagging . Over each continent was (u. *Geophys. Res. Lett.*, 27(5), pp.723–726.

Werner, M. et al., 2011. Stable water isotopes in the ECHAM5 general circulation model: Toward high-resolution isotope modeling on a global scale. *Journal of Geophysical Research: Atmospheres*, 116(15), pp.1–15.

Werner, M. & Heimann, M., 2002. Modeling interannual variability of water isotopes in Greenland and Antarctica. *Journal of Geophysical Research*, 107(D1), p.4001.

Wernicke, J. et al., 2015. Variability of summer humidity during the past 800 years on the eastern Tibetan Plateau inferred from δ18O of tree-ring cellulose. *Clim. Past*, 11(2), pp.327–337.

Whitaker, J.S. & Hamill, T.M., 2002. Ensemble Data Assimilation without Perturbed Observations. *Monthly Weather Review*, 130(7), pp.1913–1924.

White, J.W.C. et al., 1997. The climate signal in the stable isotopes of snow from Summit, Greenland: Results of comparisons with modern climate observations. *Journal of Geophysical Research*, 102(C12), p.26425.

Widmann, M. et al., 2010. Using data assimilation to study extratropical Northern Hemisphere climate over the last millennium. *Climate of the Past*, 6(5), pp.627–644.

Wilson, D.R. & Ballard, S.P., 1999. A microphysically based precipitation scheme for the UK meteorological office unified model. *Quarterly Journal of the Royal Meteorological Society*, 125(557), pp.1607–1636.

Xu, C. et al., 2015. A tree-ring cellulose δ18O-based July–October precipitation reconstruction since AD 1828, northwest Thailand. *Journal of Hydrology*.

Xu, C., Zheng, H., et al., 2013. Oxygen isotope signatures preserved in tree ring cellulose as a proxy for April-September precipitation in Fujian, the subtropical region of southeast China. *Journal of Geophysical Research: Atmospheres*, 118, pp.12805–12815.

Xu, C., Sano, M. & Nakatsuka, T., 2013. A 400-year record of hydroclimate variability and local ENSO history in northern Southeast Asia inferred from tree-ring δ18O. *Palaeogeography, Palaeoclimatology, Palaeoecology*, 386, pp.588–598.

Xu, C., Sano, M. & Nakatsuka, T., 2011. Tree ring cellulose δ18O of Fokienia hodginsii in northern Laos: A promising proxy to reconstruct ENSO? *Journal of Geophysical Research: Atmospheres*, 116(24), pp.1–12.

Xu, H., Hong, Y. & Hong, B., 2012. Decreasing Asian summer monsoon intensity after 1860 AD in the global warming epoch. *Climate Dynamics*, 39(7), pp.2079–2088.

Yaseef, N.R. et al., 2009. Ecohydrology of a semi-arid forest: partitioning among water balance components and its implications for predicted precipitation changes. *Ecohydrology*, 130(February), p.n/a–n/a.

Yoshimura, K. et al., 2003. A quantitative analysis of short-term 18O variability with a Rayleigh-type isotope circulation model. *Journal of Geophysical Research*, 108(D20), p.4647.

Yoshimura, K. et al., 2008. Historical isotope simulation using Reanalysis atmospheric data. *Journal of Geophysical Research*, 113(D19), p.D19108.

Yoshimura, K. et al., 2006. Iso-MATSIRO, a land surface model that incorporates stable water isotopes. *Global and Planetary Change*, 51(1-2 SPEC. ISS.), pp.90–107.

Yoshimura, K. & Kanamitsu, M., 2013. Incremental Correction for the Dynamical Downscaling of Ensemble Mean Atmospheric Fields. *Monthly Weather Review*, 141(9), pp.3087–3101.

Yoshimura, K., Miyoshi, T. & Kanamitsu, M., 2014. Observation system simulation experiments using water vapor isotope information. *Journal of Geophysical Research: Atmospheres*, pp.1–21.

Yoshimura, K., Oki, T. & Ichiyanagi, K., 2004. Evaluation of two-dimensional atmospheric water circulation fields in reanalyses by using precipitation isotopes databases. *Journal of Geophysical Research D: Atmospheres*, 109(20), pp.1–13.